University of Southampton

Faculty of Engineering and Physical Sciences

School of Engineering

Materials Informatics Study on Magnesium based Alloy Design Optimisation

A grain-resolved statistical study on recrystallisation and grain growth

by

Haoran Yi

Thesis for the degree of Doctor of Philosophy

https://doi.org/10.5258/SOTON/PG/T106

May 19th 2026

University of Southampton

Abstract

Faculty of Engineering and Physical Sciences

School of Engineering

Doctor of Philosophy

Materials Informatics Study on Magnesium based Alloy Design Optimisation

A grain-resolved statistical study on recrystallisation and grain growth

by

Haoran Yi

Magnesium (Mg) and its alloys are the lightest structural metal in common engineering applications, offering substantial weight reductions compared with aluminium and steel. Therefore, they are attractive for lightweight design in sectors such as automotive and aerospace. However, wider adoption remains limited by relatively unsatisfying mechanical properties, which makes the improvement of Mg alloys important for reducing vehicle mass and associated carbon emission. Most of the strengthening strategies are related to thermal mechanical processing, where plastic deformation and subsequent annealing will determine the final microstructure. During annealing, two microstructural evolution progresses—recrystallisation and grain growth, together decide the final crystallographic texture and grain size, which are two critical microstructural features for Mg alloys. Therefore, a mechanistic understanding of recrystallisation and grain growth is essential for optimising heat treatment parameters and achieving improved properties.

Nevertheless, despite decades of efforts, the mechanisms controlling recrystallisation and grain growth in Mg alloys remain disputed. For example, the origin of rare-earth texture has been variously attributed to solute drag and particle pinning, preferential nucleation and oriented growth, etc. In practice, these factors coexist and interact during annealing, making it difficult to separate an individual factor for investigation. Despite recent development in advance characterisation, the ability of efficiently quantifying microstructural evolution to perform factor resolved study is still in absence. Accordingly, the key gap is grain-resolved informatics in time-resolved datasets, i.e. tracking of individual grains throughout large datasets and synthesise statistical outcome.

Therefore, the aim of this thesis is to develop deliciated grains tracking method and combine with recent advancements in two-dimensional (2D) and three-dimensional (3D) characterisations to revisit long-standing questions, within the annealing related

microstructural evolution of Mg. The outcome contains well-structured, time-resolved dataset with tracked information of each individual grain, which not only clarify debated questions in physical metallurgy, but also accelerated materials informatics approaches for the optimisation of Mg alloys design.

For recrystallisation, quasi-in-situ electron backscatter diffraction (EBSD) was used to capture grain-scale evolution during annealing. Three datasets were collected from two alloys: Mg–3Al–1Zn (AZ31, one dataset) and Mg–2.4Zn–0.2Ce (wt.%) (ZE20, two datasets). To enable statistically robust analysis, an automated grain tracking toolbox, Track-Rex, was developed to track individual grains across large quasi-in-situ datasets. Tracking was performed for more than 40,000 grains within approximately ten minutes and outputs structured datasets are suitable for straight forward analysis. Application of Track-Rex clarifies several debated aspects of recrystallisation, including growth and shrinkage behaviour of recrystallised grains, texture evolution in rare earth containing alloy systems, and the contribution of preferential nucleation sites.

For grain growth, quasi-in-situ laboratory-based diffraction contrast tomography (LabDCT) was employed to investigate microstructural evolution in four-dimensional space (3D, 3D + time). Six interrupted annealing steps under argon flow was performed on a WE43 alloy, an effective scanning protocol and reconstruction procedure was established to yield a large, trackable 4D grain growth evolution dataset, across a 4 mm-hight, 0.8 mm-diameter rod. Track-4DGG was built for with capability of tracking grains individually, as clusters, or for user-defined subsets. The resulting statistical datasets enabled analysis of 4D growth kinetics and the behaviours of shrinking, normal growth, and abnormal growth, including a correlation with spatial position,

Overall, this work establishes practical interrupted annealing and characterisation workflows for generating large microstructural evolution datasets and delivers automated tracking toolboxes that convert such datasets into structured, analysis-ready formats. The combined experimental and informatics framework advances understanding of recrystallisation and grain growth in Mg alloys, while providing a scalable route towards predictive modelling and data-driven processing/design optimisation.

Key words: Mg alloys, recrystallisation, grain growth, texture evolution, EBSD, LabDCT, grains tracking, materials informatics.

Table of Contents

Table of Contents ..... **III**

Table of Tables ..... **VIII**

Table of Figures ..... **X**

Research Thesis: Declaration of Authorship ..... **XXI**

Acknowledgments ..... **XXIII**

Definitions and Abbreviations ..... **XXIV**

Chapter 1 Introduction **1**

Chapter 2 Literature review **4**

2.1 General information of magnesium **4**

2.2 Crystallography of magnesium **5**

2.3 Design and strengthening of magnesium alloys **11**

2.3.1 Solid solution strengthening 14

2.3.2 Precipitation strengthening 16

2.3.3 Grain refinement 18

2.3.4 Texture modification 22

2.3.5 Summary 24

2.4 Processing of magnesium alloys **24**

2.4.1 Cold deformation 25

2.4.2 Hot deformation 26

2.5 Annealing of magnesium alloys 28

2.5.1 Recrystallisation 29

2.5.2 Grain growth 31

2.5.3 Texture evolution 33

2.6 Studies of microstructural evolution in magnesium alloys 33

2.6.1 Classic investigations 34

2.6.2 Applications of advanced characterisations 37

2.6.3 Materials informatics and data-driven approaches 38

2.7 Materials informatics in alloy design 40

2.7.1 Applications in recrystallisation 44

2.7.2 Applications in grain growth 45

2.8 Alloy systems in this thesis 47

2.8.1 Mg-Al-Zn series and AZ31 49

2.8.2 Mg-Zn-RE series and ZE20 51

2.8.3 Mg-Y-RE series and WE43 53

2.8.4 Summary 54

2.9 Research focus of this thesis 55

Chapter 3 Materials and methodology 59

3.1 Materials 59

3.2 Materials processing 62

3.2.1 AZ31 cold rolling 63

3.2.2 ZE20 cold rolling 64

3.2.3 ZE20 extrusion and cold rolling 64

3.2.4 WE43 extrusion and electrical discharge machining 66

3.3 Interrupted annealing procedure 66

3.4 Materials characterisation 70

3.4.1 Optical microscope 70

3.4.2 Quasi-in-situ electron backscatter diffraction 71

3.4.3 Quasi-in-situ laboratory diffraction contrast tomography 73

3.4.4 Three-dimensional electron backscatter diffraction 80

3.5 Data Processing and toolbox development 81

3.5.1 Data processing software 81

3.5.2 Grain tracking algorithm and coding 81

3.5.3 Tracking uncertainty and confidence assessment 89

3.5.4 Comparison with existing grain-tracking approaches 91

3.5.5 Toolbox operation in MATLAB 94

3.5.6 Toolbox operation in Python 97

3.5.7 Author contribution statement 99

Chapter 4 Statistical grains tracking throughout recrystallisation 101

4.1 Introduction 101

4.2 Results 104

4.2.1 Microstructure and texture evolution 104

4.2.2 Statistical results from grains tracking 107

4.2.3 Recrystallisation at different annealing steps 112

4.3 Discussion 119

4.3.1 Recrystallisation kinetics 119

4.3.2 Texture evolution 122

4.4 Conclusion 126

Chapter 5 Specific grains tracking from shear bands 128

5.1 Introduction 128

5.2 Results 133

5.2.1 Microstructure after cold deformation 133

5.2.2 Nucleation at early-stage recrystallisation 134

5.2.3 Statistical results from grains tracking 136

5.3 Discussion 138

5.3.1 Recrystallisation kinetics and texture evolution 138

5.3.2 Recrystallisation from different nucleation sites 140

5.4 Conclusion 146

Chapter 6 Statistical grains tracking throughout grain growth 148

6.1 Introduction 148

6.2 Results 151

6.2.1 Four-dimensional grain growth kinetics 151

6.2.2 Statistical results from grains tracking 155

6.2.3 Spatially resolved grain growth behaviour 165

6.3 Discussion 169

6.3.1 Microstructural evolution and abnormal grain growth 170

6.3.2 Spatial heterogeneity and surface restriction 173

6.4 Conclusion 176

Chapter 7 Conclusive discussion and summary 180

7.1 Implications for magnesium alloy and process design 183

7.2 Positioning of this work within materials informatics 184

Chapter 8 Future work 187

8.1 Grain boundary features and abnormal grain growth 187

8.2 Comparison between LabDCT and 3D-EBSD 190

8.3 Prediction model of recrystallisation and grain growth 191

8.4 Track toolbox family 193

Appendix A [list of publications and attended conferences] 195

List of References 196

Table of Tables

Table 2.1 Common principal deformation modes in Mg. 6

Table 2.2 The CRSS values of prismatic ⟨a⟩ slip and pyramidal ⟨c+a⟩ slip in Mg alloys . 10

Table 2.3 ASTM alloy designation for Mg alloys [37]. 12

Table 2.4 ASTM temper and heat-treatment designations for Mg alloys. 13

Table 2.5 Solubility of alloying elements in Mg matrix [25]. 15

Table 2.6 summarises representative examples of materials informatics applied to alloy development and optimisation, illustrating the range of modelling approaches and the types of design questions that can be addressed. 43

Table 2.7 summarises representative examples where data-driven methods have been applied to recrystallisation and grain growth, illustrating both the modelling strategies and the kinds of questions that can be addressed. 46

Table 3.1 Nominal chemical composition of alloys used in this thesis (wt.%)..... 60

Table 3.2 Material form, sample history, and role within the thesis..... 63

Table 3.3 Quasi-in-situ annealing design for cold rolled AZ31 and ZE20 68

Table 3.4 Quasi-in-situ annealing design for ZE20 extrusion and cold rolling..... 68

Table 3.5 Quasi-in-situ annealing design for WE43 grain growth..... 69

Table of Tables

Table 4.1 Number and area fraction of recrystallized grains in the ZE20 sample. 110

Table 4.2 Number and area fraction of recrystallized grains in the AZ31 sample. 111

Table 4.3 Average grain size of the recrystallized grains in the ZE20 sample. 114

Table 4.4 Average grain size of the recrystallized grains in the AZ31 sample. 115

Table 5.1 Average grain size of quasi-in-situ annealing of ZE20 sample. 142

Table 6.1 Summarised grain growth behaviour obtained from tracking results. 164

Table of Figures

Figure 2.1 Schematic illustration of slip and twinning systems in Mg: (a) a unit cell of hexagonal close-packed crystal (b) basal, prismatic, first and second order pyramidal slip, and tension, compression twinning systems [20]. 7

Figure 2.2 Geometrical relationships between the tensile axis, slip plane, and slip direction used to calculate the resolved shear stress in a single crystal [22]. 8

Figure 2.3 Critical resolved shear stress values in pure Mg and versus temperature [25]. 9

Figure 2.4 Typical room temperature stress strain curves for Mg–Y binary alloys at different yttrium contents [49]. 16

Figure 2.5 Transmission electron microscopy results of WE43 alloy after solution treatment and hot extrusion. (a, b) Morphology and distribution of precipitated phase. (c, d) Dynamic recrystallised grains and boundary morphology. (e) Morphology of block-like phases [54]. 18

Figure 2.6 Engineering stress-strain curves of Mg–3Gd alloys at different average grain sizes obtained by different annealing conditions [57]. 20

Figure 2.7 A summarise of literature data showing (a) strength vs. grain size, (b) elongation vs. grain size for Mg and Mg alloys [58]. 21

Figure 2.8 (a) Basal pole figures for Mg–Zn–Zr–Gd and Mg–Zn–Zr–Ce for rolled and annealed states. (b) Basal pole figures for Mg–1Ce and Mg–1Gd for rolled and annealed states [15,60]. 23

Figure 2.9 Schematic relationship between alloy design, processing, microstructure and properties. 24

Figure 2.10 Directions of Mg alloys development [25]..... 48

Figure 3.1 As-extruded microstructure: (a) extruded hollow profile, (b) EBSD Inverse Pole Figure (IPF) map and (0001) pole figure..... 65

Figure 3.2 WE43 extruded bar and schematic drawing for EDM cut. 66

Figure 3.3 Optical microscopy image of as received WE43 extruded bar, sample was cut near the rod EDMed sample. The observed plan is ND-TD plane. Average grain size is calculated to be 18.9 µm. 71

Figure 3.4 Experimental setup and processing for diffraction images. 75

Figure 3.5 Raw diffraction image of the same sample projection: (a)140 minutes, (b) 800 minutes, the diffraction spots of same grains if highlighted by the red circle 78

Figure 3.6 Reconstruction quality. (a) Selected 3D volume at 12 minutes annealing time and (b) corresponding completeness distribution with mean value of 60% 79

Figure 3.7 Overview of the LabDCT outcome 79

Figure 3.8 A comparison between LabDCT and 3D-EBSD 80

Figure 3.9 Examples of grain correlation using Track-Rex in a ZE20 sample: (a) reference selection and initial displacement vector, (b) estimation of neighbour position, (c) searching, (d) matching, (e) iteration. The numbers in bracket indicate the centroid positions of reference grains and displacement vector in (a). 83

Figure 3.10 Workflow of Track-Rex. 86

Figure 3.11 Examples of grain correlation using Track-Rex in a ZE20 sample. (a-f) EBSD maps on different annealing conditions. (g-k) Evolution of the RXed grains originated from EBSD2. (l-p) Contributions of RXed grains from different annealing conditions to the microstructure. 88

Figure 3.12 Track-Rex Algorithm. 96

Figure 4.1 Raw EBSD maps of the ZE20 and AZ31 samples. The ZE20 sample of (a) as-rolled, and annealed at 400 ℃ for (b) 16 min, (c) 80 min. The AZ31 sample of (d) as-rolled, and annealed at 320 ℃ for (j) 8.5 min (d) 34 min. The corresponding pole figures of all grains in the ZE20 and AZ31 samples are shown in (g-i) and (j-l), respectively. 106

Figure 4.2 EBSD orientation and basal pole maps of: (a-h) the ZE20 sample under different annealing conditions, (i-p) the AZ31 sample under different annealing conditions. The numbers on the pole figures indicate the texture intensities. 107

Figure 4.3 Contributions of the RXed grains originated from different annealing steps to the microstructure evolution. (a-e) RXed grains in the ZE20 sample at different annealing step. (f-k) RXed grains in the AZ31 sample at different annealing step. The deformed grains are in blank while the RXed grains are coloured based on their nucleation steps. Tracked grains refer to grains for which a reliable correlation was identified between successive EBSD maps using the Track-Rex criteria. Grains without a reliable candidate in the following step were classified as consumed. 109

Figure 4.4 Recrystallisation behaviours of the RXed grains in early recrystallisation stage. (a-c) All, consumed and maintained RXed grains from ZE/2 step. (d) Maintained RXed grains at ZE/3. (e) Growth rate distribution of the maintained grains. (f-h) Shrinking, stable, and growing RXed grains from ZE/2. (i-k) All, consumed and maintained RXed grains from AZ/2 step. (l) Maintained RXed grains at AZ/3. (m) Growth rate distribution of the maintained grains. (n-p) Shrinking, stable, and growing RXed grains from AZ/2..... 113

Figure 4.5 Grain growth behaviours of the maintained RXed grains in middle recrystallisation stage. (a) Growth rate distributions of the RXed grain originated from different annealing steps. (b-g) Basal pole maps of the shrinking, stable, and growing RXed grain from ZE/2 and ZE/3 steps. (h-m) Basal pole maps of the shrinking, stable, and growing RXed grain from AZ/2 and AZ/3 steps..... 117

Figure 4.6 EBSD grain and orientation maps of newly formed recrystallized grains at different annealing steps. (a-g) ZE20 sample, (h-n) AZ31 sample..... 118

Figure 4.7 Grain growth behaviours of the maintained RXed grains in late recrystallisation stage. (a) Growth rate distributions of the RXed grain originated from different annealing steps. (b-g) Basal pole maps of the shrinking, stable, and growing RXed grain from ZE/4 and ZE/5 steps. (h-m) Basal pole maps of the shrinking, stable, and growing RXed grain from AZ/4 and AZ/6 steps. Growth rate is defined by equation (3.1). 119

Figure 4.8 Schematic of recrystallisation behaviours in the ZE20 and AZ31 sample. (a) Nucleating and consuming activities during annealing. (b) Grain size evaluation of the RXed grains from nucleation to the final annealing step. 120

Figure 4.9 Grain boundaries evaluation the ZE20 and AZ31 sample. (a, b) Misorientation angle distributions of all grains in the ZE20 sample. (c, d) Misorientation angle distributions of all grains in the AZ31 sample. (e, f) Grain boundary maps of all grains in the AZ31 sample. The axis distribution of the special misorientation boundary peaks are superimposed in misorientation angle distribution maps. The length fraction of 55-58º <$1\bar{1}00$> boundary is attached in (e, f). 125

Table of Figures

Figure 5.1 Microstructure after cold rolling: (a) EBSD IPF map, (b) corresponding band contrast map, (c) (0001) pole figure, (d) misorientation angle distribution. 134

Figure 5.2 Nucleation event at shear bands in ZE2 (annealed at 400℃ for 4 minutes): (a) EBSD IPF map, (b) tracking results with deformed grains in grey and recrystallised grains in IPF colour, (c) grain size distribution, (d) (0001) pole figure of the deformed grains and (e) recrystallised grains. 135

Figure 5.3 Entire recrystallisation process and grains tracking results: (a)-(f) IPF maps of the same region from nucleation to nearly fully recrystallised, together with texture evolution of (0001) pole figure. (a')-(f') Tracking results demonstrated by colouring grains by their nucleation sequence, a light blue grain in ZE7 means it was nucleated at ZE2 and was maintained till the final annealing step. Apart from recrystallised grains, deformed grains are coloured in grey. Tracked grains refer to grains for which a reliable correlation was identified between successive EBSD maps using the Track-Rex criteria. Grains without a reliable candidate in the following step were classified as consumed. 137

Figure 5.4 Statistical results representing the recrystallisation progress: (a) area fraction and (b) number frequency of recrystallised grains at different annealing steps. The light bule bar stands for the grains nucleated no later than 4 minutes in ZE2, of which both area fraction and number frequence drop along with annealing time..... 138

Figure 5.5 The texture evolution of recrystallised grains subsets, each row corresponds to the same group of recrystalised grains nucleated at (a) ZE2, (b) ZE3, (c) ZE4, (d) ZE5 and their texture evolution along upcoming annealing steps. 140

Figure 5.6 Average grain size of recrystallised grains formed at different annealing steps. Each group contains grains first detected at the same step and tracked through later annealing. Although the surviving early-formed grains become larger with annealing time, many of them are consumed, so their final area fraction decreases. 143

Figure 5.7 Grains behaviour of SBs induced nucleation from 4 minutes to 9 minutes: (a) all SBs nucleation no later than 4 minutes and their (a1) consumed subset and (a2) maintained subset. (b) All SBs nucleation at 9 minutes and their (b1) consumed subset and (b2) maintained subset; (a1')-(b2') grain boundaries misorientation angle distribution as well as theoretical random disorientation of grains subsets. 145

Figure 6.1 Experimental setup and results overview. (a) X-Ray Diffraction imaging condition. (b) Raw diffraction image of one projection from the first LabDCT scan and its (c) segmented diffraction spots. Reconstruction results of the 12 minutes annealing step are presented with the views of (d) the whole scanned volume and (e) select sub-volume of 500 μm height for this study. (f) The completeness distribution plot of the whole 4 mm scanned volume. 153

Figure 6.2 Grain size evolution of the Mg rod during annealing at 490 °C. (a)-(f) Reconstructed 3D volume of LabDCT at 12, 32, 80, 140, 800 and 2240 minutes, respectively..... 154

Figure 6.3 An example of abnormal grain growth behaviour between (a)-(b) 80 minutes and (c)-(d) 140 minutes. One grain exhibited a large GR of 19.7 is extracted and highlighted as G1 in (a) 80 minutes and (c) 140 minutes, with transparent surrounding grains. Neighbouring grains G2-G5 are also tracked and annotated in (b) 80 minutes and (d) 140 minutes annealing step datasets. G1 had abnormally grown and consumed G2(partially), G3 (entirely) and G5 (partially). G4 had also grown by consuming G5 (partially). 156

Figure 6.4 Grain size distribution of (a) 140 minutes annealing step and (b) 800 minutes annealing step..... 157

Figure 6.5 An example of AGG behaviour between (a)-(b) 140 minutes and (c)-(d) 800 minutes. One grain with large GR of 20.1 is extracted and highlighted as G1 in (a) 140 minutes and (c) 800 minutes, with transparent surrounding grains. Neighbouring grains G2-G8 are also tracked and annotated in (b) 140 minutes and (d) 800 minutes annealing step datasets. G1 had abnormally grown and consumed not only its small neighbours as G4 and G5 (entirely), but also its large neighbours as G2, G3, G6, G7 and G8 (partially). Similar AGG cases can be extracted using Track-4DGG within 10 minutes. 158

Figure 6.6 Grains tracking mechanism of Track-4DGG. (a) Algorithm flowchart schematic: neighbours of the input reference grain pair at order N define the matching frontier, and a spatial vector computed from the matched grains centroids displacement will direct the searching window for order N+1. Candidate grains within the window are ranked by the difference including orientation, shape parameter and boundaries features. The most matched candidate that satisfies user defined threshold is paired, otherwise considered as consumed. (b) Tracking procedure between 12 minutes and 32 minutes annealing steps, represented by the grains calculated during each iteration in 12 minutes dataset. 161

Figure 6.7 Representative 4D tracking of a single grain and its neighbour cluster: (a1)-(a6) individual grain tracking, (b1)-(b6) grain cluster tracking, (c1)-(c4) subsets of the grain clusters split by growth rate. The grain-growth classification is based on the Track-4DGG criteria described in Chapter 3. Grains were classified according to their tracked volume evolution between successive LabDCT datasets, while ambiguous or poorly reconstructed grains were treated conservatively. 161

Figure 6.8 Grain size distribution of different grain growth behaviour subsets within 80 minutes annealing step and their correspondences grains in 140 minutes dataset. (a)-(b) Consumed and shrunk subset, (c)-(d) grains with normal growth rate, (e)-(f) grains with abnormal growth rate. Volumed-weighted

average grains size DV is adopted to annotate the mean size of grains subsets..... 163

Figure 6.9 Spatially resolved grain growth behaviour during annealing from 80 to 140 minutes. Grains centroid spots in the 80 minutes annealing dataset coloured by their growth behaviour in the (a) outer, (b) middle and (c) inner sections. Volume fractions and growth rates in the spatial sections of (d) consumed and shrunk grains, (e) grains with normal GR and (f) grains with abnormal GR. 166

Figure 6.10 Grain-resolved tracking of the outermost two grain layers during the annealing series. (a1)-(a6): Evolution of the grain structure as well as grain size, from 12 to 2240 minutes. (b1)-(b5): The consumed grains subset for the surface grains at each annealing step..... 168

Figure 6.11 (a) BSE image and (b) zoomed in image near surface region, (c) EBSD IPF map, and EDS Map showing the element distributions of (d) Oxygen, (e) Yttrium and (f) Neodymium 169

Figure 6.12 General growth behaviour from 80 minutes to 140 minutes 171

Figure 6.13 Grain growth behaviour versus grain size. 172

Figure 6.14 Absorption contrast tomography (ACT) images of the same slice from different annealing time steps. (a) 12, (b) 32, (c) 80, (d) 140, (e) 800, and (f) 2240 minutes. 175

Table of Figures

Figure 8.1 Examining grain boundaries evolution for the same grains from 12 minutes to 32 minutes. 189

Figure 8.2 Preliminary results for the calculated integral curvature versus growth behaviour..... 189

Figure 8.3 A slice of the EBSD IPF map from the sample after 2240 annealing, (b) a corresponding slice from the reconstructed LabDCT dataset located in a closely adjacent region after extensive data comparison and alignment. 191

Figure 8.4 Training process for the prediction model of AGG occurrence. 192

Research Thesis: Declaration of Authorship

Print name: Haoran Yi

Title of thesis: Materials Informatics Study on Magnesium based Alloy Design Optimisation: A grain-resolved statistical study on recrystallisation and grain growth

I declare that this thesis and the work presented in it are my own and has been generated by me as the result of my own original research.

I confirm that:

1. This work was done wholly or mainly while in candidature for a research degree at this University;
2. Where any part of this thesis has previously been submitted for a degree or any other qualification at this University or any other institution, this has been clearly stated;
3. Where I have consulted the published work of others, this is always clearly attributed;
4. Where I have quoted from the work of others, the source is always given. With the exception of such quotations, this thesis is entirely my own work;
5. I have acknowledged all main sources of help;
6. Where the thesis is based on work done by myself jointly with others, I have made clear exactly what was done by others and what I have contributed myself;
7. Parts of this work have been published as:

[1]. Zeng X, **Yi H**, Zeng Z, et al. Track-Rex: A universal toolbox for tracking recrystallization nucleation and grain growth behaviors in polycrystalline materials[J]. Journal of Materials Science & Technology, 2024, 197: 149-159.

[2]. **Yi H**, Li H, Zeng X, et al. Investigation of shear bands induced nucleation and recrystallisation behaviour in a rare earth containing magnesium alloy[J]. Materials Characterization, 2025, 222: 114809.

[3]. **Yi H**, Zeng X, Guan D. Data Science Approach for EBSD Data Processing and Materials Design for Magnesium Alloy[C]//TMS Annual Meeting & Exhibition. Cham: Springer Nature Switzerland, 2024: 49-53.

[4]. **Yi H**, Douglas G, Oddershede J, Donoghue J, Liu H, Chen B, Guan D. 4D grain growth evolution and statistical tracking in a magnesium alloy using lab-based diffraction contrast tomography (LabDCT), submitted to Scripta Materialia, now under revision.

The author contributed to all the experimental work, data analysis, visualisation, and manuscript writing and editing.

Signature: Haoran Yi..... Date: 15th May 2026 .....

Acknowledgments

Back to that day in November 2021, when I flew across half of the planet for this PhD and was boredly planning my later life during the 10 hours' flight, I have no idea how this 4-year journey will be like. Today is January 2026, I am writing this last part of my thesis, and the memory of that flight reappears in my mind. Then, looking back to my late twenty's, those life plans suddenly become nothing, for the journey itself and the accompanies, are the most precious experience. It has been a golden journey I had, and here is my gratitude to the ones that make it golden.

First, my greatest thanks to my supervisor Dr. Dikai Guan, who has been supporting me during this whole journey. In research, I have received more support than I could ever wish, with regards to experiments, data analysis, also for conferences and writing. More importantly, the precious lesson I have learnt from his guidance is the way of conducting research, the flow of logic, angle of thinking and persistence for details. Beyond research, he has also been a reliable tutor in life, supported me during tough periods with strong and stable mindset.

Second, I would like to thank all colleagues that supported this project, Dr. Xun Zeng for the conceptualization of Track-Rex, also being a reliable senior in both work and life. Dr. Gareth Douglas for the acquisition of LabDCT data and Dr. Jette Oddershede for the guidance on reconstruction. Further thanks to Dr. Jack Donoghue for the 3D-EBSD and promotion of our Track-Rex toolbox, Dr. Haiming Liu for the research guidance and collaboration. Then, all my precious friends, Dr. Xingjian Zhao, Dr. Zhiyu Quan, Dr. Yanheng Xie, Dr. Yeajin Lee, without any of them, I could not have complete this journey. In the end, my thanks to Miss Qidi Zhou, for simply appears in my life, and restore the grace of it.

Finally, to my dearest parents, for their unconditional love and support, words cannot express my grateful to them but to love back.

Definitions and Abbreviations

2D/3D ..... Two/three-dimensional

3D-EBSD ..... Three-dimensional electron backscatter diffraction

3DXRD ..... Three-dimensional X-ray diffraction

4D..... Four-dimensional (3D + time)

ACT..... Absorption contrast tomography

AGG..... Abnormal grain growth

ANN..... Artificial neural network

BCC ..... Body-centred cubic

BC ..... Band contrast

BSE..... Backscattered electron

CDRX ..... Continuous dynamic recrystallisation

CRSS ..... Critical resolved shear stress

DCT ..... Diffraction contrast tomography

DRX ..... Dynamic recrystallisation

EBSD..... Electron backscatter diffraction

ECAP ..... Equal channel angular pressing

EDM..... Electrical discharge machining

EDS..... Energy dispersive spectroscopy

FCC ..... Face-centred cubic

GBCD..... Grain boundary character distribution

GND..... Geometrically necessary dislocation

GNN..... Graph neural network

GOS ..... Grain orientation spread

HAGB ..... High-angle grain boundary

HCP ..... Hexagonal close-packed

HEDM ..... High-energy diffraction microscopy

IPF ..... Inverse pole figure

LabDCT ..... Laboratory diffraction contrast tomography

LAGB..... Low-angle grain boundary

MRD..... Multiples of random distribution

MUD ..... Multiples of uniform density

NGG..... Normal grain growth

OM..... Optical microscopy

OPS ..... Oxide polishing suspension

PFZ ..... Precipitate-free zone

PSN ..... Particle-stimulated nucleation

SB ..... Shear band

SEM ..... Scanning electron microscopy

SF ..... Schmid factor

SIBM ..... Strain-induced boundary migration

SPD..... Severe plastic deformation

SPFB ..... Second-phase particles-free band

TEM..... Transmission electron microscopy

UTS ..... Ultimate tensile strength

XRD ..... X-ray diffraction

Chapter 1 Introduction

Magnesium (Mg) is the lightest structural metal, and its low density makes Mg alloys attractive for lightweight design in transportation and aerospace applications. Despite this potential, wrought Mg products remain less popular to be used at room temperature compared to aluminium alloys because the hexagonal close-packed (HCP) crystal structure promotes the development of strong basal textures and limits the number of available deformation modes, leading to restricted mechanical properties. Improving the performance of wrought Mg alloys therefore relies on controlling the composition–processing–microstructure relationship, with grain size and crystallographic texture as the primary microstructural targets. In this context, annealing-driven recrystallisation and the subsequent grain growth are of critical importance, as they restore ductility, modify texture, and determine the final grain size distribution. However, key aspects of recrystallisation and grain growth remain debated, particularly in rare-earth containing Mg alloys. Recent advances in characterisation techniques now allow time-resolved observation of microstructural evolution during annealing, but these approaches generate large and complex datasets that are difficult to be analysed using conventional manual workflows. This challenge motivates the development of automated data-processing strategies capable of extracting grain-scale statistics to support materials informatics approaches.

Materials informatics adopts data-centric methods, including data structuring, feature extraction, statistical analysis, and machine learning—to establish quantitative links between composition, processing, microstructure, and properties, thereby enabling more efficient materials development than traditional trial-and-error approaches. Nevertheless, a practical gap remains in the analysis of time-resolved microstructure datasets. Techniques such as electron

backscatter diffraction (EBSD) can provide sequential two-dimensional orientation maps, while laboratory diffraction contrast tomography (LabDCT) enables non-destructive reconstruction of four-dimensional grain structure evolution within bulk material. The resulting datasets are data-intensive, and yet still commonly analysed by low-throughput or manual approaches. Without robust and hight-throughput data processing strategies, it remains difficult to acquire well-structured, analysis-ready datasets, limiting a broader application of materials informatics to microstructural evolution investigation.

The aim of this thesis is to combine time-resolved microstructure experiments with automated data-processing methods to quantify recrystallisation and grain growth in three representative wrought Mg alloys—AZ31, ZE20, and WE43—and to develop datasets that can support predictive modelling of microstructure evolution. For recrystallisation, large quasi-in-situ EBSD datasets are acquired during interrupted annealing of AZ31 and ZE20 and analysed using Track-Rex, a toolbox developed in this work for automated grain correlation across extensive EBSD time series. Track-Rex enables the tracking of more than 40,000 grains within approximately ten minutes and outputs structured datasets suitable for statistical and data-driven analysis. The tracked EBSD results provide grain-scale insight into recrystallisation kinetic, grains shrinkage and consumption, texture evolution from different nucleation sites, the origin and development of rare-earth texture. For grain growth, quasi-in-situ LabDCT is employed to reconstruct three-dimensional grain structures in WE43 during interrupted annealing steps. A high-quality four-dimensional dataset is established and processed by Track-4DGG, a dedicated spatial tracking toolbox that enables analysis of both normal and abnormal grain growth, as well as their correlations with spatial position and crystallographic orientations.

Overall, this thesis establishes practical workflows during interrupted-annealing and characterisation for generating large microstructure evolution datasets and develops automatic tracking toolboxes that convert such datasets into structured, analysis-ready formats. These contributions help shift Mg microstructure studies from qualitative comparisons towards quantitative analysis with grain-resolved statistics, which strengthens the basis for mechanism investigation and supports a wider application of materials informatics.

The thesis is organised to build a coherent argument from background, to methodology, to grain-resolved analysis. Chapter 2 reviews the physical metallurgy of Mg alloys, with emphasis on recrystallisation, grain growth, texture evolution and data-driven approaches. Chapter 3 introduces the materials, interrupted annealing procedures, characterisation methods and grain-tracking workflows. Chapters 4 and 5 focus on recrystallisation tracking using quasi-in-situ EBSD and Track-Rex, first at the general statistical level and then at the level of shear-band-induced nucleation. Chapter 6 extends the tracking concept to four-dimensional LabDCT grain growth in WE43 using Track-4DGG. Chapter 7 integrates the main findings and discusses their implications for Mg alloy design and process optimisation, while Chapter 8 identifies future work arising from the limitations and opportunities of the present study.

Chapter 2 Literature review

This chapter reviews the literature underpinning the alloy design of Mg and related annealing driven microstructural evolution. Starting with a brief of Mg and its key information including crystallography, strengthening mechanisms and thermomechanical processing. It then reviews recrystallisation and grain growth of Mg alloys, with emphasis on how three/four-dimensional (3D/4D) characterisation techniques and materials informatics approaches can be applied to quantify microstructure evolution. This chapter concludes by introducing the studied alloy systems in this thesis and identifying research gaps and focus.

2.1 General information of magnesium

Magnesium is an abundant alkaline earth metal, constituting ~2 wt.% of the Earth's crust, meanwhile identified as the third most dissolved element in seawater (~0.13 wt.%) [1]. Owing to its high chemical reactivity, Mg exists predominantly as compounds in minerals. Commercially important Mg minerals include the carbonates dolomite ($MgCO_3 \cdot CaCO_3$) and magnesite ($MgCO_3$), the hydroxide brucite ($Mg(OH)_2$), the halide carnallite ($KCl \cdot MgCl_2 \cdot 6H_2O$), and silicates such as olivine ($(Mg,Fe)_2SiO_4$) [2]. The extraction process of metallic Mg is energy intensive due to the stability of the aforementioned minerals, necessitating high energy input. Industrial production of Mg is mainly achieved by two routes: (i) electrolysis of $MgCl_2$ derived from brines or seawater; (ii) thermal reduction of MgO which mostly from the calcination of dolomite [3]. Historically, the bright combustion of Mg enabled early applications as pyrotechnics and photographic flash, the scale of Mg production was expended during World War II due to the demand for incendiaries and lightweight components

in vehicles and aircrafts. Today, Mg are mainly applied as die-cast structural components, particularly in the automotive and aerospace sectors where mass reduction is critical, representative applications including cross-car beams and gearbox shell [4,5]. Other than structural applications, Mg is also widely adopted in body and case of portable electronics (e.g., laptop, camera, etc.), where low density and stiffness are beneficial [3,6]. In addition, biodegradable Mg are being developed for orthopaedic implants, for the avoidance of secondary removal surgery [7–9]. Nevertheless, broader utilisation remains constrained by the limitation of mechanical performance, corrosion behaviour, processing conditions, service environment, etc. [10–13]. These obstacles continue to motivate innovations on the approaches of alloy design, especially the emerging materials informatics methods, which can potentially accelerate alloy design optimisation across composition–processing–microstructure–property relationships [14,15]. The aforementioned development barriers ultimately trace back to the crystallography of Mg, which is reviewed in the following section.

2.2 Crystallography of magnesium

Mg locates in the second group and the third period of the periodic table with an atomic number of 12. At ambient conditions, pure Mg crystallises in the hexagonal close-packed structure (space group $P6_3/mmc$, No. 194) with lattice parameters a = 0.32094 nm and c = 0.52108 nm ($c/a \approx 1.624$), which is close to the ideal HCP arrangement ($c/a = 1.633$) [16]. This proximality of c/a to the ideal value reflects the close-packed atomic geometry of the Mg lattice. From alloy design perspective, substitutional solid solubility is often discussed by the Hume–Rothery criteria [17], which states an atomic size difference within 15% is generally favourable

for extensive solubility. In practice, the solubility of specific alloying elements in Mg also depends on electronic and chemical interactions and temperature [18].

The plasticity of Mg is governed by the HCP crystal structure. At room temperature, only a limited number of deformation modes is readily activated, compared with face centred cubic (FCC) and body centred cubic (BCC) metals. The crystallographic planes and directions in HCP structure are commonly described using the four index Miller indices [19], with {hkil} for the plane and <uvtw> for the direction. The common principal deformation modes in Mg are summarised and visualised in Table 2.1 and Figure 2.1 [20].

Table 2.1 Common principal deformation modes in Mg.

Deformation modes	Plane	Direction
Basal ⟨a⟩ slip	{0001}	<11$\bar{2}$0>
Prismatic ⟨a⟩ slip	{10$\bar{1}$0}	<11$\bar{2}$0>
Pyramidal I ⟨a⟩ slip	{10$\bar{1}$1}	<11$\bar{2}$0>
Pyramidal I ⟨c+a⟩ slip	{10$\bar{1}$1}	<11$\bar{2}$3>
Pyramidal II ⟨c+a⟩ slip	{11$\bar{2}$2}	<11$\bar{2}$3>
Tension twinning	{10$\bar{1}$2}	<$\bar{1}$011>
Compression twinning	{10$\bar{1}$1}	<$\bar{1}$012>
Compression twinning	{10$\bar{1}$3}	<$\bar{3}$032>

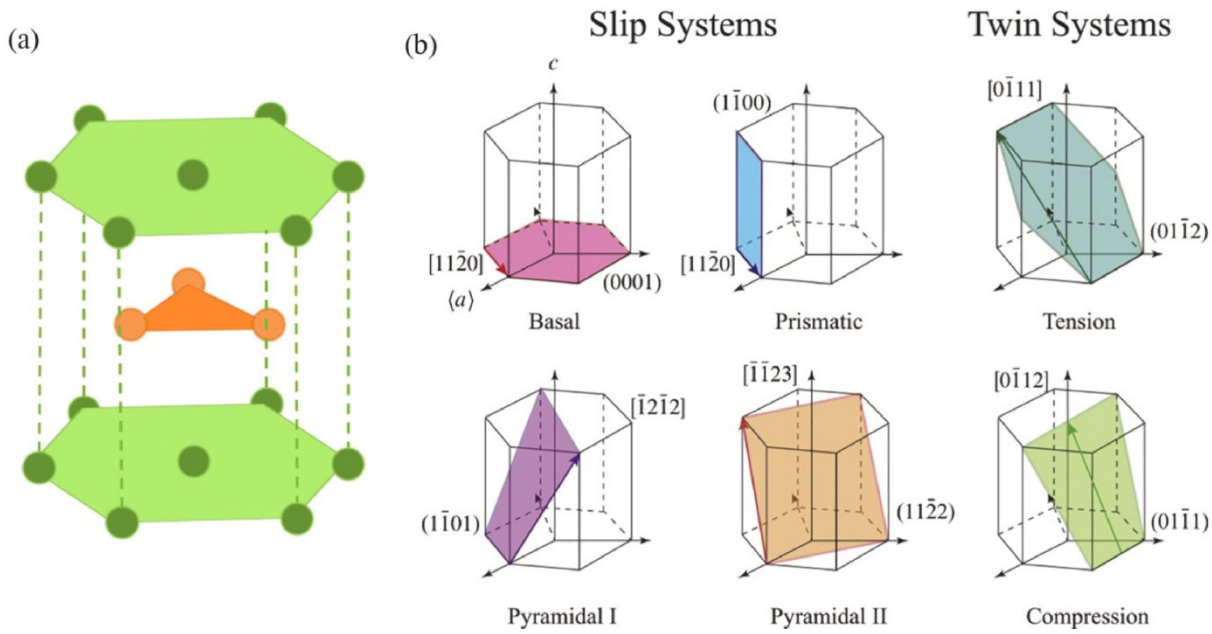

Figure 2.1 Schematic illustration of slip and twinning systems in Mg: (a) a unit cell of hexagonal close-packed crystal (b) basal, prismatic, first and second order pyramidal slip, and tension, compression twinning systems [20].

At single crystal level, plastic deformation initiates when the resolved shear stress on the slip or twinning plane reaches its critical value, which is defined as the critical resolved shear stress (CRSS). For uniaxial loading, the Schmid's law is expressed as Equation 2.1 [21].

$$\sigma_{crss} = \frac{F\cos\lambda}{A/\cos\emptyset} = \sigma_y \cos\lambda\cos\emptyset \quad (2.1)$$

Where F is the applied force, A is the plane area, σy is the loading stress, ϕ is the angle between loading axis and the plane normal, λ is the angle between loading axis and the slip/twinning direction. The value of cosλcosϕ is defined as the Schmid factor m ($0 \leq m \leq 0.5$). The geometry for resolving an applied stress along a slip/twinning plane is schematically illustrated in Figure 2.2 [22].

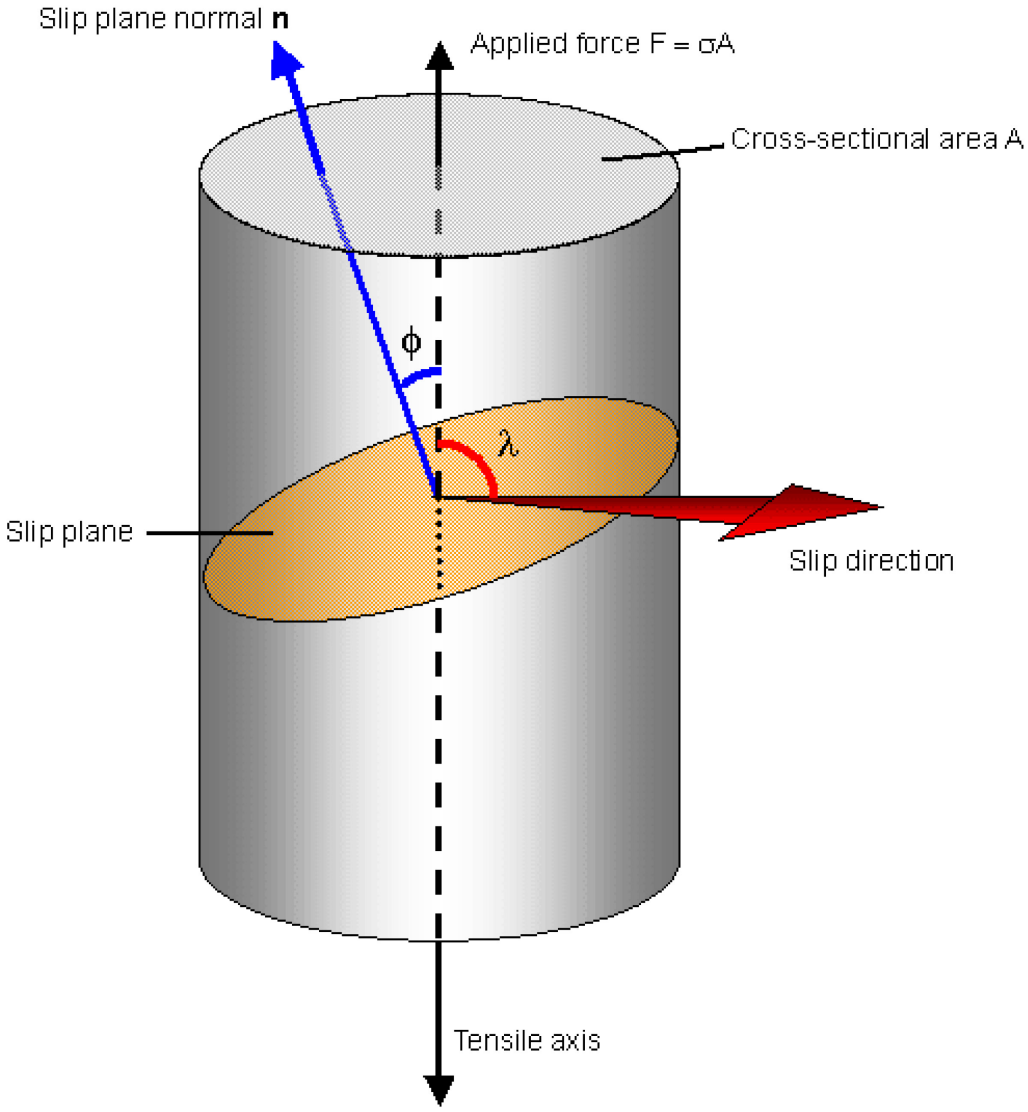

Figure 2.2 Geometrical relationships between the tensile axis, slip plane, and slip direction used to calculate the resolved shear stress in a single crystal [22].

Hypothetically, if multiple deformation modes have comparable CRSS values, the system with the largest Schmid factor would be expected to activate, which often described as the primary deformation mode. However, in Mg, the CRSS values exhibit distinct difference,

especially between basal and non-basal systems. Hence, the activation of slip or twinning in Mg is governed by both Schmid factor and CRSS value [23,24].

The CRSS values of typical deformation modes versus temperature in pure Mg is described in Figure 2.3 [25]. Basal ⟨a⟩ slip exhibits notably low CRSS value regardless the temperature, measurement in pure Mg single crystals reported a value of ~0.7 MPa [26]. By contrast, non-basal systems show much higher CRSS values at room temperature and decreases along temperature [26,27].

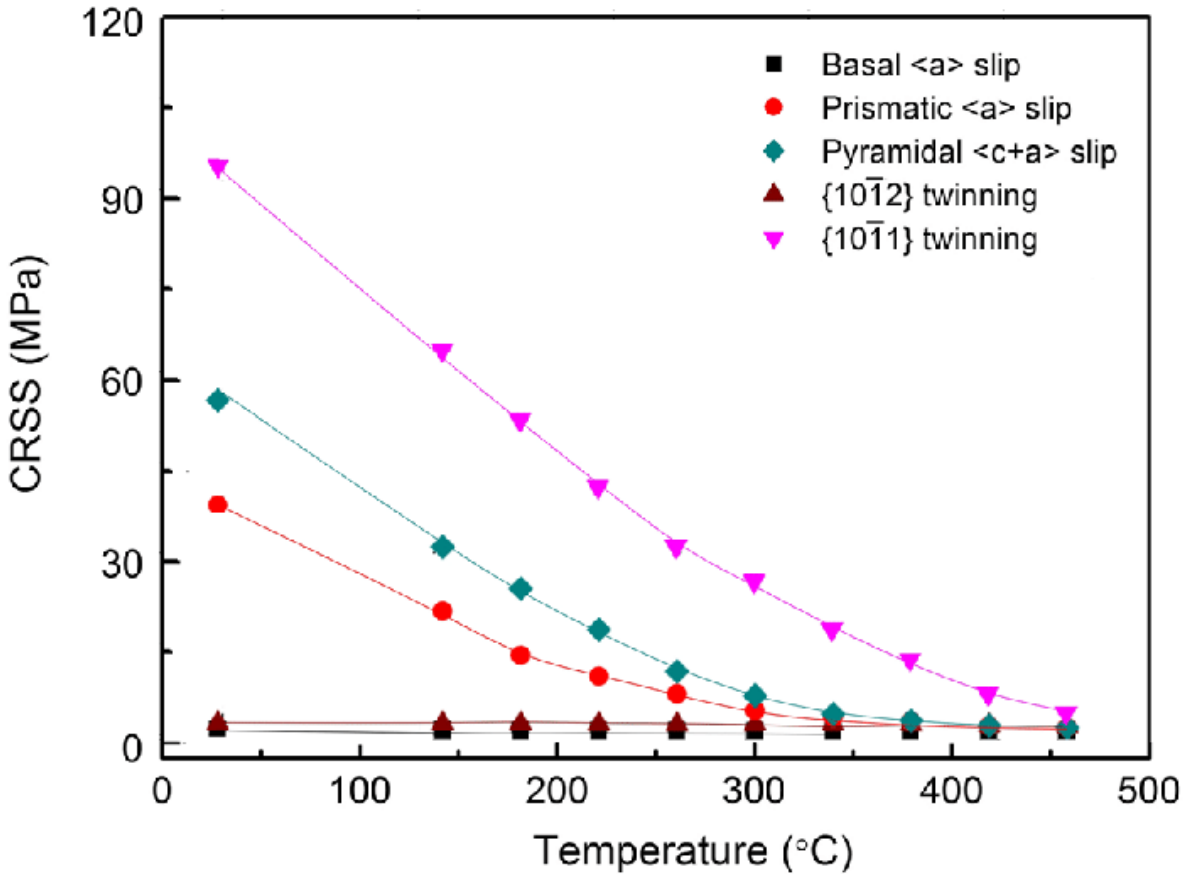

Figure 2.3 Critical resolved shear stress values in pure Mg and versus temperature [25].

Prismatic ⟨a⟩ slip typically shows moderate CRSS values and pyramidal ⟨c+a⟩ slip shows higher values under most condition. The addition of alloying elements such as rare-earth, calcium, zinc and yttrium could increase CRSS value for both basal and non-basal slip. The representative values of non-basal slips in Mg alloys at room temperature are summarised in Table 2.2. Consequently, the difference between basal and non-basal CRSS values (by order of ~10^2) makes basal slip easier to activate than non-basal systems at ambient conditions.

Table 2.2 The CRSS values of prismatic ⟨a⟩ slip and pyramidal ⟨c+a⟩ slip in Mg alloys

Slip system	Alloy system	CRSS (approximately)	Ref
prismatic〈a〉	Mg–Y–Ca	105 ± 4 MPa	[28]
pyramidal〈c + a〉	Mg–Y–Ca	203 ± 7 MPa	[28]
prismatic〈a〉	Mg–Ca–Zn	85 MPa	[29]
pyramidal〈c + a〉	Mg–Ca–Zn	85 MPa	[29]
prismatic〈a〉	Mg–Y	38 MPa	[30]
pyramidal〈c + a〉	Mg–Y	36 ± 5MPa	[30]

Hence, the plasticity of Mg at room temperature is dominated by basal slip, with tension twins providing an additional mode that accommodates c-axis deformation. However, the twin activation is orientation-dependent and often provide limited contribution [31]. Therefore, Mg possess insufficient independent systems for strain compatibility, as it cannot accommodate arbitrary shape changes along the c-axis. This limitation is commonly discussed in the context of the Von Mises criterion [32], which requires five independent systems for homogeneous plastic deformation, reflecting the importance of non-basal and twinning activation in Mg. In addition, the scarcity of available non-basal systems at low temperature results in the poor formability and promotes the development of strong basal textures during cold deformation process.

At elevated temperatures, the activation barriers for prismatic ⟨a⟩ and pyramidal ⟨c+a⟩ slips decrease substantially, enabling multiple slip activation. The increased availability of deformation modes improves strain accommodation and thus explains the better ductility and of Mg at higher temperatures [25].

In addition to temperature, alloying elements, mechanical processing and heat treatment [23,33,34] can further modify the formability and strength, these alloy design strategies are discussed in the following section.

2.3 Design and strengthening of magnesium alloys

Pure Mg exhibits poor strength and limited ductility [35]. Hence, alloy design and microstructural control are essential to achieve ideal combination of strength and ductility [36]. To avoid ambiguity in composition and condition, the American Society for Testing and

Materials (ASTM) codification system [37] is adopted throughout this thesis when referring to Mg alloys. In this designation, the first two letters stand for the two principal alloying elements, the following two numbers indicate their approximate nominal contents in weight percentage, and sometimes an additional letter (e.g., A, B) distinguishing compositional variants may follows. A temper designation (e.g., -T6) is appended to describe the processing and heat treatment condition, as detail listed in Table 2.3 and Table 2.4. For example, AZ91E-T6 denotes a high-purity variant of AZ91, which nominally has ~9 wt.% of aluminium and ~1 wt.% of zinc, with manganese additions for impurity control, in a solution treated and artificially aged condition.

Table 2.3 ASTM alloy designation for Mg alloys [37].

Alloying Element	**Abbreviation Letter**
Aluminium	A
Manganese	M
Rare Earth	E
Silver	Q
Yttrium	W
Zinc	Z
Zirconium	K

Table 2.4 ASTM temper and heat-treatment designations for Mg alloys.

Code	Condition
O	Annealed, Recrystallised (wrought)
T1	Cooled and naturally aged
T2	Annealed (cast products)
T3	Solution heat treated then cold work
T4	Solution heat treated
T5	Cooled then artificially aged
T6	Solution heat treated and artificially aged
T7	Solution heat treated and stabilised
T8	Solution treated, cold work, artificially aged
T9	Solution treated, artificially aged, cold work
T10	Cooled, artificially aged cold work

Commercial alloy systems are considerate about price and performance. For example, Mg–Al–Zn alloys (AZ series) are widely deployed for its low cost and good castability, Al and Zn provide solid solution strengthening and precipitation strengthening arises from Mg–Al intermetallic phases (e.g. β-$Mg_{17}Al_{12}$). However, wrought products of AZ series often develop

strong basal textures after mechanical processing, thus results in limited ductility and pronounced anisotropy [38–40].

By contrast, rare-earth containing alloy systems such as the Mg–Y–RE alloys (WE series), are designed with optimised properties, particularly at elevated temperature—through RE solutes and thermal stable precipitates. In addition, RE containing wrought alloys typically exhibit weakened basal textures after thermomechanical processing and annealing, which contributes to improved formability and more isotropic mechanical behaviour [41–44].

The Mg alloy design generally aims at mitigating room temperature formability without sacrificing strength or achieving improvements simultaneously, which is possible through tailoring composition, processing, and heat treatments. In other words, through combining multiple strengthening mechanisms, including solid solution strengthening, precipitation strengthening, grain refinement, and texture modification [38,45]. The following subsections focus on each mechanism specifically.

2.3.1 Solid solution strengthening

Solid solution strengthening arises when alloying elements are dissolved into matrix and increase resistance to dislocation motion through lattice–dislocation interactions. Since interstitial solid solution is limited in Mg matrix, strengthening solutes act predominantly as substitutional solid solution. The strengthening efficiency depends on solute types and concentration as well as size misfit [45–47].

Aluminium and zinc exhibit appropriate solubility in Mg matrix at solution temperature and thus provide stable strengthening effect in common wrought alloys (e.g., AZ series). By

contrast, yttrium and rare-earth solutes such as gadolinium provide stronger strengthening effect per solute atom but limited by solubilities. Once the maximum solubility is exceeded, strengthening mechanism shifts from solid solution strengthening to precipitation strengthening [38,46–48]. Figure 2.4 shows representative room temperature stress strain curves for Mg–Y binary alloys at different yttrium concentrations, illustrating how the solute additions modify the mechanical performance [49].

From a heat treatment perspective, solution treatment followed by rapid quenching is commonly applied to maximise retained solute in the matrix and establish a starting state for subsequent ageing, which is introduced in the next subsection [38,45]. Table 2.5 summarises the solubility of common alloying elements in the Mg matrix [25].

Table 2.5 Solubility of alloying elements in Mg matrix [25].

Element	at%	wt%	Condition
Aluminium	11.8	12.7	Eutectic
Manganese	1.0	2.2	Peritectic
Zinc	2.4	6.2	Eutectic
Yttrium	3.75	12.5	Eutectic
Zirconium	1.0	3.8	Peritectic
Silver	3.8	15.0	Eutectic
Lanthanum	0.04	0.23	Eutectic
Cerium	0.1	0.5	Eutectic
Neodymium	1	3	Eutectic
Samarium	1	6.4	Eutectic
Gadolinium	4.53	23.49	Eutectic
Terbium	4.6	24.0	Eutectic
Thulium	6.3	31.8	Eutectic
Ytterbium	1.2	8.0	Eutectic

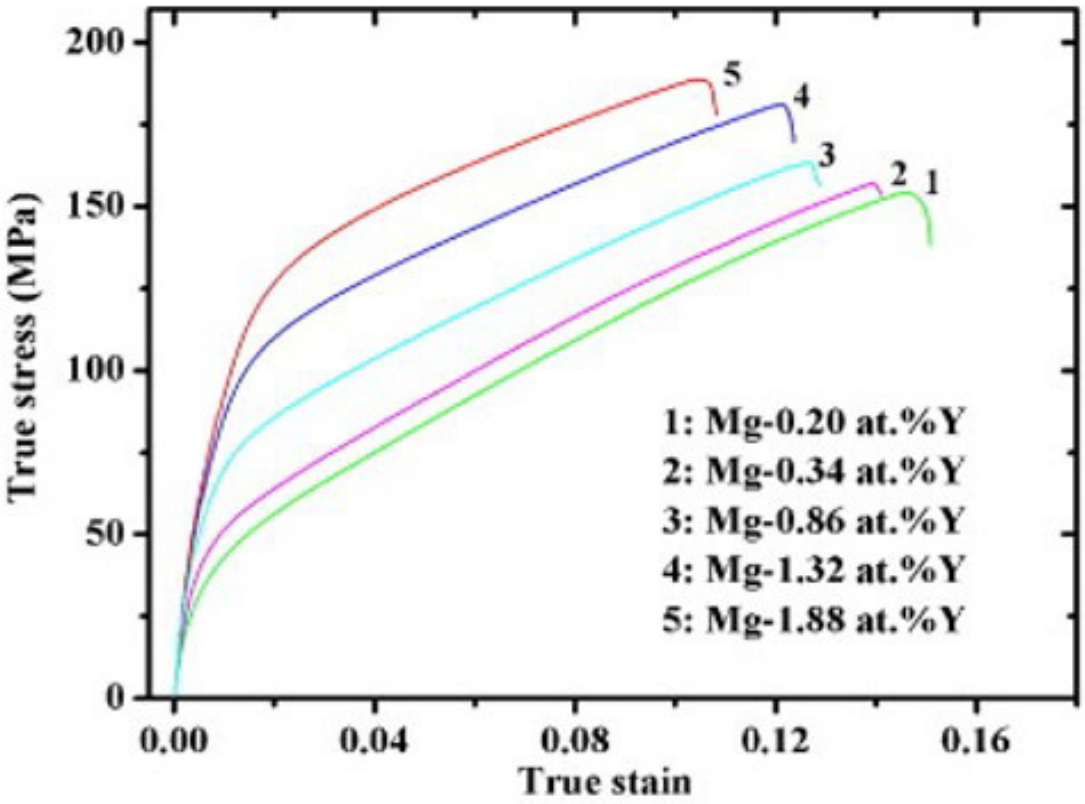

Figure 2.4 Typical room temperature stress strain curves for Mg–Y binary alloys at different yttrium contents [49].

2.3.2 Precipitation strengthening

Precipitation strengthening is achieved by establishing fine distribution of second phase particles. After solution treatment and rapid quenching, ageing promotes solute clustering and precipitation. Strength increases because precipitates impede dislocation motion, therefore the strengthening effect strongly depends on precipitate size, density, distribution and coherency [38,45].

The morphology and habit plane are two important features regarding to strengthening effect in Mg, because it decides which deformation modes are most effectively obstructed. For

example, the same β-$Mg_{17}Al_{12}$ precipitate phase exhibits different age hardening response between Mg-Al systems and Al-Mg systems. This is because the β-$Mg_{17}Al_{12}$ precipitates normally habit on non-basal planes or grain boundaries in Mg matrix, thus has limited ability to obstacle basal slip, which is often the dominant modes in Mg. On the other hand, in FCC Al matrix, multiple equivalent slip systems can be intersected more effectively, therefore gives more strengthening effect. Mg–Zn systems normally demonstrate better age hardening response, because the morphologies of Mg–Zn intermetallic (e.g., $MgZn_2$) phases are more effective against basal dislocations motions [38,45,50,51].

In rare earth containing alloys, multiple precipitation sequences can form during ageing, including plate-like or rod-like phase on prismatic plane, these morphologies can provide more effective resistance to basal dislocation motion. In addition, these precipitates can contribute to high-temperature performance because of their thermal stability against coarsening [52,53]. Figure 2.5 shows an example of transmission electron microscopy (TEM) results recording the precipitation distribution of an WE43 alloy after solution treatment and hot extrusion, where nano-size precipitation contributes to excellent mechanical properties [54].

In practice, precipitation strengthening depends on heat treatment design. Solution time and temperature, ageing scheme are often tailored to maximise fine precipitate distribution while avoid over-ageing [38,39].

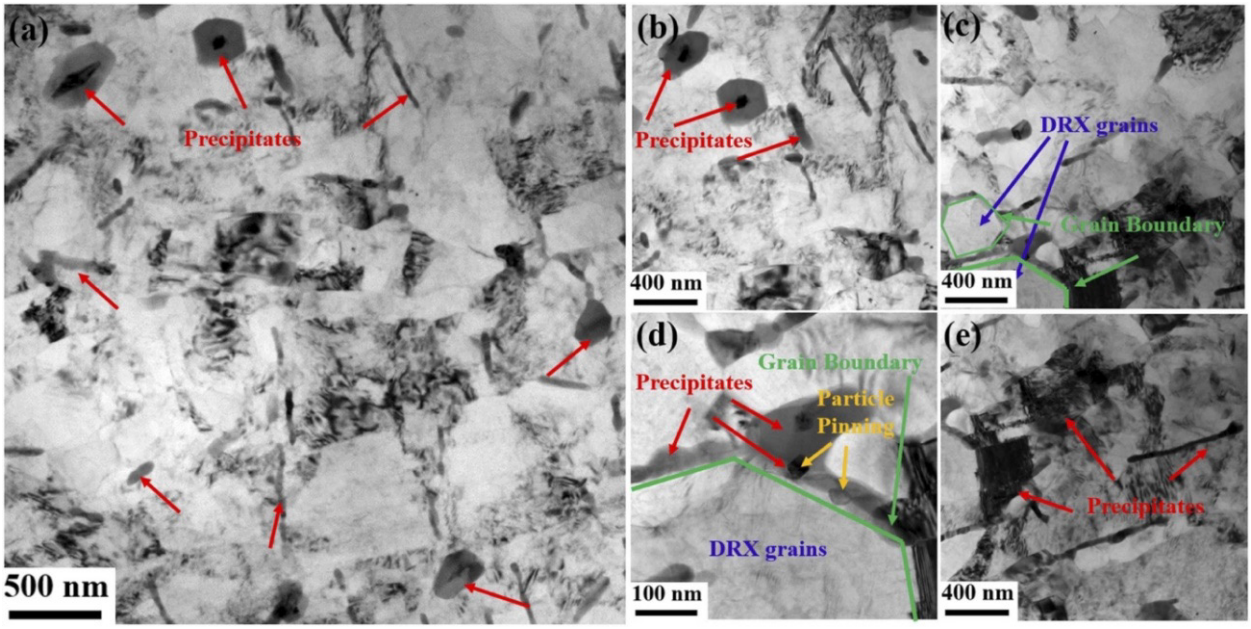

Figure 2.5 Transmission electron microscopy results of WE43 alloy after solution treatment and hot extrusion. (a, b) Morphology and distribution of precipitated phase. (c, d) Dynamic recrystallised grains and boundary morphology. (e) Morphology of block-like phases [54].

2.3.3 Grain refinement

Grain refinement is an effective strengthening mechanism in Mg alloys. Following the Hall–Petch relationship as showed in equation (2.2), the yield stress σy increases as grain size d decreases because increased boundaries fraction impedes dislocation motion. Physically, σ_0 represents the intrinsic lattice resistance to dislocation motion within grains, whereas k is the Hall–Petch coefficient quantifying the strengthening contribution from grain boundaries via dislocation pile-up effects. The value of k is relatively higher in Mg comparing with other FCC metals [55,56].

$$\sigma_y = \sigma_0 + kd^{-\frac{1}{2}} (2.2)$$

Grain size is controlled by both alloying addition and processing. Grain refiners such as Zirconium (Zr) (in Al-free systems) and Calcium (Ca) can promote heterogeneous nucleation during solidification, leading to finer as-cast grains. Thermomechanical processing such as extrusion, rolling, forging, and severe plastic deformation (SPD) routes like ECAP, dynamic and post-annealing recrystallisation can generate refined grain structure when suitable strain path and temperature are appropriately selected [40,55].

In Mg, grain refinement can also improve ductility by reducing strain localisation and promoting homogeneous activation of slip and twinning across differently oriented grains. However, very fine (ultrafine/nanocrystalline) grain sizes may reduce work-hardening capacity and can penalise uniform tensile elongation depending on alloy system and texture [40,55]. Figure 2.6 and Figure 2.7 summarise typical grain-size effects reported for Mg alloys [57,58]. Decreasing grain size increases yield strength, while the ductility response can be alloy- and processing-dependent. In several Mg–RE and Mg–Zn systems, a reduction in grain size has been reported to improve both strength and elongation, consistent with more homogeneous deformation in fine-grained HCP microstructures. Grain refinement can also improve fatigue resistance by delaying crack initiation and reducing the severity of strain concentrations at microstructural features. Overall, grain-size optimisation is a practical design lever, but it must be balanced against the tendency for grain growth during heat treatment or in-service exposure.

A further practical issue is grain-size stability: refined grains tend to coarsen during subsequent heat treatment or service exposure unless grain growth is inhibited by solute drag and/or particle pinning (Zener drag) [55,56]. The relatively high Hall–Petch coefficient in Mg is mainly associated with its HCP crystal structure and limited number of easily activated deformation modes at room temperature. Because basal <a> slip is the dominant slip mode and

cannot accommodate c-axis strain, deformation compatibility between neighbouring grains is more difficult than in many FCC metals. Grain boundaries therefore act as strong barriers to dislocation motion, slip transfer and twin propagation. With decreasing grain size, the increased boundary density raises the stress required for plastic deformation, making grain refinement particularly effective for strengthening Mg alloys.

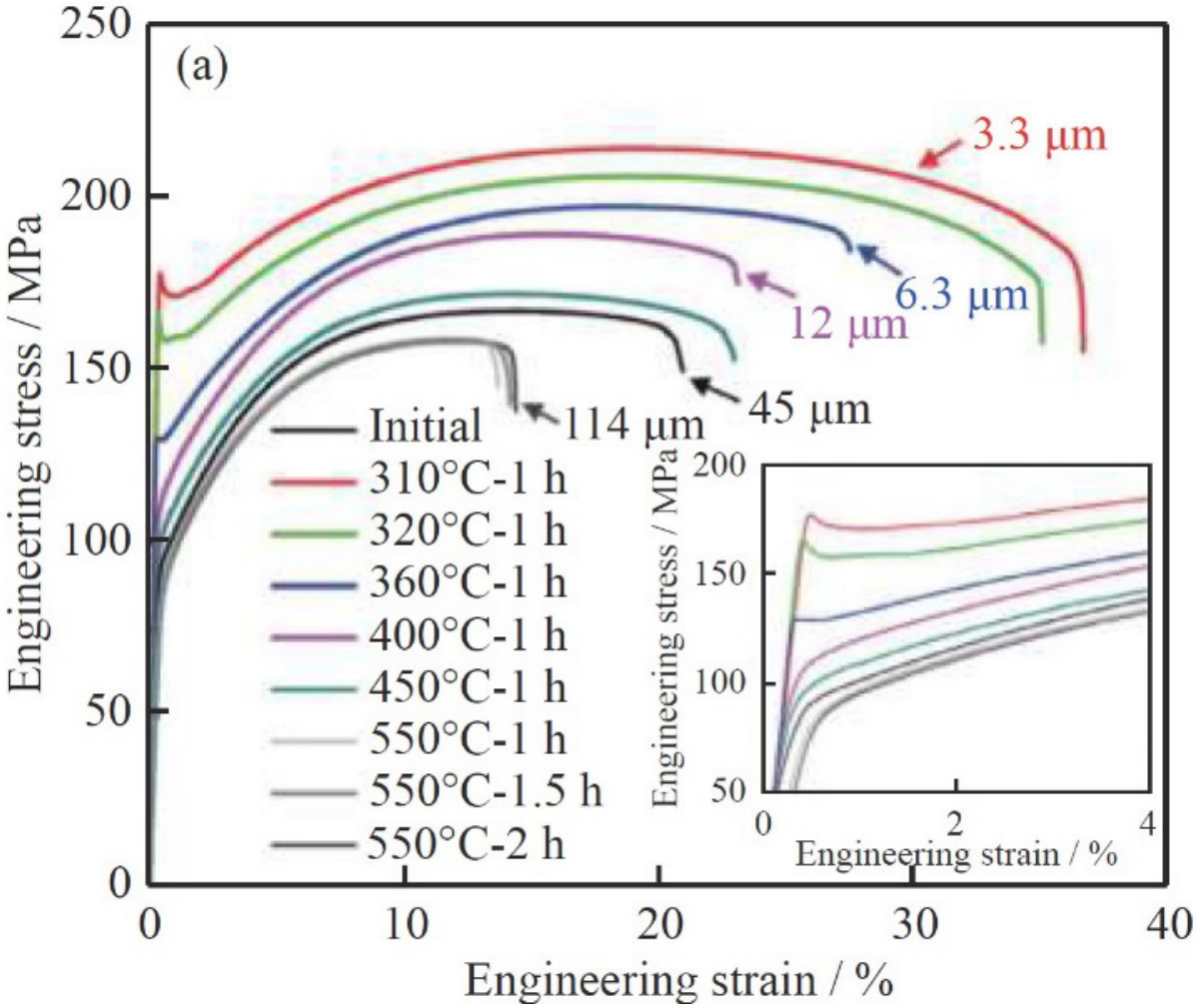

Figure 2.6 Engineering stress-strain curves of Mg–3Gd alloys at different average grain sizes obtained by different annealing conditions [57].

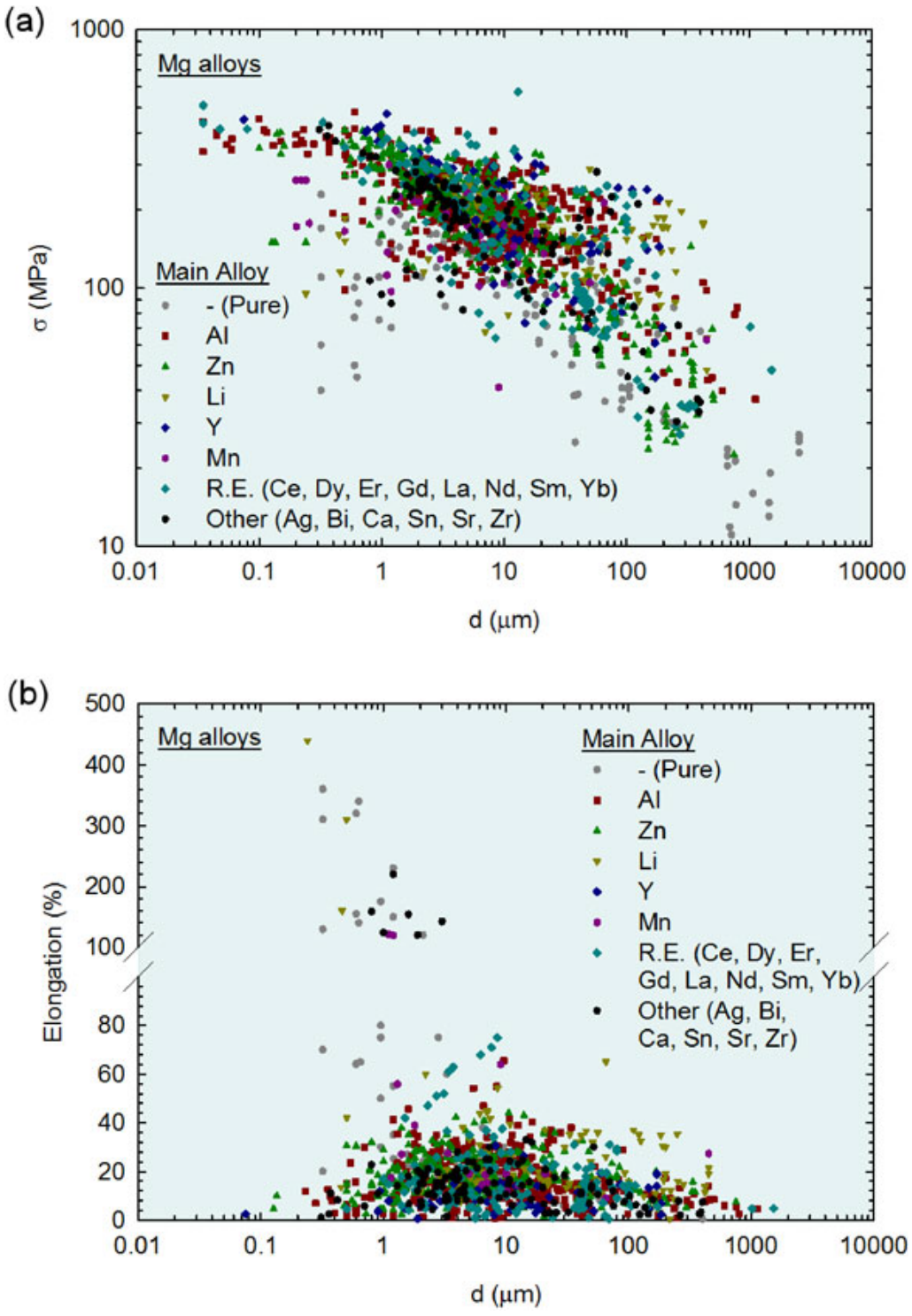

Figure 2.7 A summarise of literature data showing (a) strength vs. grain size, (b) elongation vs. grain size for Mg and Mg alloys [58].

2.3.4 Texture modification

Texture control is a critically important aspect of wrought Mg alloy design. Crystallographic texture describes the preferred orientation distribution of grains in a polycrystal. Rolled and extruded Mg alloys frequently develop strong basal textures, which contribute to anisotropic mechanical behaviour, limited formability and pronounced tension–compression asymmetry because basal slip and twinning are activated differently depending on loading direction relative to the basal poles [40].

Texture modification aims to weaken basal texture intensity and/or tilt basal poles away from the processing direction so that multiple deformation systems can be activated more uniformly. This typically improves ductility and formability and reduces anisotropy, even if the absolute strength increase is modest [42].

The most common two strategies are:

- **Alloying-driven texture modification**: RE additions (and in some systems Ca) can promote broadened or split basal pole figures after processing and annealing, often referred to as “rare-earth texture”, and are widely associated with improved ductility and more isotropic behaviour. The underlying origin is linked to changes in recrystallisation nucleation and growth selection as well as solute/precipitate effects [41–44,59].

- **Processing-driven texture modification**: strain paths that introduce additional shear—such as cross-rolling, asymmetric rolling, or modified extrusion geometries—can weaken conventional basal textures by altering the balance between deformation mechanisms and recrystallisation selection [40,42].

Because texture evolution is tightly coupled to recrystallisation, both deformation temperature and subsequent annealing schedules must be selected with care. Figure 2.8 shows an example of the as-rolled and annealing textures for the Mg–1Zn–1Ce–0.6Zr, Mg–1Zn–1Gd–0.6Zr, Mg–1Ce and Mg–1Gd to illustrate the effect of annealing addition on texture control [15,60].

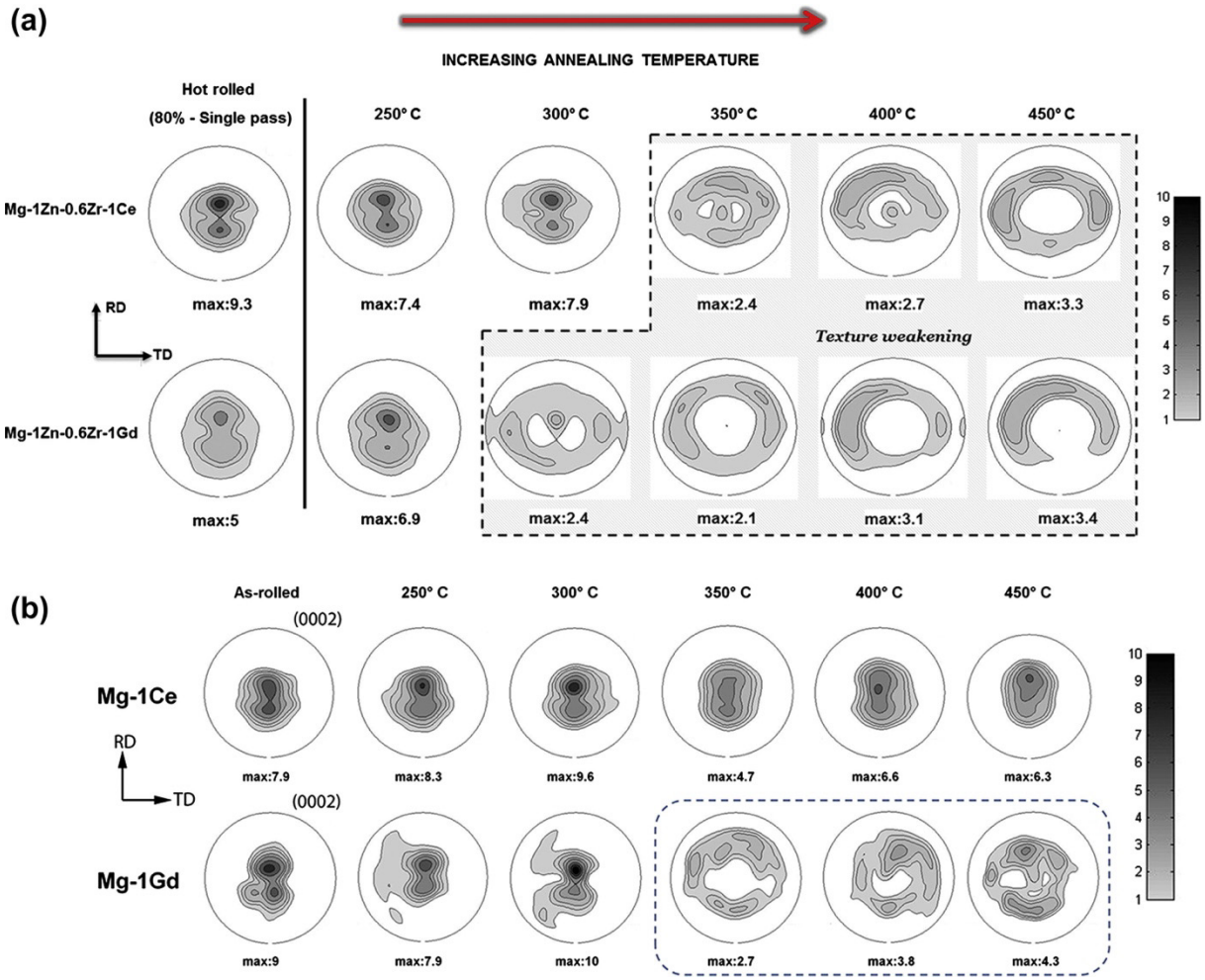

Figure 2.8 (a) Basal pole figures for Mg–Zn–Zr–Gd and Mg–Zn–Zr–Ce for rolled and annealed states. (b) Basal pole figures for Mg–1Ce and Mg–1Gd for rolled and annealed states [15,60].

2.3.5 Summary

Solid solution strengthening, precipitation strengthening, grain refinement and texture modification are not independent design tools in Mg. Alloy chemistry controls solubility and phase stability, processing governs grain size and texture development, and heat treatment determines precipitation state and microstructural stability. Magnesium alloy design is therefore best viewed as an integrated composition–processing–microstructure–property optimisation problem, as schematically summarised in Figure 2.9.

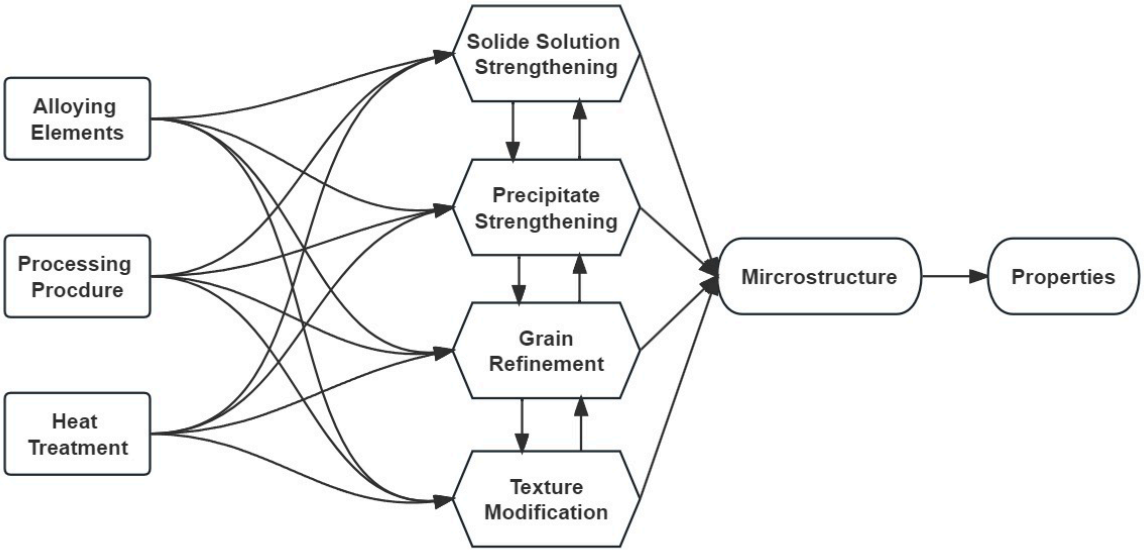

Figure 2.9 Schematic relationship between alloy design, processing, microstructure and properties.

2.4 Processing of magnesium alloys

This section reviews the principal thermomechanical processing routes for Mg alloys, emphasising the controlling role of deformation temperature. For clarity, the discussion is

organised into (i) cold deformation (near ambient temperature) and (ii) hot deformation (warm–hot working), where recovery and dynamic recrystallisation (DRX) become increasingly important in governing flow behaviour, microstructure and texture.

2.4.1 Cold deformation

Cold deformation refers to plastic shaping carried out at or near room temperature (e.g., cold rolling, bending, stamping). For Mg alloys, cold work is intrinsically challenging because the HCP crystal structure provides a limited set of readily available deformation modes at ambient temperature. Basal ⟨a⟩ slip and extension twinning are comparatively easy to activate, whereas prismatic ⟨a⟩ and pyramidal ⟨c+a⟩ slip systems typically require substantially higher stresses. Consequently, strain accommodation—particularly along the c-axis—is restricted and deformation becomes strongly orientation-dependent, which promotes localisation and early cracking in unfavourably oriented grains [39,61].

As deformation proceeds, strain is frequently partitioned into deformation heterogeneities such as twin bands, twin–twin interactions and shear bands, which generate strong gradients in dislocation density and internal stress between neighbouring regions. These features are often accompanied by rapid work hardening at low temperature, because recovery processes are kinetically limited and dislocations accumulate rather than being annihilated or rearranged. In addition, the polarity of twinning contributes to the characteristic tension–compression yield asymmetry commonly observed in many Mg products under room-temperature loading.

Microstructurally, cold-deformed Mg alloys typically develop elongated grains containing dense dislocation networks, substructure (e.g., subgrains) and a high density of

twins, together with a pronounced deformation texture. Although such stored energy can be detrimental in terms of residual stress and damage accumulation, it also provides the thermodynamic driving force for subsequent recovery and static recrystallisation during post-deformation annealing. When carefully controlled, this can be exploited to refine grain size and, in some cases, modify texture; however, the limited cold formability of many commercial Mg alloys means that industrial practice often restricts cold work to small reductions and/or uses intermediate annealing or warm-forming schedules to restore ductility and avoid cracking [61].

2.4.2 Hot deformation

Hot deformation of Mg alloys is typically conducted in the warm-to-hot regime (commonly ≈250–500 C, depending on alloy system, section thickness and process), encompassing hot rolling, extrusion and forging. With increasing temperature, the CRSS for non-basal slip systems decreases, enabling plasticity to be shared across a larger number of independent slip systems. Compared with cold deformation, this broadens the processing window for wrought Mg products by reducing the reliance on intense twinning and mitigating strain localisation [62].

A key distinguishing feature of hot working is that dynamic restoration operates concurrently with deformation. Dynamic recovery—mediated by dislocation climb, cross-slip and rearrangement into lower-energy configurations—reduces work hardening and may lead to near steady-state flow at large strains. Under suitable temperature–strain-rate conditions, dynamic recrystallisation becomes active and refines the microstructure. In Mg alloys, DRX can proceed via multiple pathways, including discontinuous DRX (grain-boundary bulging),

continuous DRX (progressive subgrain rotation) and twin-assisted DRX; the balance between mechanisms depends on alloy chemistry, initial microstructure and deformation conditions [34,63,64].

The combined influence of temperature and strain rate is often expressed using the Zener–Hollomon parameter, as expressed in equation 2.3, where ε is the strain rate, Q is the activation energy, R is the gas constant and T is the temperature. Z parameter provides a practical framework for correlating hot-working conditions with flow stress and DRX grain size. Numerous studies report that the characteristic DRX grain size decreases with increasing Z (i.e., higher strain rate and/or lower temperature), reflecting the competition between recrystallisation, recovery and grain growth during hot deformation [34,63,65,66].

$$Z = \varepsilon exp\ (Q/RT) (2.3)$$

Texture evolution during hot deformation remains influenced by the ease of basal slip, so conventional rolling/extrusion can still produce strong basal textures. However, the activation of additional slip modes and the occurrence of DRX frequently reduce texture intensity and/or rotate basal poles away from the ideal alignment. Alloying additions—particularly rare-earth elements—can further modify recrystallisation behaviour and texture selection, contributing to weaker or "split" basal textures that improve formability and reduce anisotropy. Therefore, optimisation of hot-working schedules requires integrated control of deformation temperature, strain rate, strain path, inter-pass time and cooling/annealing practice, while accounting for solute/precipitate states that influence boundary mobility through solute drag and particle pinning [40,44,61,63].

2.5 Annealing of magnesium alloys

After cold or hot deformation, Mg alloys are commonly subjected to post-processing annealing to relieve residual stresses, restore ductility and tailor grain size and crystallographic texture [34,67,68]. The as-deformed microstructure contains a high density of lattice defects (dislocations, subgrain boundaries and deformation twins), which store elastic energy. During static annealing, this stored energy is progressively reduced through three closely related processes: recovery, primary (static) recrystallisation and subsequent grain growth [34,67].

The annealing response of Mg alloys depends strongly on the prior deformation history (strain magnitude, strain path, deformation temperature, and the extent of any dynamic recovery/recrystallisation already achieved) as well as alloy chemistry (solute content, precipitation/second phases, and impurity level) [34,67,69,70]. In practice, these processes rarely occur as sharply separated stages: recovery can overlap with the early stages of recrystallisation, while recrystallised grains may begin to coarsen if the temperature is high or the holding time is extended [34,67,71].

Recovery is typically the first stage. It reduces dislocation density and internal stresses while leaving the original grain framework largely intact [34,67]. Microscopically, recovery proceeds by dislocation annihilation and rearrangement into lower-energy configurations, commonly producing subgrain structures and low-angle boundaries [34]. In Mg alloys, the extent and kinetics of recovery are sensitive to temperature and to solute/particle content: solute drag and particle populations can retard defect rearrangement and boundary motion, thereby modifying the balance between recovery and recrystallisation and influencing subsequent grain growth stability [44,70].

2.5.1 Recrystallisation

With sufficient temperature and/or time, primary (static) recrystallisation replaces the deformed microstructure with new, comparatively strain-free grains. Recrystallisation involves two coupled steps: nucleation of new grains at favourable sites and growth of those nuclei into the surrounding high-stored-energy matrix via grain boundary migration. For Mg alloys, nucleation sites and mechanisms are strongly coupled to deformation substructure (orientation gradients, dislocation structures and twins), and they ultimately determine both the recrystallised grain size and the resulting texture [15,34,67,69].

- **Grain-boundary nucleation and strain-induced boundary migration (SIBM).** High-angle grain boundaries are high-energy interfaces and commonly accumulate dense deformation structures in adjacent boundary regions. During annealing, parts of an existing boundary can bulge into a more heavily deformed neighbour, leaving behind fine recrystallised grains. This boundary-bulging process (often described as SIBM) is frequently associated with a "necklace" microstructure, in which fine recrystallised grains decorate prior grain boundaries [34].

- **Twin-assisted nucleation.** Deformation twinning provides additional internal interfaces within grains, and twin-related regions (particularly twin–twin intersections and contraction/double twins) can develop strong local orientation gradients and high stored energy. These regions can act as preferential nucleation sites, promoting recrystallisation within grain interiors rather than only along prior grain boundaries. Importantly, the potency of twin-assisted nucleation depends on twin type and the local substructure, and it can therefore bias the recrystallised orientation distribution [15,72–74].

- **Particle-stimulated nucleation (PSN).** In alloys containing sufficiently large, hard second-phase particles (typically micron-scale), deformation generates pronounced strain gradients ("particle deformation zones") due to local strain incompatibility. These high-dislocation-density zones can become preferred nucleation sites during annealing. PSN tends to weaken texture because nuclei formed around particles are less constrained to inherit parent orientations, although its net influence depends on its competition with other nucleation mechanisms and on subsequent growth selection [15,70,75].

- **Continuous recrystallisation via subgrain rotation.** Under some conditions (often when deformation and/or annealing promote extensive subgrain development), subgrain formed during recovery can progressively increase their misorientation until they evolve into high-angle boundaries, producing a more continuous transition from recovery to recrystallisation. While discontinuous nucleation routes are common in heavily cold-worked Mg, continuous routes can contribute to fine, relatively uniform recrystallised structures within selected processing windows and compositions [34,69].

Once nuclei form, their growth is driven by the reduction in stored energy: grain boundary migration consumes highly defected material and replaces it with a lower-defect lattice. Recrystallisation kinetics can be rapid at typical annealing temperatures for wrought Mg alloys, and the final grain size is largely governed by the balance between nucleation density (linked to stored energy) and boundary mobility (strongly affected by solutes and particles) [44,70].

A particularly important special case is the so-called "rare-earth effect", where certain RE additions (e.g., Y, Gd, Nd- or Ce-containing systems) are widely reported to weaken the

conventional basal texture and promote broader, off-basal components after recrystallisation. Multiple mechanisms have been proposed; recurring themes include (i) changes in the deformation substructure and nucleation landscape (e.g., increased propensity for non-basal deformation substructures and twin/shear-band related nucleation) and (ii) solute segregation/drag effects that modify boundary mobility and growth selection, potentially in an orientation-dependent manner. The practical outcome is a more dispersed orientation distribution and improved ductility/formability, which is why RE-containing alloys remain benchmark systems in texture-control studies [15,44,76–78].

2.5.2 Grain growth

If annealing continues after primary recrystallisation is largely completed, the microstructure may coarsen by grain growth, driven by the reduction of total grain boundary area and energy. Grain growth in Mg alloys is commonly discussed in terms of normal grain growth (NGG) versus abnormal grain growth (AGG), with solute/particle effects often determining which regime is observed [71,79].

In NGG, the microstructure coarsens relatively uniformly: grains compete with neighbours under curvature-driven motion, small grains shrink and disappear, and the grain size distribution remains broadly self-similar while shifting to larger sizes. A widely used kinetic form is expressed as equation 2.4 [68]:

$$D^n - D_0^n = Kt \quad (2.4)$$

where D is the characteristic grain size, D_0 is the initial size, n is the growth exponent and K is a temperature-dependent constant. Consistent with diffusion-controlled boundary

mobility, grain growth accelerates strongly with increased K. In practical Mg alloys, grain boundaries do not migrate freely. Dispersed particles (precipitates or stable second phases) exert a pinning pressure that opposes boundary motion (Zener pinning), imposing an upper bound on grain size when pinning balances the capillarity driving force. A commonly used estimate for a limiting size is determined by equation 2.5 [80]:

$$D_{limit} = \frac{4r}{3f} (2.5)$$

Where r is particle radius and f is particle volume fraction (for an idealised dispersion of spherical particles). In addition to particle pinning, solute atoms can reduce boundary mobility through solute drag and segregation effects, which can be particularly pronounced in some RE-containing systems and may influence growth selection and texture evolution [44,78].

AGG refers to a non-uniform coarsening mode where a small fraction of grains grows disproportionately large, producing a bimodal grain size distribution. In Mg alloys, AGG is commonly associated with an imbalance in growth constraints—e.g., non-uniform pinning (particle coarsening/dissolution in specific temperature windows), heterogeneous boundary mobility, or texture-related growth advantages that allow certain grains to "break away" from a pinned matrix. When AGG occurs, it can strongly affect texture because a few very large grains may dominate the volume fraction and therefore the macroscopic orientation distribution. From a processing standpoint, suppressing AGG typically requires maintaining effective pinning (through stable dispersoids/precipitates), controlling solute redistribution, and avoiding annealing windows where the pinning population becomes ineffective [81].

2.5.3 Texture evolution

Across recovery, recrystallisation and grain growth, texture evolution is best understood as a competition between (i) inheritance from the deformed state and (ii) selective nucleation/growth mechanisms that bias which orientations survive. Recovery generally preserves the deformation texture because it rearranges defects without introducing new grain orientations. During recrystallisation, texture may be retained, weakened or reoriented depending on whether nucleation is dominated by boundary bulging, twins, PSN and/or shear-band-related pathways, and on whether subsequent growth selection favours particular orientations. During grain growth, texture can remain stable if mobility differences are small, but it can also sharpen if certain orientations have a sustained growth advantage or if AGG occurs [70,72,73,76–78].

Overall, post-processing annealing in Mg alloys is a balancing act: recrystallisation is often required to restore ductility and refine the microstructure, but excessive holding risks grain coarsening and potentially undesirable texture sharpening or AGG. This trade-off—and its sensitivity to alloy chemistry and processing history—motivates more quantitative, data-rich studies of microstructure evolution in Mg alloys, which are reviewed in the following section.

2.6 Studies of microstructural evolution in magnesium alloys

Microstructure evolution underpins the performance of wrought Mg alloys. During thermomechanical processing and subsequent annealing, the microstructure evolves through (i) the accumulation and partial removal of stored defects (dislocations, subgrain boundaries and

twins), (ii) recrystallisation (static or dynamic depending on the processing route), and (iii) grain growth. These processes reshape grain-size distributions, grain-boundary character and crystallographic texture, and therefore control the balance between strength, ductility and anisotropy in service. Because Mg has a HCP lattice, microstructure evolution is strongly coupled to crystallography: deformation substructures are highly orientation-dependent, and deformation twinning can play a central role in stored-energy partitioning, nucleation, and texture evolution. As a consequence, classical frameworks developed largely from fcc systems remain valuable conceptually, but Mg often requires additional attention to twinning-assisted pathways and texture-selection effects.

2.6.1 Classic investigations

Early investigations of recrystallisation and microstructure evolution in wrought Mg alloys were largely constrained by the available characterisation methods. The standard workflow was to impose deformation, anneal for discrete time–temperature conditions, and then compare "before/after" states using metallography. Optical microscopy, combined with manual (or intercept-based) grain-size measurements, was used to identify the emergence of strain-free grains and to document subsequent coarsening at longer annealing times. Where microstructural datasets were sparse or statistically limited, the progress of recrystallisation was often inferred indirectly from macroscopic softening metrics—most commonly microhardness—because annealing typically reduces hardness as stored defects are removed and the deformed matrix is progressively replaced by recrystallised grains. A representative example is the work of Su et al. on AZ31, where recrystallisation kinetics were analysed through hardness-based "fractional softening" when direct microstructural tracking was limited [82,83].

To interpret such limited time–temperature datasets, many studies adopted phenomenological kinetic descriptions, most frequently Johnson–Mehl–Avrami–Kolmogorov (JMAK) [84] type forms. While this approach offers a pragmatic way to summarise kinetics via fitted parameters (e.g., the Avrami exponent), it rests on strong simplifying assumptions—most notably spatially random nucleation and idealised nucleation/growth rate behaviours [85]. In Mg alloys, however, recrystallisation is rarely spatially uniform: nucleation is strongly biased towards microstructural heterogeneities (grain boundaries, twins, shear bands, particle-affected zones), and both driving force and boundary mobility can vary substantially across the microstructure. Consequently, deviations from "ideal" behaviour should not be viewed as anomalies but as symptoms of heterogeneous nucleation and non-uniform growth conditions; this is explicitly reflected in kinetic analyses that separate high-stored-energy regions (e.g., twin- and shear-band-containing zones) from lower stored-energy regions [83].

Mechanistic understanding improved markedly with the increasing use of electron microscopy. A classic TEM-based study by Myshlyaev et al. [86] on hot-worked AZ31 demonstrated how twinning and its evolution with temperature introduce pronounced microstructural heterogeneity: twins were observed over a broad temperature range, twin bands developed dislocation cells and subgrains as temperature increased, and the earliest dynamically recrystallised grains were reported at twin intersections—highlighting that twinning-related interfaces can act as preferential sites for recovery/recrystallisation processes because they concentrate lattice curvature and stored energy [86]. Complementary crystallographic studies using EBSD micro-texture analysis reinforced this picture for static recrystallisation: new grains forming at compression twins in AZ31 were found to show orientation characteristics similar to subgrains within twins or shear bands, consistent with

nucleation that is strongly “microstructure-selected” rather than spatially random [87]. These insights also helped underpin later, widely cited texture arguments in Mg processing: Stanford and Barnett’s seminal extrusion study linked rare-earth additions to a weakened extrusion texture and proposed that the characteristic “rare earth” texture component arises from oriented nucleation at shear bands, explicitly tying macroscopic texture outcomes to local heterogeneity-driven nucleation [41].

Despite their importance, classical approaches have intrinsic limitations that restrict mechanistic and predictive insight. Microhardness and bulk softening curves conflate multiple concurrent processes (recovery, recrystallisation and—in some alloys—precipitation or solute redistribution), while optical microscopy provides limited crystallographic information and samples only a 2D section that may not capture the full heterogeneity of nucleation sites. TEM offers the necessary spatial resolution for substructure-level mechanisms but is inherently local and may not be statistically representative of the microstructure as a whole. More broadly, the reliance on ex-situ “snapshot” comparisons makes it difficult to separate nucleation from growth, quantify the competition between grains, or attribute final texture/microstructure to specific nucleation sites with confidence. These shortcomings echo long-standing critiques in the wider recrystallisation literature, which emphasise that genuinely predictive models remain limited by incomplete quantitative characterisation of the deformed state and an inadequate understanding of the properties of migrating boundaries.

Collectively, these constraints motivate the shift to advanced, data-intensive characterisation strategies capable of tracking microstructural evolution directly and at scale—particularly (quasi-)in situ EBSD and automated grain-correlation approaches that follow many thousands of grains through nucleation, growth, stagnation and even consumption. For example,

Track-Rex was developed explicitly to analyse quasi in situ EBSD datasets by grain correlation and to automatically track large grain populations, enabling questions about when and where nuclei form, and which grains ultimately dominate the fully recrystallised microstructure, to be answered quantitatively. Track-rex is designed to work with experimental data where crystallographic orientation is recorded.

2.6.2 Applications of advanced characterisations

Over the past two decades, microstructure-evolution studies in Mg have increasingly shifted from low-throughput comparisons to data-rich, time resolved datasets. A key enabler has been the widespread adoption of electron backscatter diffraction (EBSD), which provides quantitative orientation maps over statistically meaningful areas. EBSD makes it possible to move beyond average grain size by directly measuring grain-size distributions, misorientation statistics, grain-boundary character and texture evolution, and by mapping how these quantities vary along time within a sample.

EBSD also enables more defensible estimates of recrystallised fraction than purely hardness-based proxies, because recrystallised grains can be identified using criteria based on low internal misorientation and/or the emergence of new orientations. In situ and quasi in situ EBSD approaches strengthen this further by mapping the same area sequentially during interrupted annealing or during high-temperature EBSD experiments, allowing direct observation of which regions are consumed, which nuclei emerge, and how texture evolves as recrystallisation proceeds [88].

Where sequential EBSD datasets are available, grain-tracking approaches provide an additional step change: rather than comparing statistics between time steps, individual grains

can be followed to quantify grain-resolved trajectories (growth, stagnation or consumption) and to link these trajectories to crystallography and local neighbourhood context. Recent work has formalised such analysis through dedicated toolboxes for tracking recrystallisation nucleation and grain growth across time-resolved datasets [89,90].

Beyond two-dimensional surface mapping, three-dimensional and time-resolved (3D/4D) characterisation techniques have enabled non-destructive measurement of bulk microstructure evolution. Synchrotron-based approaches—including three-dimensional X-ray diffraction (3DXRD) methods, diffraction contrast tomography (DCT), and high-energy diffraction microscopy (HEDM)—can reconstruct 3D grain morphology and orientation, providing access to true 3D neighbourhood and topology that are difficult to infer reliably from 2D sections. When repeated during annealing or deformation, these methods enable grain-by-grain tracking in the bulk, yielding datasets that capture the distribution of behaviours rather than only an average trend [91–93].

2.6.3 Materials informatics and data-driven approaches

Despite major advances in experimental capability, much of the Mg literature still reports microstructure evolution using relatively coarse descriptors—e.g., an average grain size (or a single grain-size distribution per condition) and a single scalar “fraction recrystallised”, with texture summarised by peak intensities or a small set of pole-figure metrics. These summaries remain useful for comparing processing windows, but they can obscure the heterogeneity that often governs mechanism—specifically which grains nucleate, which grains grow, which grains shrink, and whether coarsening is uniform or dominated by a small subset of grains.

This motivates a transition towards materials informatics workflows for microstructure evolution: scalable pipelines that (i) structure microstructure datasets, (ii) extract robust grain- and boundary-level descriptors (size, orientation, internal misorientation, boundary character, neighbour counts, etc.), and (iii) where possible track grains through time with reduced user bias and improved reproducibility. Tool development in this direction (including grain-tracking toolkits for recrystallisation and grain growth) makes it feasible to treat the full dataset—rather than a small subset of images—as the primary object of this study [94,95].

Once grain-resolved datasets are available in a consistent feature space, statistical learning becomes a natural next step. Microstructures can be represented in forms that explicitly encode neighbourhood interactions (for example, graphs in which grains are nodes and boundaries are edges), enabling models that consider not only single-grain attributes but also interactions among neighbouring grains—an important requirement for predicting behaviour in polycrystals. Recent studies have demonstrated graph-based learning for polycrystal property prediction and for predicting abnormal grain growth in simulated microstructural evolution, illustrating the potential of neighbourhood-aware representations.

In parallel, topological and geometry-aware analysis offers additional ways to represent complex microstructures. Topological data analysis methods such as persistent homology have been reviewed and applied in materials contexts to capture multi-scale structural features in a manner that can be less sensitive to arbitrary threshold choices than some traditional descriptors. While such approaches are still emerging for polycrystalline microstructure-evolution problems, they align well with the central challenge in Mg: the governing mechanisms are multivariate, spatially heterogeneous, and strongly dependent on crystallography and local neighbourhood context [96,97].

Overall, research on Mg microstructure evolution is moving towards a data-rich paradigm. Classical metallurgy established the foundational concepts; modern characterisation supplies detailed, high-volume datasets; and the next step is to combine these with informatics methods that can extract grain-resolved, mechanism-relevant insight at scale. This progression motivates the following section, which reviews materials informatics methods applied to recrystallisation and grain growth and how such approaches can support alloy and processing optimisation.

2.7 Materials informatics in alloy design

Materials informatics refers to the use of data-centric methods—most commonly machine learning (ML), statistical modelling, and optimisation —to extract quantitative relationships between composition, processing, structure/microstructure, and properties (often framed as the CPSP chain) and to use those relationships to accelerate materials development. In alloy design, the motivation is pragmatic: the accessible design space expands combinatorially with the number of elements and processing variables, while conventional development pathways are frequently dominated by iterative trial-and-error. Informatics does not replace physical metallurgy; rather, it provides a systematic way to organise evidence, quantify uncertainty, and prioritise experiments or simulations when exhaustive exploration is impractical [98–100].

The uptake of materials informatics has been enabled by several converging developments. First, high-throughput experiments and simulations have increased the availability of structured data, while policy and community initiatives (e.g., the Materials Genome Initiative) have promoted data-sharing culture and digital infrastructure. Second,

modern characterisation methods—particularly microstructure mapping techniques—generate datasets that are both high dimensional and heterogeneous, which motivates automated pipelines for repeatable analysis. Third, the availability of open-source ML ecosystems and scalable computing has lowered the barrier to adopting robust modelling workflows [99–101].

A typical informatics workflow for alloy design can be summarised as [102]:

- (i) Data acquisition and curation: assembling composition, processing history, microstructure descriptors and measured properties, while documenting uncertainties and experimental context.
- (ii) Representation and feature engineering: converting raw inputs (e.g., compositions, thermomechanical schedules, microstructure maps) into descriptors that capture relevant physics and are suitable for modelling.
- (iii) Model training and validation: fitting predictive models and assessing performance with appropriate validation strategies, recognising the risks of data leakage and the limits of extrapolation.
- (iv) Deployment for decision-making: using models for screening, sensitivity analysis, multi-objective optimisation, or hypothesis generation.
- (v) Iterative improvement: expanding the dataset through targeted new experiments/simulations (often using active learning and Bayesian optimisation).

In alloy development, informatics strategies are often grouped into forward modelling and inverse design. Forward modelling predicts a target output (e.g., yield strength, corrosion rate, grain size after annealing, texture intensity) from known inputs such as composition and

processing. Depending on data volume and interpretability requirements, models may range from linear/regularised regressions to nonlinear ensembles and neural networks. Inverse design starts from a desired outcome and searches for candidate compositions and/or processing conditions predicted to achieve it. In practice this is typically implemented as an optimisation problem in which a trained ML model serves as a fast surrogate evaluator within a search strategy such as Bayesian optimisation, evolutionary algorithms, or multi-objective optimisers [102].

For magnesium alloys, materials informatics is particularly attractive because key performance limitations are microstructure-sensitive and strongly coupled: recrystallisation-mediated texture evolution, grain growth during annealing, and precipitation/solute effects interact with composition and thermomechanical history in ways that are difficult to optimise by intuition alone. At the same time, Mg datasets are often "small" in the sense that the number of distinct, fully characterised thermomechanical routes is limited, even when each experiment yields large microstructure maps. Under such conditions, robust feature design, uncertainty awareness and the integration of metallurgical constraints are essential; hybrid strategies (combining mechanistic models with data-driven inference) are therefore often preferable to purely black-box optimisation [103].

Table 2.6 summarises representative examples of materials informatics applied to alloy development and optimisation, illustrating the range of modelling approaches and the types of design questions that can be addressed.

Study (Year)	Alloy System / Focus	Informatics Approach	Key Outcome
Bhadeshia (1990s) [104]	Steels (weld metal)	ANN models trained on composition→strength data	First successful use of neural networks to model and design steel welds, accurately predicting tensile strength from composition.
Rajan (2005) [105]	Conceptual (Materials Informatics)	Data-mining concepts for materials	Defined the paradigm of materials informatics, emphasizing data-driven extraction of structure–property relationships in alloys.
Rickman *et al.* (2019) [106]	High-Entropy Alloys (multi-component)	Canonical-correlation analysis + Genetic Algorithm	Discovered a new class of ultra-hard HEAs by screening a large compositional space; predicted and experimentally confirmed hardness ~2× higher than typical alloys.
Hu *et al.* (2023) [107]	Various alloy systems (review)	Ensemble ML models for forward property prediction	Demonstrated state-of-the-art property prediction across steels, Al, Mg, etc., and highlighted the surge in ML-driven alloy development in recent years.
Mi *et al.* (2024) [108]	Mg–Mn Wrought Magnesium Alloys	Bayesian optimisation + Active Learning	Identified an optimised Mg alloy composition with ultrafine grains and high strength (UTS > 600 MPa) by iterative ML-guided experiments, accelerating development.

2.7.1 Applications in recrystallisation

Recrystallisation is central to wrought Mg because it reshapes grain structure and crystallographic texture, thereby controlling anisotropy and formability. Predicting recrystallisation is challenging because nucleation and growth depend on interacting factors such as stored deformation energy, heterogeneity, solute content, particle distributions, and the crystallographic constraints of the HCP lattice. Consequently, classical constitutive and kinetic models—while valuable—often remain limited to specific processing windows or require simplifying assumptions [103].

Materials informatics contributes to three main ways. First, ML models can serve as fast predictors of recrystallisation-related outcomes (e.g., recrystallised fraction, post-anneal grain size, or qualitative regime maps) from deformation and annealing parameters, enabling interpolation across multivariate process spaces where simple empirical fits become unreliable. Second, informatics enables more complete use of microstructure-resolved datasets. EBSD-derived descriptors (orientation statistics, boundary-character distributions, twin fractions, local misorientation measures) can be extracted at scale and linked to recrystallisation events, allowing analysis to move beyond bulk averages toward grain-resolved tendencies and spatial heterogeneity. Third, hybrid approaches integrate data-driven components with mechanistic frameworks (e.g., cellular automaton, Monte Carlo, phase-field), where optimisation /learning is used to identify parameters or rules that are difficult to specify a priori while retaining physical constraints through the simulation scaffold [100,101,103].

2.7.2 Applications in grain growth

Grain growth during annealing is a critical companion process to recrystallisation: even if recrystallisation produces a fine microstructure, subsequent coarsening can erode strength (Hall–Petch) and alter texture–property relationships. Traditional modelling approaches (parabolic growth laws, phase-field, Monte Carlo) offer mechanistic insight but can be computationally demanding and can struggle with predictive treatment of abnormal grain growth (AGG) and other non-ideal behaviours [101,109].

Informatics has begun to contribute in three complementary ways. First, ML surrogate models can emulate computationally expensive grain-growth simulations, enabling rapid "what-if" exploration of annealing schedules and microstructure sensitivities. Second, graph- and network-based representations of microstructure (grains as nodes, boundaries as edges) are well matched to AGG because they encode neighbourhood structure explicitly [110,111]; learning topological signatures can improve prediction of rare events that are not captured by bulk-average descriptors [95]. Third, data-driven correlation of composition and processing with grain-growth resistance can help quantify the roles of solute drag and particle pinning and support multi-objective trade-off studies when paired with physically meaningful descriptors rather than elemental fractions alone [99,103,112].

Table 2.7 summarises representative examples where data-driven methods have been applied to recrystallisation and grain growth, illustrating both the modelling strategies and the kinds of questions that can be addressed.

Investigated phenomenon	**Alloy & data format**	**Informatics Approach**	**Source / Key Reference**
Dynamic Recrystallisation [113]	AZ31 Mg alloys during hot deformation	Artificial neural network	Predicted flow stress using more efficiently than classic flow stress model
Dynamic Recrystallisation [114]	AZ61 Mg alloy during hot deformation	Genetic algorithm	simulation of AZ61 DRX using generated model (2024)
Abnormal Grain Growth [115]	Monte Carlo simulations	Graph Neural Network (GNN)	GNN prediction of abnormal grain growth within simulation dataset for ~73% accuracy
Normal Grain Growth [116]	Simulation dataset of stainless steel 316L	Dynamic Graph Neural Network + Deep ML	GrainGNN workflow: dynamic GNN for 3D microstructure prediction

Taken together, the literature indicates a clear trend: as datasets become richer and more time-resolved, the bottleneck shifts from data generation to data structuring, feature extraction, and predictive use. For Mg alloys—where microstructure evolution is multivariate, spatially heterogeneous, and tightly coupled to crystallography—materials informatics provides a toolkit to extract reproducible descriptors at scale, learn process–microstructure–property linkages, and guide systematic exploration of composition and processing spaces. In this thesis, these ideas are applied in a microstructure-centred manner: large annealing datasets are converted into structured, grain-resolved information that underpins both mechanistic interpretation and the development of predictive models for recrystallisation and grain growth in Mg-based alloys [64,117,118].

2.8 Alloy systems in this thesis

Modern magnesium (Mg) alloy development can be viewed as a continuing effort to balance strength, ductility/formability, corrosion behaviour, thermal stability and cost through coupled choices of composition and thermomechanical route (e.g. casting/extrusion/rolling + heat treatment). Recent reviews emphasise that, while Mg alloys have expanded in transportation and consumer applications, their wider deployment remains constrained by a combination of formability/anisotropy (texture), corrosion sensitivity and microstructural stability during processing and service exposures [40,119,120].

From a manufacturing perspective, Mg alloys are commonly grouped into cast alloys (high-volume, near-net-shape components) and wrought alloys (sheet, extrusions and forgings). Wrought products are particularly sensitive to recrystallisation and grain growth because final properties depend strongly on grain size distribution, grain-boundary network evolution and

texture intensity after deformation and annealing. This sensitivity makes wrought Mg an especially relevant platform for microstructure-centred optimisation [42,79].

In composition space, Al and Zn remain the dominant industrial alloying elements because they provide cost-effective solid-solution/precipitation strengthening and good castability/processability in conventional systems. Rare-earth (RE) additions are used in two distinct regimes: (i) lean additions (often <1 wt.%) to modify recrystallisation texture and improve room-temperature formability, and (ii) higher additions to enable precipitation strengthening and improved high-temperature stability (often via solute drag and particle pinning). Importantly, the "rare-earth texture effect" is well established experimentally, yet its mechanistic origin—particularly why very small solute levels can generate large texture changes—remains an active and debated topic. Minor elements (e.g. Mn for impurity control; Zr as a grain refiner in Al-free systems; Ca/Li/Ag in specialised systems) further expand design options by tuning oxidation resistance, creep response and microstructure evolution pathways.

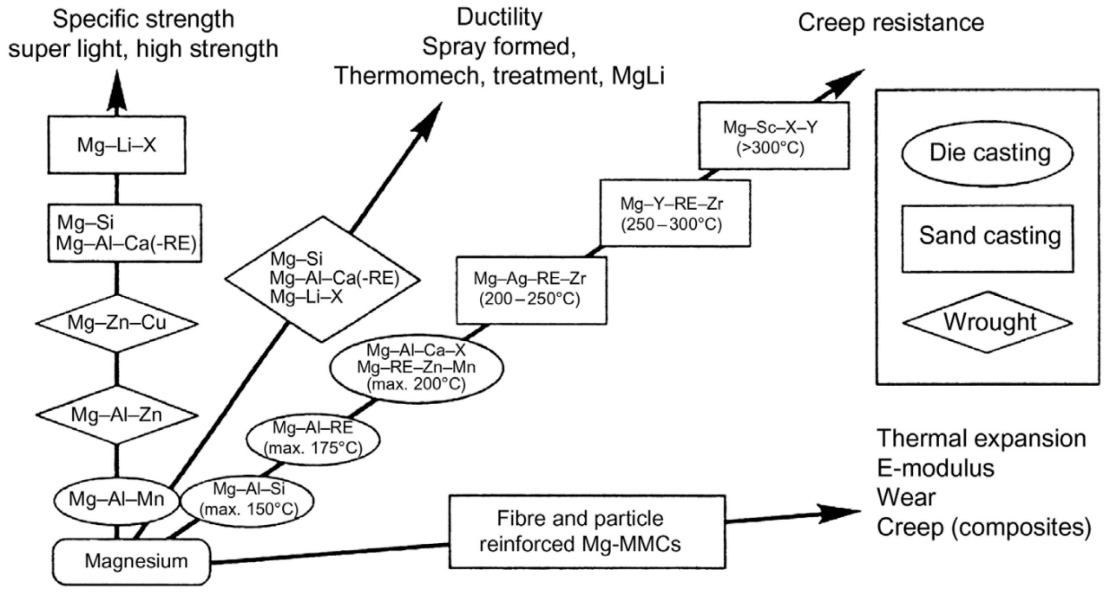

Figure 2.10 Directions of Mg alloys development [25]

Against this backdrop, this thesis focuses on three representative wrought alloys—AZ31, ZE20 and WE43—which span three contrasting microstructure-engineering philosophies relevant to recrystallisation and grain growth [40,119,121–123]:

- (i) A conventional RE-free baseline alloy with strong basal texture and limited intrinsic grain-boundary pinning (AZ31).
- (ii) A lean-RE alloy designed to trigger the rare-earth texture effect, where orientation-selective recrystallisation and growth become central (ZE20).
- (iii) An RE-rich precipitation-strengthened alloy where second phases and solute drag strongly couple precipitation, recrystallisation and grain growth kinetics (WE43).

The following subsections review each system in terms of current applications, state-of-the-art understanding and unresolved problems—specifically through the lens of recrystallisation and grain growth—and highlight where materials informatics can accelerate progress.

2.8.1 Mg-Al-Zn series and AZ31

The Mg–Al–Zn (AZ) series remains the most widely used family of commercial Mg alloys because it offers a practical compromise between cost, processability and mechanical performance. AZ31 (≈Mg–3Al–1Zn, wt.%) is among the most common wrought grades (sheet and extrusions) and is frequently used as a benchmark material for texture-control strategies and microstructure-engineering studies. In this sense, AZ31 is “well mapped” phenomenologically—deformation mechanisms, typical basal textures and recrystallisation trends are extensively reported—yet it remains a reference problem because its limitations are

closely tied to fundamental HCP plasticity and persistent basal texture strengthening during processing.

State of the art: AZ31 processing–microstructure research increasingly emphasises that recrystallisation and grain growth must be treated as a coupled problem. Even when full recrystallisation is achieved, subsequent orientation-selective growth can retain or sharpen basal texture components, sustaining anisotropy and limiting room-temperature formability. Direct, time-resolved observation approaches are now being used to quantify annealing-driven recrystallisation and grain growth more rigorously (e.g., tracking boundary motion and grain consumption rather than relying only on before/after statistics).

Key unresolved issues: (i) AZ31 often contains only a limited population of stable, thermally resistant particles in many wrought conditions; therefore, grain boundary motion can be weakly constrained and grain growth can rapidly erode strength (Hall–Petch) if annealing windows are not tightly controlled. (ii) The relative contributions of nucleation selection versus growth selection to texture evolution are still difficult to separate quantitatively at scale, particularly because heterogeneity (local strain, twins, deformation bands) strongly biases where recrystallised grains appear and how they compete. (iii) Predictive process design remains challenging because small changes in strain path, local shear, or annealing schedule can shift the balance between refined/weak-texture outcomes and coarse/strong-texture outcomes.

Trends and informatics opportunity: AZ31 is a natural “baseline” system for data-driven microstructure evolution modelling: it offers relatively clean chemistry (compared with RE-rich alloys) while still exhibiting strong texture and growth-selection behaviour. Large

EBSD datasets can be used to learn predictive links between deformation descriptors (orientation gradients, twin fractions, local misorientation measures), annealing conditions and recrystallised grain size/texture outcomes. Recent work on machine-learning pipelines for linking processing/microstructure to properties in extruded Mg alloys supports the feasibility of this approach and highlights the importance of robust feature design and validation. In this thesis, AZ31 therefore serves as the RE-free reference for quantifying nucleation and growth contributions during recrystallisation and for testing grain-growth prediction strategies [124].

2.8.2 Mg-Zn-RE series and ZE20

Lean-RE Mg–Zn–RE alloys represent a design direction where Zn provides strengthening while a small RE addition is used to trigger texture modification and improved formability. ZE20 (≈Mg–2.4Zn–0.2Ce, wt.%) is a notable lean-RE example, attracting sustained research interest because it can exhibit an off-basal/dispersed recrystallisation texture at very low RE content. The scientific interest is sharpened by the fact that the rare-earth texture effect can occur at extremely low solute levels, yet the mechanistic explanation remains incomplete—especially regarding the roles of segregation, boundary crystallography and mobility anisotropy.

State of the art: Recent work has moved from qualitative texture descriptions towards grain-resolved, time-resolved evidence. A key example is quasi-in-situ EBSD combined with automated grain tracking, enabling tens of thousands of grains to be tracked through annealing and allowing nucleation and growth contributions to be quantified directly. This type of dataset supports a much more mechanistically defensible picture: early nucleation may be promoted in high-strain features such as shear bands, but later-stage growth competition can consume

some early nuclei and reshape the final texture via orientation-selective survival and growth. Such findings reinforce that texture control in lean-RE alloys is not purely a “nucleation story”; growth selection and grain-boundary character also matter.

Key unresolved issues: (i) In lean-RE alloys, neither particle effects nor solute effects are trivially dominant; sparse particles, segregation and solute drag can all contribute, making interpretation sensitive to chemistry/defect measurement resolution and to statistics. (ii) It remains challenging to quantify, in a generalisable way, how solute–boundary interactions translate into orientation-dependent boundary mobility and therefore systematic texture evolution pathways. (iii) Processing robustness is still a practical barrier: achieving both fine grain size stability and a favourable off-basal texture consistently requires controlling deformation heterogeneity and annealing schedules [125–127].

Trends and informatics opportunity: ZE20 is an ideal candidate for materials informatics-driven analysis because its “core phenomenon” is grain-level selection. Grain-resolved datasets can be structured into features describing local neighbourhoods, stored-energy proxies and boundary character distributions, and then used to predict which grains nucleate, survive and grow. The availability of automated tracking (and open-source workflows) directly lowers the barrier to building statistically meaningful training sets for ML and to testing mechanistic hypotheses against large populations rather than selected micrographs. In this thesis, ZE20 therefore functions as the lean-RE case study where orientation-selective recrystallisation and growth are central to the texture outcome [128].

2.8.3 Mg-Y-RE series and WE43

The WE series (Mg–Y–RE, typically with Zr) was developed to exploit rare-earth effects on strength, creep resistance and thermal stability. WE43 (commonly ≈Mg–4Y–3Nd–0.5Zr, wt.%) is among the best-known alloys in this family and is used in niche, high-value applications where elevated-temperature performance is required. Compared with AZ31 and ZE20, WE43 is microstructurally rich: RE solutes and multiple precipitate/intermetallic populations (whose size, morphology and spatial distribution depend on thermal history and processing route) interact strongly with recrystallisation and grain growth [129].

State of the art: Recent studies demonstrate that thermomechanical processing routes such as hot rolling can produce high strength through combined grain refinement, precipitation strengthening and texture strengthening, but also introduce strong textures and anisotropy that must be managed. For example, multi pass hot rolling has been reported to refine WE43 grain size substantially (e.g., from ~34 μm to <10 μm) while increasing yield strength, indicating the potential of controlled DRX and second-phase evolution during processing. Systematic EBSD/TEM-based analyses further show that strength increments are often multi-mechanistic, and the challenge is to retain those benefits without triggering undesirable coarsening or instability during subsequent annealing [130,131].

Key unresolved issues: (i) Grain-growth resistance in WE43 is not fixed; it depends on the evolving precipitate state. Coarsening or partial dissolution during thermal exposure reduces Zener pinning and can shift the alloy into regimes where accelerated coarsening (or even abnormal grain growth) becomes possible. (ii) Spatial heterogeneity in precipitation and defect structures can lead to heterogeneous recrystallisation and heterogeneous growth

selection, complicating predictive control. (iii) Because precipitation, recrystallisation and grain growth occur on overlapping timescales, modelling and optimisation require integrated, multi-physics approaches and multi-modal datasets [132,133].

Trends and informatics opportunity: WE43 naturally generates high-dimensional datasets (grain structure + texture + precipitation descriptors). Informatics can help identify robust descriptors of grain growth resistance (e.g., local pinning proxies, topology and boundary-network measures) and provide fast surrogates for expensive simulations or long annealing experiments. Recent ML pipeline work in extruded Mg alloys illustrates how structured feature engineering can enable predictive structure–property modelling and suggests a pathway to extend such approaches to microstructure evolution problems (recrystallisation + growth) when sequential datasets are available. In this thesis, WE43 provides the precipitation-rich, strongly pinned case study to test whether grain growth pathways and stability can be quantified and predicted more robustly when precipitation state and grain network descriptors are included [134–136].

2.8.4 Summary

Taken together, AZ31, ZE20 and WE43 represent three distinct microstructure-engineering strategies in Mg alloy design: a conventional baseline alloy where grain growth is comparatively weakly constrained and basal textures remain strong; a lean-RE alloy where recrystallisation and grain growth become strongly orientation-selective, enabling texture weakening; and an RE-rich alloy where precipitation and solute effects promote both strengthening and microstructural stability but create a higher-dimensional optimisation problem. These contrasts motivate the central themes of this thesis: separating nucleation and

growth contributions during recrystallisation, quantifying grain growth pathways, and leveraging data-rich methods—including materials informatics—to make microstructure evolution more predictable and optimisable.

2.9 Research focus of this thesis

Chapter 2 has reviewed the state-of-the-art in Mg alloy design, microstructural evolution mechanisms, and materials informatics as applied to different research. In summary, this chapter have explored strategic alloying to refine microstructures and modify the strong basal textures typical of wrought Mg. Significant progress has been made in understanding how processing influences texture and grain size – for instance, advanced EBSD mapping now allows textures in rolled/extruded Mg alloys to be well characterized under various conditions. Likewise, mechanisms of microstructure evolution such as twinning, DRX, grain growth, and precipitation have been elucidated by numerous recent studies. In parallel, materials informatics and data-driven approaches have emerged as powerful tools for alloy development: machine learning techniques are being used to model Mg alloy behaviour, optimise microstructures, and accelerate alloy design. Throughout this chapter, contemporary literature (up to 2025) was surveyed to ensure that the review captures the current cutting-edge understanding in these domains.

Despite the advances reported in literature, several important knowledge gaps and unresolved challenges have been identified. Foremost, a complete understanding of grain growth and recrystallisation in wrought Mg remains elusive – the underlying recrystallisation mechanisms are still actively debated even with advanced characterisation techniques. For example, while adding rare-earth elements is known to weaken basal textures, the precise

mechanism (whether through solute effects, particle-stimulated nucleation, or boundary segregation) is not fully resolved. The interplay between alloying additions, deformation conditions, and microstructural evolution (including recrystallisation and subsequent grain growth) is complex, and current models do not yet capture all aspects. Predictive modelling of microstructure is particularly challenging; recent modelling efforts (e.g. multi-level cellular automata) have improved grain size predictions by accounting for concurrent phenomena like DRX and precipitation, but they highlight the necessity of including such interactions for accuracy. Moreover, data-driven prediction of microstructural outcomes in Mg alloys is still in its initial stage. While machine learning offers great promise, limitations in data availability and interpretability mean that fully reliable microstructure predictions are not yet attainable. In summary, controlling and predicting the microstructure (grain size distribution, texture) of wrought Mg alloys – especially those with complex chemistries or processing paths – remains a critical challenge. This gap is pronounced for alloys undergoing novel processing routes and for new compositions (e.g. lean rare-earth alloys). These unresolved issues underscore the need for further research, particularly studies that can observe grain-scale changes and build improved predictive frameworks.

Considering the above gaps, the present study is undertaken to advance the understanding of recrystallisation and microstructure development in wrought Mg alloys, and to develop robust workflow that promotes the connection with data-driven approaches for studying microstructural evolutions. The scope of this research spans comprehensive experimental characterisation combined with grain-level tracking and analysis. We focus on three representative Mg alloy systems – AZ31, ZE20, and WE43 – selected to cover a range from conventional to advanced alloy design. AZ31 (Mg-3Al-1Zn) is a widely used commercial

wrought alloy, serving as a baseline with well-documented behaviour. ZE20 (Mg-2Zn-0.2Ce) is a newly developed wrought Mg alloy containing a trace rare-earth addition (Ce); it was chosen for its reported improved extrudability and mechanical performance and to investigate how a lean rare-earth microalloying influences recrystallisation and texture. WE43 (Mg-4Y-3RE-0.4Zr, with Y and Nd/Gd as the main rare-earth constituents) is included as a high-strength, rare-earth-rich magnesium alloy; it is known for retaining strength up to ~300 °C and sees critical application in aerospace components. By examining these three alloys, the study covers a broad spectrum: from a traditional workhorse alloy (AZ31) to a modern extrudable alloy (ZE20) and a high-performance aerospace alloy (WE43). This range provides a strong basis to generalize findings and discern the effects of composition (particularly rare-earth content) on microstructure evolution. The experimental program is designed to induce and observe grain growth and recrystallisation under controlled conditions (i.e. isothermal annealing after deformation), while the grain-level tracking will leverage the data to assist detailed analysis at grain scale.

Objectives: Building on the literature review and gaps identified, the specific objectives of this research project are as follows:

- Perform detailed experimental characterisation of microstructure evolution in AZ31, ZE20, and WE43 during and after thermomechanical processing. This includes recording grain size, grain morphology, and crystallographic texture at various annealing stages using techniques including optical microscopy, EBSD and LabDCT. The aim is to record the grain growth and recrystallisation behaviour in 3D/4D to collect large, time-resolved and quality datasets.

- Develop and apply grain-tracking methodology to follow individual grains (or groups of grains) through recrystallisation and grain growth. Using quasi-in-situ EBSD and LabDCT, the study track how specific grains nucleate, grow, or shrink during annealing. This grain-scale analysis is intended to reveal the mechanisms of new grain formation and growth inhibition – for example, identifying where and when recrystallisation nuclei appear, which grains successfully grow, and how some grains are consumed. By directly observing these events in AZ31, ZE20 and WE43, the thesis clarifies how factors like initial deformation substructure or second-phase particles influence recrystallisation and grain growth kinetics. This objective addresses the noted gap in understanding the grain-level dynamics of recrystallisation in Mg alloys.

By achieving these objectives, the present work will fill some of the critical knowledge gaps identified in the field of physical metallurgy. The findings are expected to not only deepen scientific understanding of microstructure control in Mg alloys but also to guide the development of improved predictive models for industrial alloy processing. In the next chapter, the experimental methodology employed to accomplish these objectives is presented. This includes descriptions of the materials (alloy compositions and processing history), the deformation and annealing procedures used to drive microstructural changes, the characterisation techniques, and the analytical methods for grains tracking. Together, the methodology in Chapter 3 provides the practical foundation for addressing the research aims outlined here and sets the stage for the results and discussions in subsequent chapters.

Chapter 3 Materials and methodology

This chapter describes the materials, processing routes, interrupted heat treatments, characterisation methods, and data-processing workflows used throughout this thesis. The experimental and computational methodology is organised around three linked work packages:

- Development of Track-Rex for grain-scale tracking in quasi-in-situ EBSD datasets, using AZ31 and ZE20 rolled-sheet datasets.
- Application of Track-Rex to quantify the contribution of different recrystallisation nucleation sites, using a ZE20 extruded-profile material state and a shear-band-promoted cold-rolling condition.
- Development of Track-4DGG for 3D/4D grain tracking in volumetric datasets, using WE43 extruded bar specimens characterised by quasi-in-situ LabDCT.

The chapter first introduces the alloys and sample reference frames (Section 3.1), followed by processing routes (Section 3.2) and interrupted annealing schedules (Section 3.3). Characterisation methods are then described, focusing on quasi-in-situ EBSD (2D + time) and quasi-in-situ LabDCT (3D + time) (Section 3.4). Finally, the data-processing pipeline and the grain-tracking toolboxes (Track-Rex and Track-4DGG) are summarised (Section 3.5).

3.1 Materials

This thesis focuses on three representative wrought Mg alloys: AZ31, ZE20 and WE43. These were selected to span:

- A conventional RE-free alloy system (AZ31).
- A lean RE-modified alloy system with distinct recrystallisation/texture behaviour (ZE20).
- A RE-rich alloy system in which precipitates and second-phase particles are expected to influence grain-growth kinetics (WE43).

Unless otherwise stated, compositions are given in wt.% (Mg balance) and are summarised in Table 3.1. Material form and intended use within the thesis are summarised in Table 3.2. AZ31 is adopted as the benchmark commercial alloy, which typically reveal a strong basal texture after rolling or extrusion. ZE20 is chose to investigate the rare-earth texture development during recrystallisation. WE43 is employed for volumetric 4D (3D + time) grain growth studies. Unless otherwise stated, all alloy compositions are given in wt.% and Mg is the balance, as listed in Table 3.1. Microstructural reference coordinate follows standard wrought product conventions: rolling direction (RD), transverse direction (TD) and normal direction (ND) for sheet; and extrusion direction (ED) for extruded products.

Table 3.1 Nominal chemical composition of alloys used in this thesis (wt.%)

Alloy	Al	Zn	Ce	Y	RE	Zr	Mg
AZ31	3.0	1.0	–	–	–	–	Balance
ZE20	–	2.4	0.2	–	–	–	Balance
WE43	–	–	–	~4.0	~3.0	minor	Balance

The selection of AZ31, ZE20 and WE43 was based not only on differences in alloy chemistry, but also on their technological relevance, commercial availability and representation of different categories of wrought magnesium alloys. These three alloys provide complementary case studies for examining annealing-driven microstructural evolution in Mg alloys, rather than forming a direct one-to-one comparison under identical processing and characterisation conditions.

AZ31 was selected as a conventional RE-free Mg–Al–Zn alloy and serves as the baseline material in this thesis. It is one of the most widely used commercial wrought magnesium alloys because of its relatively low cost, good availability and established processing routes in sheet and extruded products. From an application perspective, AZ31 represents the class of general-purpose lightweight Mg alloys considered for automotive, transport and structural components where weight reduction is important but high-temperature performance is not the primary requirement. Its well-known tendency to develop a strong basal texture after deformation also makes it an appropriate reference alloy for assessing recrystallisation behaviour and the ability of grain tracking to resolve the evolution of individual recrystallised grains.

ZE20 was selected as a lean rare-earth-containing Mg–Zn–Ce alloy. Compared with AZ31, ZE20 represents a more recent alloy design strategy in which limited rare-earth addition is used to improve texture control and formability while avoiding the higher cost and alloying complexity associated with RE-rich systems. This makes ZE20 relevant to future wrought Mg products where improved deformation behaviour and weaker basal texture are required, particularly in automotive and lightweight structural applications. In this thesis, ZE20 provides a suitable case study for investigating recrystallisation, texture evolution and the contribution of specific nucleation sites, including shear bands, using quasi-in-situ EBSD and Track-Rex.

WE43 was selected as a high-performance Mg–Y–RE–Zr alloy. In contrast to AZ31 and ZE20, WE43 represents a RE-rich alloy family designed for applications where higher strength, improved thermal stability and better retention of mechanical properties are required. These characteristics make WE43 relevant to advanced aerospace, transport and high-value structural applications. Its relatively stable microstructure during annealing also makes it suitable for a 4D LabDCT-based grain growth study, where the same volume must be tracked through multiple heat-treatment steps. In this thesis, WE43 is therefore used to examine three-dimensional grain growth, abnormal grain growth and spatially resolved growth behaviour using Track-4DGG.

Taken together, the three alloys cover a practical range of wrought Mg alloy design strategies: a conventional commercial RE-free alloy, a lean-RE alloy aimed at texture modification and formability improvement, and a high-performance RE-rich alloy with enhanced thermal and microstructural stability. The purpose of using these alloys is not to isolate the effect of rare-earth additions alone, but to demonstrate how grain-resolved tracking can be applied to technologically relevant Mg alloy systems with different processing histories, application targets and microstructural evolution problems.

3.2 Materials processing

To improve clarity and align with the datasets in later chapters, the processing routes are described below in the same order as they appear in the thesis:

- AZ31 cold rolling
- ZE20 cold rolling

- ZE20 hollow-profile extrusion and subsequent cold rolling
- WE43 extruded bar + wired electrical discharge machining (EDM)

A brief summary for all the mechanical processing procedures that applied to the samples above is summarized in Table 3.2, details are provided in following subsections.

Table 3.2 Material form, sample history, and role within the thesis

Alloy	As-received form	As-received condition	Applied machining and processing	Primary usage
AZ31	Commercial rolled sheet	As-rolled	Cold rolled with 10% thickness reduction in one pass then Cut into rectangular sample	Baseline RE-free recrystallisation statistics Develop Track-Rex
ZE20	Commercial rolled sheet	As-rolled	Cold rolled with 20% thickness reduction in two passes then Cut into rectangular sample	Lean RE-modified recrystallisation statistics Develop Track-Rex
ZE20	Industrial extruded hollow profile	As extruded	Cold rolled with 20% thickness reduction in two passes then Cut into rectangular sample	Lean RE-modified recrystallisation statistics Quantify texture evolution Apply Track-Rex
WE43	Industrial extruded bar	Extruded T5	Cylindrical rods extracted along ED by wire EDM	4D grain growth statistics Spatially resolved grain growth Develop Track-4DGG

3.2.1 AZ31 cold rolling

A commercial Mg–3Al–1Zn alloy was used as the RE-free reference material for quasi-in-situ EBSD study of static recrystallisation and subsequent grain growth. Commercially rolled sheet alloy was cold rolled at room temperature with approximately 10% thickness reduction in a single pass. Further thickness reduction was limited because a small edge crack initiated at this strain level. Rectangular sample for interrupted annealing were

sectioned from the rolled sheet. The commercial rolling and applied cold rolling share the same standard RD/TD/ND coordinate frame and subsequent EBSD mappings are conducted on the TD–RD plane. The purpose of this cold rolling is to introduce a controlled deformation substructure (i.e., strong basal texture and deformation twins) that drives static recrystallisation during the subsequent interrupted annealing sequence.

3.2.2 ZE20 cold rolling

Mg–2.4Zn–0.2Ce alloy is chosen to investigate RE-modified static recrystallisation and texture evolution as well as subsequent grain growth, in comparison with the commercial AZ31 alloy. ZE20 sheet exhibited higher formability than AZ31 under the same cold-rolling conditions and was therefore rolled to a larger total thickness reduction strain of ~20% by two passes, with no comparable edge crack observed at this amount of reduction. After rolling, rectangular sample was sectioned for quasi-in-situ annealing and EBSD, again preserving the standard RD/TD/ND reference coordinate and the TD–RD plane was examined by quasi-in-situ EBSD. The purpose of this cold rolling is to introduce a controlled deformation substructure (i.e., strong basal texture and deformation twins) that drives static recrystallisation during the subsequent interrupted annealing sequence.

3.2.3 ZE20 extrusion and cold rolling

Mg–2.4Zn–0.2Ce alloy is chosen to investigate RE-modified static recrystallisation and texture evolution as well as subsequent grain growth. A ZE20 extruded hollow profile, representative of an automotive front-end subframe structure, was produced in a single hot-forming operation from billet to completed profile by direct porthole-die extrusion. The

internal mandrel forming the hollow section was supported by six bridges, and the profile reference frame is defined using ED (along the profile length) and ND/TD relative to the cross-section geometry. A rectangular plate was cut from the top section as indicated in Figure 3.1 (a). An initial EBSD observation of the ND-ED plane was conducted to exam the grain size and texture, as shown in Figure 3.1 (b). The average grain size is 39.6 μm and the (0001) basal planes is tilted from ND towards ED with an intensity of 15 MUD.

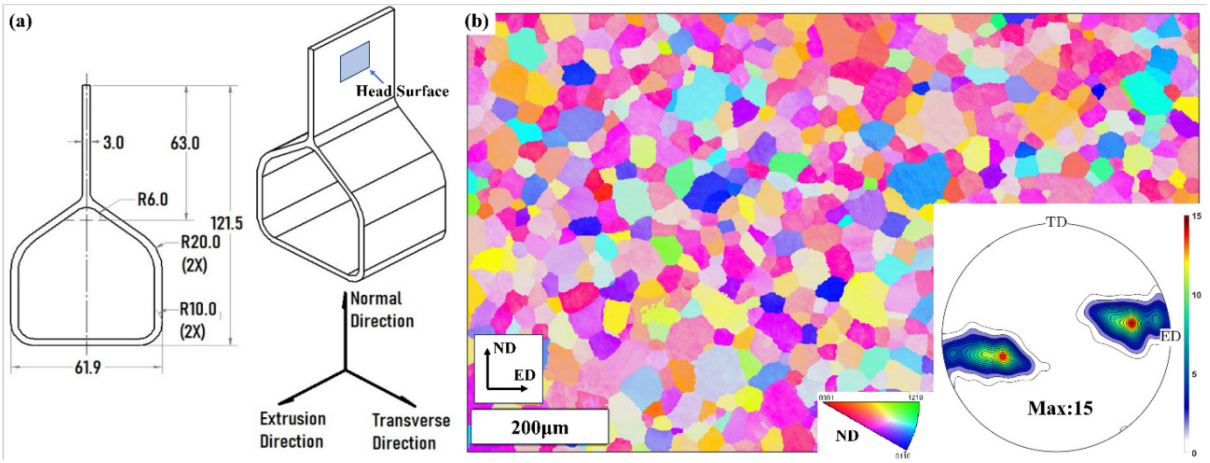

Figure 3.1 As-extruded microstructure: (a) extruded hollow profile, (b) EBSD Inverse Pole Figure (IPF) map and (0001) pole figure.

The plate was then cold rolled along ED so that the extrusion reference direction was retained during subsequent microstructure analysis. Rolling was performed using synchronous rolling mills at 10 m min^{-1} and the 20% thickness reduction over two passes specifically to promote shear bands formation prior to interrupted annealing.

3.2.4 WE43 extrusion and electrical discharge machining

Mg–4Y–3Nd alloy provided by Luxfer MEL Technologies was received as an extruded bar under the T5 condition (Ø75 mm). For the 4D grain-growth experiments based on laboratory diffraction contrast tomography, cylindrical rod specimens (Ø0.8 mm) were extracted with their axis aligned to ED using wire electrical-discharge machining (wire-EDM), to minimize preparation-induced deformation while preserving a physically meaningful processing reference direction in the reconstructed volumes. Figure 3.2 shows the cutting schematic for wire-EDM, hight of the rod is 14 mm.

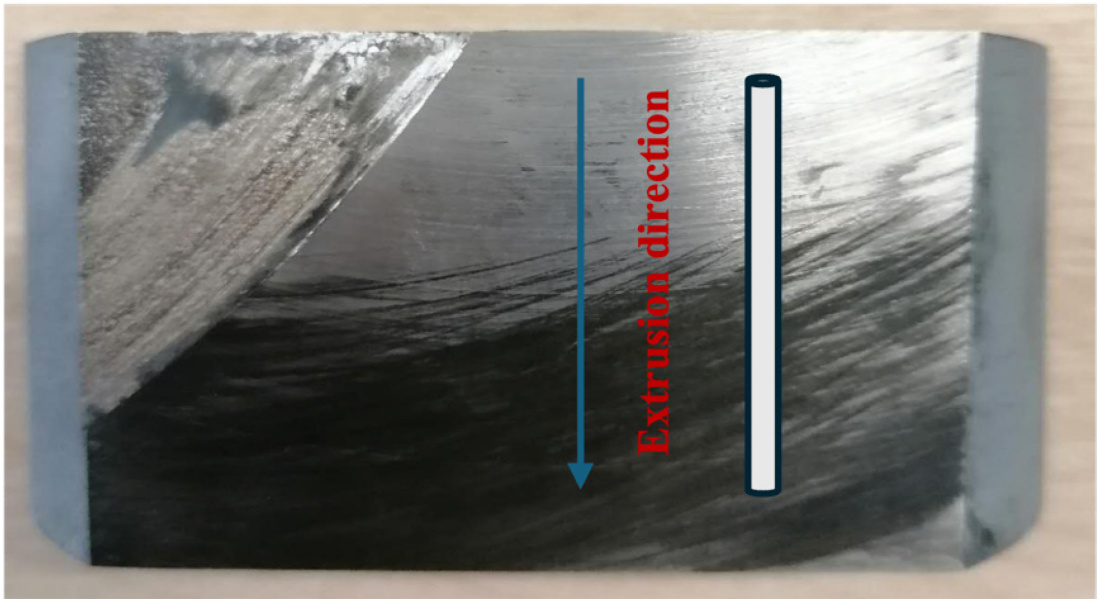

Figure 3.2 WE43 extruded bar and schematic drawing for EDM cut.

3.3 Interrupted annealing procedure

Interrupted annealing sequences was designed to capture time-resolved microstructural evolution. The same surface or volume is repeatedly characterized after cumulative annealing

times, thereby converting sequences of static characterisation snapshots into time-resolved datasets.

For 2D quasi-in-situ EBSD test, annealing was carried out in a tube furnace under protective atmosphere, and the sample was rapidly cooled after each dwell to minimise uncontrolled microstructural change. Between each annealing steps, a very light surface repolishing using 40 nm OPS suspension was applied to remove potential oxidation so that EBSD pattern quality remained stable across the sequences. The thickness reduction after this mild polishing was less than 1 μm, measured by a micrometer.

For the 4D LabDCT datasets, interrupted annealing was also carried out under protective atmosphere. Since the X-ray measurement for LabDCT is not affected by the surface condition, the sample is simply cooled in air. Table 3.3. and 3.4 summarise the cumulative time steps for recrystallisation studies.

Table 3.3 Quasi-in-situ annealing design for cold rolled AZ31 and ZE20

AZ31			ZE20		
Temperature (°C)	Time (min)	Labels	Temperature (°C)	Time (min)	Labels
320	0	AZ/1	400	0	ZE/1
320	1.5	AZ/2	400	5	ZE/2
320	4.5	AZ/3	400	10	ZE/3
320	8.5	AZ/4	400	16	ZE/4
320	12.5	AZ/5	400	24	ZE/5
320	18	AZ/6	400	35	ZE/6
320	24	AZ/7	400	50	ZE/7
320	34	AZ/8	400	80	ZE/8

Table 3.4 Quasi-in-situ annealing design for ZE20 extrusion and cold rolling

ZE20		
Temperature (°C)	Time (min)	Labels
400	0	ZE1
400	4	ZE2
400	9	ZE3
400	15	ZE4
400	25	ZE5
400	45	ZE6
400	80	ZE7

For the 4D LabDCT study, a series of annealing trials was conducted on the same batch of materials cut near the rod sample. The purpose of the trial experiments was to identify a suitable time sequence that yield quality datasets from the LabDCT, which is a grain size sensitive technique. Optical microscope was employed to exam the grain size at different annealing times, the final decided annealing sequence and expected grain sizes are summarised in Table 3.5. The initial annealing for 12 minutes was to elevate the initial grain size to meet the detection limit of LabDCT, which is around 20 μm. The following annealing was designed to detect trackable grain growth that within 10 μm between each step. However, the designed grain size was calculated on a two-dimensional surface, thus the final three-dimensional grain size might be different.

Table 3.5 Quasi-in-situ annealing design for WE43 grain growth

WE43		
Temperature (°C)	Time (min)	Expect Grain Size (μm)
490	12	20
490	32	30
490	80	40
490	140	45
490	800	50
490	2240	60

3.4 Materials characterisation

3.4.1 Optical microscope

Reflected-light optical microscopy (OM) was used as a rapid, low-cost method to (i) screen processing conditions, (ii) evaluate surface preparation quality prior to EBSD, and (iii) provide a preliminary estimate of grain size evolution for planning interrupted-annealing dwell times (particularly for the WE43 grain growth study).

Specimens for OM were prepared by standard metallographic grinding and polishing to a mirror finish, followed by a brief chemical etch suitable for magnesium alloys to reveal grain boundaries. Grain size was estimated using standard image-analysis procedures (e.g., intercept-based methods or equivalent-circle measurements), with multiple fields of view taken to reduce sampling bias. An example OM image for the design of annealing sequence of 4D grain growth is presented in Figure 3.3, it should be noticed that the edge part of the images are out of focus, which was because of bad stage condition, but it has minor effect on the grain size calculation.

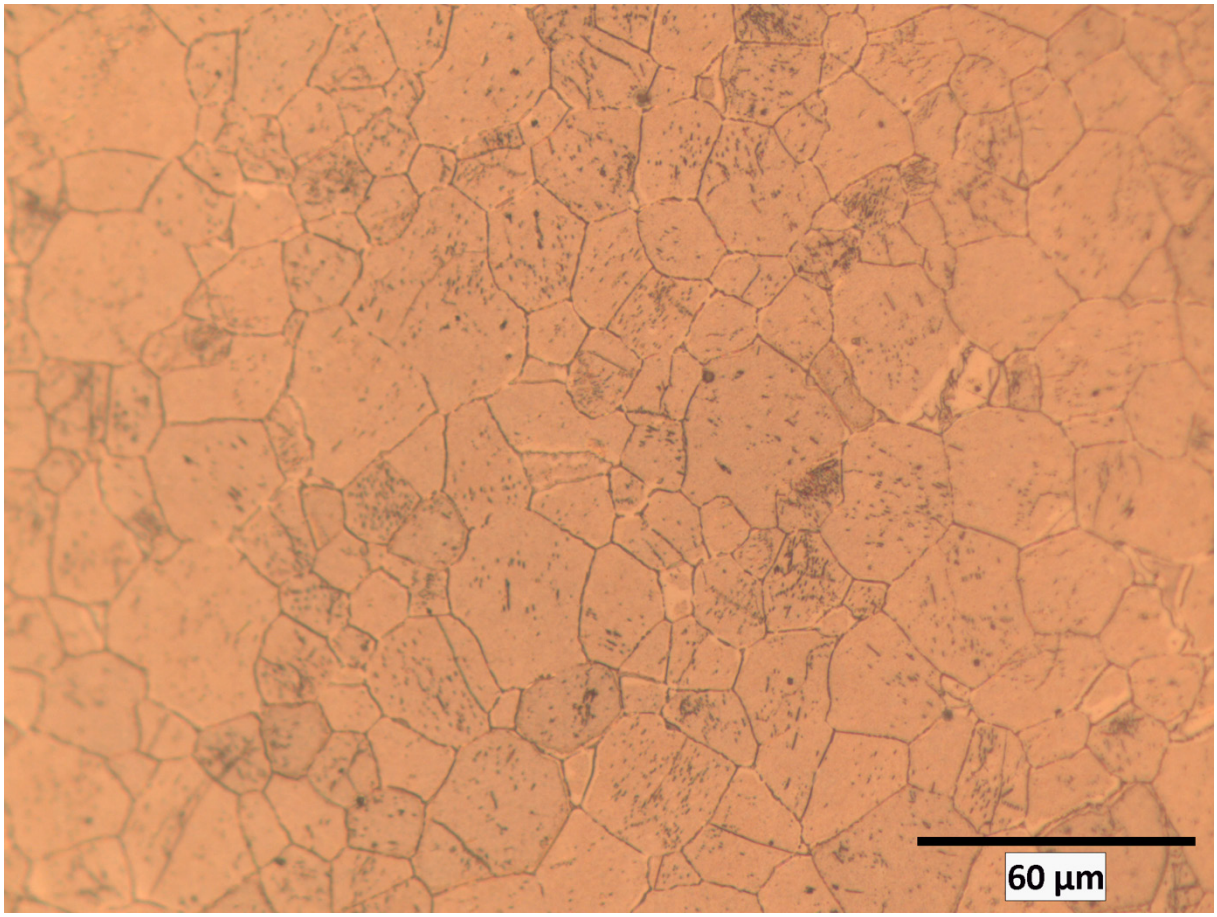

Figure 3.3 Optical microscopy image of as received WE43 extruded bar, sample was cut near the rod EDMed sample. The observed plan is ND-TD plane. Average grain size is calculated to be 18.9 µm.

3.4.2 Quasi-in-situ electron backscatter diffraction

Quasi-in-situ EBSD was employed to capture recrystallisation nucleation and grain-growth behaviour on the same mapped region across a sequence of annealing steps. EBSD provides grain-scale crystallographic orientation information and is therefore well suited to: (i) identify recrystallised grains, (ii) quantify texture evolution, and (iii) supply grain-level features required by the Track-Rex tracking pipeline.

Sample preparation and repeatability. After rolling, samples were ground and polished to obtain an EBSD-quality surface on the ND–RD plane. For quasi-in-situ sequences, after each EBSD scan the specimen was annealed for the next dwell, cooled, and returned to the SEM for remapping. A short, gentle repolish (e.g., colloidal silica/OPS) was used between steps where needed to remove oxidation while keeping material removal negligible relative to characteristic grain size. The same region was relocated between steps using SEM stage coordinates and identifiable microstructural features.

The quasi-in-situ EBSD approach used in this thesis enables microstructural evolution to be followed over relatively large areas and multiple annealing steps, but it also introduces several sources of uncertainty. Unlike continuous in-situ EBSD, the same region must be relocated after each interrupted annealing step. Although map position, microstructural landmarks and the overall grain structure were used for relocation, exact pixel-to-pixel alignment cannot be fully guaranteed. Small differences in region selection, sample tilt, scan rotation or map alignment may influence the apparent position of grain boundaries, especially for small grains or regions with rapid boundary migration.

Repeated sample handling and surface preparation may also affect EBSD data quality. Changes in surface condition, oxidation, contamination or minor polishing effects can influence pattern quality, indexing rate and grain boundary segmentation between annealing steps. In addition, interrupted annealing involves cooling and reheating between observations, so the recorded maps represent selected annealing states rather than continuous boundary migration. This limits the ability to determine the exact timing of nucleation, grain consumption or rapid local growth events.

These uncertainties were considered during tracking. The Track-Rex workflow combines spatial position, crystallographic orientation, shape information and neighbourhood consistency, rather than relying only on pixel-level overlap or nearest-centroid matching. The main conclusions are also based on statistical trends from large grain populations, reducing the influence of isolated local uncertainties. Nevertheless, ambiguous individual cases require careful interpretation. Future in-situ EBSD experiments using a heating stage could reduce relocation and repeated preparation uncertainties, although they may introduce other challenges such as thermal drift, smaller field of view and reduced long-duration stability.

EBSD acquisition. EBSD mapping was conducted using an FEI Nova 450 field-emission-gun SEM equipped with an Oxford Instruments Nordlys Nano EBSD detector. A step size of 0.4 μm was used for the quasi-in-situ tracking datasets to balance spatial resolution against mapping area. Annealing schedules (temperatures and cumulative times) for AZ31, ZE20 rolled sheet, and the ZE20 shear-band dataset are summarised in Table 3.3 and Table 3.4

Data cleaning and grain definition. Standard EBSD clean-up routines were applied to remove isolated wild spikes, reduce small unindexed regions where appropriate, and ensure consistent grain reconstruction across time steps. Grains were reconstructed using a conventional critical misorientation threshold, and grain-level features (grain ID, centroid position, mean orientation, equivalent size/area, and neighbour list) were exported for tracking analysis.

3.4.3 Quasi-in-situ laboratory diffraction contrast tomography

LabDCT was employed as a non-destructive 3D microstructure characterisation method to overcome limitations inherent to surface EBSD (notably, the inability to resolve through-

volume grain connectivity and out-of-plane growth). LabDCT provides 3D grain maps (orientation, centroid and volume) that can be repeated after interrupted annealing to form a 4D dataset (3D + time).

WE43 cylindrical specimens (Ø0.8 mm, axis aligned with ED) were used for LabDCT experiments. Interrupted annealing was performed at 490 °C for cumulative times of 12, 32, 80, 140, 800 and 2240 minutes under protective argon flow. After each dwell, the specimen was cooled to room temperature for X-ray characterisation.

X-ray imaging was performed using a ZEISS CrystalCT system equipped with a flat-panel detector. At each time step, an absorption-contrast tomography (ACT) scan was acquired to define the specimen mask and reconstruction volume, followed by LabDCT acquisition. LabDCT datasets were collected at 80 kV using a 375 × 375 µm aperture, with source–specimen and specimen–detector distances of 12 mm and 400 mm, respectively. Approximately 3000 projections per time step were acquired using a helical phyllotaxis scheme with 20 s exposure per projection.

Grain reconstruction was performed using GrainMapper3D (Xnovo Technology ApS). Diffraction images were denoised and segmented using customised routines, and low-intensity peripheral spots were excluded to improve indexing robustness. Grain indexing used a voxel size of 2.5 µm and a misorientation threshold of 0.5° for grain definition, yielding completeness values sufficient for reliable tracking. Post-processing (including surface meshing and feature statistics) was carried out using DREAM.3D and custom scripts. A sub-volume away from reconstruction boundaries was selected to minimise edge artefacts. Figure 3.4 & 3.5 provides

detailed experimental setup and raw data. Figure 3.6 shows the distribution of completeness for the selected sub-volume, and Figure 3.7 is an overview of the whole dataset.

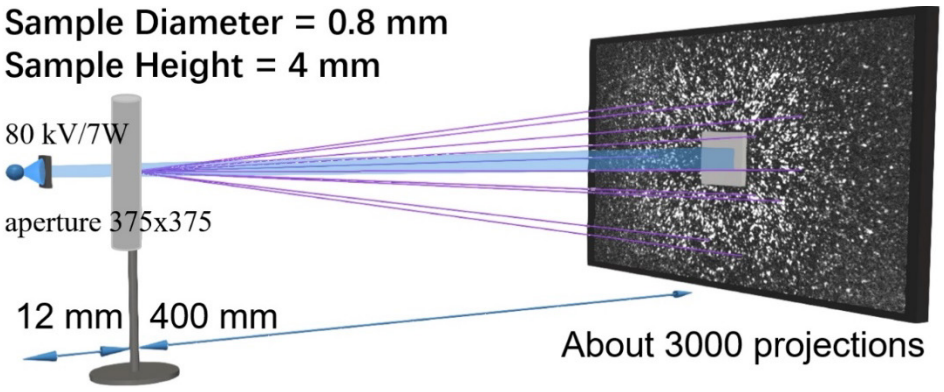

Figure 3.4 Experimental setup and processing for diffraction images.

Limitations of LabDCT-based grain characterisation. The LabDCT-based workflow used in this thesis enables non-destructive three-dimensional grain tracking during interrupted annealing, but several limitations should be considered when interpreting the results. These limitations arise from specimen preparation, spatial resolution, reconstruction completeness, segmentation quality and the difference between the EBSD and LabDCT datasets used in the thesis.

First, the WE43 specimen used for LabDCT was prepared by electrical discharge machining. This method is suitable for producing small cylindrical specimens with controlled geometry, but it may introduce a local surface-affected region, including possible thermal or mechanical alteration near the machined surface. Although the main analysis was conducted on a selected internal reconstructed volume to reduce the influence of surface preparation effects, the possibility of a locally altered near-surface microstructure cannot be completely

excluded. This should be considered when interpreting surface-related grain growth behaviour and spatial heterogeneity.

Second, LabDCT has a finite spatial resolution, which imposes a lower practical grain-size detection limit. Very small grains may not generate sufficient diffraction information to be reliably indexed and reconstructed, particularly when their size approaches the voxel size or when they are located close to larger neighbouring grains. As a result, the reconstructed grain population may underrepresent the smallest grains, especially during the early stages of annealing. Grain-size statistics and tracking results involving small grains should therefore be interpreted as conservative estimates rather than complete representations of the full grain population.

Third, reconstruction completeness and segmentation quality affect the reliability of grain-level descriptors. Incomplete reconstruction can influence the measured grain volume, equivalent spherical diameter, grain shape, centroid position and local boundary topology. These factors are important for grain tracking because Track-4DGG uses grain-level descriptors and neighbourhood information to correlate grains between successive annealing steps. Poorly reconstructed grains, grains close to the detection limit, and grains involved in complex local topology changes may therefore have lower tracking confidence. For this reason, the tracking analysis treats ambiguous or poorly reconstructed cases conservatively and focuses the main interpretation on robust statistical trends across the tracked grain population.

It should also be noted that 4D LabDCT was applied only to the WE43 alloy in this thesis, whereas AZ31 and ZE20 were studied using quasi-in-situ EBSD. Therefore, the three alloys are not compared through an identical three-dimensional characterisation route. The EBSD

datasets provide high-resolution two-dimensional information on recrystallisation and texture evolution over relatively large mapped areas, while the LabDCT dataset provides non-destructive three-dimensional information on grain growth within a selected WE43 volume. These methods are therefore complementary rather than directly equivalent.

Accordingly, the LabDCT results in Chapter 6 should be interpreted as a three-dimensional grain-growth case study for WE43, rather than as a direct 3D comparison with the AZ31 and ZE20 recrystallisation datasets. Despite the limitations associated with spatial resolution and reconstruction completeness, LabDCT provides a unique capability to track grain growth non-destructively in three dimensions. When combined with conservative tracking criteria and population-level statistical analysis, it offers valuable insight into normal grain growth, abnormal grain growth and spatial heterogeneity in Mg-RE alloys.

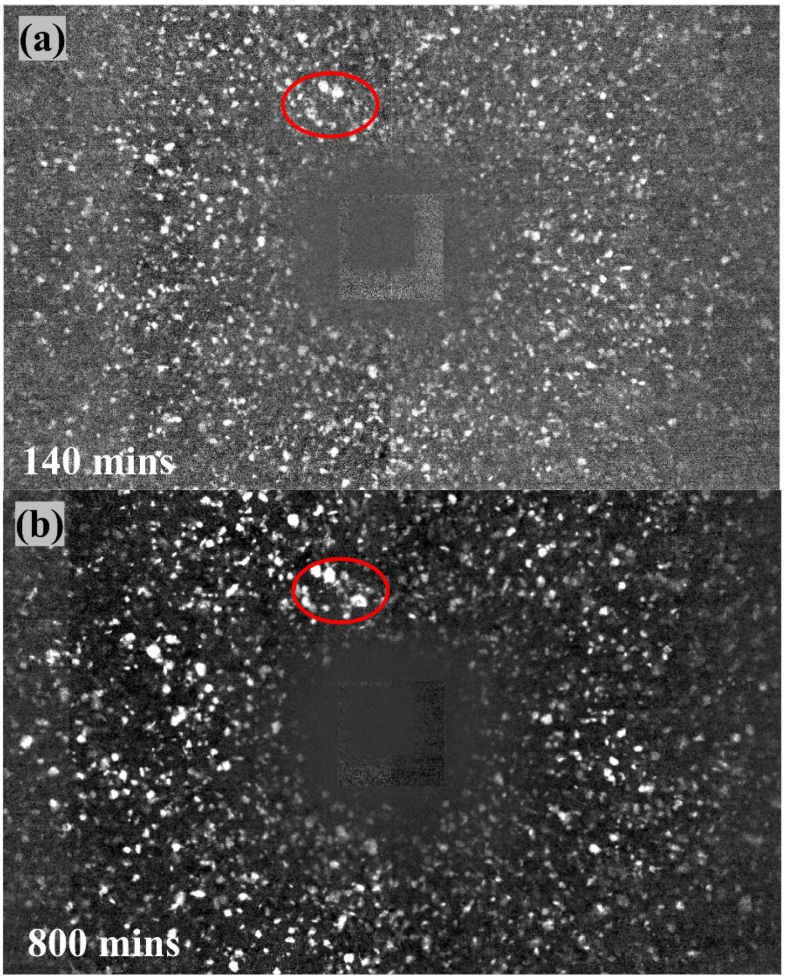

Figure 3.5 Raw diffraction image of the same sample projection: (a)140 minutes, (b) 800 minutes, the diffraction spots of same grains if highlighted by the red circle

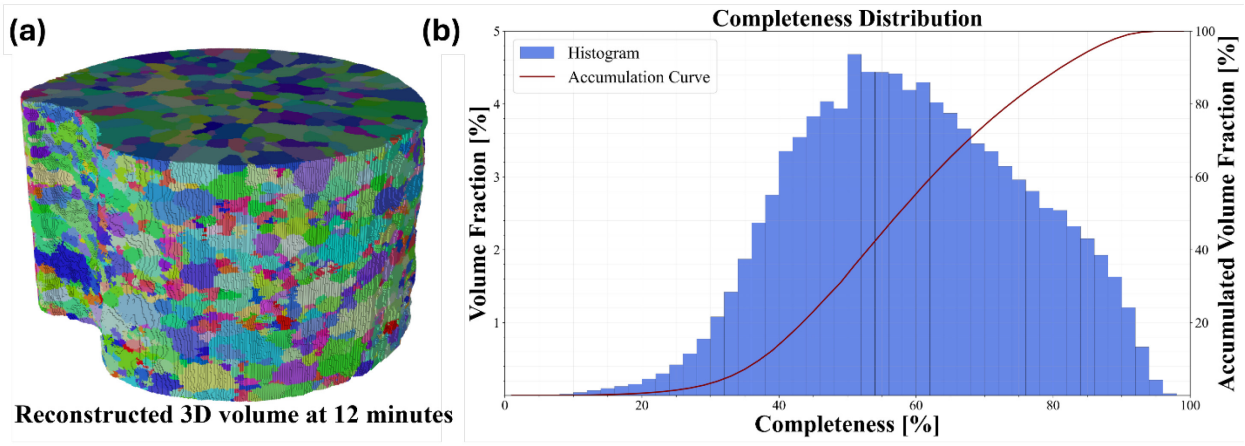

Figure 3.6 Reconstruction quality. (a) Selected 3D volume at 12 minutes annealing time and (b) corresponding completeness distribution with mean value of 60%

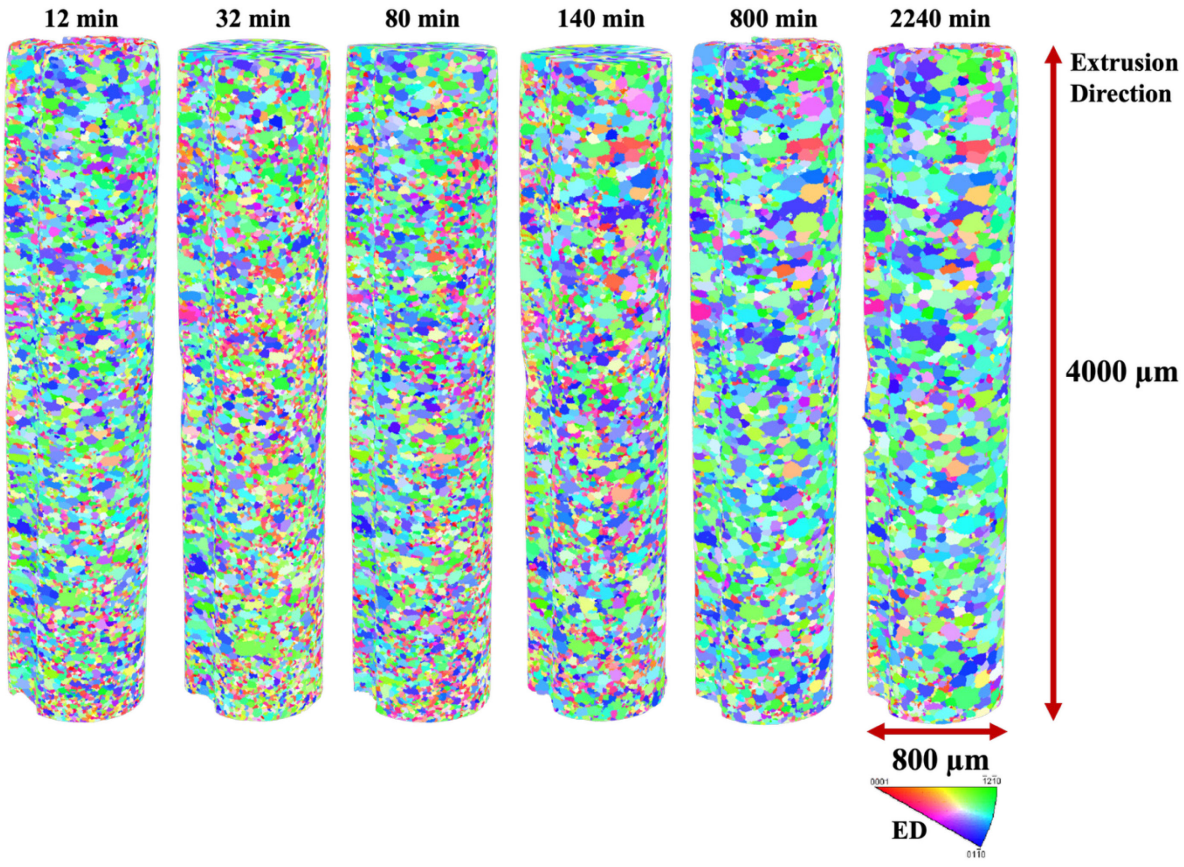

Figure 3.7 Overview of the LabDCT outcome

3.4.4 Three-dimensional electron backscatter diffraction

Three-dimensional EBSD by serial sectioning provides an alternative route to obtain 3D crystallographic orientation information by repeatedly removing thin layers and acquiring an EBSD map after each slice, followed by alignment and reconstruction. Compared with LabDCT, serial sectioning can achieve finer spatial resolution in some cases but is destructive and typically limited by acquisition time and alignment uncertainty over large volumes.

In the context of this thesis, serial sectioning is considered as a complementary approach for future extension of the tracking pipeline to higher-resolution 3D datasets, especially where very small grains or fine orientation gradients must be resolved. The non-destructive LabDCT route is adopted here as the primary 3D/4D method because it enables repeated measurement of the same volume across long annealing times. Figure 3.8 shows a comparison between LabDCT and 3D-EBSD

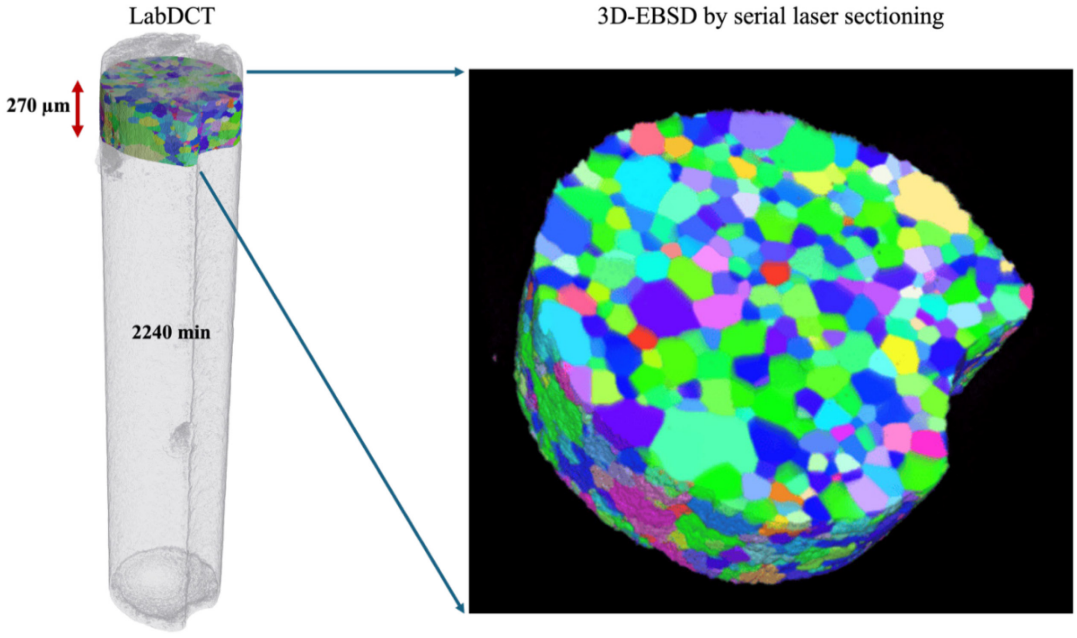

Figure 3.8 A comparison between LabDCT and 3D-EBSD

3.5 Data Processing and toolbox development

3.5.1 Data processing software

The data pipeline combines established microstructure toolchains with custom scripts:

EBSD processing and grain reconstruction: MATLAB-based processing using MTEX for grain segmentation, texture calculation, and extraction of grain features required for tracking.

2D grain tracking: custom MATLAB toolbox Track-Rex (this work) built around MTEX grain objects and additional correlation logic.

LabDCT reconstruction and feature extraction: vendor software for grain mapping, followed by post-processing and feature export using open-source microstructure tools (e.g., DREAM.3D) and custom scripts.

3D/4D tracking and modelling preparation: Python scripts for data structuring, feature assembly, and preparation of inputs for subsequent modelling (Chapter 5 onwards).

All datasets are converted into consistent grain-resolved tables such that each grain has a unique ID per time step, grain-level features, and an explicit mapping to its correlated "same-grain" identity across time.

3.5.2 Grain tracking algorithm and coding

The process begins with data preparation, where a reduced dataset is cropped from the raw EBSD data to ensure consistent mapping areas for Track-Rex. The reduced datasets

provide magnified views of several thousand grains, revealing statistically reliable and detailed information about the recrystallisation process. For instance, more than 4000 and 2000 grains are observed in the ZE20 and AZ31 samples, respectively, after a single pass annealing. The ZE20 sample with a high nucleation activity demonstrates a higher number of recrystallized grains compared to the AZ31 sample within the similar selected region size of 810×610 um^2. These counts serve as the reference of grain correlation because of the higher indexing rate of ZE/2 and AZ/2 compared to the as-rolled condition. MTEX package is utilized on the reduced EBSD datasets for grain correlation. Five key features are extracted from the grain properties, including grain ID, position, orientation, size and neighbours. Grain ID serves as the direct input and output of Track-Rex toolbox with which other properties can be referred. Grain position and orientation are two major criteria for indexing the same grain on different EBSD scans.

Figure 3.9 illustrates how Track-Rex correlates grains on two EBSD datasets of the ZE20 sample, while the detailed algorithm is illustrated in Figure 3.10. The first step is to select a reference grain that appears on both EBSD scans (g1 and g1') with similar locations and orientations (misorientation angle <= 5º), Figure 3.9 (a). The misorientation angle of 5° ensures the identification of the same grain across different EBSD scans, while minimizing the potential misindexing of two or more matching grains. To link the reference positions (grain centroid) on two EBSD maps, a displacement vector D1 is introduced. The next step is to assign D1 to the 1st order (N = 1) neighbouring grains (for example g2) of the reference. Since g1 and g2 are adjacent to each other, it is reasonable to assume that if g2 is retained on EBSD2, it should exhibit a comparable displacement vector to D1. That is, the position of g2 on EBSD2 can be roughly calculated with its positions on EBSD1 and D1, as indicated by the white

rectangle in Figure 3.9 (b). After that, a searching process is carried out to identify grains located within a predefined searching area (Figure 3.9 (c)) surrounding the estimated position of g2. The misorientations between g2 (EBSD1) and each grain in the searching area (EBSD2) are then calculated.

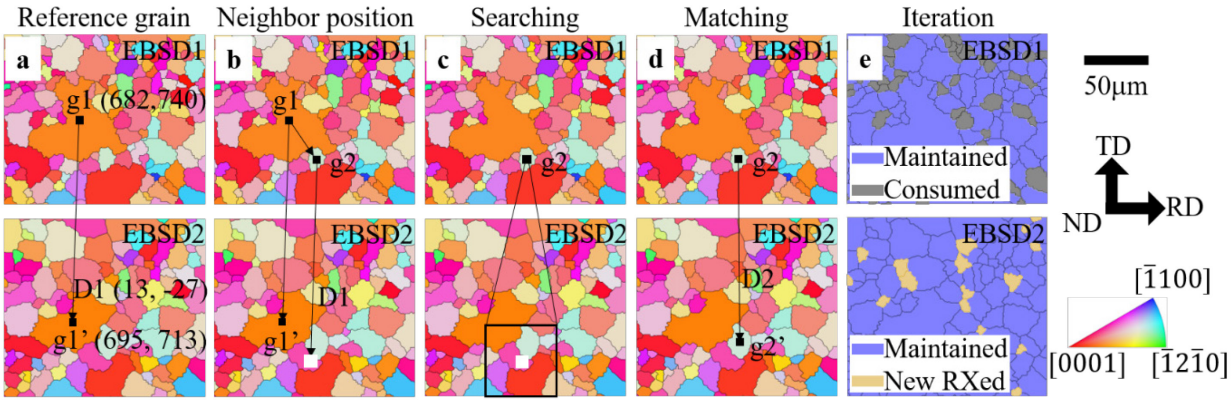

Figure 3.9 Examples of grain correlation using Track-Rex in a ZE20 sample: (a) reference selection and initial displacement vector, (b) estimation of neighbour position, (c) searching, (d) matching, (e) iteration. The numbers in bracket indicate the centroid positions of reference grains and displacement vector in (a).

The core objective of grain tracking is to establish grain-to-grain correspondence between consecutive characterisation steps. This is non-trivial because:

- new grains can appear due to recrystallisation nucleation,
- grains can disappear due to consumption/impingement,
- segmentation and indexing quality can vary between maps,
- local distortions and polishing material removal can introduce small coordinate shifts.

Track-Rex addresses these issues by combining position-based prediction with orientation-based validation and a neighbour-assisted iterative propagation strategy.

(i) Pairwise grain correlation between two EBSD maps.

For two consecutive EBSD scans (EBSD1 and EBSD2), a reference grain that appears in both maps is first identified. A displacement vector is defined from the centroid shift of this reference grain between maps. For each grain in EBSD1, its expected position in EBSD2 is predicted by applying the displacement vector, and a local search window is built around the predicted position. Candidate grains in EBSD2 are evaluated using:

- centroid proximity to the predicted location,
- misorientation relative to the EBSD1 grain orientation,
- consistency of local neighbourhood/grain-size scale (used as a secondary constraint).
- The best candidate satisfying the misorientation threshold is selected as the most probable correspondence.

(ii) Iterative neighbour propagation and voting strategy.

Because a single reference grain may not represent local distortions everywhere in the map, Track-Rex expands correspondence outward using a neighbour-propagation strategy: once a grain is reliably matched, it can act as a local reference to predict and match its neighbours. Where multiple local references propose correspondences for the same grain, a voting/consensus step is used to resolve conflicts and improve robustness.

(iii) Multi-step tracking across an entire quasi-in-situ dataset.

After pairwise matching is established between each consecutive map pair (EBSD1–EBSD2, EBSD2–EBSD3, …), Track-Rex links correspondences across the full time series. Each grain can then be assigned a “life history” including:

- first appearance time step (nucleation/visibility time),
- whether it survives to later steps,
- growth/consumption behaviour,
- orientation evolution and contribution to texture at each step.

Depending on the number of grains on EBSD2 that match the predefined misorientation angle tolerance of 5º, there are three potential situations, as shown in Figure 3.10. First, no grain within the searching area of EBSD2 shows a misorientation angle below 5º to the corresponding 1st order neighbour on EBSD1. Assuming that EBSD1 has a shorter annealing time than EBSD2, it means the neighbour grain g2, which only appears on earlier annealing condition but disappears on the next one, is consumed during the annealing process. On the contrary, the grains only observed on EBSD2 are newly formed grains. The second situation is one-to-one match: there is only one grain in the searching area of EBSD2 that shows a similar orientation to the 1st order neighbour on EBSD1. In this case, the neighbouring grain g2 is correlated between two EBSD scans, as shown in Figure 3.9 (d). Its displacement vector is calibrated which is further assigned to the next order neighbour, the 2nd order neighbour of reference grain. The last situation is that two or more matching grains are found on EBSD2, leading to an ambiguous correlation between two EBSD scans. To determine the most likely correlated grain, we apply a voting strategy which is similar to the triplet indexing of Kikuchi

bands in EBSD software. All potential correlated grains, along with their neighbours, are marked. Subsequently, the number of correctly indexed (one-to-one matching) neighbours is calculated, with each good index getting a vote. The grain with the highest vote count among all candidates is designated as the most probable correlated grain.

With this iteration of all grains on EBSD1, we can distinguish the grains that appear on both EBSD (maintained grains), and others that are either only observed on EBSD1 (consumed grains) or EBSD2 (new RXed grains), Figure 3.9 (e). Movie S1 shows that the grain correlation of two EBSD datasets can be accomplished within only 6 minutes, demonstrating the remarkable efficiency of the Track-Rex toolbox in handling large datasets.

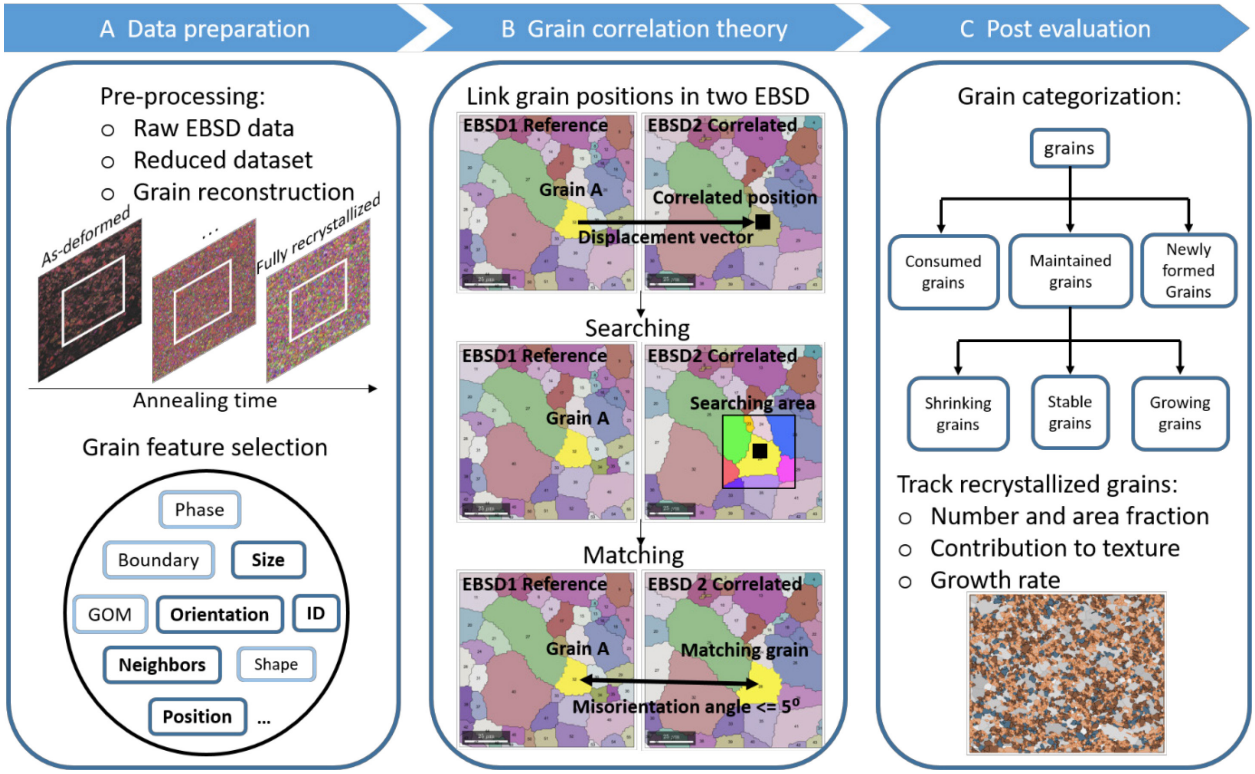

Figure 3.10 Workflow of Track-Rex.

Apart from the grain correlation to identify the maintained, consumed, and newly formed grains between two EBSD scans, what is more important for the recrystallisation study is the history of RXed grains, for example, when the RXed grains are formed and how they evolve. Track-Rex enables us to track the RXed grains originated from a specific annealing step and their contributions to the microstructure and texture evolution. Figure 3.11 (a-f) shows magnified regions of EBSD orientation maps from as-deformed (EBSD1) to fully recrystallized condition (EBSD6) in a ZE20 sample. By comparing EBSD2 to the reference EBSD1, 93 grains on EBSD2 are indexed as RXed grains, Figure 3.11 (g). With the next grain correlation between EBSD2 and EBSD3, 43 out of 93 RXed grains originated from EBSD2 are maintained in Figure 3.11 (h). These RXed grains are further tracked to EBSD6 on which only 9 of them remain on the grain map, while the others are consumed during annealing, Figure 3.11 (k). This grain tracking routine is applied to all RXed grains from different annealing steps which are separately marked in Figure 3.11 (l-p). Details of individual grain tracking process are shown in Movie S2. The entire grain tracking process of eight EBSD scans takes about only 1.5 hours. This is much less than using the conventional methods. For example, manual tracking could take up to several months to obtain the statistical results from large EBSD datasets containing thousands of grains.

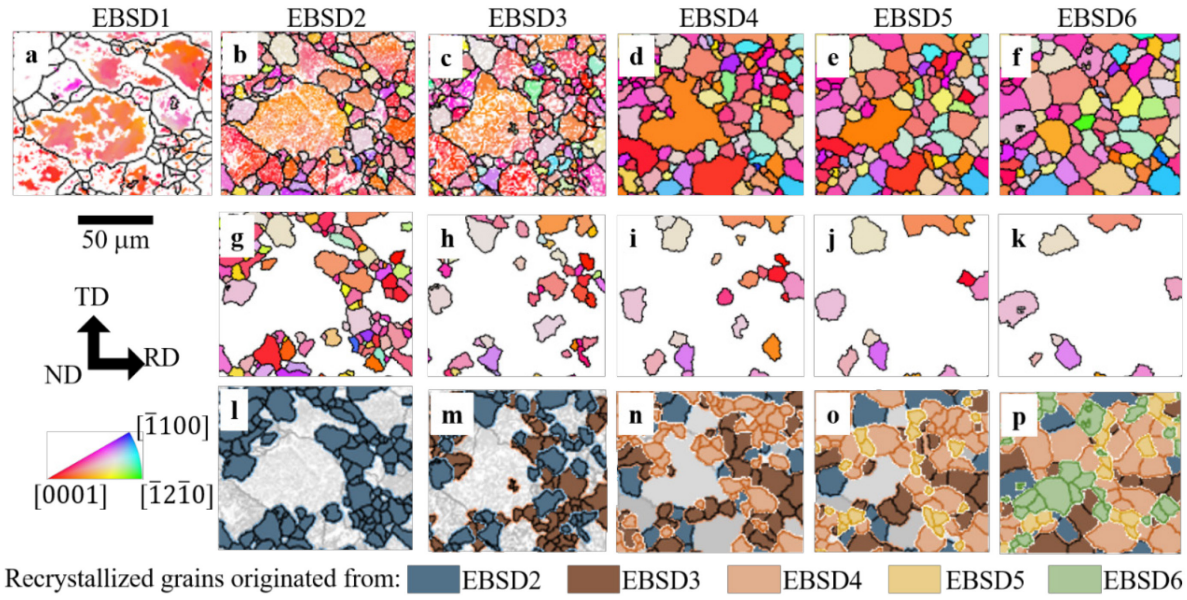

Figure 3.11 Examples of grain correlation using Track-Rex in a ZE20 sample. (a-f) EBSD maps on different annealing conditions. (g-k) Evolution of the RXed grains originated from EBSD2. (l-p) Contributions of RXed grains from different annealing conditions to the microstructure.

As the grains are categorized into maintained, consumed and newly formed grains based on their presence, the next step is to investigate the grain growth behaviours of the maintained grains. A factor of growth rate, g, is introduced as:

$$g = \frac{G.S._2 - G.S._1}{G.S._1} \quad (3.1)$$

where $G.S._1$ and $G.S._2$ are the grain sizes of the same grain on the first and second EBSD scans. With this factor, the grains are further divided into growing, stable, and shrinking groups. The grains with a growth rate between -0.2 and 0.2 are stable grains, while those lower than -

0.2 and higher than 0.2 are shrinking and growing grains, respectively. The criteria of 0.2 and -0.2 are set to include a comparable number of grains in three groups.

3.5.3 Tracking uncertainty and confidence assessment

The grain-tracking results presented in this thesis should be interpreted together with the uncertainties associated with time-resolved EBSD and LabDCT datasets. Tracking uncertainty can arise from several sources, including imperfect spatial alignment between successive datasets, segmentation differences, indexing quality, reconstruction completeness, grain boundary migration, grain rotation and complex topological events such as apparent grain merging, splitting and consumption. These effects are unavoidable in interrupted annealing experiments, where each dataset represents a discrete microstructural state rather than a continuous record of boundary motion.

For the quasi-in-situ EBSD datasets, alignment uncertainty mainly arises from relocating the same region after each annealing step and from small differences in scan position, rotation, surface condition and indexing quality. These factors may slightly change the apparent centroid position, grain boundary location or grain shape between two maps. For the LabDCT datasets, uncertainty can also arise from reconstruction completeness, segmentation quality and the limited recovery of small grains. Therefore, the tracking results should not be interpreted as exact pixel-by-pixel or voxel-by-voxel correlations. Instead, they represent grain-level correlations based on the combined consistency of several descriptors.

To reduce the influence of these uncertainties, Track-Rex and Track-4DGG do not rely on a single matching criterion. Candidate matches are evaluated using a combination of centroid position, predicted displacement, crystallographic misorientation, grain shape and

local neighbourhood consistency. The predicted displacement is estimated from a user-verified reference grain pair, while neighbour-based propagation allows local spatial relationships to be considered rather than applying only a global rigid alignment. This approach makes the tracking less sensitive to small alignment errors and local map distortions.

Grain rotation is handled through the crystallographic misorientation criterion. Small orientation differences between two annealing steps can be accepted when they remain within the defined tolerance and are supported by consistent spatial and neighbourhood information. However, a large misorientation difference is treated as evidence against a match unless there is strong supporting evidence from the local microstructure. In this way, the algorithm allows reasonable orientation variation while reducing the risk of linking two different grains with similar positions but different crystallographic identities.

Grain consumption, merging and splitting require conservative interpretation. In recrystallisation and grain growth, a grain may disappear because it is consumed by neighbouring grains, because it falls below the detection limit, or because segmentation changes between two datasets. Similarly, apparent merging or splitting may reflect true microstructural evolution, sectioning effects in 2D EBSD, or reconstruction and segmentation changes in LabDCT. The algorithms therefore do not force a match when the candidate descriptors are inconsistent. If no reliable candidate is found, the grain is classified as consumed or left unmatched, depending on the specific analysis. This conservative treatment reduces false positive matches and avoids over-interpreting uncertain local events.

The confidence of a tracked pair is therefore based on the agreement between multiple descriptors. A high-confidence match is one in which the predicted spatial position,

crystallographic orientation, grain shape and neighbouring grains are mutually consistent. A lower-confidence or ambiguous case is one in which one or more descriptors are inconsistent, for example when a grain is very small, located near the map boundary, poorly reconstructed, or involved in apparent merging or splitting. Such ambiguous cases are suitable for population-level classification only when treated conservatively and require manual inspection if they are used for detailed mechanistic interpretation.

The main conclusions of this thesis are based on statistical trends from large populations of tracked grains rather than on isolated individual events. This reduces the influence of occasional local mismatches on the overall interpretation. Nevertheless, the tracking results should be regarded as grain-level statistical correlations with defined confidence, rather than exact continuous trajectories of every boundary segment. This distinction is important when interpreting figures and statistics in Chapters 4–6, particularly for consumed grains, newly identified grains, abnormal growth events and small-grain populations close to the resolution limit.

3.5.4 Comparison with existing grain-tracking approaches

The grain-tracking workflows developed in this thesis were designed to address the practical limitations of existing approaches for analysing large time-resolved microstructural datasets. In conventional quasi-in-situ EBSD or three-dimensional characterisation studies, grain evolution is often assessed by comparing maps visually, manually selecting representative grains, or correlating a limited number of grains using their position and orientation. These approaches are useful for detailed case studies, but they become inefficient

when thousands of grains must be followed across multiple annealing steps. They also make it difficult to generate statistically meaningful grain histories for the entire dataset.

A simpler automated strategy is to use global image registration followed by nearest-centroid or nearest-neighbour matching. However, this approach is not sufficiently robust for interrupted annealing datasets. Between two experimental steps, the same region may experience local distortion, small alignment errors, grain boundary migration, grain rotation, grain growth, shrinkage and grain consumption. In such cases, the nearest grain in space is not always the same physical grain, particularly in regions where grain size changes rapidly or where new recrystallised grains appear. Therefore, a reliable tracking method must consider not only spatial proximity, but also crystallographic and neighbourhood information.

Track-Rex and Track-4DGG were developed to overcome these limitations by combining user-verified reference matching, local displacement estimation, neighbour propagation and multi-parameter candidate evaluation. The initial reference grain pair provides an experimentally grounded displacement vector between two datasets. Tracking then propagates through neighbouring grains, so that local rather than only global spatial relationships are used. Candidate grains are evaluated using a combination of centroid position, crystallographic misorientation, shape similarity and neighbourhood consistency. This combined strategy improves robustness compared with tracking based only on grain position or grain ID, both of which can change between successive EBSD or LabDCT datasets.

In terms of computational efficiency, the developed workflows allow large datasets to be processed within a practical time scale. Instead of manually checking thousands of grains, the algorithms automatically search, rank and assign candidate matches. In the recrystallisation

datasets analysed in this thesis, Track-Rex enabled tens of thousands of grains to be correlated within minutes, allowing grain-level statistical analysis to be performed across complete quasi-in-situ EBSD sequences. Similarly, Track-4DGG allowed grains and grain clusters to be extracted and followed through successive three-dimensional LabDCT datasets, making it possible to analyse 4D grain growth behaviour at both individual-grain and population levels.

The reliability of the tracking results is improved by using multiple descriptors rather than a single matching criterion. A grain is accepted as a valid match only when its spatial position, orientation and local neighbourhood are mutually consistent with the predicted evolution. This is particularly important for recrystallisation and grain growth, where individual grains may grow, shrink or be consumed. If no candidate satisfies the defined matching criteria, the algorithm does not force a match. Instead, the grain is classified as consumed or treated as an unmatched case. This conservative strategy reduces the risk of falsely linking two different grains and makes the resulting grain histories more suitable for statistical interpretation.

Complex topological events, such as grain merging and splitting, require careful interpretation. In three-dimensional datasets, apparent merging can often be related to the growth of one grain into the volume previously occupied by neighbouring grains, while apparent splitting may arise from reconstruction artefacts, segmentation changes or incomplete grain recovery. In two-dimensional EBSD datasets, such events are even more difficult to interpret because the observed section may not represent the full three-dimensional topology. For this reason, Track-Rex and Track-4DGG do not assume that all apparent merging or splitting events can be uniquely resolved. Instead, the methods prioritise robust one-to-one grain histories where the matching confidence is high and treat ambiguous cases conservatively.

Individual ambiguous cases can then be inspected manually if they are used for mechanistic discussion.

Overall, the originality of the tracking approach developed in this thesis lies in its combination of practical automation and physically meaningful descriptors. The workflows are not limited to visual comparison or nearest-neighbour matching, but use spatial, crystallographic, shape and neighbourhood information to generate traceable grain histories. This makes it possible to convert large time-resolved EBSD and LabDCT datasets into structured datasets suitable for statistical analysis, mechanistic interpretation and future materials-informatics applications. At the same time, the limitations of the method are recognised: the tracking accuracy depends on the quality of the input segmentation, the spatial alignment between datasets, the reconstruction completeness in LabDCT, and the ability of 2D or 3D characterisation to capture the relevant grain topology.

3.5.5 Toolbox operation in MATLAB

Figure 3.12 shows the algorithm of Track-Rex to correlation the same grains on different EBSD scans. The first step is to choose the reference for grain correlation, the grains which appear on both EBSD with similar locations and orientations (misorientation angle <= 5º). The IDs of the same reference grain are used as the input. The initial displacement vector is calculated as: D = (X2, Y2) – (X1, Y1), where (X1, Y1) and (X2, Y2) are the centroid positions of the same reference grains on EBSD2 and EBSD1, respectively. It is one of the grain features and can be referred by grain ID. The next step is to assign the initial displacement vector D0 to the 1st (N0 = 1) order neighbouring grains on the reference EBSD. Since the 1st order neighbours are adjacent to the reference grain on EBSD1, it is reasonable to assume that they,

if are maintained on EBSD2, should have comparable displacement vectors to the initial D0 of the reference. That is, the roughly estimated positions of 1st order neighbours on EBSD2 can be calculated with their positions on EBSD1 and D0. After that, a searching area of 50 × 50 μm2 is defined with its centre locating in the correlation position of every 1st order neighbours on EBSD2. Then the misorientation between 1st order neighbours (EBSD1) and corresponding grains within the searching area (EBSD2) are calculated.

There are three situations of this grain correlation depending on the number of grains on EBSD2 that match the pre-defined misorientation anlge tolerance of 5º. First, no grains on EBSD2 have misorientation angles below 5º to the corresponding 1st order neighbour on EBSD1. Assuming that the annealing time for EBSD2 is longer than EBSD1, so the neighbouring grains which only appear on earlier annealing condition but disappear on the next one are consumed during the annealing process. On the contrary, the grains are only observed on EBSD2 are newly formed grains. The second situation is one to one match that there is only one grain in the searching area of EBSD2 show similar orientation to the 1st order neighbour on EBSD1. In this case, the neighbouring grain is correlated on two EBSD. The displacement vector of the 1st order neighbour is calibrated which is furtherly assigned to its neighbour, the 2nd order neighbour of reference grain. Movie. S1 shows the iteration of renewing and re-assigning of displacement vector in all grains, and Track-Rex check if the grains are retained in both EBSD. The above two situations correctly index the neighbour grain on EBSD1 as consumed or correlated grain during annealing, but there can be a case that two or more grains matching grains are found on EBSD2, leading to the ambiguous correlation between two EBSD. To determine the most likely correlated grain, a voting strategy is introduced after the iteration of all grains on EBSD1. This voting is very similar to the triplet indexing of kikuchi bands in

EBSD software. To begin with, every possible correlated grain together with its neighbours are marked out. Then, the number of correctly indexed (1 to 1 matching) grains is calculated, with each good index getting a vote. The grain with most votes among all candidates is selected as the most probable correlated grain. To minimize the influence of reference selection on the accuracy of grain correlation, different reference grains are picked from 4 corners and centre of two EBSD scans. There is a matching list for each reference grain, and all the matching list are summarised as the final output of grain correlation.

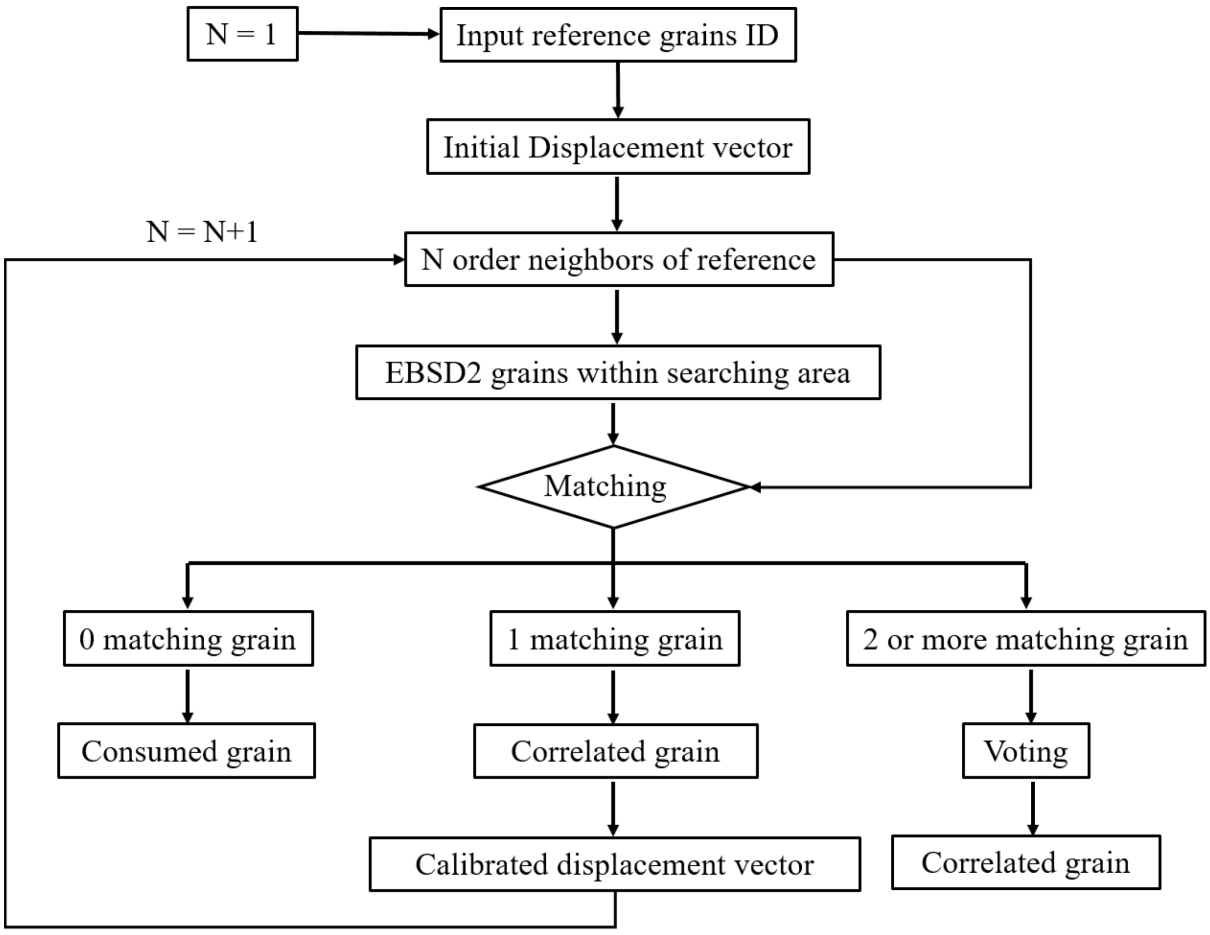

Figure 3.12 Track-Rex Algorithm.

Track-Rex is implemented in MATLAB and designed to run with MTEX-processed EBSD data. The practical workflow is:

Check: quick visual inspection and parameter estimation (reference grain IDs, misorientation threshold, search range) using representative map pairs.

Match: automatic pairwise correlation between two consecutive EBSD maps, producing a mapping table from EBSD1 grain IDs to EBSD2 grain IDs, along with summary plots (e.g., pole figures, size distributions).

Track: aggregation of all pairwise mappings to produce full time-series tracking results across the dataset.

The toolbox outputs (i) full grain-history tables suitable for statistical analysis (e.g., nucleation sequence fractions, survival probability), and (ii) optional "specific tracking" outputs that extract trajectories for a user-defined subset of grains/regions. The codebase and demonstration datasets are maintained in the public Track-Rex repository (see Section 3.5.3 notes at the end of this response for the exact repository pointers and settings).

3.5.6 Toolbox operation in Python

For LabDCT datasets, the tracking problem is extended from 2D maps to 3D volumes, introducing additional challenges such as partial grain visibility near volume boundaries and grain fragmentation/merging artefacts arising from reconstruction uncertainties.

In this thesis, 3D/4D tracking is performed using a Python workflow that takes, for each annealing step, a grain list containing at minimum: grain ID, centroid (x, y, z), mean orientation, and volume. The tracking follows the same fundamental logic as the 2D Track-Rex approach:

Initial seed pairing: a small set of high-confidence grain correspondences between consecutive steps is established (either manually verified or automatically selected based on combined centroid proximity and low misorientation).

Local displacement estimation: the seed pair defines an initial displacement estimate, which is used to predict candidate locations for neighbouring grains at the next step.

Candidate evaluation: for each grain, a candidate set is built within a spatial search radius; candidates are ranked using a composite score that favours small centroid separation, low misorientation, and consistent grain size/shape descriptors where available.

Neighbour propagation and conflict resolution: matched grains become local references to propagate matching through the 3D neighbourhood; conflicts are resolved by consensus rules to enforce a one-to-one mapping where appropriate.

Time-series linking consecutive-step mappings are chained to generate full 4D grain trajectories, enabling extraction of individual growth curves and population-level kinetics.

This Python pipeline produces grain-resolved growth histories in 3D, which can be directly compared with 2D EBSD-derived trends while also revealing through-volume effects that are inaccessible to surface EBSD.

3.5.7 Author contribution statement

The research presented in this thesis was carried out within a collaborative research environment. The author's individual contributions are therefore clarified here to distinguish experimental data generation, algorithm development, code implementation, data processing and scientific interpretation.

The experimental datasets analysed in Chapters 4 and 5 were collected by collaborators. The author was responsible for subsequent data processing, grain tracking, statistical analysis and interpretation of these datasets. The work presented in Chapter 6 was designed and experimentally conducted by the author. This included the design of the interrupted annealing schedule, the development of the LabDCT-based characterisation workflow, and the collection of the four-dimensional grain growth dataset.

The conceptual design of the grain-tracking methodology was developed jointly by the author and a postdoctoral researcher within the research group. Following this conceptual design, the complete code implementation was carried out by the author. This includes the construction of the Track-Rex code for quasi-in-situ EBSD datasets and the Track-4DGG code for four-dimensional LabDCT datasets.

The author also carried out all subsequent applications of the tracking algorithms. This included applying the codes to the experimental datasets, tracking individual grains across successive annealing steps, extracting grain-level descriptors, classifying grain behaviour, generating statistical outputs, producing the associated figures and interpreting the results. These analyses form the basis of the recrystallisation, texture evolution and grain growth studies presented in Chapters 4–6.

Accordingly, the main methodological contribution of the author lies in the implementation, coding, application and interpretation of the grain-tracking workflows developed in this thesis. These workflows convert large time-resolved microstructural datasets into structured grain histories and provide the data-driven basis for the analyses presented in the following results chapters.

Chapter 4 Statistical grains tracking throughout recrystallisation

4.1 Introduction

This chapter is the first results chapter of the thesis and establishes the grain-resolved framework used to analyse recrystallisation in two-dimensional time-resolved EBSD datasets. Building upon the methodology introduced in Chapter 3, Track-Rex is applied to quasi-in-situ EBSD datasets of AZ31 and ZE20 to follow individual recrystallised grains from their first appearance to later stages of growth, shrinkage or consumption. The purpose of this chapter is therefore not only to describe recrystallisation in two magnesium alloys, but also to demonstrate how automated grain tracking converts a sequence of EBSD maps into a structured dataset of grain histories.

The chapter addresses the first major research question of the thesis: how do recrystallised grains nucleate, survive, grow or disappear during annealing, and how do these behaviours differ between a conventional RE-free Mg alloy and a lean-RE Mg alloy? By comparing AZ31 and ZE20, this chapter provides a broad statistical basis for interpreting recrystallisation as a dynamic process rather than a simple sequence of nucleation followed by uniform growth. The findings also provide the foundation for Chapter 5, where the analysis is narrowed to one specific nucleation feature, namely shear bands, and for Chapter 6, where the tracking concept is extended from two-dimensional EBSD maps to three-dimensional LabDCT volumes.

Mg alloys, with their high specific strength, emerge as promising candidates to fulfil the increasing demands of lightweight materials in the automobile industry. However, the inherent anisotropy of the hexagonal close-packed (HCP) structure results in a strong basal-type texture in Mg products, rendering them susceptible to cracking during deformation. The addition of rare earth elements (RE) to Mg is an effective way to weaken the basal texture and enhance the ductility of Mg products. The weakening of the deformation texture by RE is related to its alterations in precipitation strengthening [137–139] and stacking fault energy [140,141], which have been extensively discussed in the literature. Additionally, RE influences the recrystallisation texture evolution of Mg alloys by promoting oriented nucleation and preferential grain growth. Compared to RXed grains formed at traditional grain boundary, those originated from large particles [142–144], shear bands [145–147], and twin boundaries [148–150] show more randomized orientations. Nevertheless, these theories are challenged by their contributions to the recrystallisation [148,151–153]. Preferential grain growth theory [154] has been proposed that the grain boundary mobility can be altered by RE segregation, leading to different texture developments during recrystallisation [153,155–157]. Quasi in situ experiments provide valuable insights about the roles of double twin [150,158], compression twins [159] and shear bands [160,161] in shaping the RE texture. It is found that double twins play a key role in the formation of RE texture, while compression twins and shear bands cannot significantly influence the final texture due to restricted growth. Additionally, grain boundary segregation [162,163] and mobility [164] are reported to impact grain growth, resulting in a random texture.

Numerous theories abound regarding the impacts of RE on the texture evolution of Mg alloys during recrystallisation, yet a consensus remains elusive. The understanding of

recrystallisation behaviours in Mg alloys holds significance due to their pivotal role in altering the microstructure and texture, subsequently influencing material properties [165]. To unveil valuable insights into the recrystallisation process, in-situ EBSD technique has been developed, boasting high acquisition speed (up to 4,500 Hz) and real-time observation capabilities [166–168]. Nevertheless, this technique usually generates large datasets, posing significant challenges to data evaluation: (1) Prior studies often focus on localized regions with specific features like twins [169,170] and shear bands [168,171]. Yet, interpretation of the macro-recrystallisation behaviours from these small regions with a very limited number of recrystallized (RXed) grains is problematic. (2) Recrystallisation nucleation and grain growth are believed to dominate different recrystallisation stages [165]. Nonetheless, recrystallisation is a dynamic process that involves continuous nucleation and grain growth. Additionally, it is not clear whether the nucleation and grain growth behaviours vary as recrystallisation progresses. (3) The lack of an efficient tracking method restricts our understanding of individual grain behaviour during recrystallisation, including their nucleation timing and whether they shrink or grow. Besides, it remains elusive about which RXed grains dominate the microstructure and texture at specific stages of recrystallisation, and whether this dominance persists throughout the full recrystallisation.

To overcome these challenges, we have developed Track-Rex, a new and powerful toolbox built upon the open-source EBSD analysis toolbox MTEX [172]. Track-Rex enables effective grain-scale analysis to simultaneously track thousands of grains, from their nucleation to the fully recrystallized state. One of our key findings is that the main component of the fully recrystallized microstructure is the RXed grains formed in the middle recrystallisation stages, while the majority of those formed in the early stages are consumed. Oriented nucleation and

preferential grain growth are observed in two Mg alloys, responsible for the recrystallisation texture. Track-Rex shows its exceptional capacity for unveiling insights into recrystallisation compared to conventional approaches. More importantly, it can be easily customized and applied to various polycrystalline materials, significantly reducing the data processing time from several months to some hours with high confidence and statistical results.

Accordingly, the following sections first present the overall microstructure and texture evolution of the AZ31 and ZE20 datasets. The tracking results are then used to separate recrystallised grains according to their nucleation step and subsequent behaviour. This structure is intended to move beyond conventional map-by-map interpretation and to show how the temporal history of each grain contributes to the final recrystallised microstructure and texture.

4.2 Results

4.2.1 Microstructure and texture evolution

The microstructure and texture of the AZ31 and ZE20 samples under different annealing conditions are shown in Figure 4.1 and Figure 4.2 . It is to note that these reduced EBSD datasets can represent the general recrystallisation behaviours of two samples, as the raw data in Figure 4.1 exhibits comparable trends of microstructure and texture evolution. Severe shear banding is observed in the as-rolled ZE/1 condition, Figure 4.2 (a). Due to the low indexing rate of shear bands (black regions), the corresponding texture shows two strong peaks tilted from ND to RD. It should be mentioned that the same specimen reference with RD and TD aligned parallel to X and Y axis, respectively, is used for all EBSD maps afterwards. After one pass annealing, a large number of RXed grains are formed in the ZE20 sample, accompanied

by a reduction in texture intensity from 24.4 to 8.4 MRD (multiple of random distribution), as shown in Figure 4.2 (b). As the annealing time increases, the RXed grains start to grow out of the previous shear bands, Figure 4.2 (d). An almost fully recrystallized microstructure is obtained at ZE/6, while the RD split deformation texture is fully changed to the off-basal texture (Figure 4.2 (f)). This texture is slightly reinforced afterwards.

The as-rolled AZ31 sample exhibits a bimodal microstructure, comprising both coarse and fine deformed grains, Figure 4.2 (i). In the early stages of annealing, the recrystallisation in the AZ31 sample is delayed as most of the basal oriented grains coloured in red are maintained, Figure 4.2 (j and k). However, a rapid recrystallisation process occurs from AZ/3 to AZ/4, coinciding with a reduction in texture intensity from 22.4 to 16.6 MRD. There are no significant changes with the coarse deformed grains until they start to be consumed by some RXed grains at AZ/6, leading to a noticeable basal spread texture component since the overshadowing effect of coarse grains is decreased, Figure 4.2 (n). Compared to the ZE20 sample in which the deformation texture is fully changed, the basal texture can only be weakened in the AZ31 sample.

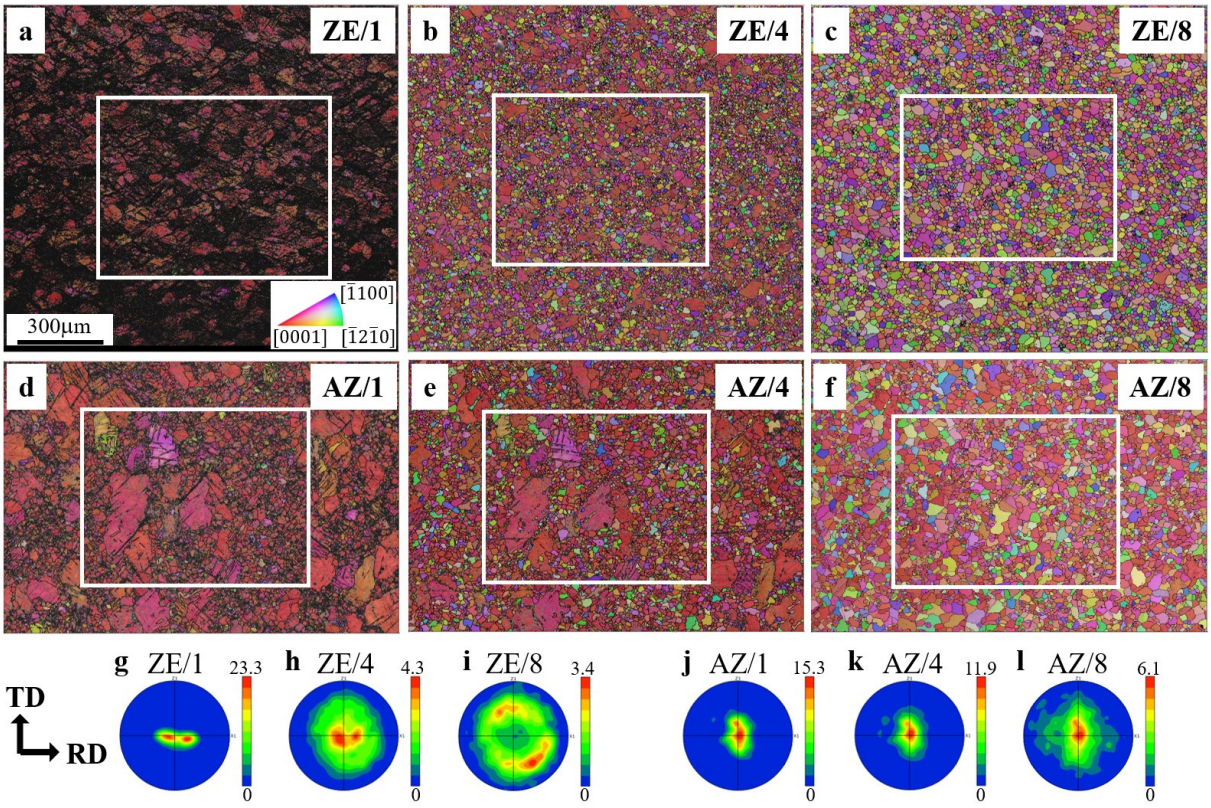

Figure 4.1 Raw EBSD maps of the ZE20 and AZ31 samples. The ZE20 sample of (a) as-rolled, and annealed at 400 °C for (b) 16 min, (c) 80 min. The AZ31 sample of (d) as-rolled, and annealed at 320 °C for (j) 8.5 min (d) 34 min. The corresponding pole figures of all grains in the ZE20 and AZ31 samples are shown in (g-i) and (j-l), respectively.

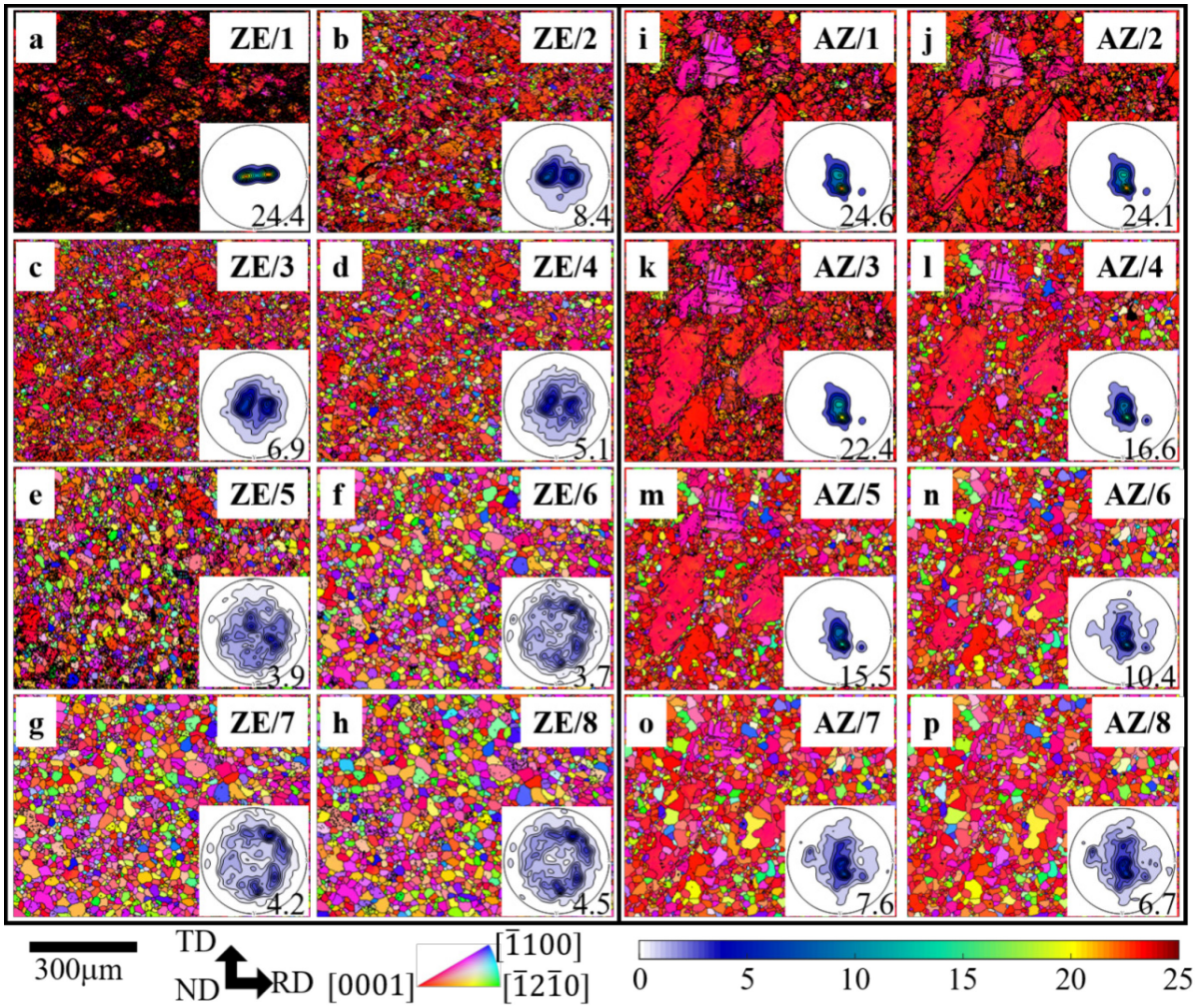

Figure 4.2 EBSD orientation and basal pole maps of: (a-h) the ZE20 sample under different annealing conditions, (i-p) the AZ31 sample under different annealing conditions. The numbers on the pole figures indicate the texture intensities.

4.2.2 Statistical results from grains tracking

Track-Rex enables systematic investigation of recrystallisation kinetics, specifically regarding the area fraction evolution of RXed grains over multiple annealing steps. Figure 4.3 shows the RXed grains extracted by Track-Rex in the ZE20 and AZ31 samples. Advanced nucleation activity is observed within shear bands at ZE/2 step (Figure 4.3 (a)), in agreement

with the microstructure evolution in Figure 4.2 (a and b). However, the majority of these RXed grains do not grow, but are replaced by new RXed grains at ZE/3 in shear bands, Figure 4.3 (b). This phenomenon highlights the exceptional capability of the toolbox to reveal recrystallisation behaviours that were previously unrecognized. Table 4.1 and 4.2 exhibit the statistical data of the RXed grains for the ZE20 and AZ31 samples, respectively. Each table row indicates the development of grain number and area fraction of the RXed grains from a specific annealing step, while each column shows the contributions of RXed grains from different steps to the overall recrystallisation. There are 4077 RXed grains with a recrystallisation area fraction (Fx) of 36.4% at ZE/2 step (Table 4.1). However, only 1580 of them are maintained at ZE/3 while another 2183 new RXed grains are formed. After that, the RXed grains from ZE/2 and ZE/3 grow at the expense of the large deformed grains, and the nucleation sites of new RXed grains become more randomized since the shear bands are consumed (Figure 4.3 (c)). With the continuous nucleation and grain growth process, an almost full recrystallisation microstructure (Fx = 92.1%) is observed at ZE/6 (Figure 4.3 (e)).

After the initial two annealing steps of the AZ31 sample, the recrystallisation stays negligible, with a few RXed grains occupying a limited area fraction of the microstructure, as shown in Figure 4.3 (f and g) and Table 4.2. However, 1455 newly formed RXed grains suddenly appear at AZ/4 step (Figure 4.3 (h)), constituting an area fraction of 37.1%. These RXed grains from AZ/4 step grow fast and become the main component (Fx = 52.5%) of the fully recrystallisation microstructure at AZ/7 step (Figure 4.3 (k)). A notable trend is observed that the area fraction of newly formed RXed grains firstly increases and then decrease in both samples, though their amounts continuously decrease (Table 4.1 and 4.2).

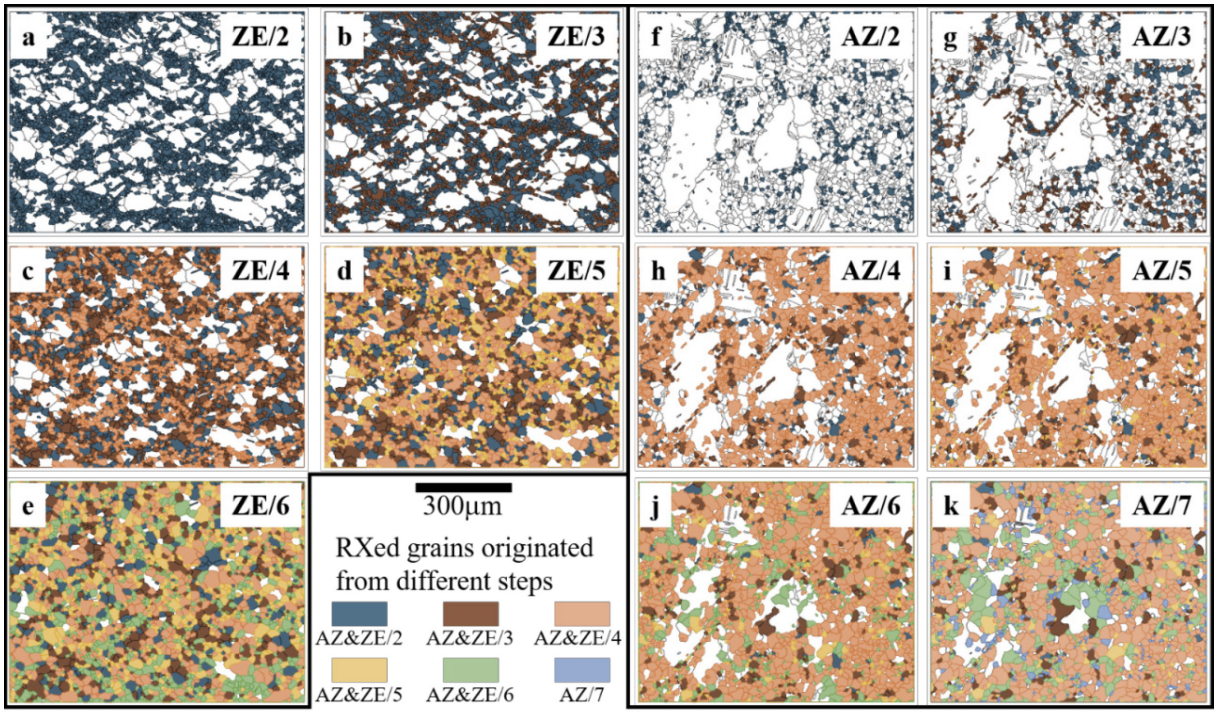

Figure 4.3 Contributions of the RXed grains originated from different annealing steps to the microstructure evolution. (a-e) RXed grains in the ZE20 sample at different annealing step. (f-k) RXed grains in the AZ31 sample at different annealing step. The deformed grains are in blank while the RXed grains are coloured based on their nucleation steps. Tracked grains refer to grains for which a reliable correlation was identified between successive EBSD maps using the Track-Rex criteria. Grains without a reliable candidate in the following step were classified as consumed.

Table 4.1 Number and area fraction of recrystallized grains in the ZE20 sample.

Annealing condition		**ZE/2**	**ZE/3**	**ZE/4**	**ZE/5**	**ZE/6**
Total grain number		4984	4228	4024	3081	2556
Number and area fraction of RXed grains originated from:	ZE/2	4077, 36.4%	1580, 23.6%	830, 19.9%	449, 16.4%	247, 12.9%
	ZE/3		2183, 20.9%	1186, 25.5%	669, 22.2%	359, 17.1%
	ZE/4			1715, 20.2%	1010, 28.9 %	619, 28.2%
	ZE/5				789, 11.8 %	523, 18.6%
	ZE/6					745, 15.3%
Total recrystallisation fraction		36.4%	44.5%	65.6%	79.3%	92.1%

Table 4.2 Number and area fraction of recrystallized grains in the AZ31 sample.

Annealing condition		**AZ/2**	**AZ/3**	**AZ/4**	**AZ/5**	**AZ/6**	**AZ/7**
Total grain number		2931	2549	2643	2631	2265	2234
Number and area fraction of the RXed grains originated from	AZ/2	923, 9.1%	523, 11.8%	193, 5.0%	154, 4.0%	48, 1.9%	29, 1.6%
	AZ/3		701, 8.2%	354, 9.3%	311, 9.1%	205, 8.7%	145, 8.3%
	AZ/4			1455, 37.1%	1358, 40.5%	1095, 53.1%	903, 52.5%
	AZ/5				254, 1.9%	172, 4.3%	132, 4.5%
	AZ/6					486, 10.1%	415, 17.5%
	AZ/7						409, 5.8%
Total recrystallisation fraction		9.1%	20.0%	51.4%	55.5%	78.1%	90.2%

4.2.3 Recrystallisation at different annealing steps

Track-Rex enables an in-depth analysis of the nucleation and grain growth processes and their effects on microstructure and texture evolution in different recrystallisation stages. The ZE20 sample initially exhibits a more advanced recrystallisation than the AZ31 sample. Considering that the recrystallisation area fractions of both samples are relatively low (< 40%) after the first annealing and do not increase much after the second one (Table 4.1 and 4.2), we can assume ZE/2~ZE/3 and AZ/2~AZ/3 as the early recrystallisation stages. The microstructure and texture maps of the RXed grains originated from ZE/2 and AZ/2 steps is shown in Figure 4.4. The RXed grains at ZE/2 within shear bands exhibit a weak off-basal texture with c-axis tilting 40 – 60º from the ND, Figure 4.4 (a). This texture differs significantly from the RD split deformation texture, responsible to the reduction of texture intensity in Figure 4.2 (a and b). About 60% (Table 4.1) of these RXed grains disappear at ZE/3 step, namely consumed grains (Figure 4.4 (b)), while others are maintained during the annealing, Figure 4.4 (c and d). Both the maintained and consumed RXed grains exhibit off-basal textures despite of a slightly higher texture intensity in the maintained ones.

However, it is unclear whether the weakened texture in ZE20 sample is solely dependent on the preferential nucleation of off-basal RXed grains and their survival, or if the grain growth advantage also plays a role in the texture evolution. To address this question, an indicator of growth rate g is introduced which is detailed in the Methodology section. Table 4.3 and 4.4 provide the average grain size of RXed grains at different steps, including the separate average grain size of the consumed and maintained RXed grains. For instance, the average grain size of maintained RXed grains in the former EBSD scan evolves into the average size of all RXed grains in the later EBSD. In the ZE20 sample (Table 4.3), the average grain size of 1580

maintained RXed grains originated from ZE/2 slightly increases from 11.7 μm at ZE/2 (Figure 4.4 (c)) to 14.3 μm at ZE/3 (Figure 4.4 (d)). The growing RXed grains (g > 0.2) with a number fraction of 50.0% show a more obvious off-basal texture with tilted c-axis forming the off-basal ring component (Figure 4.4 (h)), compared to the stable (Figure 4.4 (g)) and shrinking grains (Figure 4.4 (f)). This observation confirms the off-basal growth preference in the ZE20 sample.

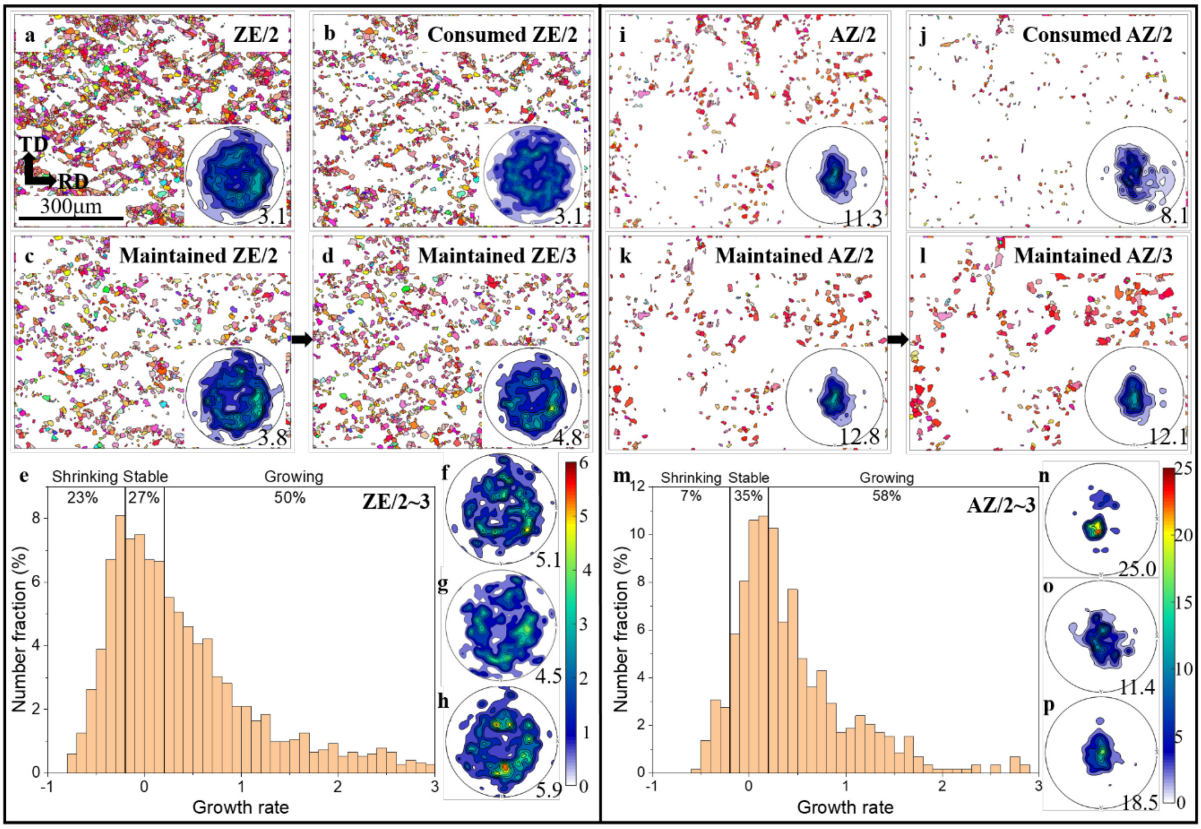

Figure 4.4 Recrystallisation behaviours of the RXed grains in early recrystallisation stage. (a-c) All, consumed and maintained RXed grains from ZE/2 step. (d) Maintained RXed grains at ZE/3. (e) Growth rate distribution of the maintained grains. (f-h) Shrinking, stable, and growing RXed grains from ZE/2. (i-k) All, consumed and maintained RXed grains from

AZ/2 step. (l) Maintained RXed grains at AZ/3. (m) Growth rate distribution of the maintained grains. (n-p) Shrinking, stable, and growing RXed grains from AZ/2.

Table 4.3 Average grain size of the recrystallized grains in the ZE20 sample.

Annealing condition		**ZE/2**	**ZE/3**	**ZE/4**	**ZE/5**	**ZE/6**
Average grain size of RXed grains from different step: All RXed grains (maintained grains, consumed grains) (μm)	ZE/2	10.5 (11.7, 9.7)	14.3 (16.4, 11.5)	16.1 (19.7, 11.7)	19.5 (24.6, 14.0)	21.8
	ZE/3		11.9 (13.1, 10.0)	15.4 (19.0, 11.2)	19.2 (23.4, 14.4)	21.1
	ZE/4			11.9 (13.2, 9.3)	17.9 (20.7, 12.8)	20.5
	ZE/5				13.3 (14.6, 10.8)	18.2
	ZE/6					14.3

Table 4.4 Average grain size of the recrystallized grains in the AZ31 sample.

Annealing condition		AZ/2	AZ/3	AZ/4	AZ/5	AZ/6	AZ/7
Average grain size of RXed grains from different step: All Rxed grains (maintained grains, consumed grains) (μm)	AZ/2	11.2 (12.5, 9.3)	16.4 (20.9, 14.6)	16.5 (18.1, 11.6)	16.6 (21.0, 14.5)	20.0 (23.7, 13.2)	23.9
	AZ/3		12.2 (12.4, 11.8)	16.7 (18.0, 10.4)	17.7 (21.2, 11.9)	20.4 (24.0, 11.5)	21.1
	AZ/4			16.5 (17.1, 9.1)	17.9 (19.8, 10.3)	21.7 (24.4, 10.9)	23.9
	AZ/5				9.6 (10.0, 8.7)	15.3 (16.9, 9.1)	17.3
	AZ/6					14.2 (14.9, 9.6)	18.9
	AZ/7						11.00

In contrast, fewer RXed grains are observed at AZ/2 than those at ZE/2 step. The AZ31 sample has 523 maintained RXed grains (Figure 4.4 (k)), showing more concentrated basal peaks compared to the consumed ones (Figure 4.4 (j)). In the meantime, a significant grain growth from 12.5 to 16.4 μm (Table 4.4) is found in the maintained RXed grains, Figure 4.4 (k and l). Compared to the ZE20 sample, the AZ31 sample exhibits a higher number fraction of growing grains. Only 38 maintained grains with a number fraction of 7.3% shrink, leading to a strong basal peak (Figure 4.4 (n)). Despite the differences in texture intensities, all maintained RXed grains in the AZ31 sample generally show similar basal orientations, indicating a uniform grain growth process.

With increasing annealing time, new RXed grains are formed as well as the early formed ones grow. The recrystallisation fractions reach about 60% at ZE/4 and AZ/4 steps, Figure 4.3 (c) and (h), indicating the middle recrystallisation stages of ZE/3~ZE/4 and AZ/3~AZ/4. The growth rate distributions of the maintained RXed grains from different steps are separately shown in Figure 4.5 (a). For brevity, kernel smoothing is applied to the growth rate distributions. Notably, the growth rate peaks of the early formed RXed grains originated from AZ/2 and ZE/2 (black curves) shift to the shrinking zone compared to those from AZ/3 and ZE/3 (red curves). This shift is also supported by the decreasing average grain size of early formed RXed grains in both samples (Table 4.3 and 4.4). For example, the maintained RXed grains originated from ZE/2 decrease in size from 16.4 μm at ZE/3 step to 16.1 μm at ZE/4 step. Additionally, the RXed grains in the AZ31 sample are more likely to grow, indicated by the larger grain size in Table 4.3 and 4.4, while those in the ZE20 undergo vibrant shrinking processes. Apart from the growth rate distribution, the textures of each growing, stable and shrinking group are investigated. Similar to the subgroup textures in Figure 4.4, the growing RXed grains in the

ZE20 sample originated from both ZE/2 (Figure 4.5 (d)) and ZE/3 (Figure 4.5 (g)) steps also show more pronounced off-basal textures compared to the stable or shrinking grains. On the contrary, the RXed grains in the AZ31 sample always show basal textures, although the texture intensities are much higher owing to the small amount of RXed grains.

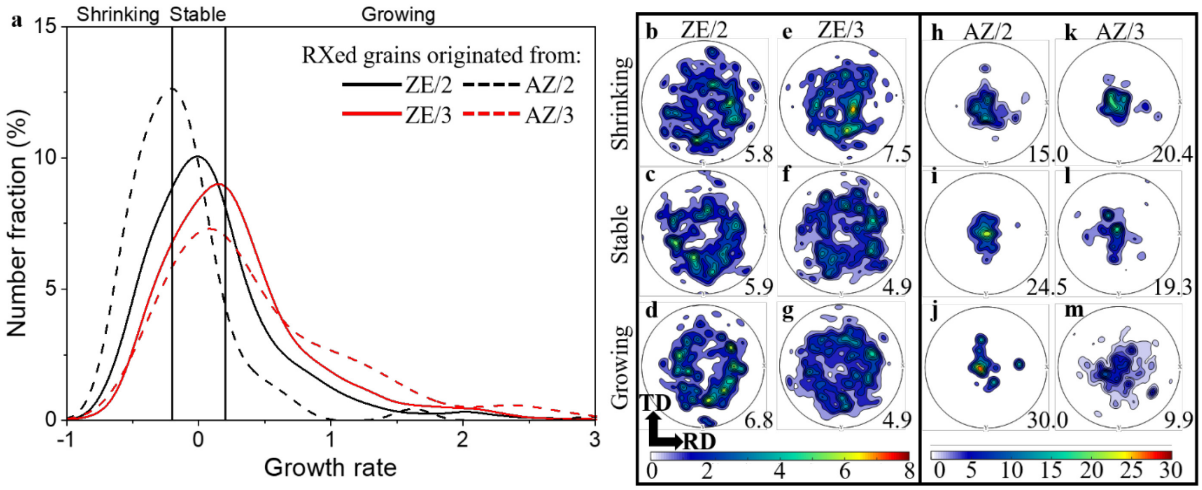

Figure 4.5 Grain growth behaviours of the maintained RXed grains in middle recrystallisation stage. (a) Growth rate distributions of the RXed grain originated from different annealing steps. (b-g) Basal pole maps of the shrinking, stable, and growing RXed grain from ZE/2 and ZE/3 steps. (h-m) Basal pole maps of the shrinking, stable, and growing RXed grain from AZ/2 and AZ/3 steps.

The off-basal nucleation and growth of the RXed grains in the ZE20 are consistent through all recrystallisation stages. Even though the new RXed grains in the late recrystallisation stages come from different nucleation sites than the previous ones, for example, shear bands (ZE/2~3) and random positions (ZE/5~6), they share similar trends of off-basal nucleation (Figure 4.6) and growth (Figure 4.7). It should be mentioned that Figure 4.7 only includes the growth rate distributions and textures of RXed grains from the middle and later

recrystallisation stages, which constitute the main components of the recrystallized microstructure. This nucleation and growth preference in the ZE20 sample are also confirmed in Movie S2 that all RXed grains exhibit scattered off-basal orientations upon nucleation, which are further strengthened during subsequent annealing. In the AZ31 sample, basal textures are observed in the RXed grains despite of their origins from small grain region (AZ/2~5) or coarse deformed grains (AZ/6~8). Besides, there is no obvious growth advantage in the AZ31 sample as the growing, stable, and shrinking RXed grains are basal oriented (Figure 4.7).

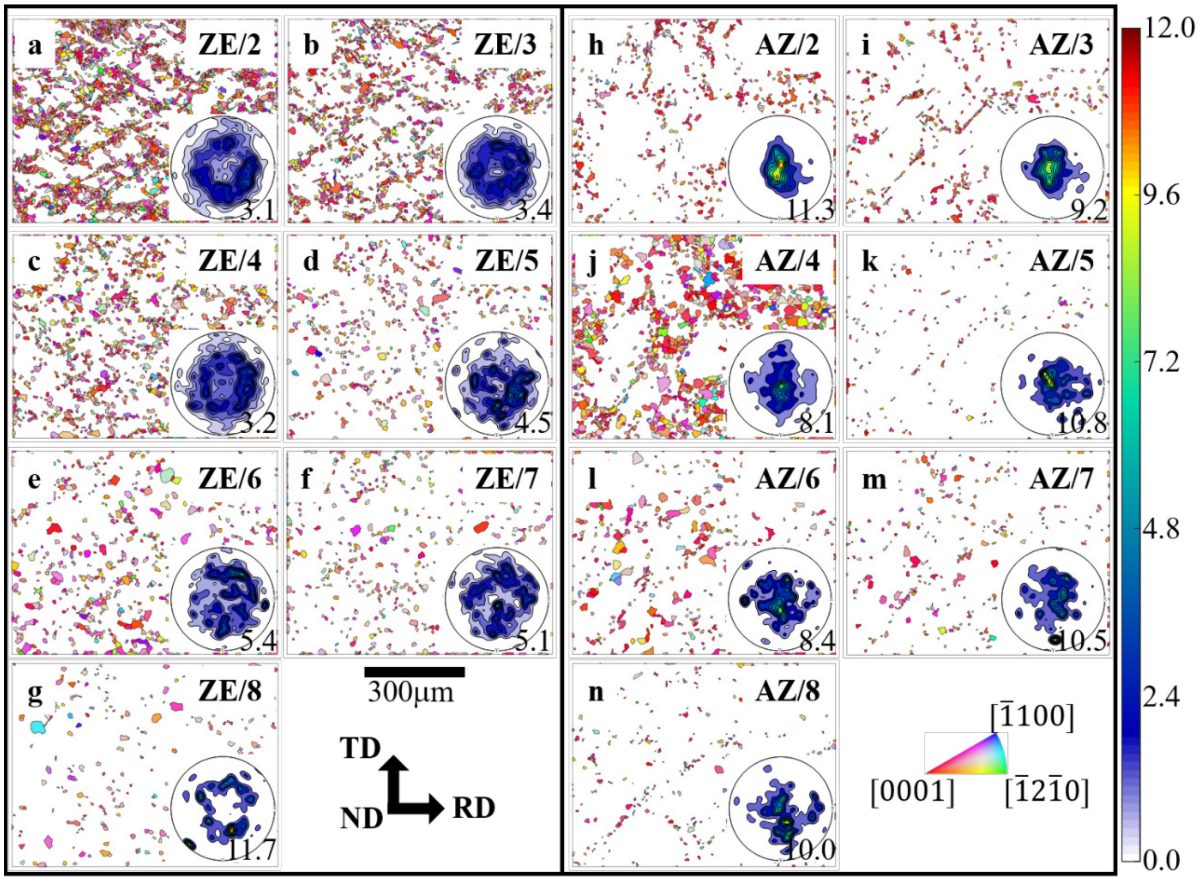

Figure 4.6 EBSD grain and orientation maps of newly formed recrystallized grains at different annealing steps. (a-g) ZE20 sample, (h-n) AZ31 sample.

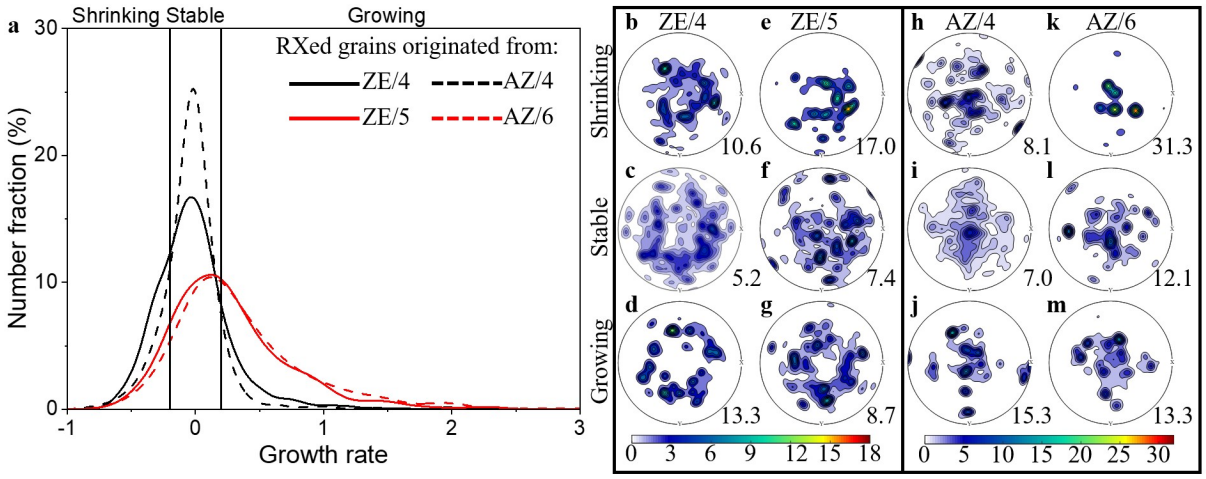

Figure 4.7 Grain growth behaviours of the maintained RXed grains in late recrystallisation stage. (a) Growth rate distributions of the RXed grain originated from different annealing steps. (b-g) Basal pole maps of the shrinking, stable, and growing RXed grain from ZE/4 and ZE/5 steps. (h-m) Basal pole maps of the shrinking, stable, and growing RXed grain from AZ/4 and AZ/6 steps. Growth rate is defined by equation (3.1).

4.3 Discussion

4.3.1 Recrystallisation kinetics

According to classic recrystallisation theory, the early recrystallisation stage is dominated by nucleation, while grain growth plays a more important role afterwards. However, our results show the continuous nucleation and grain growth of the RXed grains throughout all recrystallisation stages. For instance, obvious grain growth already occurs in the early recrystallisation stage (Figure 4.4), and considerable numbers of new RXed grains (Table 4.1 and 4.2) are also formed in the late recrystallisation stage. Nevertheless, the possibility cannot be excluded that the new grains appearing in the late annealing steps might be the existing

grains growing from beneath the sampling area. To clarify the origin of these new grains at the late stage of recrystallisation process, the combination of in-situ 3D characterisation [173,174] and effective tracking method like Track-Rex will be required, which will be published in our future work. Another finding is that the RXed grains do not consistently grow after their nucleation; in fact, some early RXed grains can shrink or even be consumed (Figure 4.3 and Figure 4.4), thus making a limited contribution to the recrystallisation (Table 4.1 and 4.2). This phenomenon also explains the findings that the fully recrystallized microstructure is mainly derived from the RXed grains formed in the middle recrystallisation stage.

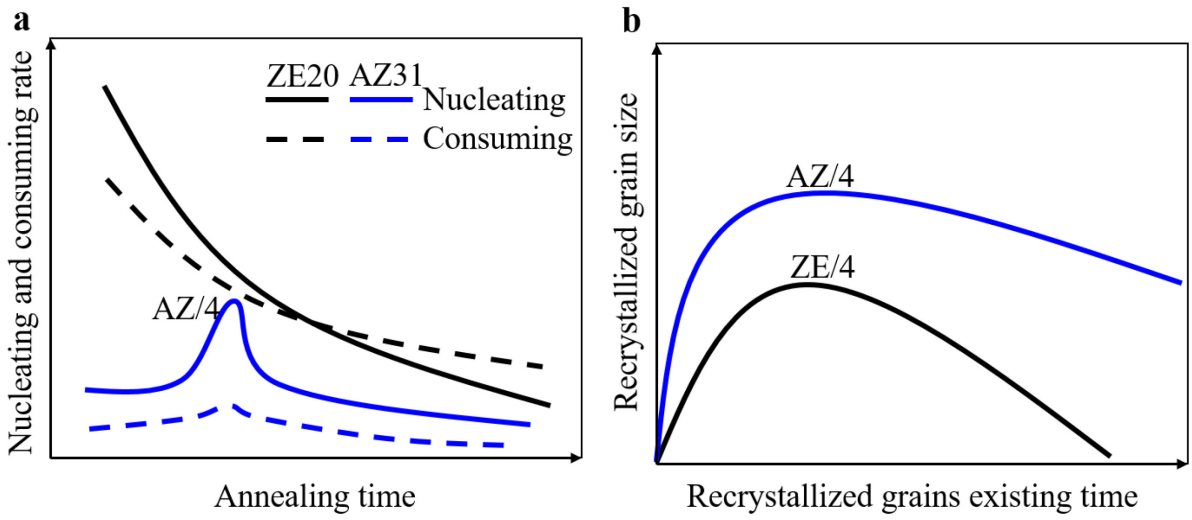

Figure 4.8 Schematic of recrystallisation behaviours in the ZE20 and AZ31 sample. (a) Nucleating and consuming activities during annealing. (b) Grain size evaluation of the RXed grains from nucleation to the final annealing step.

The recrystallisation kinetics of the ZE20 and AZ31 samples can be schematically summarised in Figure 4.8. The ZE20 sample shows a high nucleating activity (Figure 4.8 (a)), which generally decreases with the annealing time as the driving force and preferred sites like

shear bands for nucleation are being consumed. However, the nucleating rate decreases faster than the consuming rate. For example, there are 2497 RXed grains consumed from ZE/2 to ZE3 while 2183 grains are newly formed (Table 4.1), leading to a reduced total grain count from 4984 (ZE/2) to 2556 (ZE/6). In the AZ31 sample, the nucleating and consuming activities of RXed grains initially occur at low rates, followed by a sudden increase of nucleation at AZ/4 step. Figure 4.8 (b) exhibits the relationship between grain size of the RXed grains and their existing time since nucleation. On the x-axis, grains with short existing time indicate they are newly formed in the late recrystallisation stages, whereas those with long existing time are old RXed grains originated from the early recrystallisation stages. In both samples, the RXed grains experience an initial growth phase, reach a peak grain size, and then undergo shrinking. As annealing proceeds, some new RXed grains can be formed that hold a growth advantage over the old RXed grains. In this case, the newly formed grains grow at the expense of the old ones, leading to a decreased average grain size of the maintained RXed grains from early recrystallisation stages (Table 4.3 and 4.4). The RXed grains originated from the middle recrystallisation stages, such as AZ/4 and ZE/4, reach their peak grain size in the fully recrystallized condition because of their existing time and fewer competitors (new RXed grains formed in the late recrystallisation stage). The combination of rapid nucleation and peak grain size of the RXed grains originated from AZ/4 step results in their predominance in the fully recrystallized microstructure at AZ/7 step. The RXed grains in the ZE20 sample grow slower and shrink faster compared to those in the AZ31 sample, which is confirmed by the smaller average grain size and lower fraction of the growing grains (Table 4.3 and 4.4). Consequently, the RXed grains from different annealing steps of the ZE20 sample play more comparable roles in the fully recrystallized microstructure than the AZ31 sample (Table 4.1 and 4.2).

4.3.2 Texture evolution

Oriented nucleation and grain growth preference are believed to play key roles in the formation of RE texture. During annealing, the ongoing oriented nucleation and grain growth of the off-basal RXed grains in ZE20 sample lead to the transition from RD split texture to RE texture. In contrast, all the RXed grains in the AZ31 sample show basal textures without obvious grain growth preference. Consequently, the basal texture in the AZ31 sample can only be weakened, rather than fully altered.

To understand the underlying mechanisms of the different texture evolutions between two samples, it is important to investigate the roles of deformation stored energy and grain boundary configuration in recrystallisation [165]. Firstly, deformation stored energy acts as the driving force for recrystallisation, providing the necessary energy to overcome the barriers to nucleation and growth of new grains. Comparing with the AZ31 sample, the as-rolled ZE20 sample shows a higher area fraction of shear bands (Figure 4.2 (a)), indicating higher deformation stored energy as shear bands denote severely deformed regions with a notable concentration of dislocations [175,176]. This aligns with the advanced nucleation in the early recrystallisation stages of the ZE20 sample (Figure 4.3 (a)). However, it is challenging to explain the phenomenon that most of the RXed grains (defect-free with no deformation stored energy) formed at ZE/2 step are replaced by new RXed grains at ZE/3, considering the energy consumption during the nucleation process at ZE/2. Divergent nucleation and growth behaviours in the two alloys may be attributed to their unique kinetic parameters, including nucleation energy and growth energy [177]. Furthermore, the elevated thermodynamic stability of the secondary phase [178,179] in the ZE20 sample acts as an impediment to the rapid growth of recrystallized grains, resulting in a finer grain size and a subdued texture.

The effects of boundary configuration, including grain boundary curvature, misorientation, and boundary pinning, on grain growth should be taken into account. Since the RXed grains in both samples are equiaxed with comparable initial grain size, it is difficult to relate the preferential grain growth of the off-basal grains in the ZE20 sample to boundary curvature. The pinning effects of boundary precipitation have been reported to hinder the rapid growth of basal RXed grains from prior grain boundaries [180], leading to an increased contribution of the RXed grains from twins and shear bands with random orientations. This phenomenon is responsible for the observed texture weakening in previous studies [146,158,162,181]. In our study, the ZE20 sample produces stable Zn-RE rich precipitates at grain or twin boundaries and shear bands, aiming to reduce the lattice misfits caused by alloying elements, as reported by many researchers [147,182]. Different from previous studies that suggest different orientations for RXed grains from various sites, our results show that the RXed grains in the ZE20 sample, regardless of their nucleation sites and stages, tend to show the off-basal orientations during nucleation. Rather than suppressing the fast growth of basal RXed grains from prior grain boundary by precipitate pinning, all the RXed grains in the ZE20 sample exhibit a consistent off-basal growth advantage. The growing grains show more obvious off-basal orientations compared with the shrinking and stable RXed grains (Figure 4.4 and Figure 4.5).

Certain grain boundaries with specific misorientations, such as 30º about <0001> axis misorientation boundary in Mg alloys [153,157,183], have been reported to exert a growth advantage over other boundaries during recrystallisation. This advantage is attributed to the formation of ∑13 coincidence site lattice (CSL) [184] or dislocation slip-induced grain rotation [185]. Figure 4.9 (a-b) shows that there are no specific misorientation boundaries in the ZE20

sample. The boundary length fractions of the two major peaks (30º about <0001> and 64º about <$\bar{1}$101> misorientation boundaries) are below 1%, due to their homogeneous distribution of misorientation angle and low misorientation axis intensities. Thus, the preferential nucleation and growth in the ZE20 sample are not associated with special misorientation grain boundary. On the contrary, the AZ31 sample has a strong peak of 55º about <$\bar{1}$100> misorientation, which is significantly weakened from 26.7 (AZ/3) to 10.1 MRD (AZ/4), as shown in Figure 4.9 (c-d). The corresponding boundary length fraction decreases from 8.2% at AZ/3 to 2.0% at AZ/4, Figure 4.9 (e-f), in accompany with the rapid nucleation process in Figure 4.3 (h). Some researchers attribute these boundaries to the tensile-tensile double twin boundaries characterized by 60º about <$\bar{1}$100> misorientation axis [186–188]. Considering the occurrence of this double twin boundary and the 5º misorientation angle difference with the observed peak in this work, we are cautious about relating the observed specific boundaries to double twin boundaries. Further study is needed to fully understand the effects of these misorientation boundaries on the recrystallisation behaviours of the AZ31 sample.

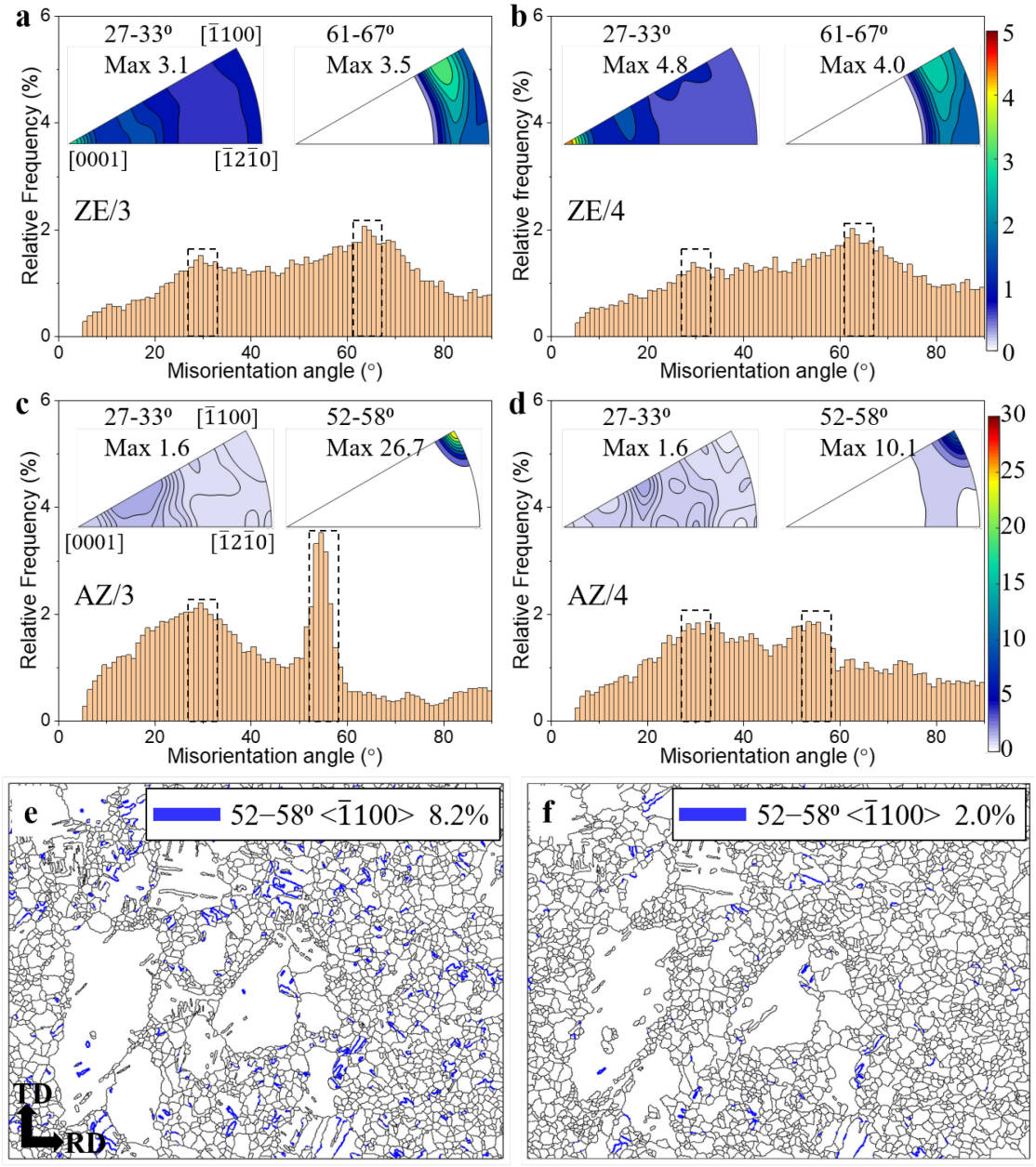

Figure 4.9 Grain boundaries evaluation the ZE20 and AZ31 sample. (a, b) Misorientation angle distributions of all grains in the ZE20 sample. (c, d) Misorientation angle distributions of all grains in the AZ31 sample. (e, f) Grain boundary maps of all grains in the AZ31 sample. The axis distribution of the special misorientation boundary peaks are superimposed in misorientation angle distribution maps. The length fraction of 55-58° <$\bar{1}$100> boundary is attached in (e, f).

4.4 Conclusion

This work investigated the recrystallisation process of commercial and RE containing Mg alloys by applying the grain correlation approach. It is the first time to simultaneously track thousands of RXed grains from nucleation to fully recrystallized condition. Different from the classic nucleation and grain growth theory, it shows the continuous and dynamic nucleation and grain growth processes. The texture weakening mechanisms of RE addition are investigated. The main conclusions are given below:

1. Recrystallisation does not occur at a constant rate. The severely deformation shear bands in the ZE20 sample promote nucleation, while the recrystallisation is initially low followed by a sudden increase of recrystallisation fraction in the AZ31 sample.

2. The RXed grains do not always grow, but they can also shrink or even be consumed. This is because the newly formed grains grow at the expense of the old ones.

3. The early formed RXed grains have minor contributions to the fully recrystallized microstructure and texture as most of them are consumed during annealing.

4. RXed grains in the ZE20 sample show off-basal texture which is independent of the nucleation sites and recrystallisation stages. This oriented nucleation is the origin of RE texture. Basal orientation is the main texture component of the RXed grains in the AZ31 sample, meanwhile a basal spread is found in the middle recrystallisation stage. Thus, the basal texture can only be weakened but not changed in the AZ31 sample.

5. Preferential grain growth is observed in the ZE20 sample that the growing grains show a more pronounced off-basal texture compared to the stable and shrinking ones. There is no obvious grain growth preference in the AZ31 sample.

Within the narrative of this thesis, this chapter demonstrates that recrystallisation in Mg alloys cannot be fully interpreted from the final recrystallised microstructure alone. The Track-Rex results show that a grain may nucleate early but later shrink or be consumed, whereas other grains nucleating at later stages may dominate the final microstructure. This distinction between nucleation frequency and grain survival is central to the grain-resolved approach developed in this thesis. It also provides the motivation for the next chapter, where the role of a specific microstructural feature, shear bands, is examined in greater detail.

Chapter 5 Specific grains tracking from shear bands

5.1 Introduction

Chapter 4 established the general capability of Track-Rex to follow recrystallised grains across large quasi-in-situ EBSD datasets and showed that grain survival, rather than nucleation alone, controls the final recrystallised microstructure. This chapter builds directly on that conclusion by focusing on a more specific metallurgical question: the role of shear bands as recrystallisation nucleation sites in a lean-RE ZE20 magnesium alloy. Shear bands have often been treated as preferential nucleation sites for texture modification in Mg-RE alloys, but their actual contribution to the final recrystallised texture depends on whether the grains formed within them are retained during subsequent annealing.

The aim of this chapter is therefore to move from general recrystallisation tracking to feature-specific tracking. Instead of considering all recrystallised grains as a single population, the analysis separates grains nucleated at or near shear bands from those associated with other microstructural regions. This allows the contribution of shear-band-induced nucleation to be assessed not only at the moment of nucleation, but throughout the entire annealing sequence. In this way, the chapter links a classical recrystallisation question—the role of preferred nucleation sites—to the central thesis theme of grain-resolved, time-resolved microstructure analysis.

With the increasing demand for lightweight materials in automotive and aerospace industries, magnesium (Mg) alloys are drawing attention because of their high strength-to-weight ratio. However, the application of Mg alloys is restricted as they tend to form strong

basal crystallographic texture during deformation. The basal texture hinders the activation of deformation modes like basal slip and tension twinning [189,190] during subsequent thermomechanical treatments, leading to premature failure. One common approach to modify the deformation textures is recrystallisation annealing [191], through which weakened textures can be obtained, particularly in some magnesium rare earth containing alloys (Mg-RE alloys) [192,193] and some lean Mg-Zn-Ca alloys [194]. The rare earth (RE) textures are formed through statistical or dynamic recrystallisation processes. Typical RE textures demonstrate a fiber with the $<11\bar{2}1>$ axis of grains parallels to the extrusion direction (ED) after extrusion [195,196] and a weakened texture with tilted basal pole from normal direction (ND) towards the transverse direction (TD) after rolling [197,198].

The origin of RE textures remains a matter of debate over the past two decades, numerous factors have been considered to play roles during recrystallisation procedure, including solute drag [199,200] and particle pinning along specific grain boundaries (GBs) [201–203], preferential nucleation sites [195,204–206] and oriented grain growth [207,208]. However, real-time recrystallisation progress is usually associated with the synergies of aforementioned factors, making it difficult to establish their individual effects on the RE textures formation. For instance, the preferential nucleation sites in Mg alloys include second phase particles [205,206,209], grain boundaries and subgrain boundaries [209–211], deformation twins [204,212–214] and shear bands (SBs)[195,214–216]. This range of nucleation sites raises the questions: (1) what are the individual contribution of each nucleation site to the final texture; (2) dose the microstructure evolution differ depend on different nucleation sites; (3) does the initial recrystallised texture retain or there is growth advantage regarding to nucleation sites or specific orientation? It could be difficult to elucidate and validate potential answers considering

all nucleation sites within one work. Therefore, only the mechanism of SBs induced nucleation is investigated in this work.

It is important to study the SBs induced nucleation as they are the predominant microstructural feature and preferential nucleation sites in severely deformed materials. Stanford and Barnett [195] first reported SBs in Mg-RE alloys have higher nucleation propensity than deformed grain boundaries. Basu et al. [215] further confirmed this in both Mg-1Ce and Mg-1Gd alloys, where recrystallisation is dominated by SBs induced nucleation with random orientation. However, after fully recrystallised, only Mg-1Gd presents RE texture while Mg-1Ce maintains basal texture. The negligible texture changes within Mg-1Ce attributes to the fine distribution of fragmented Mg12Ce precipitates, which restricts subsequent grain growth. Nevertheless, the insights into texture evolution of SBs induced nucleation remains unclear. Later, the texture modification of deformed Mg-1Ce was achieved with Zn and Zr addition [217], promoting the formation of both SBs and precipitation. Hence, it cannot be distinguished whether SBs induced nucleation or particle stimulated nucleation (PSN) should be responsible for the weakened texture. On the other hand, Zeng et al. [210] demonstrated the random orientation of GBs nucleation in a Mg-0.3Zn-0.1Ca alloy, Han et al. [211] also found GBs nucleated grains exhibit RE texture in a fine-grained Mg-3Gd alloy. Nevertheless, the contribution of these GBs nucleation to the final microstructure cannot be distinguished from other nucleation sites like SBs or PSN. Apart from nucleation, grain growth also plays a significant role in the formation of RE texture. Guan et al. [216] revealed the orientated growth of off-basal grains at elevated temperature in WE43 alloy. Zeng et al. [218] demonstrated that apart from growth, recrystallised grains can also shrink or be consumed by neighbouring grains. Prior to this work, the individual effect of double twins and SBs in WE43

alloy were systematically investigated using quasi-in-situ Electron Backscatter Diffraction (EBSD) method [213,216]. The results indicates that grains nucleated at double twins exhibit RE texture, which is preserved during subsequent uniform grain growth [213]. Conversely, SBs induced nucleation shows random orientation, and a weakened RE texture was obtained owing to the growth advantage of off-basal grains. This oriented grain growth attributes to the absence of particle pinning effect at GBs [216]. However, other researchers have also reported basal textures after annealing in Mg-RE alloys with SBs dominant microstructure, and non-RE alloys with intensive SBs show obvious basal texture after annealing[215,219,220]. Recently, Li et al. [221] proposed that the grains nucleated at SBs dominate the recrystallisation in a Mg-1Al-1Zn-0.1Ca-0.2Y alloy and observe only weakened basal texture. However, a quantitative evaluation is still necessary to confirm the contribution of SBs induced nucleation to the final texture. Hence, the role of SBs during nucleation and grain growth needs to be thoroughly investigated and quantified with representative microstructure dataset and advanced data processing methods.

The possibility remains that early formed recrystallised grains from SBs could be gradually consumed during recrystallisation, necessitating the clarification regarding the contribution of PSN or GBs nucleation. In either case, there is an inevitable need to track large number of grains from nucleation to fully recrystallised state, after which the contribution of specific group of grains can be calculated. Nonetheless, conventional grains tracking within in-situ datasets is manually conducted at small regions, which is not only less representative but also time consuming. Moreover, the tracking task is becoming more challengeable because of the fast-expanding data size facilitated by the advancements in data acquisition speed. Recently, the authors have developed Track-Rex, a toolbox which allows researchers to efficiently track

large number of grains within in-situ or quasi-in-situ EBSD datasets. Details regarding the tracking algorithm, scripted code, as well as text and video instructions are available at open-source GitHub repository [https://github.com/TrackRex/Track-Rex]. In the accompanying publication [222], the entire recrystallisation process of two Mg alloys (AZ31 and ZE20) were examined, but detailed contribution from SBs induced nucleation was not fully discussed in our previous works [216,222].

To clarify the role of SBs as nucleation sites during recrystallisation and grain growth, as well as resolve their contribution to the recrystallised texture, we employed Track-Rex to investigate the entire annealing process of a ZE20 alloy using quasi-in-situ EBSD method. The sample was firstly subjected to tailored mechanical processing to maximise the volume fraction of SBs, followed by multiple interrupted annealing steps until the recrystallisation process was nearly completed. After tracking all 40900 grains presented in the EBSD dataset, we confirmed that the recrystallised grains from SBs exhibited scattered RE texture upon nucleation. However, most of them were gradually consumed as the recrystallisation progressed and thus only provide limited contribution (20.89%) to the final texture. Moreover, basal-oriented grains within shear bands were progressively consumed, while off-basal grains demonstrated higher possibility to survive during subsequent annealing. As a result, the grains nucleated from SBs exhibit RE texture with off-basal peaks at fully recrystallised state. In addition, the consumed SBs grains reflect a higher content of low-angle grain boundaries compared to the maintained ones, suggesting that GBs have a significant impact on grain behaviour during recrystallisation. These findings will enhance the understanding of recrystallisation process and pave the way for the development of new wrought Mg alloys with tailored crystallographic texture.

The chapter is organised as follows. The initial deformed microstructure is first described to identify the distribution of shear bands and potential recrystallisation sites. The subsequent quasi-in-situ EBSD maps are then analysed using Track-Rex to determine where recrystallised grains first appear, how their area fraction evolves, and whether shear-band-nucleated grains are retained or consumed during annealing. The final part of the chapter discusses how these grain histories affect the interpretation of shear bands as effective texture-modifying features.

5.2 Results

5.2.1 Microstructure after cold deformation

Figure 5.1 (a) presents EBSD IPF map of the cold-rolled ZE1 surface, with an index rate of 30%, attributed to the large plastic strain introduced by cold rolling. Figure 5.1 (b) shows the corresponding band contrast (BC) map, where the SBs was prominent in the deformed microstructure (dark areas in BC map and non-indexed areas in IPF map). Figure 5.1 (c) shows (0001) pole figure of the IPF map, exhibited strong basal texture with peak intensity slightly tilted off from basal centre. Figure 5.1 (d) displays the misorientation angle distribution, a broad spectrum with peak angle at ~30°, ~89° was observed. It is clear that the SBs was the dominate deformation microstructure feature.

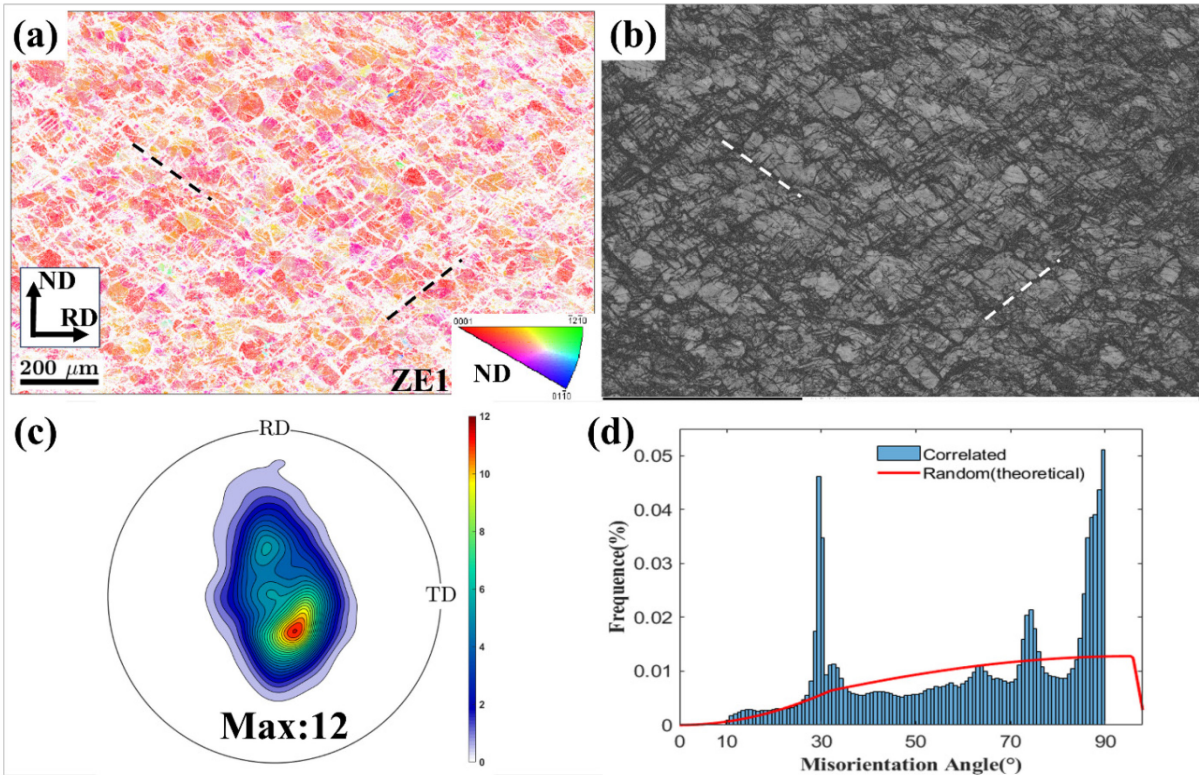

Figure 5.1 Microstructure after cold rolling: (a) EBSD IPF map, (b) corresponding band contrast map, (c) (0001) pole figure, (d) misorientation angle distribution.

5.2.2 Nucleation at early-stage recrystallisation

To investigate the nucleation event, a quasi-in-situ EBSD scan was conducted on the same region after annealing at 400°C for 4 minutes (ZE2). Figure 5.2 (a) shows IPF map and (0001) pole figure of ZE2. In comparison to the deformed state (Figure 5.1(a)), a greater number of small, recrystallised grains were observed, accompanied by a decrease in peak texture intensity from 12 Multiples of Uniform Distribution (MUD) to 10 MUD in the whole EBSD area. In addition, grains in ZE2 were categorized into two groups depending on their correlation with ZE1: the residual deformed parent grains coloured in grey, and the newly formed recrystallised grains coloured by their orientations, as demonstrated in Figure 5.2 (b).

These recrystallised grains formed a band-like feature, corresponding to the previous SBs, as demonstrated by the black arrows and dash lines in Figure 5.2 (b), Figure 5.1 (a) and (b). This indicates the SBs were acting as primary nucleation sites at this stage of annealing. In the grains size distribution of Figure 5.2 (c), the deformed and recrystallised grains showed average size of 18.7 μm and 5.9 μm, respectively. Figure 5.2 (d) demonstrates the (0001) pole figure of deformed grains in ZE2, exhibited similar texture to ZE1 (Figure 5.1 (c)). On the other hand, the recrystallised grains exhibited scattered off-basal distribution with an intensity of 3.9 MUD (Figure 5.1 (e)). It should be mentioned that some deformed grains were mistakenly identified as recrystallised grains, as indicated by the red arrows in Figure 5.2 (b). This error was introduced by the sample misalignment during quasi-in-situ procedure. Because of the limited volume, this error does not affect the finding that SBs acted as primary nucleation sites and the recrystallised grains at SBs exhibit off-basal textures.

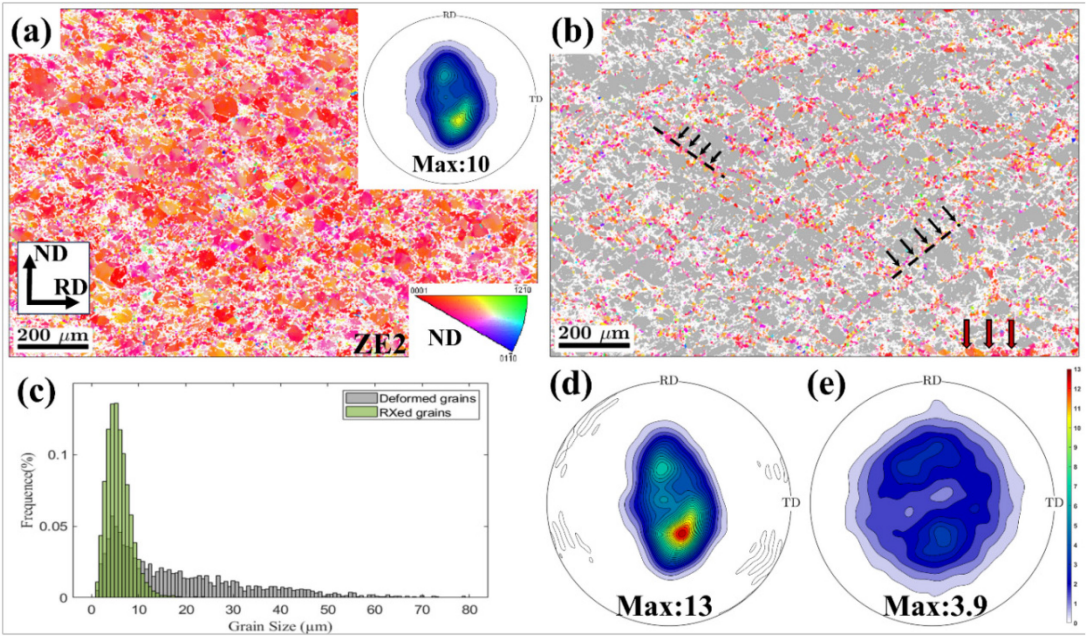

Figure 5.2 Nucleation event at shear bands in ZE2 (annealed at 400°C for 4 minutes): (a) EBSD IPF map, (b) tracking results with deformed grains in grey and recrystallised grains in

IPF colour, (c) grain size distribution, (d) (0001) pole figure of the deformed grains and (e) recrystallised grains.

5.2.3 Statistical results from grains tracking

To clarify the contribution of SBs induced nucleation, the recrystallisation progress of the same region was examined. Figure 5.3 (a)-(f) depict the microstructure and texture evolution with IPF maps and (0001) pole figures. The tracking results divided grains into subsets based on their nucleation sequence, as shown in Figure 5.3(a′)-(f′). For instance, light blue grains in ZE7 (Figure 5.3(f′)) were nucleated from ZE2 (Figure 5.3(a′)), which means they were nucleated no later than 4 minutes of annealing and survived the total 80 minutes of annealing. Hence, for each individual grain appears in this dataset, its nucleation sequence, grain size and orientation were recorded in the output file of Track-Rex. From the tracking results, the recrystallisation is initially concentrated within the shear bands (Figure 5.3(a′)-(b′)) and later transferred to the conventional deformed grain boundaries. Notably, the recrystallised grains originated from ZE4 (Figure 5.3(c′)) continuously grow, constituting the main component of the fully recrystallisation microstructure (Figure 5.3(f′)). To quantitively analyse the contribution of SBs induced nucleation at different stages, both area fraction and number frequency of grains subsets are calculated, as presented in Figure 5.4. The light bule and dark blue bars represent the area fraction (Figure 5.4(a)) and number frequence (Figure 5.4(b)) of grains nucleated no later than 4 minutes and 9 minutes. After matching the positions of recrystallised grains in ZE2 and ZE3 with the position of SBs in deformed sample ZE1, it is clear that a great majority of recrystallised grains shown in both maps (Figure 5.3 (a′-b′)) were nucleated from SBs in sample ZE1. After two interrupted annealing steps, the area fraction of recrystallised grains from SBs is up to 51.2%. However, when the recrystallisation is nearly

finished, the area fraction and number fraction of these recrystallised grains only occupy 20.89% and 14.74% in sample ZE7. Therefore, it can be confirmed that, although SBs were the dominant deformed microstructure and acted as primary nucleation site in the early stages of annealing, the grains nucleated from SBs were progressively consumed through recrystallisation procedure and provide limited contribution to the final texture.

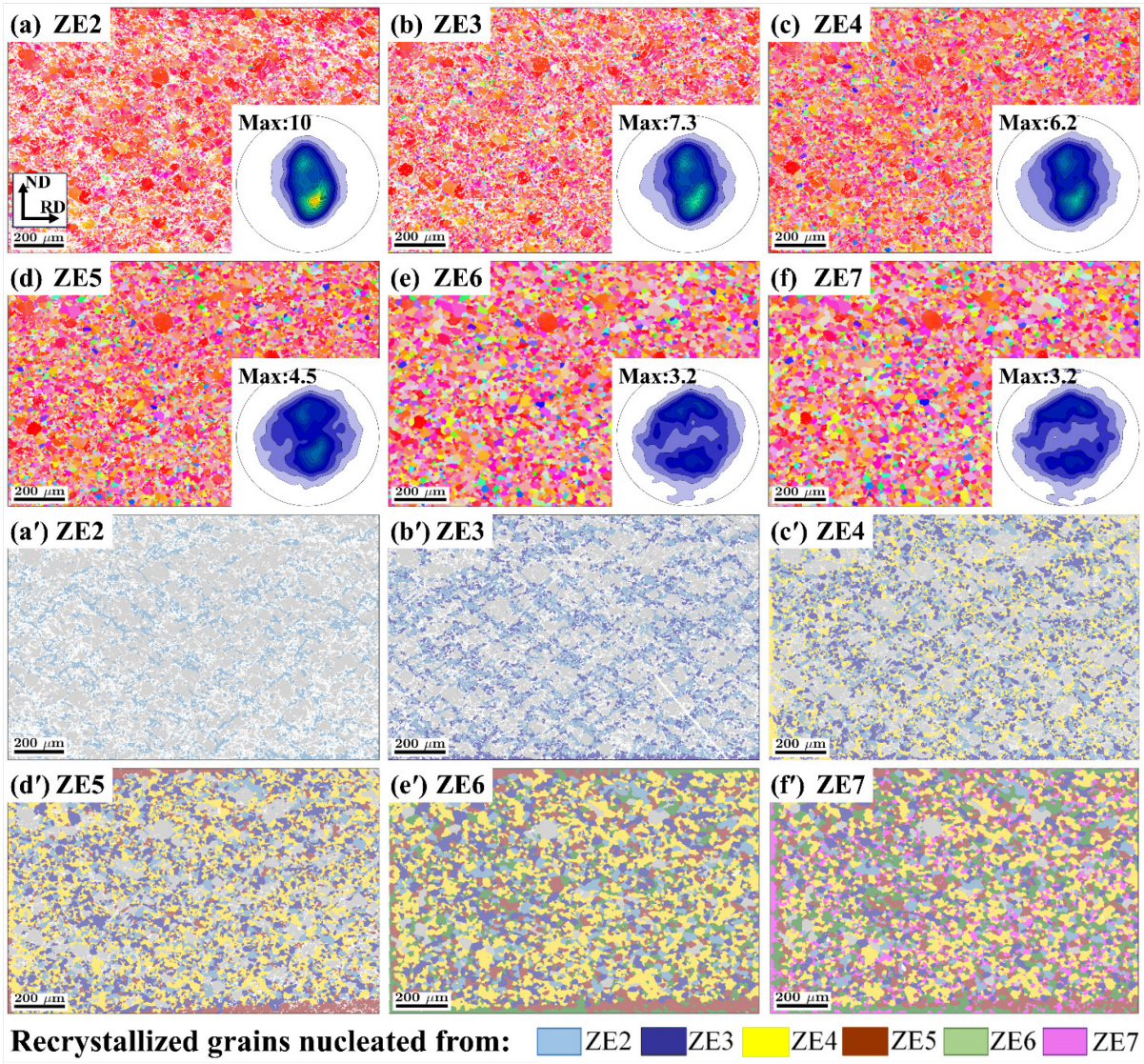

Figure 5.3 Entire recrystallisation process and grains tracking results: (a)-(f) IPF maps of the same region from nucleation to nearly fully recrystallised, together with texture evolution of

(0001) pole figure. (a′)-(f′) Tracking results demonstrated by colouring grains by their nucleation sequence, a light blue grain in ZE7 means it was nucleated at ZE2 and was maintained till the final annealing step. Apart from recrystallised grains, deformed grains are coloured in grey. Tracked grains refer to grains for which a reliable correlation was identified between successive EBSD maps using the Track-Rex criteria. Grains without a reliable candidate in the following step were classified as consumed.

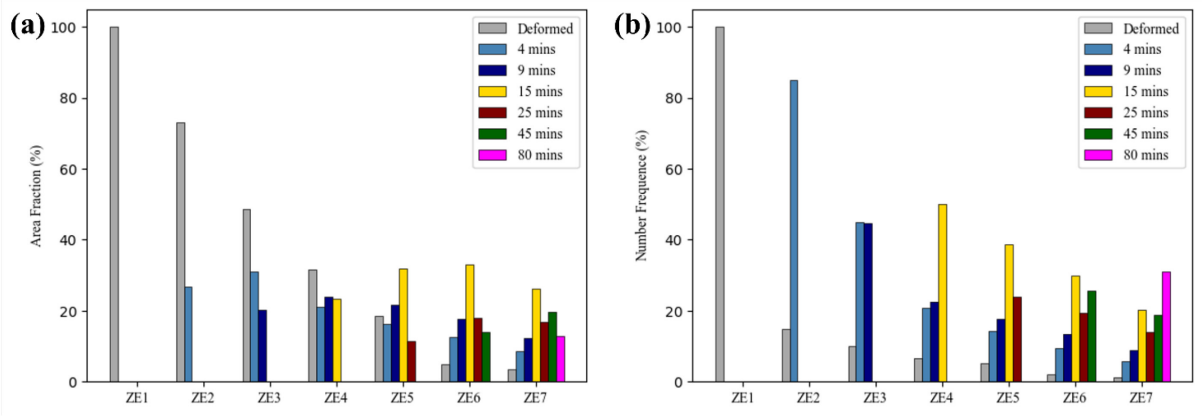

Figure 5.4 Statistical results representing the recrystallisation progress: (a) area fraction and (b) number frequency of recrystallised grains at different annealing steps. The light bule bar stands for the grains nucleated no later than 4 minutes in ZE2, of which both area fraction and number frequence drop along with annealing time.

5.3 Discussion

5.3.1 Recrystallisation kinetics and texture evolution

As showed in Figure 5.3 (a)-(f), the deformed basal texture was gradually weakened through annealing progress and eventually replaced by a RE texture with peak intensity of 3.2

MUD. To investigate the origin of this weakening effect, the texture evolution of recrystallised grains from different annealing times is demonstrated in Figure 5.5. Each row represents the texture development of grains nucleated from the same sequence, while each column corresponds to the component of the entire recrystallised texture. For example, row (a) illustrates the texture evolution of grains nucleated no later than 4 minutes (ZE2), whereas column 80 mins represents the texture components of the recrystallised sample (ZE7). In row (a) and (b), there was a clear trend that the scattered off-basal texture component was strengthened with increasing annealing time. The texture intensity increased from 3.9 to 9.4 MUD for grains nucleated from ZE2, and from 4.0 to 6.2 MUD for grains nucleated from ZE3. However, there is no obvious strengthening of any texture component regarding to row (c) and (d). This difference should be attributed to the nucleation sites, as row (a) and (b) represent the grains mostly nucleated from SBs (Figure 5.3 (a′)-(b′)), while row (c) and (d) demonstrate the grains mostly nucleated at prior GBs (Figure 5.3 (c′)-(d′)). It should be mentioned that despite the difference in nucleation sites, all recrystallised grains showed scattered off-basal orientations upon nucleation (Figure 5.5(a)-(d)) and share similar trend of basal-orientated grains being consumed.

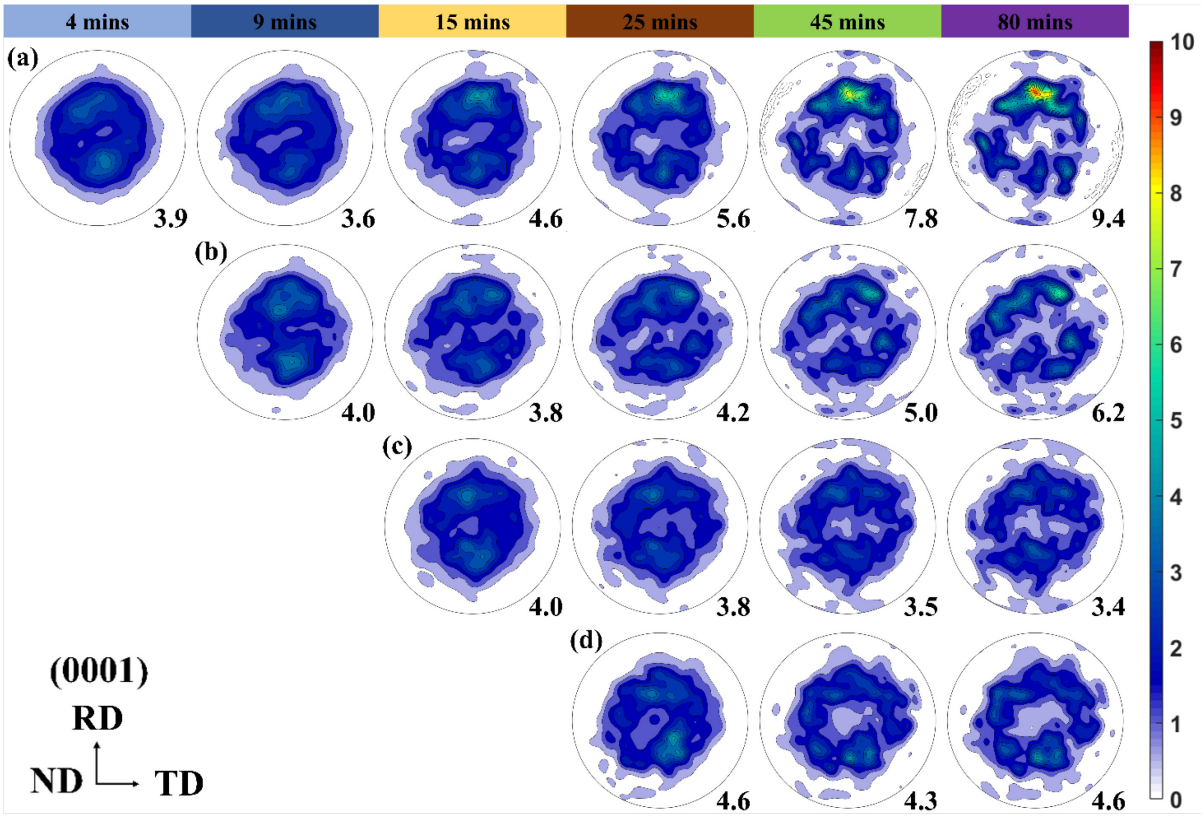

Figure 5.5 The texture evolution of recrystallised grains subsets, each row corresponds to the same group of recrystalised grains nucleated at (a) ZE2, (b) ZE3, (c) ZE4, (d) ZE5 and their texture evolution along upcoming annealing steps.

5.3.2 Recrystallisation from different nucleation sites

It is generally accepted that the prior grain and subgrain boundaries, deformation twins, SBs, and second phase particles are the preferred nucleation sites in Mg alloys. With the grains tracking approach, this study reveals insights into the recrystallisation behaviours in a ZE20 Mg alloy with server shear banding feature. The tracking results clearly show that SBs are the primary nucleation site at early stage of recrystallisation, as shown in Figure 5.2 (b). This finding aligns with most literature, and it was also generally accepted that this preferable

nucleation site would dominate the entire recrystallisation process and be responsible for the texture weakening. However, the tracking results in Figure 5.3 (b′) depict the nucleation event between 4 minutes and 9 minutes, where the recrystallisation nucleation stared to take place at prior GBs. This shift in preferred nucleation site became more obvious in Figure 5.3 (c′), where most of the recrystallised grains from 9 minutes to 15 minutes appears to be prior GBs nucleation. Hence, the assumption of SBs guiding or dominating recrystallisation progress is not rigorous and needs to be clarified. Instead of qualitative analysis, quantitative calculation is for the first time achieved in a large dataset containing 40900 grains, to validate the contribution of SBs nucleation. Figure 5.4 presents the contribution of grains subsets, where the trend of grains nucleated no later than 9 minutes is clear to be gradually reduced along annealing. Therefore, it can be confirmed that the SBs nucleation provide limited contribution to the final microstructure, with less than 20.89% in area fraction and less than 14.74% in number frequence. On the other hand, within the nearly fully recrystallised sample (ZE7), the grains nucleated at GBs between 9 minutes and 15 minutes contribute the most to the whole microstructure, with 26.34% in area fraction and 20.34% in number frequence. This suggests that the GBs nucleation plays a more significant role regarding to the texture weakening effect. It should be mentioned that according to the tracking results, there were still recrystallised grains nucleated between 45 minutes and 80 minutes. These “recrystallised grains” identified by Track-Rex might not be the real newly formed recrystallised grains in most cases. On the contrary, they are more likely to be grains growing from beneath the sample surface, as recrystallisation was nearly complete. However, it is difficult to investigate these "recrystallised grains" because no spatial information can be obtained in conventional 2D EBSD characterisation. Hence, the recrystallised grains identified by Track-Rex after 45 minutes are not included in any analysis, and this does not affect any aforementioned findings

since there was no obvious grain growth until 45 minutes of annealing (ZE6), according to Figure 5.3 (d′)-(e′) and Table 5.1.

Table 5.1 Average grain size of quasi-in-situ annealing of ZE20 sample.

Total annealing time [minutes]	Sample designation	Average grain size [μm]
4	ZE2	7.8
9	ZE3	8.1
15	ZE4	8.8
25	ZE5	10.0
45	ZE6	13.3
80	ZE7	13.8

Figure 5.6 presents the growth behaviour of grains subsets according to nucleation sequence. The recrystallised grains no later than 4 minutes (ZE2) started with an average size of 5.9 μm (point A) and grow to 7.6 μm (point A′) at 9 minutes, whereas the grains nucleated between 4 minutes and 9 minutes exhibit a smaller average size of 6.2 μm (point B). It is obvious that the average size of recrystallised grains continues to increase along annealing, however the area fraction (Figure 5.4 (a)) of the grains subsets tend to decrease. For instance, the grains nucleated in ZE2 continued to grow till 16.6 μm in the final stage, while their area fraction decreased from 26.89% in ZE2 to 8.47% in ZE7. This phenomenal should attribute to

the consumption of old recrystallised grains, which was acting as the expense of the growth of newly recrystallised grains. Despite the high amount (13033) of nuclei in ZE2, only 471 of the grains survived after 80 minutes of annealing. In this case, the total area fraction decreased while the average grain size increased.

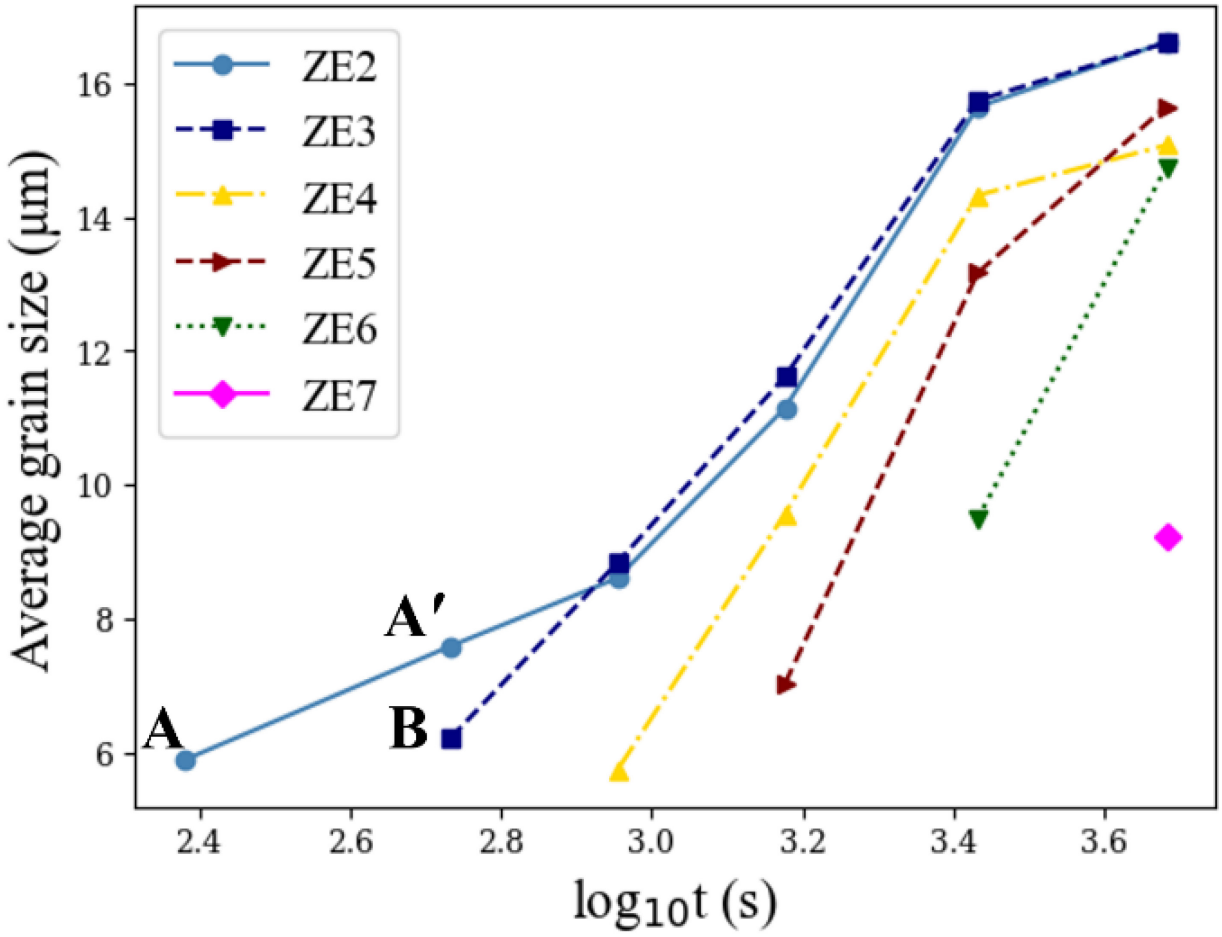

Figure 5.6 Average grain size of recrystallised grains formed at different annealing steps. Each group contains grains first detected at the same step and tracked through later annealing. Although the surviving early-formed grains become larger with annealing time, many of them are consumed, so their final area fraction decreases.

In addition to the quantitative analysis of texture contribution and grain growth behaviour, detailed analysis of texture development based on nucleation sequence is enabled by the tracking procedure. The results have shown that all recrystallised grains exhibit scattered off-basal orientation upon nucleation. They further shared a similar trend of basal orientated grains progressively consumed while off-basal grains possess higher possibility of maintenance, regardless to the different nucleation sites, as clearly demonstrated in Figure 5.5. This similarity in features of nucleation and evolution should be responsible for the texture weakening effect. The scattered random nucleation at SBs and GBs has been reported in different Mg alloys, while the progress of basal grains consumption remains unexplained. Zeng et al. [210] found that the recrystallised grains with c-axes parallel to parent grains would exhibit growth advantages, which is on the opposite to the tracking results. Thus, resolving the factors that affect the grains behaviour of maintenance or consumption will unveil the origination of texture weakening. The first factor that should be considered is the GBs, Figure 5.7 represents the procedure of recrystallised grains nucleated at SBs no later than 4 minutes (Figure 5.1 (b)) evolving to the next annealing step. All the recrystallised grains (Figure 5.7 (a)) are firstly divided into consumed grains (a1) and maintained grains (a2), which then evolved to the next annealing step (b). The GBs misorientation angle distribution is presented in Figure 5.7 (a1′)-(b2′), and the distribution of consumed and retained SBs nucleated grains exhibit different characteristics. The feature difference indicates that the grains with low angle grain boundaries (LAGBs) in the recrystallised grains are prone to be consumed, as shown in Figure 5.7 (a1′). This is because the LAGBs often have a high density of dislocations, making the grain boundaries unstable and thus easily consumed during recrystallised process. Compared to the consumed recrystallised grains, the retained recrystallised grains have a higher proportion of high angle grain boundaries (HAGBs), primarily concentrated between 60°-80°, as shown in

Figure 5.7 (a2′) and (b2′). There are also slightly changes in the content of other angle boundaries, suggesting that GBs features have a significant impact on grain behaviour during recrystallisation However, further analysis should be combined with computational methods like density functional theory [223,224] or molecular dynamics [225] that can simulate the boundaries mobility to help explain how the GBs features will affect the grains behaviour.

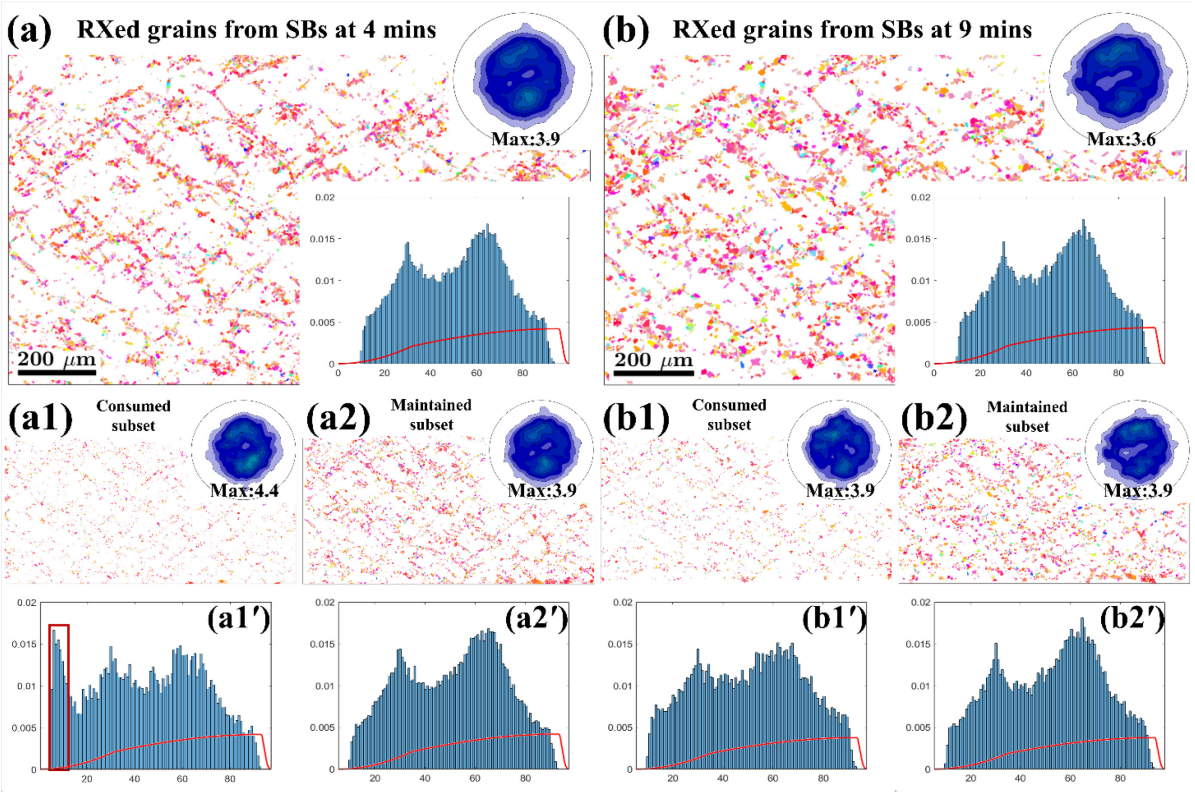

Figure 5.7 Grains behaviour of SBs induced nucleation from 4 minutes to 9 minutes: (a) all SBs nucleation no later than 4 minutes and their (a1) consumed subset and (a2) maintained subset. (b) All SBs nucleation at 9 minutes and their (b1) consumed subset and (b2) maintained subset; (a1′)-(b2′) grain boundaries misorientation angle distribution as well as theoretical random disorientation of grains subsets.

5.4 Conclusion

This study investigated the recrystallisation process of a ZE20 rare earth magnesium alloy with severe shear banding feature, using the grains tracking toolbox Track-Rex. To clarify the role of shear bands as nucleation sites, 40900 grains were simultaneously tracked from nucleation to nearly fully recrystallisation in less than 10 minutes. The tracking results demonstrates a continuous and dynamic nucleation and grain growth process, where the role of shear bands induced nucleation is thoroughly investigated. The findings will improve the understanding of recrystallisation mechanisms and pave the way for developing new wrought Mg alloys with tailored texture. Moreover, the toolbox greatly accelerates data processing speed and can be easily adopted by other researchers, thereby making a meaningful contribution to the broader research community. The main conclusions are as follows:

(1) Shear bands act as preferential nucleation sites during early stage of recrystallisation. However, early formed recrystallised grains from shear bands were progressively consumed, especially those with low-angle grain boundaries.

(2) The recrystallised grains formed from prior grain boundaries makes the major contributions to the fully recrystallised microstructure and texture.

(3) Recrystallised grains exhibit an off-basal texture (e.g., RE texture) independent from nucleation sites and recrystallisation stages. The texture evolution shows a clear trend of basal orientated grains consumption and off-basal grains maintenance, acting as the origin of the RE texture development.

In the context of the thesis as a whole, this chapter refines the interpretation developed in Chapter 4 by showing that preferential nucleation sites do not necessarily make a proportional contribution to the final recrystallised microstructure. Although shear bands promote early nucleation, many of the grains formed in these regions are later consumed. The contribution of a nucleation site must therefore be evaluated through the complete grain history rather than from early-stage observations alone. This conclusion is important for Mg alloy processing, because it suggests that texture control requires both favourable nucleation and favourable subsequent grain retention. The next chapter extends this grain-history concept into three dimensions, where grain growth and abnormal grain growth are analysed using LabDCT and Track-4DGG.

Chapter 6 Statistical grains tracking throughout grain growth

6.1 Introduction

The previous two chapters used quasi-in-situ EBSD and Track-Rex to investigate recrystallisation in two-dimensional time-resolved datasets. Chapter 6 extends the same grain-resolved philosophy to a three-dimensional grain growth problem. Instead of tracking recrystallised grains on a polished surface, this chapter uses laboratory diffraction contrast tomography (LabDCT) to reconstruct and follow grain growth in a WE43 magnesium alloy volume during interrupted annealing. This represents a shift from recrystallisation to grain growth, and from 2D + time to 3D + time analysis.

The purpose of this chapter is to demonstrate how the tracking framework developed in this thesis can be generalised from surface EBSD maps to volumetric datasets. The use of LabDCT allows the evolution of grain volume, morphology and position to be analysed across multiple annealing steps. This is particularly important for grain growth because boundary motion is inherently three-dimensional and can be strongly affected by local neighbourhoods, curvature, spatial position and surface proximity. Accordingly, this chapter addresses the second major microstructural evolution process in the thesis: the statistical and spatially resolved behaviour of grains during normal and abnormal grain growth.

Grain growth is a fundamental microstructural evolution process that significantly influences mechanical properties of metallic materials [226], including strength [227,228],

ductility [229–231], and creep resistance [228]. In magnesium (Mg) alloys, which are increasingly used in lightweight structural applications, controlling grain growth is essential for optimising microstructure and mechanical performance [71,229,230,232]. Despite decades of research, key questions remain unresolved, including the mechanisms of abnormal grain growth (AGG), the role of boundary pinning, and the influence of triple junctions and initial crystallographic textures on the growth kinetics [226,233,234].

Grain growth is a 3D phenomenon: boundary motion depends on the curvature and topology of the 3D grain network, where junctions and interfaces evolve collectively to reduce total interfacial energy. (Quasi) in-situ two-dimensional (2D) electron backscatter diffraction (EBSD) has been extensively used to elucidate the temporal evolution of grain growth study grain growth, while it is inherently limited to surface observations and requires destructive sample preparation [235,236]. Our recently developed Track-Rex toolbox enables us to automatically track recrystallisation and grain growth behaviour during annealing in magnesium Mg alloys [90,237]. Nevertheless, there are limitations to limitations of obtaining grain boundary and neighbouring grains beneath the sampling surfaces, such 2D methods cannot fully illustrate curvature-driven growth, orientated grain growth, and volume changes where full-field 3D information is required. hindering us from capturing full 3D morphology of boundary migrations, texture evolution, grains consumption, etc. inside the bulk volume or beneath the sampling surface.

Recently, advanced synchrotron-based techniques (e.g., 3D x-ray diffraction microscopy) have also been employed to investigate recrystallisation and grain growth in various alloys [89,238–240]. However, these methods are often constrained by limited accessibility and tedious data analysis. Alternatively, Laboratory-based diffraction contrast tomography

(LabDCT) not only enables non-destructive, volumetric mapping of grain structures, but also offers a more accessible option for 4D (3D + time) investigations, with demonstrated success in materials such as Al-Cu [241–243], iron [244,245], and Ni [246,247] alloys. These capabilities are particularly advantageous for studying spatially dependent grain growth behaviour and validating current grain growth mechanisms [226]. However, to our best knowledge, LabDCT work focusing on studying grain growth behaviour of pure Mg or Mg alloys has not been reported so far. 4D methods, tracking the same grain(s) through successive annealing steps and enabling mechanistic insight into statistical grain growth behaviour—particularly relevant for anisotropic hexagonal close-packed alloys like Mg, has not been reported so far.

In this work, we present a quasi-in-situ 4D investigation of grain growth behaviour in a rare-earth (RE) containing Mg–RE alloy using LabDCT. Our approach enables high-confidence 3D reconstruction of grain morphology and orientation across multiple annealing steps. A tracking toolbox (Track-4DGG) is developed with capability of resolving individual, clustered, and ensembled grain evolution in 4D. By sectioning the dataset base on grain positions, we reveal spatially dependent grain growth behaviour. Furthermore, surface grains layers are extracted and analysed to refine the understanding of surface effect on the growth kinetics. This study not only demonstrates the feasibility of LabDCT for 4D grain growth studies but also provides a framework for statistical analysis and mechanistic interpretation of grain evolution in other alloy systems, offering new insights into grain growth control strategies.

The following sections first summarise the overall four-dimensional grain size evolution during annealing. The tracked grain histories are then used to classify grains into shrinking, normally growing and abnormally growing populations. Finally, the spatial distribution of

these behaviours is analysed to reveal how surface proximity and local heterogeneity influence grain growth kinetics. In doing so, this chapter connects the statistical tracking strategy developed in the preceding chapters with a fully volumetric interpretation of microstructural evolution.

6.2 Results

6.2.1 Four-dimensional grain growth kinetics

The as-received extruded WE43 T5 bar (⌀ 75 mm) was supplied by Luxfer MEL Technologies Ltd. A cylindrical rod (⌀ 0.8 mm × 12 mm height) was cut along the extrusion direction (ED) by wire electrical discharge machining. Interrupted annealing was performed at 490 °C for cumulative times of 12, 32, 80, 140, 800 and 2240 minutes in a tube furnace under argon protection, followed by air cooling. X-ray imaging was operated on a ZEISS CrystalCT equipped with a flat-panel detector and beam stop. After each dwell, an absorption-contrast tomography scan was acquired to determine the volume for subsequent diffraction imaging and reconstruction. LabDCT datasets were collected at 80 kV using an aperture size of 375 × 375 μm, with source–specimen and specimen–detector distances of 12 mm and 400 mm, respectively. There are approximately 3200 projections covering a height of 4 mm from the top surface at each annealing step, operated through a helical phyllotaxis scheme with an exposure time of 20s. Energy dispersive spectroscopy (EDS) and EBSD characterisation were conducted on the cross section after the last annealing and LabDCT scan, to confirm the final microstructure.

Raw diffraction images were denoised, segmented and reconstructed using GrainMapper3D (Xnovo Technology ApS) [242]. Grain mapping was conducted with a voxel size of 2.5 μm and a misorientation threshold of 0.5°. Post processing of boundary meshing and features statistics were performed in DREAM.3D [248]. A sub-volume with a height of 500 μm was selected for this study. Figure 6.1 presents details about the scanning setup, segmentation, reconstruction, and initial results. Figure 6.2 summarises the progress of grain coarsening by number-averaged grain size DN and volume-weighted average grain size DV, calculated by equation (1) and (2). For an individual grain i, Di represents its equivalent spherical diameter and Vi is its total volume. Through annealing, DV is constantly higher than DN, indicating the presence of large grains within the volume matrix, based on equations (1-2) [249].

$$D_N = \frac{\sum_i D_i}{N} \quad (6.1) \qquad D_V = \frac{\sum_i V_i D_i}{\sum_i V_i} \quad (6.2)$$

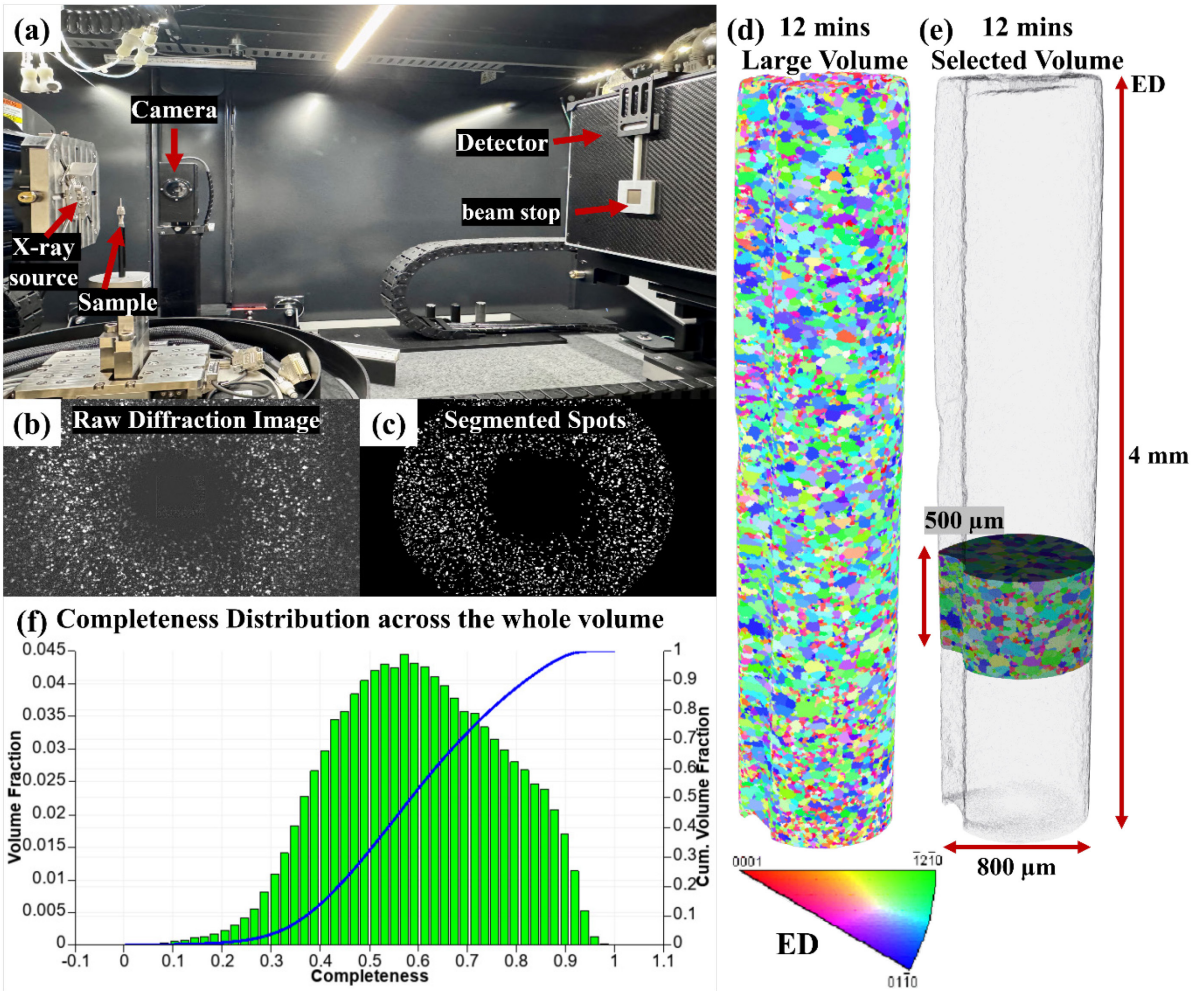

Figure 6.1 Experimental setup and results overview. (a) X-Ray Diffraction imaging condition. (b) Raw diffraction image of one projection from the first LabDCT scan and its (c) segmented diffraction spots. Reconstruction results of the 12 minutes annealing step are presented with the views of (d) the whole scanned volume and (e) select sub-volume of 500 µm height for this study. (f) The completeness distribution plot of the whole 4 mm scanned volume.

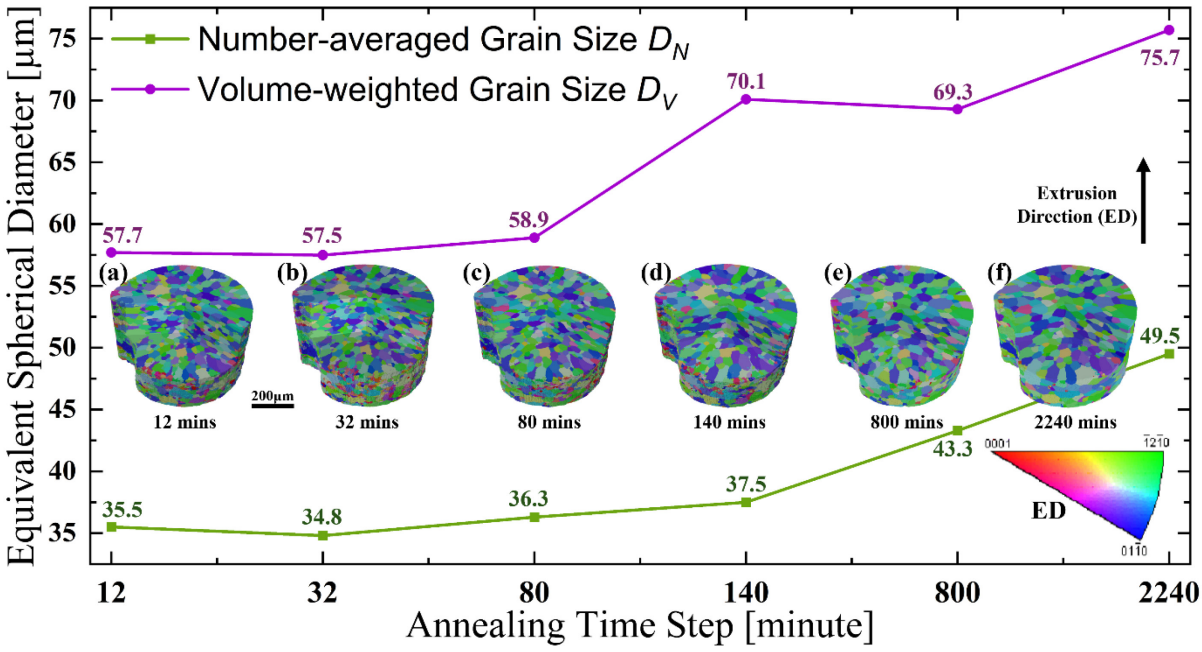

Figure 6.2 Grain size evolution of the Mg rod during annealing at 490 °C. (a)-(f) Reconstructed 3D volume of LabDCT at 12, 32, 80, 140, 800 and 2240 minutes, respectively.

After annealing the sample from 12 to 32 minutes, the average grain size slightly decreased. This is attributed to a detection threshold artifact of the LabDCT technique: Previously undetected small grains at the annealing step of 12 minutes became indexable after 32 minutes annealing, thus decreased DN and DV. Figure 6.1 (f) gives the completeness distribution, which stands for the index confidence of Lab-DCT. Until 80 minutes, grain growth was sluggish. The reason for this is that the sample was initially extruded and T5 treated, so the second-phase particles along the ED and fine precipitates formed during T5 can effectively pin the grain boundaries and delay boundary migration [250]. Fitting the six values of DN to the parabolic growth law as equation (3), it yields a growth exponent of n≈6.5, which is above the value of n=2 for curvature driven normal grain growth (NGG). The elevated exponent is consistent with reported Mg–RE alloys, where n varies from 5 to 8, caused by

solute drag of RE elements (e.g., Y, Nd, Gd) and Zener pinning by pre-existing second phase particles or even nanoscale precipitates [251,252].

$$D^n - D_0^n = Kt \quad (6.3)$$

6.2.2 Statistical results from grains tracking

At the annealing step of 140 minutes, DV exhibited a pronounced increase from 58.9 to 70.1 μm while DN increased only modestly. This divergence implies a subset of grains had grown disproportionately large by consuming pre-existing large grains, thus not reflected on the grain count or DN. For example, Figure 6.3 clearly shows the initial small grain G1 at 80 minutes annealing grew to a large grain at 140 minutes annealing by consuming adjacent grains including G2, G3 and G5, which is normally considered as abnormal grain growth (AGG) [253]. Chronologically, after the AGG event, DV slightly decreased at 800 minutes annealing while DN increased following the parabolic scheme. This difference suggests the growth during this step was mainly caused by consuming small grains, reflected by the reduced grain count and steady DV. Figure 6.4 confirmed the decreased area fraction of small grains with the grain size distributions between 140 and 800 minutes annealing. Moreover, some grains have growth advantage over both neighbouring small and large grains, resulting in a slight decrease of DV. A typical example provided in Figure 6.5 demonstrates a small grain G1 at 140 minutes annealing became a giant grain at 800 minutes annealing by consuming adjacent small grains G4 and G5, and large grains G2, G3, G6, G7 and G8. Despite the topological disadvantages, the preferential growth of smaller grains after AGG occurrence has also been reported whilst the mechanism remains unresolved [247,254]. The final annealing step revealed uniform growth with both DN and DV increasing approximately 6 μm. Throughout annealing, the total

grain count declined from 6000 towards 2000 (Table 6.1), consistent with coarsening by consumption. However, one grain can exhibit distinct growth behaviours at different stages (e.g., normal growth at early annealing stage, AGG during subsequent annealing and followed by NGG or grain shrinkage in the late annealing stage because large grains impinge [226,245]). There might be innumerable combinations of these behaviour sequences, and all have occurred in the presented dataset. Thus, detailed analysis at grain-scale with statistical results is indispensable, similar with other synchrotron-based large datasets [255].

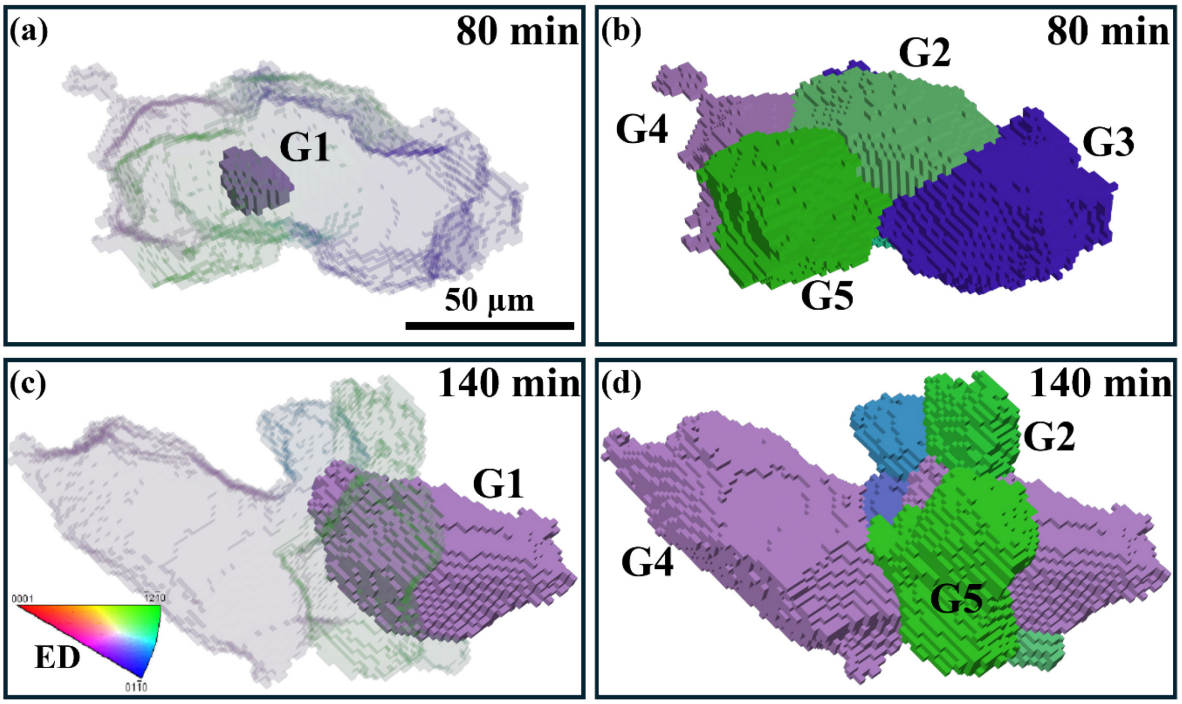

Figure 6.3 An example of abnormal grain growth behaviour between (a)-(b) 80 minutes and (c)-(d) 140 minutes. One grain exhibited a large GR of 19.7 is extracted and highlighted as G1 in (a) 80 minutes and (c) 140 minutes, with transparent surrounding grains. Neighbouring grains G2-G5 are also tracked and annotated in (b) 80 minutes and (d) 140 minutes annealing step datasets. G1 had abnormally grown and consumed G2(partially), G3 (entirely) and G5 (partially). G4 had also grown by consuming G5 (partially).

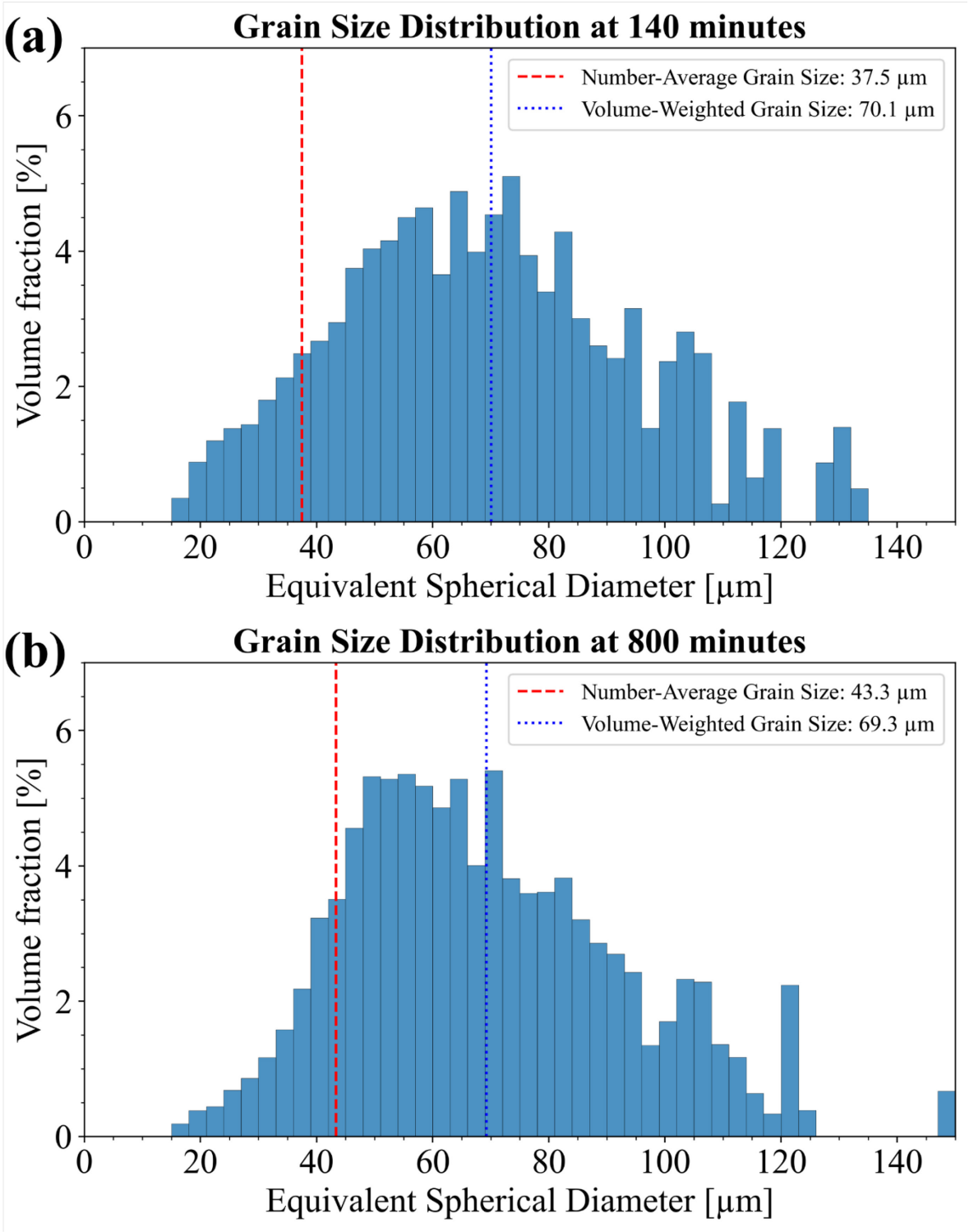

Figure 6.4 Grain size distribution of (a) 140 minutes annealing step and (b) 800 minutes annealing step

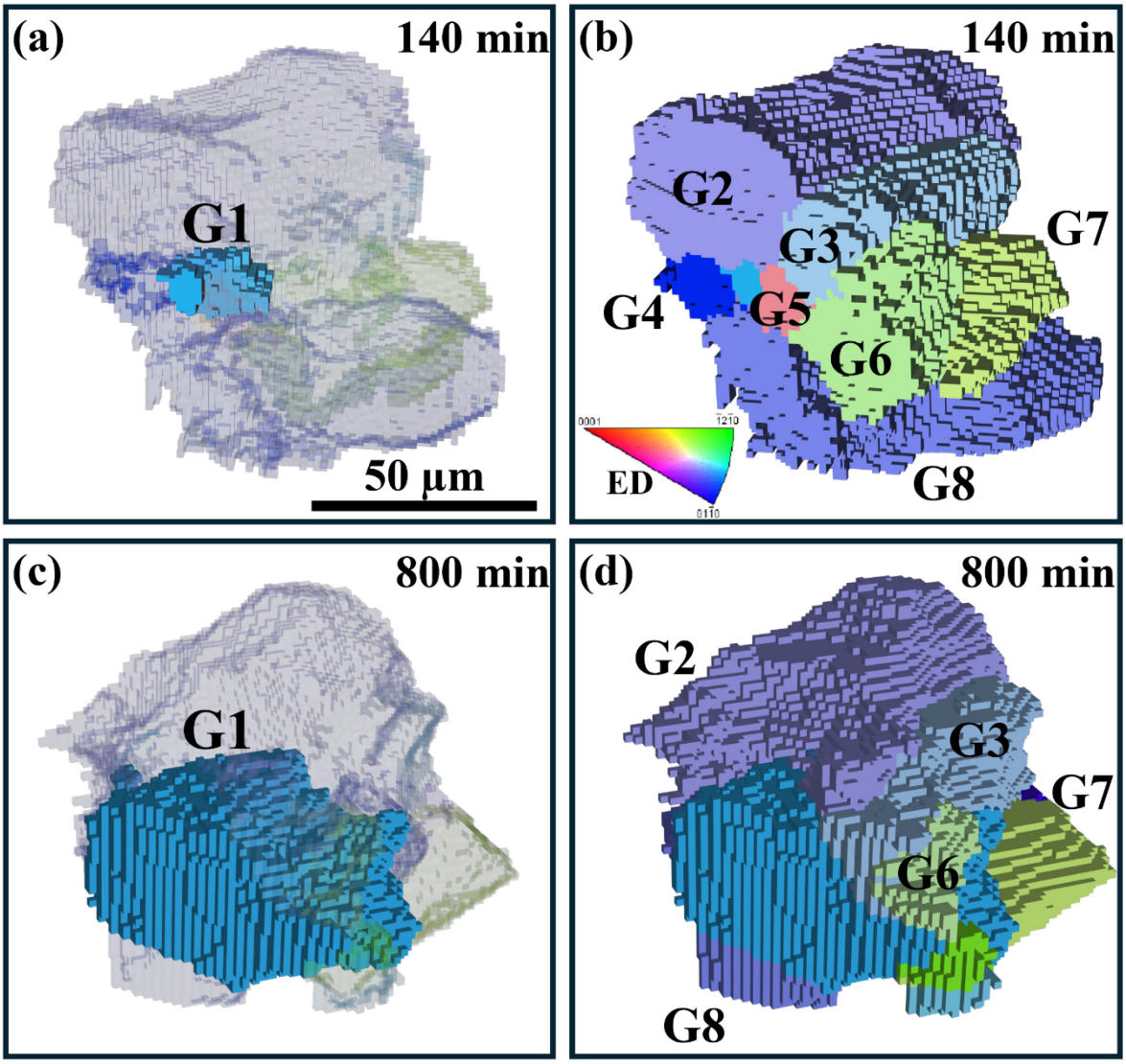

Figure 6.5 An example of AGG behaviour between (a)-(b) 140 minutes and (c)-(d) 800 minutes. One grain with large GR of 20.1 is extracted and highlighted as G1 in (a) 140 minutes and (c) 800 minutes, with transparent surrounding grains. Neighbouring grains G2-G8 are also tracked and annotated in (b) 140 minutes and (d) 800 minutes annealing step datasets. G1 had abnormally grown and consumed not only its small neighbours as G4 and G5 (entirely), but also its large neighbours as G2, G3, G6, G7 and G8 (partially). Similar AGG cases can be extracted using Track-4DGG within 10 minutes.

To facilitate grain-scale analysis and track growth behaviour efficiently, an in-house Track-4DGG toolbox based on our released Track-Rex has been developed to conduct grain tracking in 4D space [90,256]. The tracking procedure is initialized with a single, user-verified grain pair and proceeds iteratively and automatically. A schematic diagram of the algorithm is provided in Figure 6.6. Track-4DGG allows us to easily correlate consecutive datasets (i.e. Figure 6.2 (a)-(b)) within 5 minutes and track all six LabDCT datasets within 30 minutes, significantly reducing data processing time. Figure 6.7 demonstrates tracking results at both the individual grain and grain cluster scales. A relatively stable grain from the matrix centre was picked as a reference grain, as shown in Figure 6.7 (a1)–(a6). This grain grew from 88.7 to 117.5 μm and then shrunk to 111.6 μm, while its sphericity drops slightly at early stage and later rises to 0.50. More importantly, the evolution of other properties (e.g., shape factor, boundary curvature, boundary velocity, etc.) can also be extracted from the tracking results. Grain cluster tracking was performed for the neighbours of the reference grain, where their volume fraction increased from 1.0% to 1.8% by 800 minutes, followed by a modest reduction to 1.7%, as in Figure 6.7 (b1)–(b6).

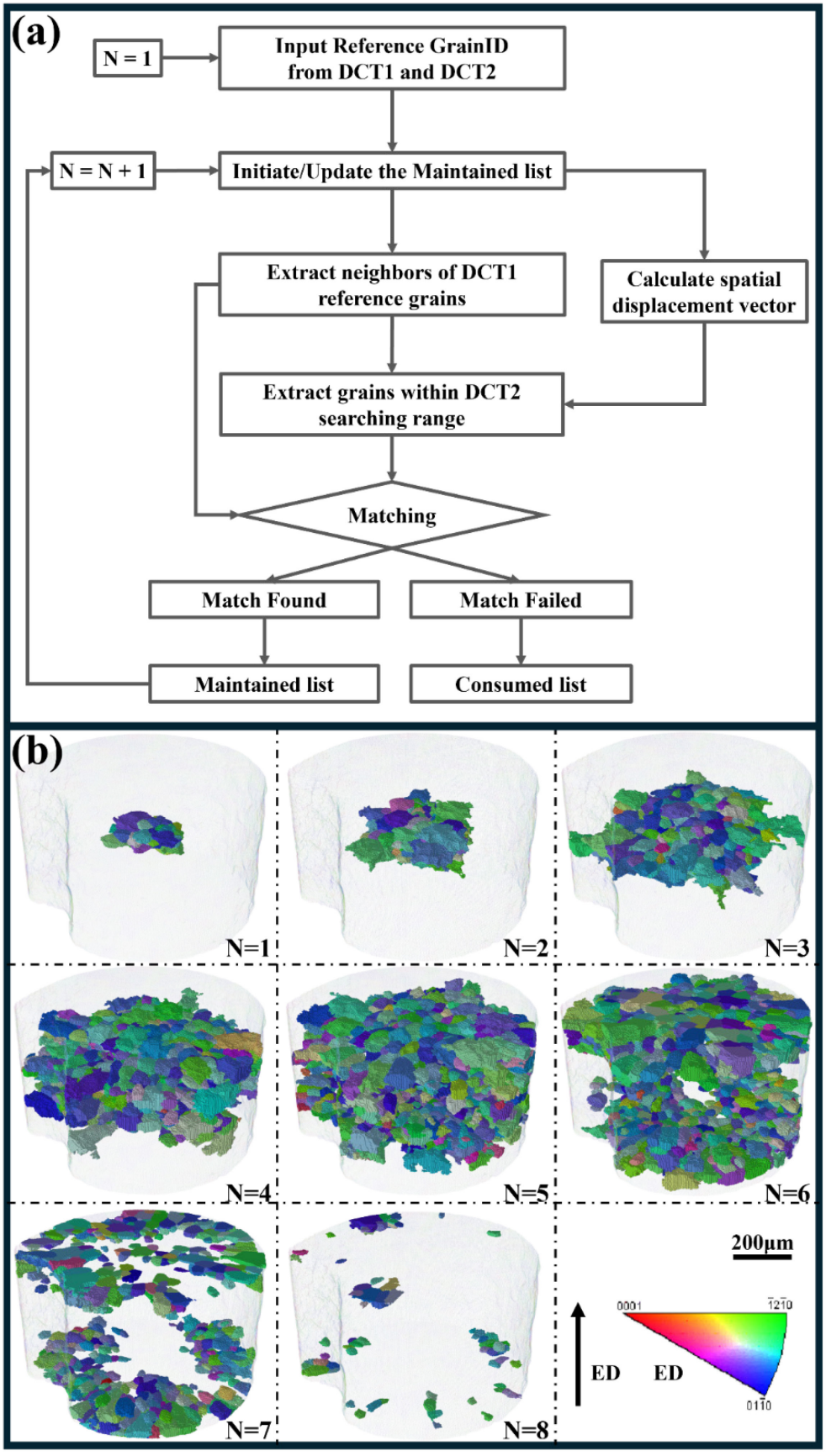
(a)
N = 1
Input Reference GrainID from DCT1 and DCT2
N = N + 1
Initiate/Update the Maintained list
Extract neighbors of DCT1 reference grains
Calculate spatial displacement vector
Extract grains within DCT2 searching range
Matching
Match Found
Match Failed
Maintained list
Consumed list
(b)
N=1
N=2
N=3
N=4
N=5
N=6
N=7
N=8
200μm
ED
ED
0001
$\bar{1}2\bar{1}0$
01$\bar{1}$0

Figure 6.6 Grains tracking mechanism of Track-4DGG. (a) Algorithm flowchart schematic: neighbours of the input reference grain pair at order N define the matching frontier, and a spatial vector computed from the matched grains centroids displacement will direct the searching window for order N+1. Candidate grains within the window are ranked by the difference including orientation, shape parameter and boundaries features. The most matched candidate that satisfies user defined threshold is paired, otherwise considered as consumed. (b) Tracking procedure between 12 minutes and 32 minutes annealing steps, represented by the grains calculated during each iteration in 12 minutes dataset.

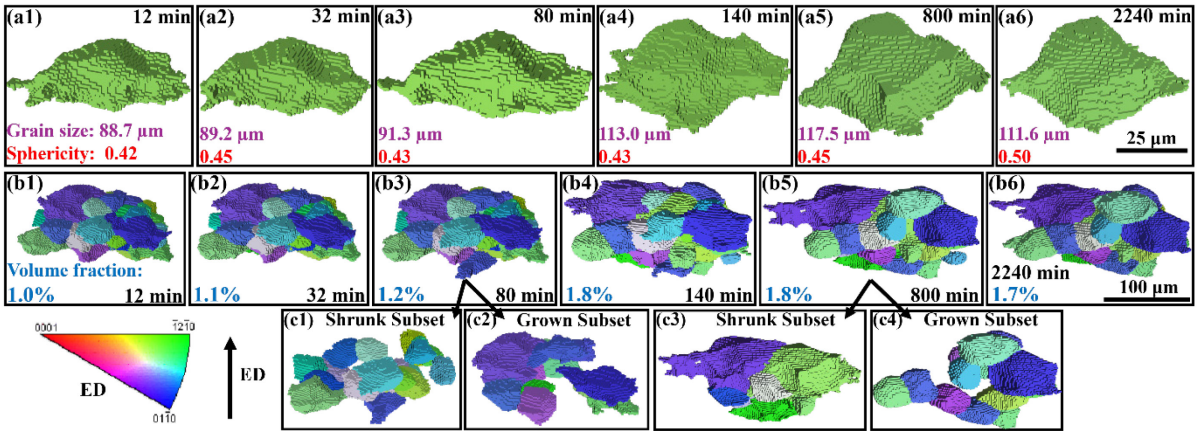

Figure 6.7 Representative 4D tracking of a single grain and its neighbour cluster: (a1)-(a6) individual grain tracking, (b1)-(b6) grain cluster tracking, (c1)-(c4) subsets of the grain clusters split by growth rate. The grain-growth classification is based on the Track-4DGG criteria described in Chapter 3. Grains were classified according to their tracked volume evolution between successive LabDCT datasets, while ambiguous or poorly reconstructed grains were treated conservatively.

To quantify the growth behaviour, growth rate (GR) was calculated using equation (4), Vt and Vt+1 are the grain volume at annealing step t and t+1, which can be obtained from the

tracking results. Therefore, the grains can be divided into shrunk grains (GR<0) and grown grains (GR>0). For example, the grain clusters in Figure 6.7 (b3) and (b5) are divided into shrunk subsets (Figure 6.7 (c1), (c3)) and grown subsets. 2 (c2), (c4)). Furthermore, grains with GRs that are five times greater than the mean positive GR of the grown subset are defined as AGG grains.

$$GR = \frac{V_{t+1} - V_t}{V_t} (6.4)$$

Hence, the AGG grains and their growth evolution from 80 to 140 minutes can be efficiently identified as presented in Figure 6.8, where abnormal grains grew from 27.6 to 82.2 μm, and the normal grains grew from 68.7 to 78.9 μm. Further to this step, the AGG events at other steps were summarised in Table. S1. The average GR for AGG was initially around 10.8 (12–32 minutes annealing) and increased to the peak value of 34.8 (80–140 minutes annealing) then decreased to 26.3 (800–2240 minutes annealing).

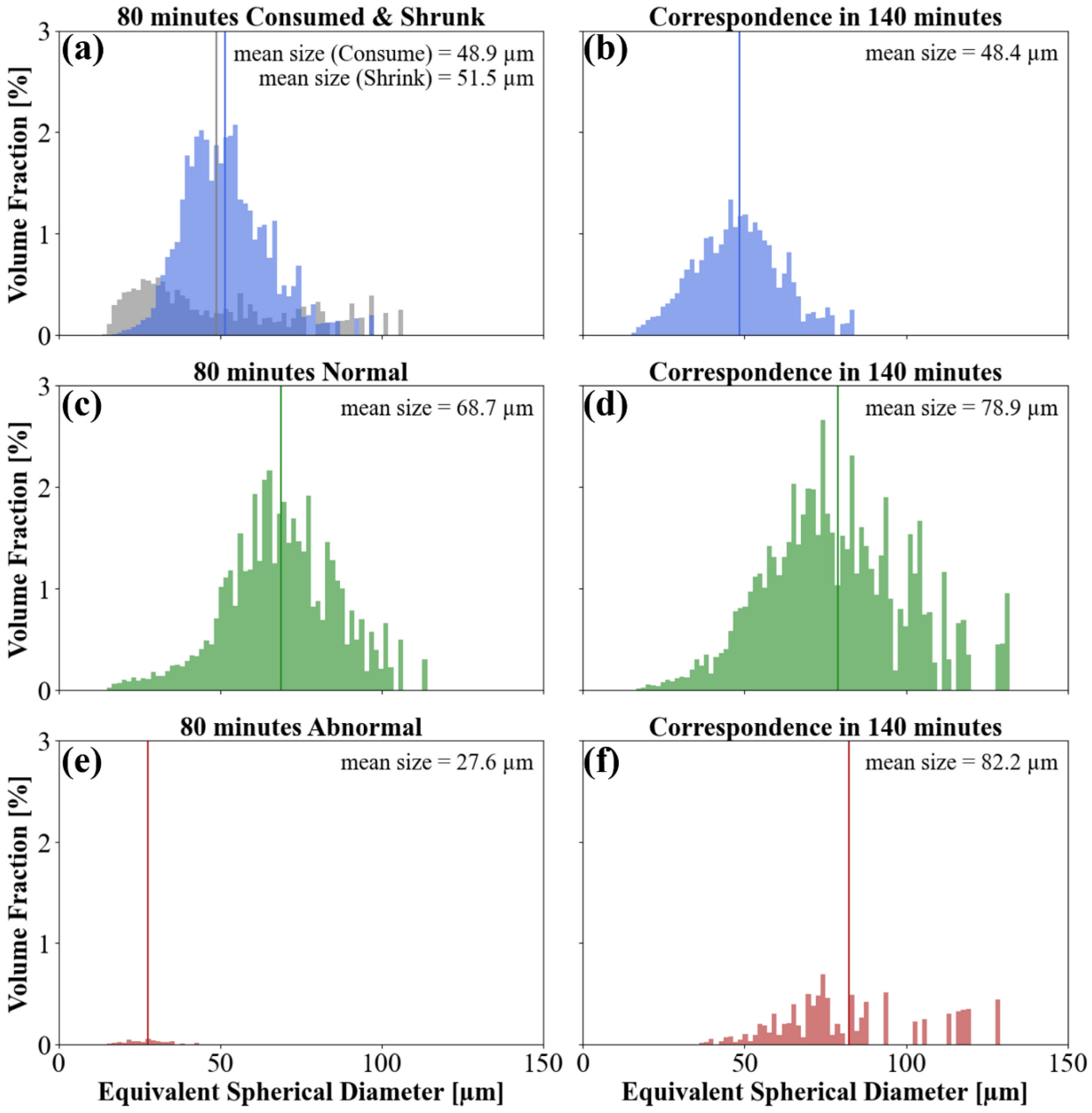

Figure 6.8 Grain size distribution of different grain growth behaviour subsets within 80 minutes annealing step and their correspondences grains in 140 minutes dataset. (a)-(b) Consumed and shrunk subset, (c)-(d) grains with normal growth rate, (e)-(f) grains with abnormal growth rate. Volumed-weighted average grains size DV is adopted to annotate the mean size of grains subsets.

Table 6.1 Summarised grain growth behaviour obtained from tracking results.

Time Step [minutes]	Total grain count	Consumed			Shrunk			Normal			Abnormal		
		Count	D_V	GR	Count	D_V	GR	Count	D_V	GR	Count	D_V	GR
12	6260	1517	49.3	NaN	2089	60.7	-0.2	2422	56.5	+0.2	232	23.7	+10.8
32	6562	2200	46.3	NaN	2168	59.2	-0.3	1979	58.6	+0.3	216	25.8	+15.7
80	5757	2298	48.9	NaN	2019	51.5	-0.4	1303	68.7	+0.9	137	27.6	+34.8
140	4523	2107	69.5	NaN	974	74.4	-0.3	1319	64.7	+0.8	124	28.1	+20.6
800	3517	1355	56.2	NaN	876	74.8	-0.3	1154	69.6	+0.4	133	34.7	+26.3
2240	2411	NaN	NaN	NaN	NaN	NaN	NaN	NaN	NaN	NaN	NaN	NaN	NaN

6.2.3 Spatially resolved grain growth behaviour

It has long been recognized that grain growth behaviour exhibits difference between surface and bulk volume. For example, thermal grooving [79,257] at the junction between grain boundaries and free surface exerts pinning effect for boundary migration due to the balance of surface tension. Hence, NGG at the sample surface is restricted, and sometimes AGG could be triggered by different thermal grooving depth at various grain boundaries with different neighbouring grain orientations. For instance, AGG is often observed in thin sheets materials [226,254,255]. For bulk materials, most of the grain growth studies focus on investigating sample surfaces (e.g., in-situ heating EBSD). However, it is challenging to make a solid conclusion whether the grain growth behaviour beneath the surface layer is similar to what is observed on the surface layer. To examine spatial variations in growth kinetic, the LabDCT data were partitioned into outer, middle, and inner sections comprising 35%, 30% and 35% of the total volume, respectively. Figure 6.9 shows the grain growth behaviour in the three sections between 80 and 140 minutes annealing, where peak AGG GR was found as demonstrated in Table S1. For visualization, grains are represented by their centroid positions and coloured by their growth rates (consumed grains (grey), shrunk grains (blue), grains with normal growth rate (green) and grains with abnormal growth rate (red)), as demonstrated in Figure 6.9(a-c). DV of the three sections is calculated to be 60.3, 58.6 and 56.3 μm, respectively.

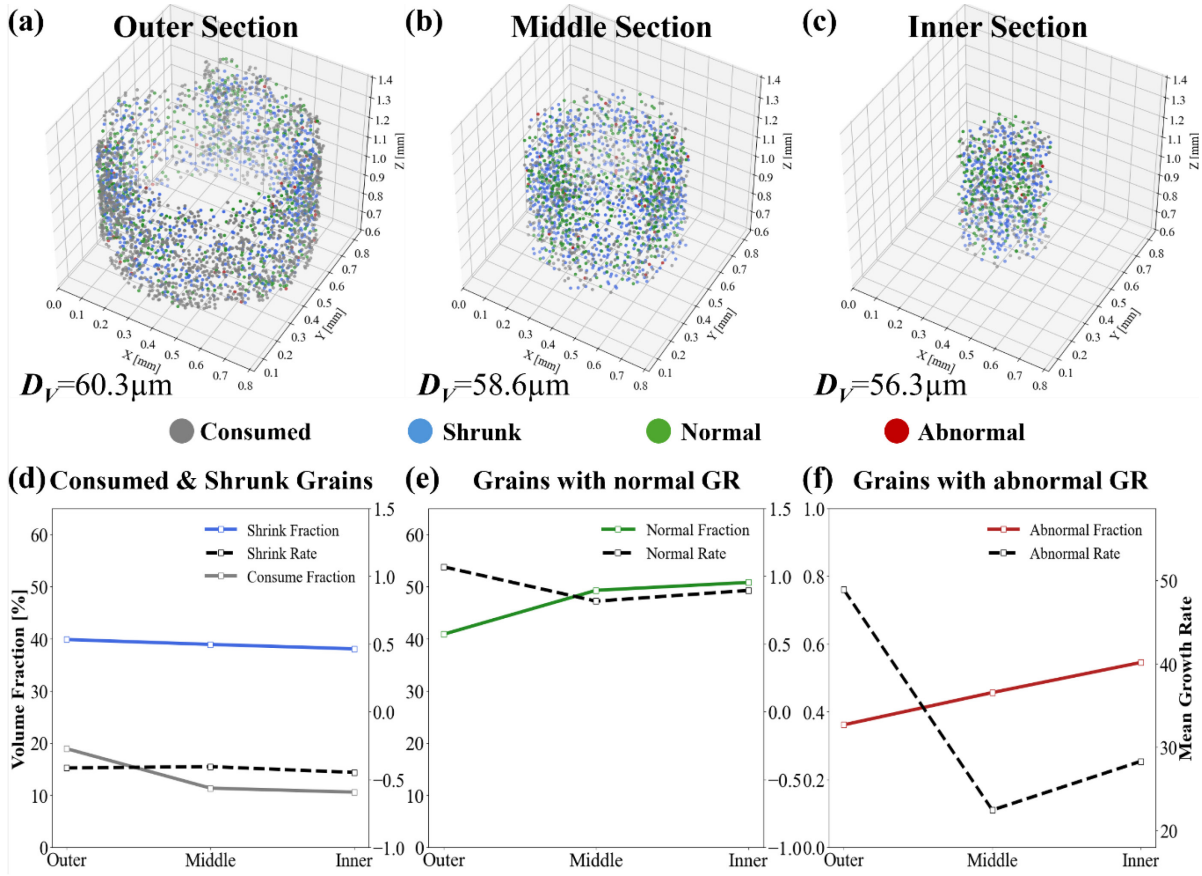

Figure 6.9 Spatially resolved grain growth behaviour during annealing from 80 to 140 minutes. Grains centroid spots in the 80 minutes annealing dataset coloured by their growth behaviour in the (a) outer, (b) middle and (c) inner sections. Volume fractions and growth rates in the spatial sections of (d) consumed and shrunk grains, (e) grains with normal GR and (f) grains with abnormal GR.

For the consumed and shrunk grains, negligible differences are found across three sections, as shown in Figure 6.9(d). For grains with normal GR (Figure 6.9(e)), the outer section contains a smaller fraction (40.9%) compared with the middle (49.3%) and inner (50.8%) section, consistent with the surface restriction of NGG. For grains with abnormal GR (Figure 6.9(f)), although AGG fraction increased slightly from 0.38% (outer) to 0.48% (middle)

and 0.54% (inner), considering the small size of AGG grains within the 80 minutes matrix (27.6 μm in Figure 6.8), it still indicates the middle and inner sections hold more AGG grains than the outer section. This does not conflict with the surface promotion of AGG, because a higher GR of 49 is observed for outer section, which is almost twice compared to middle and inner sections. Therefore, the sample surface primarily accelerates the growth kinetics of AGG events, rather than their occurrence.

A direct observation of grain evolution towards sample surface is presented in Figure 6.10 (a1-a6). The outermost two layers of surface grains at 12 minutes were tracked to 2240 minutes using Track-4DGG. Despite the average grain size increasing from 61 to 85 μm, the total volume fraction decreased from 20.3% to 9.1%. Therefore, ~55% of the original surface grains were consumed and replaced by inner grains growing outward. Grains smaller than 20 μm were treated as consumed, as their sizes were below the LabDCT indexing limit. Consumed grain subsets were extracted efficiently using Track-4DGG (Figure 6.10(b1-b5)). A rapid fraction decrease (7.6%) occurred from 12 to 32 minutes, where the consumed grains were small (DV=22 μm) and the surviving grains grew only 2 μm, as shown in Figure 6.10(b1). Subsequent step exhibited modest changes, consistent with the growth kinetic in Figure 6.2. During 80-140 minutes, a slight fraction decrease (1.7%) and increase of consumed grain size (25 to 35 μm) reflected enhanced abnormal growth. After 800 minutes annealing, the surviving fraction decreased to 7.2%, then slightly recovered to 9.1% after 2240 minutes annealing.

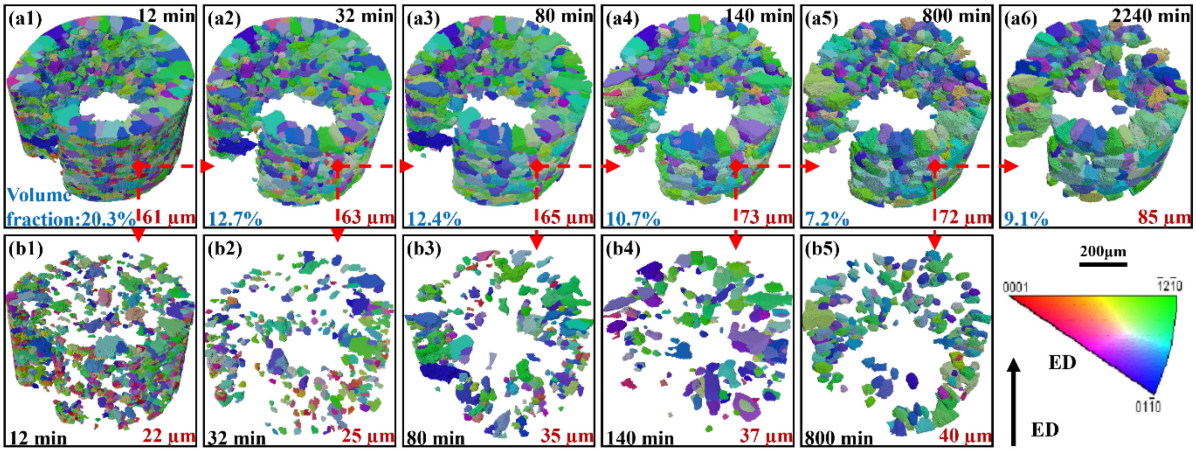

Figure 6.10 Grain-resolved tracking of the outermost two grain layers during the annealing series. (a1)-(a6): Evolution of the grain structure as well as grain size, from 12 to 2240 minutes. (b1)-(b5): The consumed grains subset for the surface grains at each annealing step.

Figure 6.11(a-f) presents one slice of the SEM/EBSD/EDS results of the sample after 2240 minutes annealing. Figure 6.11(a) is a typical SEM image obtained using a backscattered electrons detector. It clearly shows there is a second-phase particles-free band (SPFB) towards the surface layer. Combining the result of corresponding EDS and EBSD, the width of this SPFB is similar to the size of grains in the outmost layer. The solutes at the outer section were dragged to the sample surface and formed an oxide layer at this high annealing temperature of 490 °C, leaving the ring-like SPFB (especially Y shown in Figure 6.11 (e)). This phenomenon was also reported in copper containing various oxide dispersions during annealing [258]. The ACT results also clearly show the SPFB started to appear just after 140 minutes annealing (Figure 6.14). This indicates that the grain growth behaviours on and beneath the sample surface in some alloys (especially alloys with considerable amount of micro-sized second-phase particles and/or nano-sized precipitates) are different during annealing and should be investigated using non-destructive 3D instead of 2D imaging techniques.

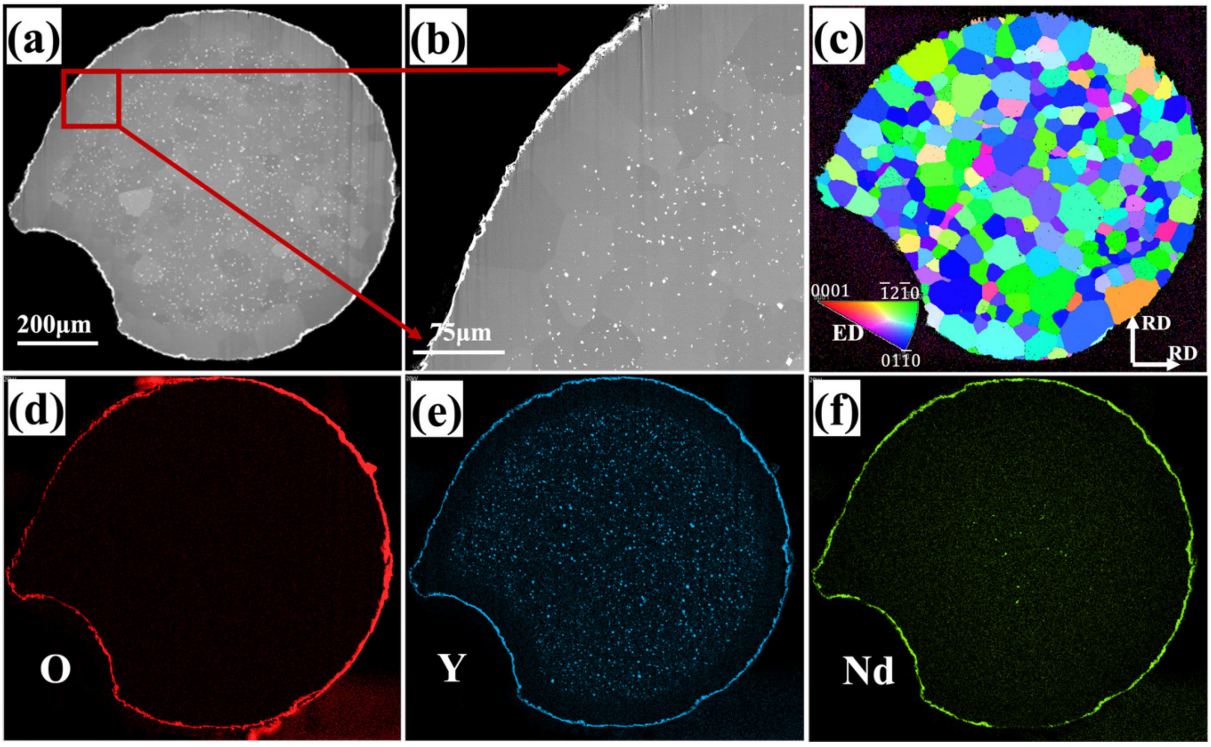

Figure 6.11 (a) BSE image and (b) zoomed in image near surface region, (c) EBSD IPF map, and EDS Map showing the element distributions of (d) Oxygen, (e) Yttrium and (f) Neodymium

6.3 Discussion

The above results provide a comprehensive picture of microstructural evolution during grain growth in a WE43 Mg alloy, and they highlight several key mechanisms and phenomena. In this discussion, we situate these findings in the context of existing knowledge on grain growth – particularly abnormal grain growth (AGG) – and emphasize the unique insights gained through our 4D LabDCT approach with Track-4DGG.

6.3.1 Microstructural evolution and abnormal grain growth

Consistent with classical theory, we observed that normal grain growth (NGG) involves a self-similar coarsening where all grains increase in size gradually. However, our experiment deviated from NGG behaviour at intermediate times by entering an AGG regime, wherein only a select few grains grew rapidly and consumed their neighbours. This led transiently to a bimodal grain size distribution (very large grains coexisting with much smaller ones), analogous to secondary recrystallisation phenomena. AGG has been widely reported in magnesium alloys and other metals, but its driving mechanisms can vary. In our WE43 alloy, the evidence points strongly to solute drag and particle pinning as the controlling factors for AGG. The rare-earth additions (Y, Nd) in WE43 produce solute atmospheres and precipitates that pin grain boundaries; AGG occurred when and where this pinning influence was locally reduced, allowing certain grains to break away and grow abnormally fast. This aligns with mechanism (ii) in the literature, which attributes AGG to the uneven overcoming of Zener drag: for example, Basu et al. found that in Mg-Gd, a few grains could overcome solute pinning at 450 °C and grow abnormally, whereas in a Mg-Dy alloy (with different pinning characteristics) AGG did not occur. Our results echo this behaviour – pinning inhibited most grains, but once a grain's boundary attained sufficient mobility (due to local precipitate dissolution or favourable orientation), it rapidly outstripped the others. Figure 6.12 shows the general grain growth behaviour from 80 minutes to 140 minutes of annealing, after tracking, the detailed grain growth behaviour as well as the growth rate can be summarised. The pronounced AGG behaviour is revealed by a sharp increase in volume fraction from 0.4% to 9.6%.

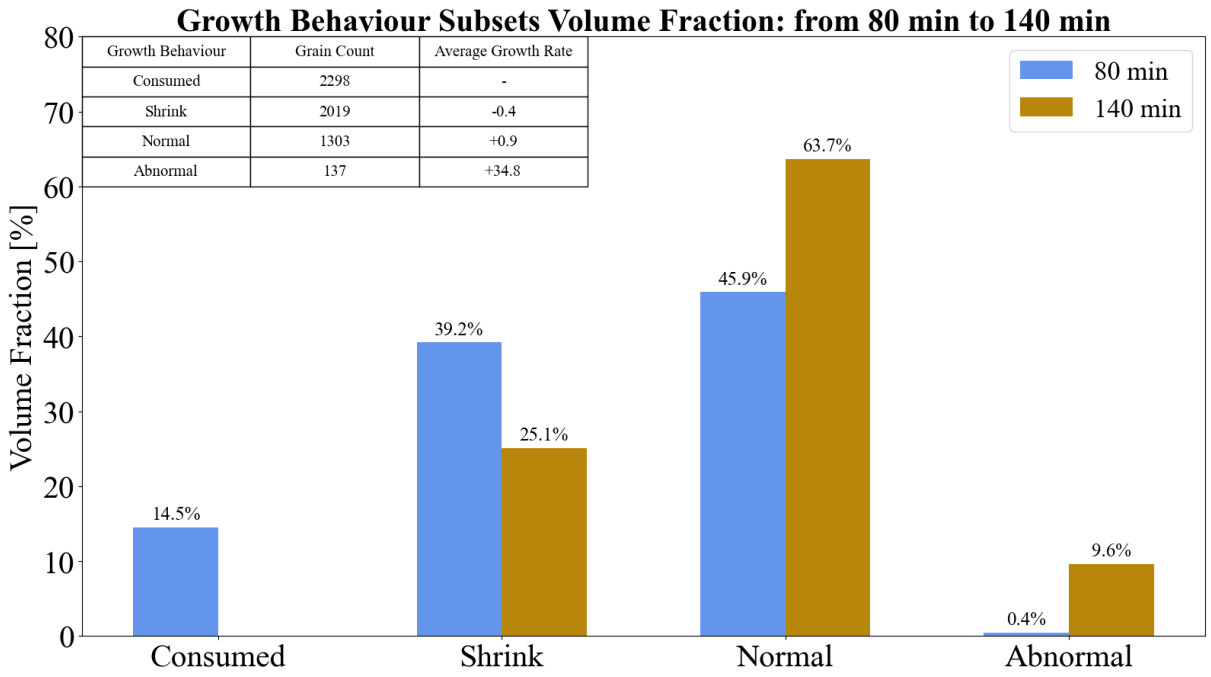

Figure 6.12 General growth behaviour from 80 minutes to 140 minutes

Other AGG mechanisms from literature, such as anisotropic grain boundary energy/mobility (favoring certain misorientation boundaries) or the presence of special low-energy boundaries, may also contribute to which grain wins the competition. For instance, we noted cases of relatively small grains becoming the abnormal growers, possibly due to possessing high-mobility boundaries (e.g. special coincidence boundaries or a favourable orientation relative to the surrounding texture). While our experiment did not focus on crystallographic texture changes, we did not observe the emergence of a strong new texture during grain growth, implying that oriented selective growth was muted under the 490 °C, precipitate-containing conditions (consistent with D. Guan et al.'s finding that precipitation during annealing suppresses orientation-driven growth). Had the alloy been annealed at higher temperature (above the solvus of the precipitates), we might expect orientation effects to play a larger role, as off-basal grains in Mg-RE alloys are known to grow faster once pinning is

removed. In our case, any orientation advantage was secondary to the pinning effects; abnormal grains did not share one specific orientation but rather were defined by their local environment (e.g. proximity to the surface or a particle-free zone). Figure 6.13 gives the relevance between grain size and their growth behaviour, by sectioning the volume fraction between different grain growth behaviour subset with in different grain size range.

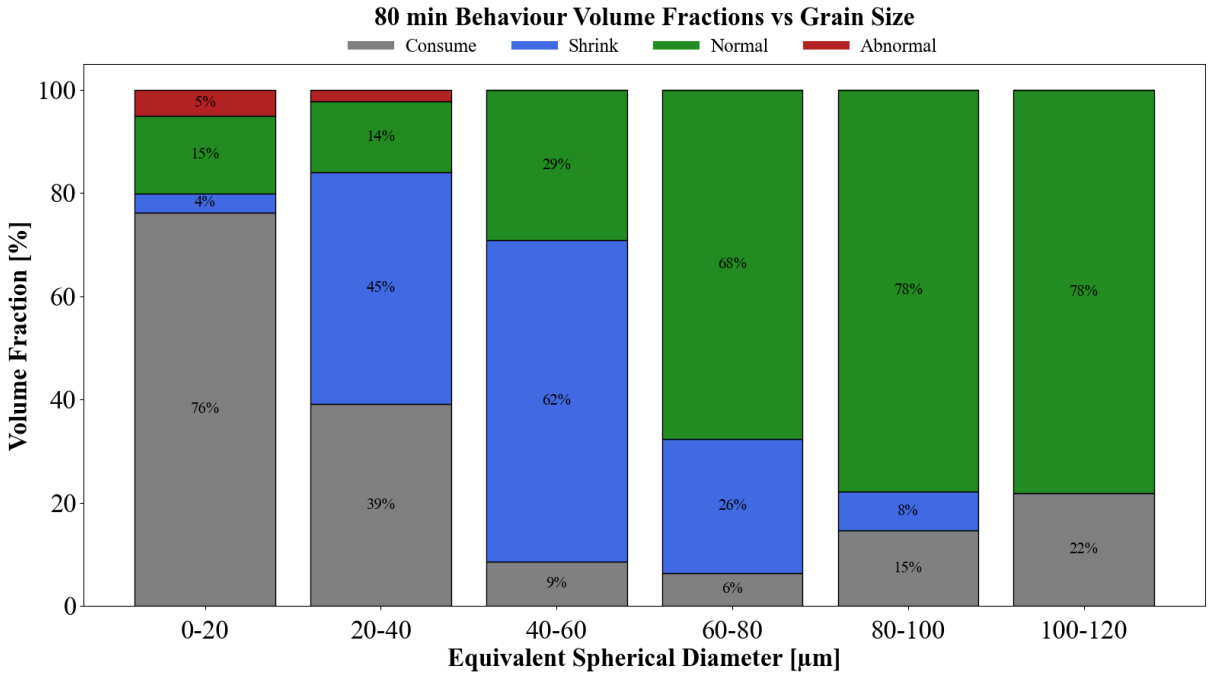

Figure 6.13 Grain growth behaviour versus grain size.

A particularly intriguing observation is the temporal sequence of growth behaviours in individual grains. By tracking grains through multiple annealing steps, we saw that a single grain could experience normal growth in one interval, abnormal growth in the next, and even shrinkage at a later time if it became surrounded by larger competitors. Such behaviour underscores the dynamic nature of grain growth – it is not a predetermined path for each grain, but rather a result of neighbourhood interactions and changing conditions. This dynamic was

suggested in prior simulations and 2D observations, but our 4D data directly capture it. It also resonates with the "solid-state wetting" concept (mechanism (iv)), where a grain boundary that suddenly finds a low-energy configuration can sweep through surrounding grains (analogous to wetting), although in Mg alloys the evidence for classical wetting is limited. In essence, our findings reinforce that AGG in Mg alloys is a multi-factor phenomenon: pinning provides the general constraint, and when that constraint locally vanishes, the intrinsic boundary characteristics (energy, mobility, curvature advantage) of that lucky grain determine how far it can go.

6.3.2 Spatial heterogeneity and surface restriction

One of the most significant outcomes of this work is the clear demonstration that grain growth in the bulk interior can be quite different from grain growth near a free surface. Traditionally, many grain growth studies in Mg (and other metals) relied on metallographic cross-sections or surface EBSD, implicitly assuming that the observed behaviour represents the whole sample. Our results call this assumption into question for alloys with heterogeneous pinning. We found that the sample surface region had its own microstructural evolution – formation of a precipitate-free zone and an associated spur of abnormal growth – that is not representative of the interior behaviour. Specifically, the surface suppresses continuous normal coarsening but accelerates intermittent abnormal growth. This confirms anecdotal evidence from thin-film or surface studies that AGG often initiates at surfaces. In fact, AGG is more frequently reported in thin samples or surface-heated specimens, partly because a free surface can reduce the constraints on boundary motion. Our 3D data show that in a bulk sample, those surface-driven AGG events coexist with a more normal growth interior. The interior, laden with precipitates, exhibited slower kinetics and a greater proportion of grains that were

consumed rather than dramatically growing. This dichotomy suggests that engineering the uniformity of second-phase distribution is critical: any gradient (for example, precipitate denudation at surfaces or along certain regions) can become a seedbed for AGG in those specific locales.

The discovery of the SPFB (second-phase-particles-free band) around the sample periphery is a novel insight into how thermal exposure can redistribute solute and particles. It appears analogous to the precipitate-free zones (PFZs) often observed along grain boundaries in age-hardenable alloys (where depletion of solute near boundaries occurs due to precipitate formation). In our case, however, the PFZ is at the free surface, likely caused by outward diffusion of Y and Nd to the surface (and their subsequent oxidation). A similar phenomenon was reported in Cu alloys containing oxide dispersions, where near-surface regions became denuded of oxides upon high-temperature annealing. The effect of the SPFB on grain growth was clearly deleterious to uniformity: once the pinning particles were removed, the local grain boundaries experienced a sudden increase in mobility. Consequently, grains at or near the surface either grew extremely quickly or were immediately consumed by those that did – a classic setup for abnormal growth. The formation of this precipitate-free surface layer thus essentially "triggers" AGG at the surface by providing an easy path for certain boundaries. In practice, this implies that high-temperature exposure of precipitate-strengthened alloys can lead to surface coarsening that outpaces interior coarsening, potentially affecting surface properties (like creep or fatigue, which are sensitive to grain size). It also highlights an often overlooked aspect of heat treatment: protecting or maintaining a uniform particle distribution even near free surfaces may be necessary to avoid abnormal grain growth from the outside in.

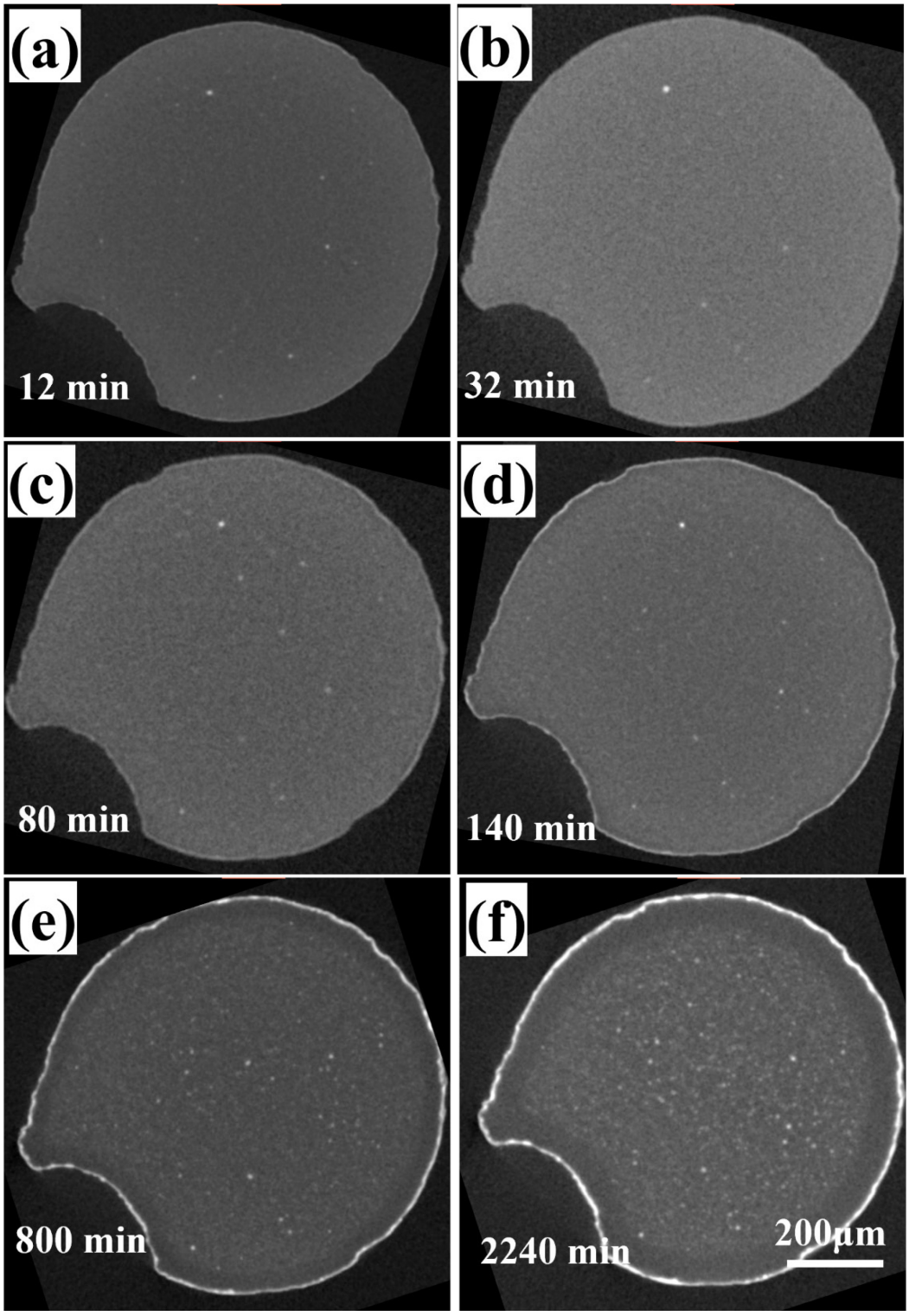

Figure 6.14 Absorption contrast tomography (ACT) images of the same slice from different annealing time steps. (a) 12, (b) 32, (c) 80, (d) 140, (e) 800, and (f) 2240 minutes.

6.4 Conclusion

Beyond the material-specific findings, this study demonstrates the power of combining laboratory X-ray diffraction contrast tomography (LabDCT) with automated 4D grain tracking (Track-4DGG) to investigate microstructural evolution. Previous 3D in-situ studies of grain growth were mostly limited to synchrotron X-ray techniques and often did not have the capability to track individual grains through multiple time steps. Here, using LabDCT – a lab-based system – we achieved time-resolved 3D mapping of thousands of grains, and with the Track-4DGG toolbox we correlated grain identities across six sequential states in an automated fashion. This allowed us to compile statistics on grain volumes, growth rates, and even neighbourhood changes that would be practically impossible to gather manually. The result is a grain-resolved, statistically significant analysis of grain growth kinetics in 4D. We directly captured phenomena like grain shrinkage and disappearance, which are usually inferred but not observed in cross-sectional studies. The ability to pinpoint, for example, that "55% of surface grains were consumed" or to define a quantitative threshold for AGG (grains growing five times faster than average) and see how many grains meet it at each time – these are unique benefits of the 4D approach.

Moreover, by segmenting the dataset into spatial regions (outer vs. inner), we quantified the concept of spatially heterogeneous grain growth. Traditional analyses might average these together and miss the divergence; our approach clearly separated them. This underscores that non-destructive 3D/4D imaging is crucial for capturing bulk material behaviour. Had we relied on 2D surface EBSD alone, we might have concluded that the alloy exhibits rampant AGG (seeing only the surface-consuming big grains). Conversely, a bulk metallography on a cross-section might have missed the surface effect or misinterpreted it. The take-home message for

methodology is that advanced characterisation tools like LabDCT, combined with intelligent analysis algorithms, open new avenues to study time-evolving phenomena in materials. As highlighted in a recent study by Zeng et al. [89] on recrystallisation tracking, grains can even shrink or reverse growth, and only by tracking the same grain can one uncover such behaviour. Our findings mirror that notion in the grain growth context – not all grains continuously grow; some are doomed to shrink from the start, being overtaken by others.

Comparison with Prior Work: The observed grain growth behaviour in WE43 can be compared with prior studies on Mg and other alloy systems. Pei et al. reported that in pure Mg, AGG occurred at a relatively low annealing temperature (220 °C) but not at higher temperatures like 350 °C. They hypothesized that a gradient in dislocation density (residual from incomplete recrystallisation) gave certain grains an early size advantage at 220 °C, while at 350 °C the faster kinetics led to uniform growth. In our alloy, the situation is different: the driving force from residual defects is likely smaller (due to the prior extrusion and recrystallisation), and instead the presence of precipitates governs AGG onset. Indeed, our AGG manifested at an intermediate temperature (490 °C) when pinning was partially active – an interesting contrast to pure Mg which showed AGG at low T but not high T. This suggests that in Mg alloys containing pinning particles, the worst-case scenario for AGG may be intermediate temperatures: low enough that precipitates/particles do not dissolve (maintaining drag), but high enough that some boundaries can surmount the drag. At much lower temperatures, grain boundaries are essentially locked (no growth at all), and at very high temperatures, all boundaries move (normal growth or texture-driven growth). Our findings fit this narrative – 490 °C is around the aging temperature where precipitates exist but can coarsen; accordingly we saw AGG. By 545 °C (as per Dikai Guan's study), those precipitates dissolve

and the growth mode shifts to orientation-driven without pronounced AGG in the classical sense (grains grow, but more uniformly, just with a texture change).

It's also instructive to compare with Al alloys or Fe alloys studied by 4D methods. For instance, 4D studies in pure iron showed normal grain growth with some grains temporarily stagnating or accelerating, but without second-phase particles the behaviour was largely curvature-driven. In WE43, the second-phase and solute effects introduce a significant deviation: growth exponents are higher and growth is more sporadic. The SPFB phenomenon is likely unique to alloys with substantial solute/particle content and might not appear in high-purity metals. Thus, our work expands the understanding of grain growth into the realm of complex, multi-component alloys. It demonstrates how coupling between microchemistry (precipitate distribution) and grain topology can lead to spatially non-uniform growth – an insight that could not be fully captured by older techniques. As a final point, the effective statistical approach enabled by Track-4DGG (correlating thousands of grains across time) provides confidence in these conclusions. We did not rely on a single anecdotal abnormal grain or a single surface observation; rather, we quantified the prevalence and rate of AGG events, the fraction of grains affected, and the time windows in which they occur. This comprehensive dataset lends weight to mechanisms that were previously speculative. For example, the notion that "surfaces promote AGG" is now supported by quantitative data on growth rates and consumed fractions. Likewise, the idea that "pinning can both delay growth and cause sudden AGG" is evident from the growth exponent analysis and mid-anneal divergence we recorded.

In summary, the discussion of our findings highlights that grain growth in a magnesium WE43 alloy is controlled by a synergy of pinning effects and local boundary conditions. The abnormal grain growth observed is a consequence of heterogeneous pinning – once a critical

threshold is crossed, a few grains explosively grow. The presence of a free surface exacerbates this heterogeneity, creating a precipitate-free zone that serves as a hotspot for AGG. These results bridge prior knowledge from 2D experiments and theoretical models, providing a 4D perspective that captures both spatial and temporal aspects of grain growth. Ultimately, the insights gained here – particularly regarding surface effects and the importance of maintaining uniform microchemistry to avoid abnormal growth – could inform better heat treatment strategies and alloy design to optimise grain structure in magnesium alloys. Moreover, the success of the 4D LabDCT + Track-4DGG approach lays the groundwork for applying similar analyses to other alloy systems, enabling deeper understanding of microstructural evolution that has until now been hidden from view. The ability to see and quantify every grain's journey through growth and coarsening is a significant step forward in materials informatics for microstructure optimisation.

This chapter completes the main experimental narrative of the thesis by extending grain tracking from two-dimensional recrystallisation datasets to three-dimensional grain growth datasets. The results demonstrate that grain growth in WE43 is not spatially uniform and cannot be fully represented by average grain size metrics alone. By tracking individual grains through the LabDCT volumes, the analysis reveals how shrinking, normal growth and abnormal growth coexist within the same specimen, and how these behaviours depend on spatial position. This chapter therefore provides the volumetric counterpart to the EBSD-based analyses in Chapters 4 and 5 and establishes the final dataset required for the integrated discussion in Chapter 7.

Chapter 7 Conclusive discussion and summary

This thesis has developed and applied grain-resolved tracking approaches to investigate annealing-driven microstructural evolution in magnesium alloys. Rather than treating recrystallisation and grain growth only through final-state microstructures or averaged descriptors, the work follows individual grains through time-resolved EBSD and LabDCT datasets. The central contribution is therefore an integrated experimental and data-processing framework that converts large microstructural image sequences into structured grain histories. These histories reveal when grains nucleate, whether they grow or shrink, how they are consumed, and how their behaviour contributes to the final texture and grain structure.

The thesis consists of three connected experimental studies. Chapter 4 establishes the use of Track-Rex for statistical recrystallisation tracking in AZ31 and ZE20. Chapter 5 narrows the analysis to shear-band-induced nucleation in ZE20 and shows that preferential nucleation does not necessarily guarantee a dominant contribution to the final recrystallised microstructure. Chapter 6 extends the tracking concept to 4D LabDCT data and demonstrates that grain growth in WE43 is spatially heterogeneous, with abnormal growth behaviour depending strongly on local position and microstructural environment. Taken together, these chapters show that grain-resolved tracking provides information that cannot be obtained from isolated EBSD maps, final-state microstructures or average grain size trends alone.

Three representative alloys were selected to span distinct microstructure-engineering strategies. AZ31 (Mg–Al–Zn) provides a conventional rare-earth-free baseline with strong basal textures; ZE20 (Mg–Zn–Ce) represents a lean rare-earth alloy where texture weakening is observed at very low RE content; and WE43 (Mg–Y–RE–Zr) exemplifies an RE-rich,

precipitation-strengthened alloy where solute and second-phase particles are expected to dominate grain-growth kinetics.

A principal enabling outcome is the development and application of automated tracking tools—Track-Rex for EBSD datasets (2D + time) and Track-4DGG for LabDCT datasets (3D + time)—which convert sequential microstructure maps into structured, grain-resolved histories. These histories make it possible to quantify nucleation, growth, shrinkage, and consumption events at scale, and to build analysis-ready datasets for subsequent statistical learning and predictive modelling.

The integrated message from these chapters is that microstructural evolution in Mg alloys should be understood as a population of competing grain histories. In recrystallisation, the key question is not only where new grains first form, but which of them survive and become significant components of the final microstructure. In grain growth, the key question is not only how the average grain size changes, but which individual grains grow abnormally, which grains are consumed, and where these events occur within the specimen. This thesis therefore shifts the analysis from static microstructural description to dynamic grain-resolved interpretation.

For clarity, the thesis-level conclusions can be summarised as follows:

(1) Recrystallisation in wrought Mg alloys proceeds continuously and competitively; recrystallised grains can shrink and be consumed, so early nucleation events do not necessarily dominate the final microstructure.

(2) In ZE20, the off-basal ("rare-earth") recrystallisation texture is largely independent of nucleation site and stage, indicating that oriented nucleation is central to the RE texture effect.

(3) Shear bands promote early nucleation in ZE20, but their contribution to the final recrystallised state is limited because many early shear-band nuclei are consumed; grain-boundary nucleation and subsequent growth competition provide a major contribution to the final texture.

(4) In AZ31, recrystallisation weakens the basal texture but does not fundamentally change it; preferential growth effects are weak compared with ZE20.

(5) Grain growth in WE43 is influenced by solute drag and particle/precipitate pinning, producing spatially heterogeneous growth and surface-sensitive abnormal grain growth under intermediate pinning conditions.

(6) Automated grain tracking (Track-Rex and Track-4DGG) provides an enabling materials-informatics pipeline that converts large microstructure datasets into reproducible, mechanism-relevant descriptors, supporting predictive modelling and, ultimately, data-driven optimisation of composition and processing.

This thesis has demonstrated that the combination of advanced microstructure characterisation with automated, grain-resolved tracking can expose mechanisms of recrystallisation and grain growth in Mg alloys that are not accessible through conventional, averaged descriptors. By moving from qualitative snapshots to quantitative grain histories, it

becomes possible to test long-standing assumptions (e.g., about the dominance of certain nucleation sites) and to identify the true drivers of texture evolution and microstructure stability.

The overarching message is that microstructure evolution is best understood as a competition process operating on heterogeneous grain populations, with outcomes determined by both crystallography (orientation-dependent nucleation/growth) and local boundary environments (pinning, solute drag, and surface effects). The experimental and informatics framework developed here offers a scalable route for turning modern microstructure datasets into predictive insight, and it provides the groundwork for the future-work directions outlined in Chapter 8.

7.1 Implications for magnesium alloy and process design

The grain-resolved observations presented in this thesis provide direct implications for magnesium alloy design and thermomechanical processing optimisation. The results show that final grain size and texture are not determined only by average grain size, nucleation density or final-state microstructure. Instead, they are controlled by the histories of individual grains, including where grains nucleate, whether they survive, how they grow, and how they interact with neighbouring grains during annealing.

For recrystallisation, Chapters 4 and 5 show that nucleation frequency alone is not sufficient to control the final recrystallised microstructure. Recrystallised grains in AZ31 and ZE20 can grow, shrink or be consumed during subsequent annealing. In ZE20, shear bands act as important early-stage nucleation sites, but many shear-band-nucleated grains are later consumed. This indicates that thermomechanical processing routes should be designed not only

to promote nucleation, but also to retain grains with favourable orientations. For texture weakening in Mg alloys, off-basal grains must both form and survive during growth competition.

For grain growth, Chapter 6 shows that average grain-size metrics can conceal important local behaviour. In WE43, shrinking, normally growing and abnormally growing grains coexist within the same specimen, and their behaviour depends on spatial position and local microstructural environment. Heat-treatment optimisation should therefore consider the distribution of grain-growth behaviour, surface-affected regions and local heterogeneity, rather than relying only on average grain size evolution.

Overall, this thesis suggests that magnesium alloy and process design should incorporate grain-level descriptors, including grain size, orientation, nucleation site, neighbouring environment, boundary character, spatial position and growth history. These descriptors provide a more direct link between processing, microstructural evolution and final properties. The grain-tracking framework developed here therefore provides a mechanistic basis for future thermomechanical processing optimisation and for data-driven prediction of recrystallisation and grain growth in magnesium alloys.

7.2 Positioning of this work within materials informatics

The work presented in this thesis should be viewed as an enabling step towards materials informatics for microstructural evolution, rather than as a complete predictive modelling or alloy optimisation framework. In the broader field of materials informatics, predictive models require reliable, structured and physically meaningful datasets. For recrystallisation and grain

growth, such datasets are difficult to generate because the relevant microstructural features evolve continuously in space and time, and because conventional post-mortem characterisation does not preserve the history of individual grains.

The central contribution of this thesis is to bridge this gap between time-resolved experimental characterisation and materials-informatics-ready datasets. In-situ and quasi-in-situ EBSD and LabDCT experiments can generate large datasets containing thousands of grains across multiple annealing steps. However, without tracking, the same grain may have different labels in different datasets, and its history cannot be directly reconstructed. The tracking workflows developed and applied in this thesis assign a unique identity to each grain and correlate this identity across successive experimental steps. As a result, each grain can be described not only by its state at a single time point, but also by its temporal evolution.

This grain-level linkage converts experimental image datasets into labelled microstructural datasets. For each tracked grain, descriptors such as size, orientation, position, neighbouring environment and growth behaviour can be connected with its earlier and later states. In the recrystallisation datasets, this allows grains to be labelled according to nucleation timing, survival, shrinkage, growth or consumption. In the grain growth dataset, it enables grains to be classified into shrinking, normally growing and abnormally growing populations, while retaining their spatial position and local microstructural context. The resulting data structure therefore provides a direct link between experimental observation and quantitative descriptors that can be used in future statistical or machine-learning models.

In this sense, the thesis contributes to materials informatics by making microstructural evolution traceable at the grain level. Rather than treating EBSD or LabDCT maps as

independent snapshots, the developed workflows establish continuity between successive states. This continuity makes it possible to ask data-driven questions that are otherwise difficult to address, such as which grains are likely to survive, which descriptors are associated with abnormal growth, and how local neighbourhoods influence subsequent microstructural evolution. The work therefore provides the labelled and physically interpretable datasets required for future predictive modelling of recrystallisation and grain growth.

Accordingly, the thesis does not claim to complete the full materials informatics loop from experimental data to autonomous alloy design. Instead, it establishes the experimental and computational foundation needed for such future work. By transforming large time-resolved microstructural datasets into structured grain histories, the thesis links advanced characterisation with materials informatics and creates a route towards future modelling, prediction and optimisation of magnesium alloy processing.

Chapter 8 Future work

The future work proposed in this chapter follows directly from the limitations and findings of the grain-resolved framework developed in this thesis. Chapters 4 and 5 showed that recrystallisation is controlled not only by nucleation site density, but also by the survival and consumption of individual grains during annealing. Chapter 6 showed that grain growth in WE43 is spatially heterogeneous and that abnormal grain growth can only be properly interpreted when grain histories are tracked in three dimensions. Future work should therefore focus on three linked directions: enriching the descriptors used to explain grain behaviour, validating the tracking results with complementary three-dimensional characterisation, and using the structured grain-history datasets as inputs for predictive modelling.

8.1 Grain boundary features and abnormal grain growth

The first future direction is to expand the descriptor space used to interpret grain survival and abnormal grain growth. The present thesis has demonstrated that grain histories can be extracted from both EBSD and LabDCT datasets, but the mechanistic interpretation of these histories still requires more complete information about grain boundary character. In particular, boundary area, misorientation, curvature, connectivity and local neighbourhood topology are expected to influence whether a grain shrinks, grows normally or undergoes abnormal growth. Future work should therefore combine Track-4DGG with a more detailed boundary-resolved analysis.

A major enabling development from this work is that Track-4DGG does not only correlate grains across time steps but also provides a route to extract evolving geometric and

crystallographic descriptors beyond grain volume/size, including boundary-related quantities such as boundary curvature and boundary velocity. This capability is already latent in the current tracking framework, where additional geometric quantities (e.g. shape factor, boundary curvature, boundary velocity) can be extracted once grain identities are linked across time. From a physical perspective, grain growth is classically described as a capillarity-driven phenomenon: grain boundaries migrate to reduce total interfacial energy, and the migration velocity is often written in the form

$$V = MP (8.1)$$

where V is the boundary normal velocity, M is a mobility, and P is the local driving pressure. In the simplest isotropic case, $P$is proportional to the product of boundary energy and curvature, so that boundary motion becomes curvature driven. This “curvature flow” picture is rooted in Mullins’ foundational treatment of grain-boundary motion. Grain boundary “character” is not fully specified by misorientation alone. In general, five macroscopic degrees of freedom are required: three to describe the lattice misorientation, and two to describe the boundary plane orientation. This is the basis of the five-parameter grain boundary character distribution (GBCD) framework. Consequently, a boundary with a given misorientation can still behave differently depending on its plane normal, and vice versa. Future work should therefore prioritise extracting not only misorientation distributions but also boundary plane and boundary area statistics, enabling the construction of boundary-population descriptors comparable to GBCD-style analyses. Figure 8.1 & 8.2 gives the preliminary observations of grain boundaries evolution during grain growth process.

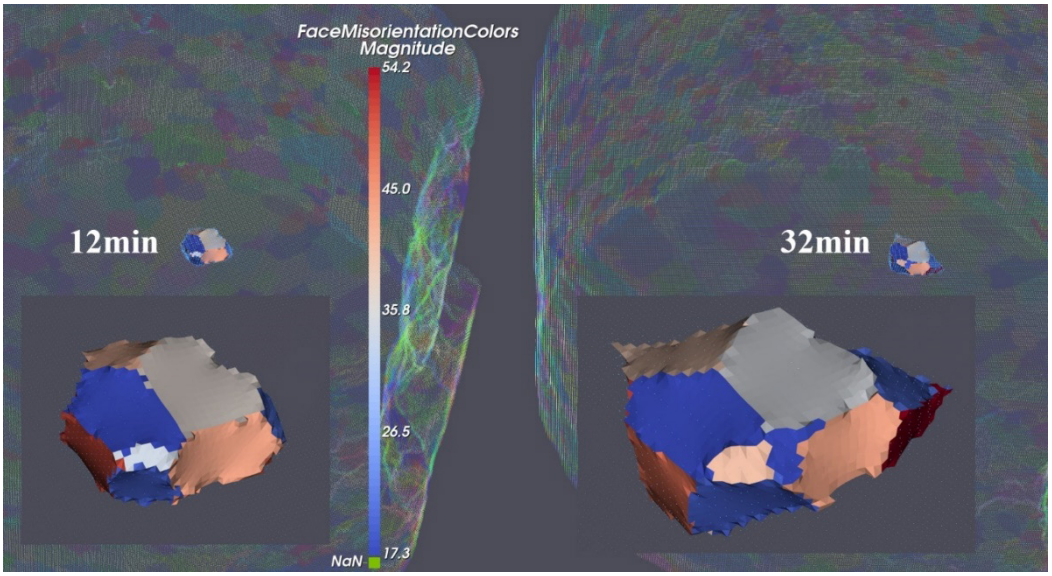

Figure 8.1 Examining grain boundaries evolution for the same grains from 12 minutes to 32 minutes.

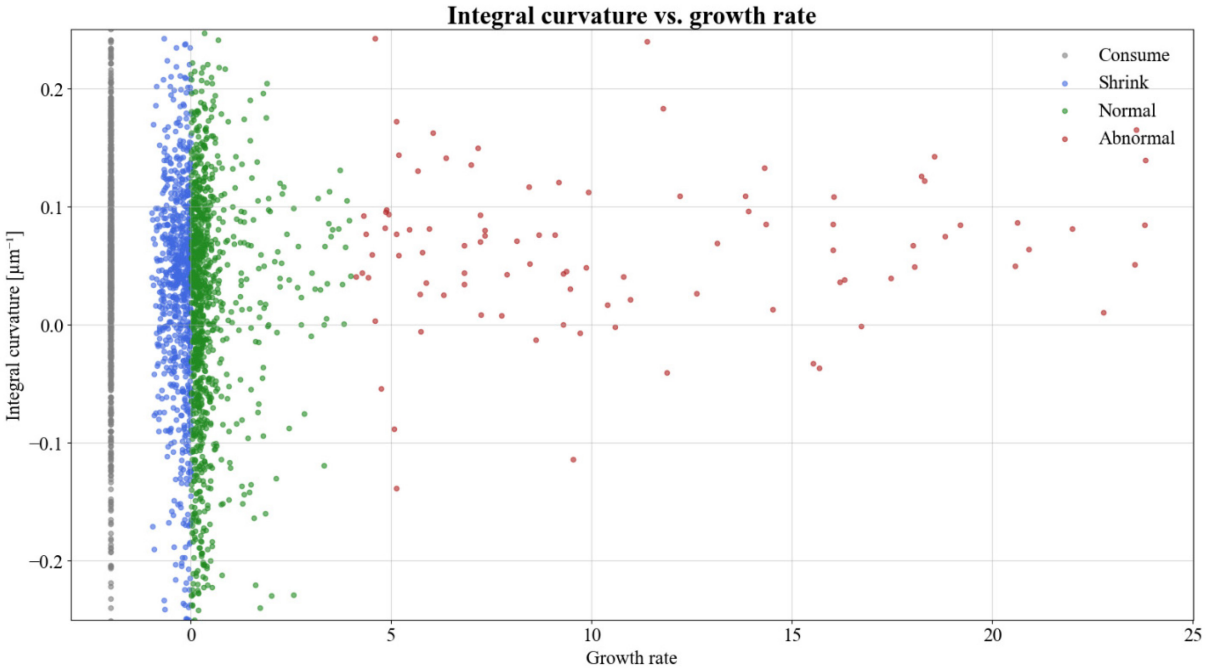

Figure 8.2 Preliminary results for the calculated integral curvature versus growth behaviour

8.2 Comparison between LabDCT and 3D-EBSD

The second future direction is to further validate the LabDCT-based tracking results using complementary high-resolution three-dimensional characterisation. LabDCT enables non-destructive tracking of large volumes over multiple annealing steps, but its spatial resolution and completeness limit the detection of small grains and fine boundary features. Three-dimensional EBSD, although destructive and more time-consuming, can provide higher spatial resolution and more accurate boundary morphology. A combined LabDCT and 3D-EBSD workflow would therefore allow the large-volume statistical advantage of LabDCT to be linked with the boundary-level accuracy of 3D-EBSD.

Future work will include a systematic comparison between Lab-based Diffraction Contrast Tomography (LabDCT) and a serial sectioning three-dimensional Electron Backscatter Diffraction (3D EBSD) for characterising grain structure and evolution. The thickness of each EBSD sectioning is 1 μm reduced by laser-FIB and a total number of 500 EBSD layers has been collected. By applying both techniques to the same material states and, where possible, overlapping volumes, their respective capabilities in resolving grain morphology, orientation accuracy, boundary characterisation and small-grain detection will be quantitatively assessed. Particular attention will be paid to differences arising from spatial resolution, sampling volume, and detection limits, as well as their influence on measured grain growth kinetics and statistical descriptors. Figure 8.3 shows a comparison of the long axis cross-section of the WE43 sample by 3D EBSD and LabDCT.

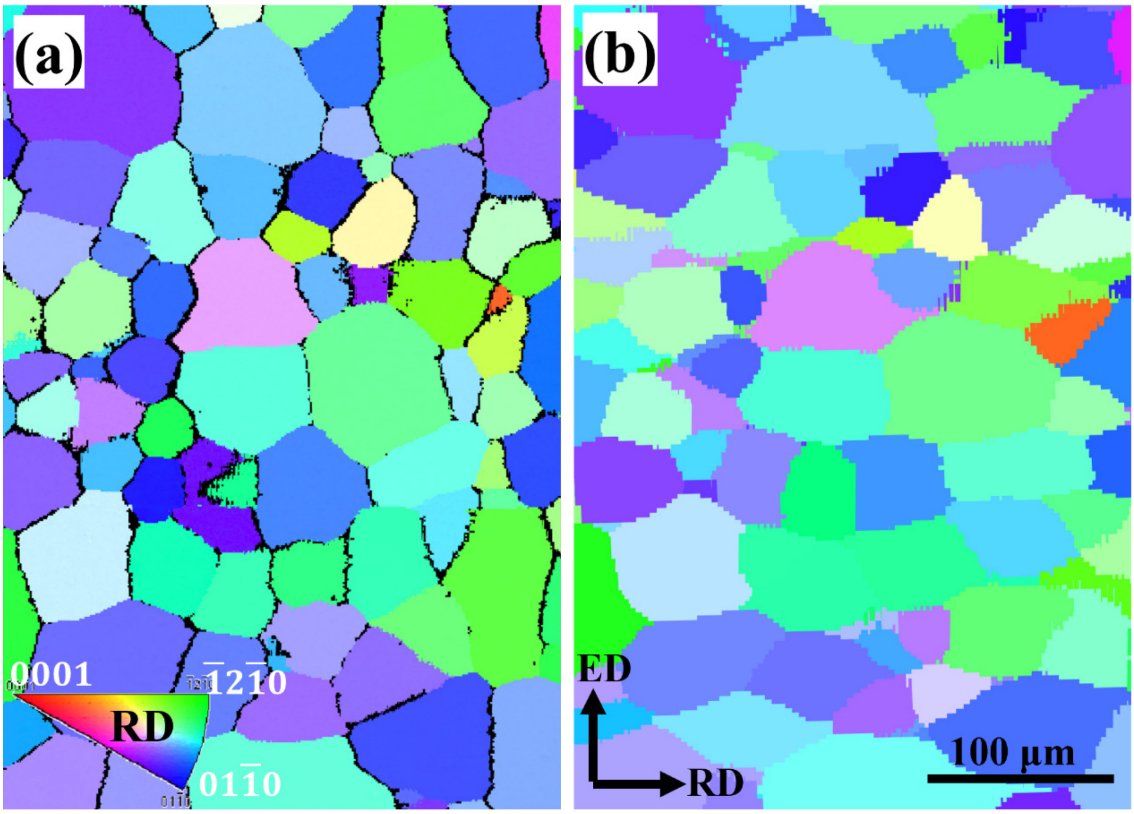

Figure 8.3 A slice of the EBSD IPF map from the sample after 2240 annealing, (b) a corresponding slice from the reconstructed LabDCT dataset located in a closely adjacent region after extensive data comparison and alignment.

8.3 Prediction model of recrystallisation and grain growth

The third future direction is to transform the tracked grain histories generated in this thesis into predictive datasets. Each tracked grain contains an initial state, a local microstructural environment and a later outcome, such as growth, shrinkage or consumption. This structure is well suited to supervised learning, where the input descriptors may include grain size, orientation, neighbourhood misorientation, boundary curvature and spatial position, while the output labels describe the subsequent grain behaviour. Such models would not

replace physical interpretation, but could identify the most important descriptors controlling recrystallisation and grain growth, thereby supporting future alloy and process optimisation.

The key advantage of the present workflow is that it yields supervised labels and consistent temporal continuity at grain scale, rather than isolated snapshots. In practical terms, Track-Rex and Track-4DGG convert sequential maps into analysis-ready grain histories (including survival/consumption and neighbourhood context), enabling the construction of learning targets such as the AGG occurance. This thesis has already demonstrated proof-of-concept prediction capability using deep learning models trained on these tracked datasets. Figure 8.4 gives the training record of a neural network model for predicting AGG occurrence, however the initial accuracy was around 54%.

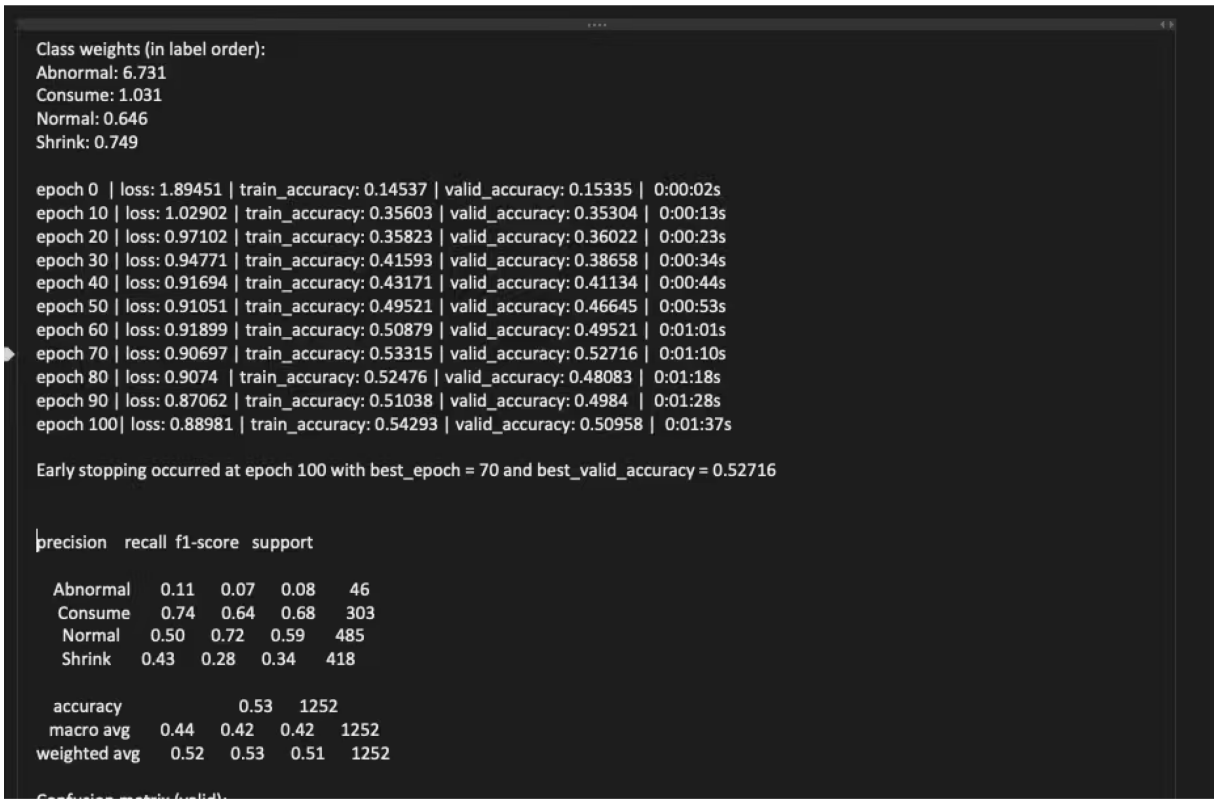

Figure 8.4 Training process for the prediction model of AGG occurrence.

8.4 Track toolbox family

The final future direction is to extend the tracking strategy developed here into a broader family of microstructure-evolution toolboxes. Track-Rex and Track-4DGG were developed for recrystallisation and grain growth, respectively, but the same conceptual framework can be adapted to other processes where individual microstructural features evolve through time. Potential examples include deformation tracking, twin evolution, phase transformation and precipitation-related microstructural change. Expanding the toolbox family would strengthen the connection between time-resolved characterisation and materials informatics by providing structured, labelled datasets across multiple microstructural phenomena.

Track-Rex and Track-4DGG demonstrate that the main bottleneck in extracting knowledge from modern microstructure datasets is often not the measurement itself, but the conversion of sequential maps into consistent identity-linked histories. This is especially relevant because 3D/4D characterisation methods are becoming more widely available and are now capable of producing large, time-resolved datasets at the grain scale. For example, laboratory diffraction contrast tomography (LabDCT) has been developed as a laboratory-based route to non-destructive 3D grain mapping, and multiple studies have established reconstruction workflows and implementation strategies for LabDCT-based grain mapping. More broadly, the “four-dimensional materials science” community has highlighted rapid growth in time-resolved X-ray microscopy and diffraction-based methods, which increasingly generate datasets that are too large and complex for manual analysis.

Overall, future work should move from tracking grain histories to explaining and predicting them. The present thesis establishes the experimental and computational foundation

for this progression by demonstrating that individual grain trajectories can be extracted from large 2D and 3D time-resolved datasets. The next step is to enrich these trajectories with boundary-level descriptors, validate them across complementary characterisation methods and use them to train physically informed predictive models. In this way, the grain-resolved framework developed in this thesis can evolve into a more complete materials-informatics route for magnesium alloy and process design.

Appendix A [list of publications and attended conferences]

List of publications:

[1]. Zeng X, **Yi H**, Zeng Z, et al. Track-Rex: A universal toolbox for tracking recrystallization nucleation and grain growth behaviors in polycrystalline materials[J]. Journal of Materials Science & Technology, 2024, 197: 149-159.

[2]. **Yi H**, Li H, Zeng X, et al. Investigation of shear bands induced nucleation and recrystallisation behaviour in a rare earth containing magnesium alloy[J]. Materials Characterization, 2025, 222: 114809.

[3]. **Yi H**, Zeng X, Guan D. Data Science Approach for EBSD Data Processing and Materials Design for Magnesium Alloy[C]//TMS Annual Meeting & Exhibition. Cham: Springer Nature Switzerland, 2024: 49-53.

[4]. **Yi H**, Douglas G, Oddershede J, Donoghue J, Liu H, Chen B, Guan D. 4D grain growth evolution and statistical tracking in a magnesium alloy using lab-based diffraction contrast tomography (LabDCT), submitted to Scripta Materialia, now under revision.

List of attended conferences

1. The UK Solidification Workshop 2022, Uxbridge, United Kingdom, 2022
2. The Minerals, Metals & Materials Society 2024 Annual Meeting & Exhibition, Orlando, Florida USA, 2024 **(Oral presentation)**
3. The 8th International Conference on Magnesium & the 13th International Conference on Magnesium Alloys and their Applications, Chongqing, China, 2024 **(Oral presentation)**
4. Royal Microscopical Society EBSD 2025, Glasgow, United Kingdom, 2025 **(Oral presentation)**

List of References

[1] V. Londono, S. Deloach-Overton, Magnesium in Second Quarter 2025, (n.d.). https://www.usgs.gov/centers/national-minerals- (accessed January 12, 2026).

[2] Magnesium processing | Techniques & Methods | Britannica, (n.d.). https://www.britannica.com/technology/magnesium-processing (accessed January 12, 2026).

[3] J. Tan, S. Ramakrishna, Applications of magnesium and its alloys: A review, Applied Sciences (Switzerland) 11 (2021). https://doi.org/10.3390/APP11156861.

[4] A.A. Luo, Magnesium casting technology for structural applications, Journal of Magnesium and Alloys 1 (2013) 2–22. https://doi.org/10.1016/J.JMA.2013.02.002.

[5] L. Karabin, W. Hunt, Die Cast Magnesium in Automotive Applications, (n.d.). www.materialstechnology.org (accessed January 12, 2026).

[6] Recycling Magnesium Alloy Housings for Notebook Computers, (n.d.).

[7] V. Tsakiris, C. Tardei, F.M. Clicinschi, Biodegradable Mg alloys for orthopedic implants – A review, Journal of Magnesium and Alloys 9 (2021) 1884–1905. https://doi.org/10.1016/J.JMA.2021.06.024.

[8] Y. Chen, Z. Xu, C. Smith, J. Sankar, Recent advances on the development of magnesium alloys for biodegradable implants, Acta Biomater. 10 (2014) 4561–4573. https://doi.org/10.1016/J.ACTBIO.2014.07.005.

[9] Z. Tang, H. Huang, J. Niu, L. Zhang, H. Zhang, J. Pei, J. Tan, G. Yuan, Design and characterizations of novel biodegradable Zn-Cu-Mg alloys for potential biodegradable implants, Mater. Des. 117 (2017) 84–94. https://doi.org/10.1016/J.MATDES.2016.12.075.

[10] W. Yi Wang, J. Li, W. Liu, Z.K. Liu, Integrated computational materials engineering for advanced materials: A brief review, Comput. Mater. Sci. 158 (2019) 42–48. https://doi.org/10.1016/J.COMMATSCI.2018.11.001.

[11] A. Atrens, Z. Shi, S.U. Mehreen, S. Johnston, G.L. Song, X. Chen, F. Pan, Review of Mg alloy corrosion rates, Journal of Magnesium and Alloys 8 (2020) 989–998. https://doi.org/10.1016/J.JMA.2020.08.002.

[12] X.N. Gu, Y.F. Zheng, A review on magnesium alloys as biodegradable materials, Frontiers of Materials Science in China 2010 4:2 4 (2010) 111–115. https://doi.org/10.1007/S11706-010-0024-1.

[13] M. Bamberger, G. Dehm, Trends in the development of new Mg alloys, Annu. Rev. Mater. Res. 38 (2008) 505–533. https://doi.org/10.1146/ANNUREV.MATSCI.020408.133717/CITE/REFWORKS.

[14] M. Ghorbani, M. Boley, P.N.H. Nakashima, N. Birbilis, A machine learning approach for accelerated design of magnesium alloys. Part A: Alloy data and property space, Journal of Magnesium and Alloys 11 (2023) 3620–3633. https://doi.org/10.1016/J.JMA.2023.09.035.

[15] I. Basu, T. Al-Samman, Triggering rare earth texture modification in magnesium alloys by addition of zinc and zirconium, Acta Mater. 67 (2014) 116–133. https://doi.org/10.1016/J.ACTAMAT.2013.12.015.

[16] P. Li, G. Gao, Y. Wang, Y. Ma, Crystal Structures and Exotic Behavior of Magnesium under Pressure, Journal of Physical Chemistry C 114 (2010) 21745–21749. https://doi.org/10.1021/JP108136R.

[17] Y.M. Zhang, S. Yang, J.R.G. Evans, Revisiting Hume-Rothery's Rules with artificial neural networks, Acta Mater. 56 (2008) 1094–1105. https://doi.org/10.1016/J.ACTAMAT.2007.10.059.

[18] A. Martin, M. Thuo, Beyond Hume-Rothery Rules, Acc. Mater. Res. 4 (2023) 809–813. https://doi.org/10.1021/ACCOUNTSMR.3C00126.

[19] F.C. Frank, On Miller–Bravais indices and four-dimensional vectors, Urn:Issn:0365-110X 18 (1965) 862–866. https://doi.org/10.1107/S0365110X65002116.

[20] L. Tian, L. Wang, H. Wu, H. Wang, L. Zheng, K.S. Shin, Recent research advances in Mg single crystal based on the crystal orientations： A review, Journal of Materials Research and Technology 27 (2023) 5572–5593. https://doi.org/10.1016/J.JMRT.2023.10.273.

[21] W. Abuzaid, H. Sehitoglu, Critical resolved shear stress for slip and twin nucleation in single crystalline FeNiCoCrMn high entropy alloy, Mater. Charact. 129 (2017) 288–299. https://doi.org/10.1016/J.MATCHAR.2017.05.014.

[22] A. Kedharnath, R. Kapoor, A. Sarkar, Classical molecular dynamics simulations of the deformation of metals under uniaxial monotonic loading: A review, Comput. Struct. 254 (2021). https://doi.org/10.1016/j.compstruc.2021.106614.

[23] M. Lentz, M. Risse, N. Schaefer, W. Reimers, I.J. Beyerlein, Strength and ductility with {10 11}-{1012} double twinning in a magnesium alloy, Nat. Commun. 7 (2016). https://doi.org/10.1038/NCOMMS11068.

[24] Y. Yu, Y. Wei, Y. Song, H. Shou, L. He, Mechanisms of temperature effects on the tensile properties and dislocation behavior of Mg-Zn-Ca alloys, Sci. Rep. 15 (2025). https://doi.org/10.1038/S41598-025-01805-6.

[25] I.J.. Polmear, David. StJohn, J.-Feng. Nie, Ma. Qian, Light alloys : metallurgy of the light metals, Butterworth-Heinemann, 2017.

[26] K. Fukuda, Y. Koyanagi, M. Tsushida, H. Kitahara, T. Mayama, S. Ando, Activation stress for slip systems of pure magnesium single crystals in pure shear test, Mater. Trans. 58 (2017) 587–591. https://doi.org/10.2320/matertrans.M2016402.

[27] H.Q. Ang, Anelastic behaviour of commercial die-cast magnesium alloys: Effect of temperature and alloy composition, Materials 14 (2021). https://doi.org/10.3390/MA14237220.

[28] M. Yu, Y. Cui, J. Wang, Y. Chen, Z. Ding, T. Ying, J. Llorca, X. Zeng, Critical resolved shear stresses for slip and twinning in Mg-Y-Ca alloys and their effect on the ductility, n.d.

[29] J. Wang, Y. Chen, Z. Chen, J. Llorca, X. Zeng, Deformation mechanisms of Mg-Ca-Zn alloys studied by means of micropillar compression tests, n.d.

[30] L. Wang, Z. Huang, H. Wang, A. Maldar, S. Yi, J.S. Park, P. Kenesei, E. Lilleodden, X. Zeng, Study of slip activity in a Mg-Y alloy by in situ high energy X-ray diffraction microscopy and elastic viscoplastic self-consistent modeling, Acta Mater. 155 (2018) 138–152. https://doi.org/10.1016/j.actamat.2018.05.065.

[31] H. Somekawa, R. Ueji, A. Singh, Mechanical response in tension of twin-induced Mg alloys in wide strain rate regimes, Materials Science and Engineering: A 897 (2024). https://doi.org/10.1016/j.msea.2024.146319.

[32] P.D. Barsanescu, A.M. Comanici, von Mises hypothesis revised, Acta Mech. 228 (2017) 433–446. https://doi.org/10.1007/s00707-016-1706-2.

[33] Q. Yu, L. Qi, R.K. Mishra, J. Li, A.M. Minor, Reducing deformation anisotropy to achieve ultrahigh strength and ductility in Mg at the nanoscale, Proc. Natl. Acad. Sci. U. S. A. 110 (2013) 13289–13293. https://doi.org/10.1073/PNAS.1306371110.

[34] A. Rollett, F. Humphreys, G.S. Rohrer, M. Hatherly, Recrystallization and Related Annealing Phenomena: Second Edition, Recrystallization and Related Annealing Phenomena: Second Edition (2004) 1–628. https://doi.org/10.1016/B978-0-08-044164-1.X5000-2.

[35] S.K. Sahoo, R.K. Sabat, S. Panda, S.C. Mishra, S. Suwas, Mechanical Property of Pure Magnesium: From Orientation Perspective Pertaining to Deviation from Basal

Orientation, Journal of Materials Engineering and Performance 2015 24:6 24 (2015) 2346–2353. https://doi.org/10.1007/S11665-015-1522-1.

[36] B.L. Mordike, T. Ebert, Magnesium: Properties — applications — potential, Materials Science and Engineering: A 302 (2001) 37–45. https://doi.org/10.1016/S0921-5093(00)01351-4.

[37] Practice for Codification of Unalloyed Magnesium and Magnesium-Alloys, Cast and Wrought, (2018). https://doi.org/10.1520/B0951-11R18.

[38] J.F. Nie, Precipitation and Hardening in Magnesium Alloys, Metallurgical and Materials Transactions A 2012 43:11 43 (2012) 3891–3939. https://doi.org/10.1007/S11661-012-1217-2.

[39] B. Song, J. She, N. Guo, R. Qiu, H. Pan, L. Chai, C. Yang, S. Guo, R. Xin, B. Song, J. She, N. Guo, R. Qiu, H. Pan, L. Chai, C. Yang, S. Guo, R. Xin, Regulating Precipitates by Simple Cold Deformations to Strengthen Mg Alloys: A Review, Materials 2019, Vol. 12, 12 (2019). https://doi.org/10.3390/MA12162507.

[40] J. Wu, L. Jin, J. Dong, F. Wang, S. Dong, The texture and its optimization in magnesium alloy, J. Mater. Sci. Technol. 42 (2020) 175–189. https://doi.org/10.1016/J.JMST.2019.10.010.

[41] N. Stanford, M.R. Barnett, The origin of “rare earth” texture development in extruded Mg-based alloys and its effect on tensile ductility, Materials Science and Engineering: A 496 (2008) 399–408. https://doi.org/10.1016/J.MSEA.2008.05.045.

[42] T. Nakata, S. Kamado, Towards tailoring basal texture of rolled Mg alloy sheet by recrystallization for high room-temperature formability: A review, Journal of Magnesium and Alloys 11 (2023) 3992–4010. https://doi.org/10.1016/J.JMA.2023.08.006.

[43] B. Shi, C. Yang, Y. Peng, F. Zhang, F. Pan, Anisotropy of wrought magnesium alloys: A focused overview, Journal of Magnesium and Alloys 10 (2022) 1476–1510. https://doi.org/10.1016/J.JMA.2022.03.006.

[44] J.D. Robson, Effect of Rare-Earth Additions on the Texture of Wrought Magnesium Alloys: The Role of Grain Boundary Segregation, Metallurgical and Materials Transactions A 2013 45:8 45 (2013) 3205–3212. https://doi.org/10.1007/S11661-013-1950-1.

[45] S. Eswarappa Prameela, P. Yi, Y. Hollenweger, B. Liu, J. Chen, L. Kecskes, D.M. Kochmann, M.L. Falk, T.P. Weihs, Strengthening magnesium by design: Integrating alloying and dynamic processing, Mechanics of Materials 167 (2022) 104203. https://doi.org/10.1016/J.MECHMAT.2021.104203.

[46] L. Gao, R.S. Chen, E.H. Han, Solid solution strengthening behaviors in binary Mg–Y single phase alloys, J. Alloys Compd. 472 (2009) 234–240. https://doi.org/10.1016/J.JALLCOM.2008.04.049.

[47] M.Z. Butt, P. Feltham, Solid-solution hardening, J. Mater. Sci. 28 (1993) 2557–2576. https://doi.org/10.1007/BF00356192/METRICS.

[48] M. Mezbahul-Islam, A.O. Mostafa, M. Medraj, Essential Magnesium Alloys Binary Phase Diagrams and Their Thermochemical Data, J. Mater. 2014 (2014) 704283. https://doi.org/10.1155/2014/704283.

[49] L. Gao, R.S. Chen, E.H. Han, Solid solution strengthening behaviors in binary Mg–Y single phase alloys, J. Alloys Compd. 472 (2009) 234–240. https://doi.org/10.1016/J.JALLCOM.2008.04.049.

[50] K.N. Braszczyńska-Malik, Discontinuous and continuous precipitation in magnesium–aluminium type alloys, J. Alloys Compd. 477 (2009) 870–876. https://doi.org/10.1016/J.JALLCOM.2008.11.008.

[51] L.Y. Wei, G.L. Dunlop, H. Westengen, Precipitation Hardening of Mg-Zn and Mg-Zn-RE alloys, Metallurgical and Materials Transactions A 1995 26:7 26 (1995) 1705–1716. https://doi.org/10.1007/BF02670757.

[52] S. Kandalam, P. Agrawal, G.S. Avadhani, S. Kumar, S. Suwas, Precipitation response of the magnesium alloy WE43 in strained and unstrained conditions, J. Alloys Compd. 623 (2015) 317–323. https://doi.org/10.1016/J.JALLCOM.2014.09.179.

[53] C.M. Cepeda-Jiménez, M. Castillo-Rodríguez, M.T. Pérez-Prado, Origin of the low precipitation hardening in magnesium alloys, Acta Mater. 165 (2019) 164–176. https://doi.org/10.1016/J.ACTAMAT.2018.11.044.

[54] T. Cheng, Y. Zeng, Z. Cui, L. Fan, S. Li, J. Miao, S. Xu, M. Liu, Preparation of nanoprecipitates and ultrafine grains for WE43 alloy to enhance mechanical properties

by pre-aging treatment prior to extrusion, J. Alloys Compd. 1013 (2025) 178607. https://doi.org/10.1016/J.JALLCOM.2025.178607.

[55] H. Yu, Y. Xin, M. Wang, Q. Liu, Hall-Petch relationship in Mg alloys: A review, J. Mater. Sci. Technol. 34 (2018) 248–256. https://doi.org/10.1016/J.JMST.2017.07.022.

[56] D.H. StJohn, M. Qian, M.A. Easton, P. Cao, Z. Hildebrand, Grain refinement of magnesium alloys, Metallurgical and Materials Transactions A 2005 36:7 36 (2005) 1669–1679. https://doi.org/10.1007/S11661-005-0030-6.

[57] X. Luo, Z. Feng, T. Yu, J. Luo, T. Huang, G. Wu, N. Hansen, X. Huang, Transitions in mechanical behavior and in deformation mechanisms enhance the strength and ductility of Mg-3Gd, Acta Mater. 183 (2020) 398–407. https://doi.org/10.1016/J.ACTAMAT.2019.11.034.

[58] A.P. Carvalho, R.B. Figueiredo, An Overview of the Effect of Grain Size on Mechanical Properties of Magnesium and Its Alloys, Mater. Trans. 64 (2023) 1272–1283. https://doi.org/10.2320/MATERTRANS.MT-MF2022005.

[59] R. Mahjoub, N. Stanford, The electronic origins of the “rare earth” texture effect in magnesium alloys, Sci. Rep. 11 (2021). https://doi.org/10.1038/S41598-021-93703-W.

[60] I. Basu, T. Al-Samman, G. Gottstein, Shear band-related recrystallization and grain growth in two rolled magnesium-rare earth alloys, Materials Science and Engineering: A 579 (2013) 50–56. https://doi.org/10.1016/J.MSEA.2013.04.076.

[61] J.F. Nie, K.S. Shin, Z.R. Zeng, Microstructure, Deformation, and Property of Wrought Magnesium Alloys, Metall. Mater. Trans. A Phys. Metall. Mater. Sci. 51 (2020) 6045–6109. https://doi.org/10.1007/S11661-020-05974-Z/FIGURES/54.

[62] B.L. Mordike, T. Ebert, Magnesium Properties - applications - potential, Materials Science and Engineering A 302 (2001) 37–45. https://doi.org/10.1016/S0921-5093(00)01351-4.

[63] H. Mirzadeh, Grain refinement of magnesium alloys by dynamic recrystallization (DRX): A review, Journal of Materials Research and Technology 25 (2023) 7050–7077. https://doi.org/10.1016/J.JMRT.2023.07.150.

[64] M. Murugesan, J.H. Yu, W. Chung, C.W. Lee, Hybrid Artificial Neural Network-Based Models to Investigate Deformation Behavior of AZ31B Magnesium Alloy at Warm Tensile Deformation, Materials 16 (2023). https://doi.org/10.3390/MA16155308.

[65] C.I. Chang, C.J. Lee, J.C. Huang, Relationship between grain size and Zener–Holloman parameter during friction stir processing in AZ31 Mg alloys, Scr. Mater. 51 (2004) 509–514. https://doi.org/10.1016/J.SCRIPTAMAT.2004.05.043.

[66] S.W. Xu, S. Kamado, T. Honma, Recrystallization mechanism and the relationship between grain size and Zener–Hollomon parameter of Mg–Al–Zn–Ca alloys during hot compression, Scr. Mater. 63 (2010) 293–296. https://doi.org/10.1016/J.SCRIPTAMAT.2010.04.012.

[67] R.D. Doherty, D.A. Hughes, F.J. Humphreys, J.J. Jonas, D. Juul Jensen, M.E. Kassner, W.E. King, T.R. McNelley, H.J. McQueen, A.D. Rollett, Current issues in recrystallization: a review, Materials Science and Engineering: A 238 (1997) 219–274. https://doi.org/10.1016/S0921-5093(97)00424-3.

[68] J.E. Burke, D. Turnbull, Recrystallization and grain growth, Progress in Metal Physics 3 (1952) 220–292. https://doi.org/10.1016/0502-8205(52)90009-9.

[69] S.S.A. Shah, M. Liu, A. Khan, F. Ahmad, U.M. Chaudry, M.Y. Khan, M.R. Abdullah, S. Xu, Z. Peng, Recrystallization aspects and factors affecting their roles in Mg alloys: A comprehensive review, Journal of Magnesium and Alloys 13 (2025) 1879–1914. https://doi.org/10.1016/J.JMA.2025.03.020.

[70] Y. Zhang, H. Jiang, Y. Wang, Z. Xu, Effects of Second-Phase Particles on Microstructure Evolution in Mg-2Zn Based Magnesium Alloys during Annealing Treatment, Metals 2020, Vol. 10, Page 777 10 (2020) 777. https://doi.org/10.3390/MET10060777.

[71] Q. Chen, R. Chen, J. Su, Q. He, B. Tan, C. Xu, X. Huang, Q. Dai, J. Lu, The mechanisms of grain growth of Mg alloys: A review, Journal of Magnesium and Alloys 10 (2022) 2384–2397. https://doi.org/10.1016/J.JMA.2022.09.001.

[72] W. Jiang, X. Ren, L. Yu, J. Sun, S. Ni, Y. Huang, M. Song, Twinning-assisted static recrystallization and texture evolution in a Mg-Gd-Y-Zr alloy, Journal of Materials Research and Technology 28 (2024) 4250–4261. https://doi.org/10.1016/J.JMRT.2024.01.007.

[73] X. Ye, Z. Suo, Z. Heng, B. Chen, Q. Wei, J. Umeda, K. Kondoh, J. Shen, An in-situ study of static recrystallization in Mg using high temperature EBSD, Journal of Magnesium and Alloys 12 (2024) 1419–1430. https://doi.org/10.1016/J.JMA.2023.01.021.

[74] F.J. Humphreys, The nucleation of recrystallization at second phase particles in deformed aluminium, Acta Metallurgica 25 (1977) 1323–1344. https://doi.org/10.1016/0001-6160(77)90109-2.

[75] M. Bignon, M. Bernacki, Particle pinning during grain growth—A new analytical model for predicting the mean limiting grain size but also grain size heterogeneity in a 2D polycrystalline context, Acta Mater. 277 (2024) 120174. https://doi.org/10.1016/J.ACTAMAT.2024.120174.

[76] I.H. Jung, M. Sanjari, J. Kim, S. Yue, Role of RE in the deformation and recrystallization of Mg alloy and a new alloy design concept for Mg–RE alloys, Scr. Mater. 102 (2015) 1–6. https://doi.org/10.1016/J.SCRIPTAMAT.2014.12.010.

[77] N. Stanford, D. Atwell, M.R. Barnett, The effect of Gd on the recrystallisation, texture and deformation behaviour of magnesium-based alloys, Acta Mater. 58 (2010) 6773–6783. https://doi.org/10.1016/J.ACTAMAT.2010.09.003.

[78] D. Guan, X. Liu, J. Gao, L. Ma, B.P. Wynne, W.M. Rainforth, Exploring the mechanism of “Rare Earth” texture evolution in a lean Mg–Zn–Ca alloy, Scientific Reports 2019 9:1 9 (2019) 7152-. https://doi.org/10.1038/s41598-019-43415-z.

[79] R. Pei, S. Korte-Kerzel, T. Al-Samman, Normal and abnormal grain growth in magnesium: Experimental observations and simulations, J. Mater. Sci. Technol. 50 (2020) 257–270. https://doi.org/10.1016/J.JMST.2020.01.014.

[80] P.A. Manohar, M. Ferry, T. Chandra, Five Decades of the Zener Equation, ISIJ International 38 (1998) 913–924. https://doi.org/10.2355/ISIJINTERNATIONAL.38.913.

[81] S. Liu, H. Ning, C. Wang, K. Guan, Z. Meng, H. Zhang, H. Wang, The inhibition mechanism of abnormal grain growth in dilute Mg–Al–Ca–Mn alloy through trace Gd addition, Journal of Magnesium and Alloys 13 (2025) 4364–4378. https://doi.org/10.1016/J.JMA.2025.07.010.

[82] H. Li, E. Hsu, J. Szpunar, H. Utsunomiya, T. Sakai, Deformation mechanism and texture and microstructure evolution during high-speed rolling of AZ31B Mg sheets, J. Mater. Sci. 43 (2008) 7148–7156. https://doi.org/10.1007/S10853-008-3021-3.

[83] J. Su, M. Sanjari, A.S.H. Kabir, J.J. Jonas, S. Yue, Static recrystallization behavior of magnesium AZ31 alloy subjected to high speed rolling, Materials Science and Engineering: A 662 (2016) 412–425. https://doi.org/10.1016/J.MSEA.2016.03.047.

[84] K. Shirzad, C. Viney, A critical review on applications of the Avrami equation beyond materials science, J. R. Soc. Interface 20 (2023). https://doi.org/10.1098/RSIF.2023.0242/65046.

[85] J. Farjas, P. Roura, Modification of the Kolmogorov-Johnson-Mehl-Avrami rate equation for non-isothermal experiments and its analytical solution, n.d.

[86] M.M. Myshlyaev, H.J. McQueen, A. Mwembela, E. Konopleva, Twinning, dynamic recovery and recrystallization in hot worked Mg–Al–Zn alloy, Materials Science and Engineering: A 337 (2002) 121–133. https://doi.org/10.1016/S0921-5093(02)00007-2.

[87] X. Li, P. Yang, L.N. Wang, L. Meng, F. Cui, Orientational analysis of static recrystallization at compression twins in a magnesium alloy AZ31, Materials Science and Engineering: A 517 (2009) 160–169. https://doi.org/10.1016/J.MSEA.2009.03.045.

[88] H. Liu, S. Zhu, T.B. Abbott, Z. Zhen, J.-F. Nie, Quasi-in-situ EBSD Study of the Microstructure and Texture Evolution During Static Recrystallization in an Extruded Mg-Mn-Ce Alloy, JOM 74 (2022) 2592–2608. https://doi.org/10.1007/s11837-022-05321-0.

[89] X. Zeng, H. Yi, Z. Zeng, L. Yuan, S. Yi, J. Gao, M. Rainforth, D. Guan, Track-Rex: A universal toolbox for tracking recrystallization nucleation and grain growth behaviors in polycrystalline materials, J. Mater. Sci. Technol. 197 (2024) 149–159. https://doi.org/10.1016/J.JMST.2024.02.013.

[90] H. Yi, H. Li, X. Zeng, H. Liu, D. Guan, Investigation of shear bands induced nucleation and recrystallisation behaviour in a rare earth containing magnesium alloy, Mater. Charact. 222 (2025) 114809. https://doi.org/10.1016/J.MATCHAR.2025.114809.

[91] H. Poulsen, Three-Dimensional X-Ray Diffraction Microscopy, 205 (2004). https://doi.org/10.1007/B97884.

[92] W. Ludwig, P. Reischig, A. King, M. Herbig, E.M. Lauridsen, G. Johnson, T.J. Marrow, J.Y. Buffire, Three-dimensional grain mapping by x-ray diffraction contrast tomography and the use of Friedel pairs in diffraction data analysis, Review of Scientific Instruments 80 (2009) 33905. https://doi.org/10.1063/1.3100200/351823.

[93] J. V. Bernier, R.M. Suter, A.D. Rollett, J.D. Almer, High-Energy X-Ray Diffraction Microscopy in Materials Science, Annu. Rev. Mater. Res. 50 (2020) 395–436. https://doi.org/10.1146/ANNUREV-MATSCI-070616-124125/CITE/REFWORKS.

[94] M. Dai, M.F. Demirel, Y. Liang, J.M. Hu, Graph neural networks for an accurate and interpretable prediction of the properties of polycrystalline materials, Npj Computational Materials 2021 7:1 7 (2021) 103-. https://doi.org/10.1038/s41524-021-00574-w.

[95] R. Cohn, E.A. Holm, Graph convolutional network for predicting abnormal grain growth in Monte Carlo simulations of microstructural evolution, Scientific Reports 2024 14:1 14 (2024) 30259-. https://doi.org/10.1038/s41598-024-81349-3.

[96] S.S. Sørensen, T. Du, C.A.N. Biscio, L. Fajstrup, M.M. Smedskjaer, Persistent homology: A tool to understand medium-range order glass structure, Journal of Non-Crystalline Solids: X 16 (2022) 100123. https://doi.org/10.1016/J.NOCX.2022.100123.

[97] P. Thome, L.F. Arciniaga, S. Tin, “Microstructure Informatics” of Polycrystalline Ni-Base Superalloys Using Computer Vision Techniques to Understand Properties and Performance, Minerals, Metals and Materials Series (2024) 17–32. https://doi.org/10.1007/978-3-031-63937-1_2/FIGURES/10.

[98] K. Rajan, Materials informatics, Materials Today 8 (2005) 38–45. https://doi.org/10.1016/S1369-7021(05)71123-8.

[99] L. Himanen, A. Geurts, A.S. Foster, P. Rinke, Data-Driven Materials Science: Status, Challenges, and Perspectives, Advanced Science 6 (2019). https://doi.org/10.1002/ADVS.201900808.

[100] R. Batra, L. Song, R. Ramprasad, Emerging materials intelligence ecosystems propelled by machine learning, Nat. Rev. Mater. 6 (2021) 655–678. https://doi.org/10.1038/S41578-020-00255-Y.

[101] K. Choudhary, B. DeCost, C. Chen, A. Jain, F. Tavazza, R. Cohn, C.W. Park, A. Choudhary, A. Agrawal, S.J.L. Billinge, E. Holm, S.P. Ong, C. Wolverton, Recent advances and applications of deep learning methods in materials science, NPJ Comput. Mater. 8 (2022). https://doi.org/10.1038/S41524-022-00734-6.

[102] P. Xu, X. Ji, M. Li, W. Lu, Small data machine learning in materials science, NPJ Comput. Mater. 9 (2023). https://doi.org/10.1038/S41524-023-01000-Z.

[103] Y. Cheng, L. Wang, C. Yang, Y. Bai, H. Wang, W. Cheng, H.R. Tiyyagura, A. Komissarov, K.S. Shin, A brief review of machine learning-assisted Mg alloy design, processing, and property predictions, Journal of Materials Research and Technology 30 (2024) 8108–8127. https://doi.org/10.1016/J.JMRT.2024.05.139.

[104] H.K.D.H. Bhadeshia, Neural networks and information in materials science, Stat. Anal. Data Min. 1 (2009) 296–305. https://doi.org/10.1002/sam.10018.

[105] K. Rajan, Materials informatics, Materials Today 8 (2005) 38–45. https://doi.org/10.1016/S1369-7021(05)71123-8.

[106] H. Wang, R. Kumar, A. Pattanaik, R. Kumar, A.S.O. Khawaf Aljaberi, M.A. Abass, Computational methods and artificial intelligence-based modeling of magnesium alloys: a systematic review of machine learning, deep learning, and data-driven design and optimization approaches, Front. Mater. 12 (2025). https://doi.org/10.3389/FMATS.2025.1645227.

[107] D.E.P. Klenam, T.K. Asumadu, M. Vandadi, N. Rahbar, F. McBagonluri, W.O. Soboyejo, Data science and material informatics in physical metallurgy and material science: An overview of milestones and limitations, Results in Materials 19 (2023). https://doi.org/10.1016/J.RINMA.2023.100455.

[108] H. Wang, R. Kumar, A. Pattanaik, R. Kumar, A.S.O. Khawaf Aljaberi, M.A. Abass, Computational methods and artificial intelligence-based modeling of magnesium alloys: a systematic review of machine learning, deep learning, and data-driven design and optimization approaches, Front. Mater. 12 (2025) 1645227. https://doi.org/10.3389/FMATS.2025.1645227/FULL.

[109] P. Tep, M. Bernacki, High-fidelity grain growth modeling: Leveraging deep learning for fast computations, Acta Mater. 301 (2025). https://doi.org/10.1016/J.ACTAMAT.2025.121486.

[110] Y. Chen, Q. Li, X. Chen, J. Tan, H. He, Simulation of recrystallization grain growth in AZ61 magnesium alloy based on GA and 3D CA, Mater. Lett. 377 (2024). https://doi.org/10.1016/J.MATLET.2024.137452.

[111] X. Mi, X. Jing, H. Wang, J. Xu, J. She, A. Tang, B. Holmedal, F. Pan, A machine learning enabled ultra-fine grain design strategy of Mg–Mn-based alloys, Journal of Materials Research and Technology 23 (2023) 4576–4590. https://doi.org/10.1016/J.JMRT.2023.02.091.

[112] J.M. Rickman, H.M. Chan, M.P. Harmer, J.A. Smeltzer, C.J. Marvel, A. Roy, G. Balasubramanian, Materials informatics for the screening of multi-principal elements and high-entropy alloys, Nat. Commun. 10 (2019). https://doi.org/10.1038/S41467-019-10533-1.

[113] M. Murugesan, M. Sajjad, D.W. Jung, M. Murugesan, M. Sajjad, D.W. Jung, Hybrid Machine Learning Optimization Approach to Predict Hot Deformation Behavior of Medium Carbon Steel Material, Metals 2019, Vol. 9, 9 (2019). https://doi.org/10.3390/MET9121315.

[114] Y. Chen, Q. Li, X. Chen, J. Tan, H. He, Simulation of recrystallization grain growth in AZ61 magnesium alloy based on GA and 3D CA, Mater. Lett. 377 (2024) 137452. https://doi.org/10.1016/J.MATLET.2024.137452.

[115] R. Cohn, E.A. Holm, Graph convolutional network for predicting abnormal grain growth in Monte Carlo simulations of microstructural evolution, (2021). https://arxiv.org/pdf/2110.09326 (accessed January 19, 2026).

[116] Y. Qin, S. DeWitt, B. Radhakrishnan, G. Biros, GrainGNN: A dynamic graph neural network for predicting 3D grain microstructure, J. Comput. Phys. 510 (2024). https://doi.org/10.1016/j.jcp.2024.113061.

[117] X. Mi, L. Dai, X. Jing, J. She, B. Holmedal, A. Tang, F. Pan, Accelerated design of high-performance Mg-Mn-based magnesium alloys based on novel bayesian optimization, Journal of Magnesium and Alloys 12 (2024) 750–766. https://doi.org/10.1016/J.JMA.2024.01.005.

[118] M. Ghorbani, M. Boley, P.N.H. Nakashima, N. Birbilis, An active machine learning approach for optimal design of magnesium alloys using Bayesian optimisation, Sci. Rep. 14 (2024). https://doi.org/10.1038/S41598-024-59100-9.

[119] B. Liu, J. Yang, X. Zhang, Q. Yang, J. Zhang, X. Li, Development and application of magnesium alloy parts for automotive OEMs: A review, Journal of Magnesium and Alloys 11 (2023) 15–47. https://doi.org/10.1016/J.JMA.2022.12.015.

[120] J. Zhang, J. Miao, N. Balasubramani, D.H. Cho, T. Avey, C.Y. Chang, A.A. Luo, Magnesium research and applications: Past, present and future, Journal of Magnesium and Alloys 11 (2023) 3867–3895. https://doi.org/10.1016/J.JMA.2023.11.007.

[121] Y. Zhu, S. Lv, T. Li, Y. Ren, Z. Wang, D. Hou, Direct observation of annealing-driven recrystallization behavior in magnesium alloy at low strain condition, Journal of Magnesium and Alloys 13 (2025) 4985–4996. https://doi.org/10.1016/J.JMA.2024.11.016.

[122] J. Yang, Y. Zhai, T. Kang, M. Fu, S. Wang, X. Liu, S. Zhou, W. Xie, W. Wang, X. Liu, Evolution of the microstructure and mechanical properties of WE43 magnesium alloy during multipass hot rolling, International Journal of Minerals, Metallurgy and Materials 32 (2025) 1681–1692. https://doi.org/10.1007/S12613-024-2983-8.

[123] R. Kushwaha, V. Choudhari, P. Dash, W. Muhammad, S.K. Sahoo, S. Gollapudi, R.K. Sabat, Mechanism of precipitation distribution in WE43 alloy, Mater. Charact. 197 (2023). https://doi.org/10.1016/J.MATCHAR.2023.112660.

[124] M.K. Guru, J. Bohlen, R.C. Aydin, N. Ben Khalifa, Machine learning pipeline for Structure–Property modeling in Mg-alloys using microstructure and texture descriptors, Acta Mater. 295 (2025) 121132. https://doi.org/10.1016/J.ACTAMAT.2025.121132.

[125] S.C. Sutton, A.A. Luo, Constitutive behavior and processing maps of a new wrought magnesium alloy ZE20 (Mg-2Zn-0.2Ce), Journal of Magnesium and Alloys 8 (2020) 111–126. https://doi.org/10.1016/J.JMA.2019.11.007.

[126] J.E. Plumeri, L. Madej, W.Z. Misiolek, Development of extrusion technology for magnesium alloy ZE20, Procedia Eng. 207 (2017) 389–394. https://doi.org/10.1016/J.PROENG.2017.10.793.

[127] X. Ma, Z. Huang, M. Li, J.E. Allison, Recrystallization Behavior of the Magnesium Alloy ZE20, Magnesium Technology 2015 (2015) 177–182. https://doi.org/10.1007/978-3-319-48185-2_33.

[128] J.E. Plumeri, Development and Application of a Numerical Model for the Prediction of Hot Deformation Processing of a Novel ZE20 Magnesium Alloy, (2018).

[129] L.M. Calado, M.J. Carmezim, M.F. Montemor, Rare Earth Based Magnesium Alloys—A Review on WE Series, Front. Mater. 8 (2022) 804906. https://doi.org/10.3389/FMATS.2021.804906/FULL.

[130] W. Xu, J. Li, Z. Zhang, H. Yuan, G. An, H. Shi, C. Cai, W. Jiang, W. Li, Q. Wei, Laser powder bed fusion of WE43 magnesium alloy with superior balance of strength and ductility, Journal of Magnesium and Alloys 13 (2025) 1275–1293. https://doi.org/10.1016/J.JMA.2024.03.012.

[131] T. Cheng, Y. Zeng, Z. Cui, L. Fan, S. Li, J. Miao, S. Xu, M. Liu, Preparation of nanoprecipitates and ultrafine grains for WE43 alloy to enhance mechanical properties by pre-aging treatment prior to extrusion, J. Alloys Compd. 1013 (2025) 178607. https://doi.org/10.1016/J.JALLCOM.2025.178607.

[132] L. Li, Z. Zhang, D. Zhang, F. Qi, Y. Dai, W. Wei, X. Ouyang, Effects of metal ion implantation (Fe, Ti, Zn and Zr) on mechanical properties, corrosion resistance and biocompatibility of WE43 Mg alloy, Journal of Magnesium and Alloys 13 (2025) 296–310. https://doi.org/10.1016/J.JMA.2024.05.005.

[133] L. Zhou, T. Huang, G. Ren, Z. Wang, F. Wang, Z. Wei, P. Mao, Z. Liu, Microstructural, Mechanical, and Damping Properties of WE43 Alloy, JOM 2025 77:5 77 (2025) 3723–3735. https://doi.org/10.1007/S11837-025-07250-0.

[134] M.Z. Farooq, Y. Wu, L. Lu, M. Zheng, Combustion phases of magnesium alloys based on predicted heating rate using machine learning, Measurement 242 (2025) 116192. https://doi.org/10.1016/J.MEASUREMENT.2024.116192.

[135] A. Maqbool, A. Khalad, N.Z. Khan, Prediction of corrosion rate for friction stir processed WE43 alloy by combining PSO-based virtual sample generation and machine learning, Journal of Magnesium and Alloys 12 (2024) 1518–1528. https://doi.org/10.1016/J.JMA.2024.04.012.

[136] H. Yin, Y. Yang, H. Song, P. Liu, X. Cui, G. Jin, L. Zhao, P. She, Enhanced protection of WE43 Mg alloy via laser-cladded FeCoNiCuAl/Cu9Al gradient HEA coatings: ML-assisted property prediction, Mater. Chem. Phys. 351 (2026) 131976. https://doi.org/10.1016/J.MATCHEMPHYS.2025.131976.

[137] J.F. Nie, Precipitation and Hardening in Magnesium Alloys, Metallurgical and Materials Transactions A 2012 43:11 43 (2012) 3891–3939. https://doi.org/10.1007/S11661-012-1217-2.

[138] J.F. Nie, X. Gao, S.M. Zhu, Enhanced age hardening response and creep resistance of Mg–Gd alloys containing Zn, Scr. Mater. 53 (2005) 1049–1053. https://doi.org/10.1016/J.SCRIPTAMAT.2005.07.004.

[139] J.F. Nie, Effects of precipitate shape and orientation on dispersion strengthening in magnesium alloys, Scr. Mater. 48 (2003) 1009–1015. https://doi.org/10.1016/S1359-6462(02)00497-9.

[140] S. Sandlöbes, M. Friák, J. Neugebauer, D. Raabe, Basal and non-basal dislocation slip in Mg–Y, Materials Science and Engineering: A 576 (2013) 61–68. https://doi.org/10.1016/J.MSEA.2013.03.006.

[141] S.R. Agnew, L. Capolungo, C.A. Calhoun, Connections between the basal I1 “growth” fault and ⟨ c + a ⟩ dislocations, Acta Mater. 82 (2015) 255–265. https://doi.org/10.1016/J.ACTAMAT.2014.07.056.

[142] E.A. Ball, P.B. Prangnell, Tensile-compressive yield asymmetries in high strength wrought magnesium alloys, Scripta Metallurgica et Materialia 31 (1994) 111–116. https://doi.org/10.1016/0956-716X(94)90159-7.

[143] L.W.F. Mackenzie, B. Davis, F.J. Humphreys, G.W. Lorimer, The deformation, recrystallisation and texture of three magnesium alloy extrusions, Materials Science and Technology 23 (2007) 1173–1180. https://doi.org/10.1179/174328407X226509.

[144] J.D. Robson, D.T. Henry, B. Davis, Particle effects on recrystallization in magnesium–manganese alloys: Particle-stimulated nucleation, Acta Mater. 57 (2009) 2739–2747. https://doi.org/10.1016/J.ACTAMAT.2009.02.032.

[145] N. Stanford, M.R. Barnett, The origin of “rare earth” texture development in extruded Mg-based alloys and its effect on tensile ductility, Materials Science and Engineering: A 496 (2008) 399–408. https://doi.org/10.1016/J.MSEA.2008.05.045.

[146] I. Basu, T. Al-Samman, G. Gottstein, Shear band-related recrystallization and grain growth in two rolled magnesium-rare earth alloys, Materials Science and Engineering: A 579 (2013) 50–56. https://doi.org/10.1016/J.MSEA.2013.04.076.

[147] I. Basu, T. Al-Samman, Triggering rare earth texture modification in magnesium alloys by addition of zinc and zirconium, Acta Mater. 67 (2014) 116–133. https://doi.org/10.1016/J.ACTAMAT.2013.12.015.

[148] X. Li, P. Yang, L.N. Wang, L. Meng, F. Cui, Orientational analysis of static recrystallization at compression twins in a magnesium alloy AZ31, Materials Science and Engineering: A 517 (2009) 160–169. https://doi.org/10.1016/J.MSEA.2009.03.045.

[149] T. Al-Samman, K.D. Molodov, D.A. Molodov, G. Gottstein, S. Suwas, Softening and dynamic recrystallization in magnesium single crystals during c-axis compression, Acta Mater. 60 (2012) 537–545. https://doi.org/10.1016/J.ACTAMAT.2011.10.013.

[150] I. Basu, T. Al-Samman, Twin recrystallization mechanisms in magnesium-rare earth alloys, Acta Mater. 96 (2015) 111–132. https://doi.org/10.1016/J.ACTAMAT.2015.05.044.

[151] J. Bohlen, M.R. Nürnberg, J.W. Senn, D. Letzig, S.R. Agnew, The texture and anisotropy of magnesium–zinc–rare earth alloy sheets, Acta Mater. 55 (2007) 2101–2112. https://doi.org/10.1016/J.ACTAMAT.2006.11.013.

[152] N. Stanford, M. Barnett, Effect of composition on the texture and deformation behaviour of wrought Mg alloys, Scr. Mater. 58 (2008) 179–182. https://doi.org/10.1016/J.SCRIPTAMAT.2007.09.054.

[153] T. Al-Samman, X. Li, Sheet texture modification in magnesium-based alloys by selective rare earth alloying, Materials Science and Engineering: A 528 (2011) 3809–3822. https://doi.org/10.1016/J.MSEA.2011.01.080.

[154] A. Imandoust, C.D. Barrett, A.L. Oppedal, W.R. Whittington, Y. Paudel, H. El Kadiri, Nucleation and preferential growth mechanism of recrystallization texture in high purity binary magnesium-rare earth alloys, Acta Mater. 138 (2017) 27–41. https://doi.org/10.1016/J.ACTAMAT.2017.07.038.

[155] L.L. Rokhlin, Magnesium alloys containing rare earth metals: structure and properties, Magnesium Alloys Containing Rare Earth Metals (2003). https://doi.org/10.1201/9781482265163/MAGNESIUM-ALLOYS-CONTAINING-RARE-EARTH-METALS-ROKHLIN.

[156] S. Yi, H.G. Brokmeier, D. Letzig, Microstructural evolution during the annealing of an extruded AZ31 magnesium alloy, J. Alloys Compd. 506 (2010) 364–371. https://doi.org/10.1016/J.JALLCOM.2010.07.008.

[157] C.D. Barrett, A. Imandoust, H. El Kadiri, The effect of rare earth element segregation on grain boundary energy and mobility in magnesium and ensuing texture weakening, Scr. Mater. 146 (2018) 46–50. https://doi.org/10.1016/J.SCRIPTAMAT.2017.11.004.

[158] D. Guan, W.M. Rainforth, L. Ma, B. Wynne, J. Gao, Twin recrystallization mechanisms and exceptional contribution to texture evolution during annealing in a magnesium alloy, Acta Mater. 126 (2017) 132–144. https://doi.org/10.1016/J.ACTAMAT.2016.12.058.

[159] A. Levinson, R.K. Mishra, R.D. Doherty, S.R. Kalidindi, Influence of deformation twinning on static annealing of AZ31 Mg alloy, Acta Mater. 61 (2013) 5966–5978. https://doi.org/10.1016/J.ACTAMAT.2013.06.037.

[160] S.W. Lee, S.H. Park, Static recrystallization mechanism in cold-rolled magnesium alloy with off-basal texture based on quasi in situ EBSD observations, J. Alloys Compd. 844 (2020) 156185. https://doi.org/10.1016/J.JALLCOM.2020.156185.

[161] D. Guan, W.M. Rainforth, J. Gao, L. Ma, B. Wynne, Individual effect of recrystallisation nucleation sites on texture weakening in a magnesium alloy: Part 2- shear bands, Acta Mater. 145 (2018) 399–412. https://doi.org/10.1016/J.ACTAMAT.2017.12.019.

[162] Z.R. Zeng, Y.M. Zhu, S.W. Xu, M.Z. Bian, C.H.J. Davies, N. Birbilis, J.F. Nie, Texture evolution during static recrystallization of cold-rolled magnesium alloys, Acta Mater. 105 (2016) 479–494. https://doi.org/10.1016/J.ACTAMAT.2015.12.045.

[163] T. Nakata, Z.H. Li, T.T. Sasaki, K. Hono, S. Kamado, Role of grain boundary segregation on microstructural development in basal-textured Mg-Al-Zn alloy sheet, Scr. Mater. 218 (2022) 114828. https://doi.org/10.1016/J.SCRIPTAMAT.2022.114828.

[164] M.G. Jiang, C. Xu, H. Yan, T. Nakata, Z.W. Chen, C.S. Lao, R.S. Chen, S. Kamado, E.H. Han, Quasi-in-situ observing the rare earth texture evolution in an extruded Mg-Zn-Gd alloy with bimodal microstructure, Journal of Magnesium and Alloys 9 (2021) 1797–1805. https://doi.org/10.1016/J.JMA.2020.09.001.

[165] F. Humphreys, M. Hatherly, Recrystallization and related annealing phenomena, (2012). https://books.google.com/books?hl=zh-CN&lr=&id=Kt11V4m2bqEC&oi=fnd&pg=PP1&ots=RszRLmpkrw&sig=IrI5mLs8xg9AZX9cnLyQhmyWeE0 (accessed January 9, 2026).

[166] P.J. Hurley, F.J. Humphreys, A study of recrystallization in single-phase aluminium using in-situ annealing in the scanning electron microscope, J. Microsc. 213 (2004) 225–234. https://doi.org/10.1111/j.0022-2720.2004.01300.x.

[167] H.J. Lee, H.N. Han, D.H. Kim, U.H. Lee, K.H. Oh, P.R. Cha, In situ observation of the grain growth of the copper electrodeposits for ultralarge scale integration, Appl. Phys. Lett. 89 (2006) 161924. https://doi.org/10.1063/1.2364119/129661.

[168] S.I. Wright, M.M. Nowell, A review of in situ EBSD studies, in: Electron Backscatter Diffraction in Materials Science, Springer US, 2009: pp. 329–337. https://doi.org/10.1007/978-0-387-88136-2_24.

[169] K. Mirpuri, H. Wendrock, S. Menzel, K. Wetzig, J. Szpunar, Texture evolution in Copper film at high temperature studied in situ by electron back-scatter diffraction, Thin Solid Films 496 (2006) 703–717. https://doi.org/10.1016/J.TSF.2005.08.353.

[170] D.P. Field, L.T. Bradford, M.M. Nowell, T.M. Lillo, The role of annealing twins during recrystallization of Cu, Acta Mater. 55 (2007) 4233–4241. https://doi.org/10.1016/J.ACTAMAT.2007.03.021.

[171] Y. Xu, H.J. Yang, M.A. Meyers, Dynamic recrystallization in the shear bands of Fe–Cr–Ni monocrystal: Electron backscatter diffraction characterization, Scr. Mater. 58 (2008) 691–694. https://doi.org/10.1016/J.SCRIPTAMAT.2007.12.006.

[172] R. Hielscher, H. Schaeben, A novel pole figure inversion method: Specification of the MTEX algorithm, J. Appl. Crystallogr. 41 (2008) 1024–1037. https://doi.org/10.1107/S0021889808030112.

[173] J. Zhang, Y. Zhang, W. Ludwig, D. Rowenhorst, P.W. Voorhees, H.F. Poulsen, Three-dimensional grain growth in pure iron. Part I. statistics on the grain level, Acta Mater. 156 (2018) 76–85. https://doi.org/10.1016/J.ACTAMAT.2018.06.021.

[174] A. Bhattacharya, Y.F. Shen, C.M. Hefferan, S.F. Li, J. Lind, R.M. Suter, G.S. Rohrer, Three-dimensional observations of grain volume changes during annealing of polycrystalline Ni, Acta Mater. 167 (2019) 40–50. https://doi.org/10.1016/J.ACTAMAT.2019.01.022.

[175] S. Sandlöbes, S. Zaefferer, I. Schestakow, S. Yi, R. Gonzalez-Martinez, On the role of non-basal deformation mechanisms for the ductility of Mg and Mg–Y alloys, Acta Mater. 59 (2011) 429–439. https://doi.org/10.1016/J.ACTAMAT.2010.08.031.

[176] M.R. Barnett, M.D. Nave, C.J. Bettles, Deformation microstructures and textures of some cold rolled Mg alloys, Materials Science and Engineering: A 386 (2004) 205–211. https://doi.org/10.1016/J.MSEA.2004.07.030.

[177] Y. Pang, D. Sun, Q. Gu, K.C. Chou, X. Wang, Q. Li, Comprehensive Determination of Kinetic Parameters in Solid-State Phase Transitions: An Extended Jonhson–Mehl–Avrami–Kolomogorov Model with Analytical Solutions, Cryst. Growth Des. 16 (2016) 2404–2415. https://doi.org/10.1021/ACS.CGD.6B00187.

[178] Q. Luo, Y. Guo, B. Liu, Y. Feng, J. Zhang, Q. Li, K. Chou, Thermodynamics and kinetics of phase transformation in rare earth–magnesium alloys: A critical review, J. Mater. Sci. Technol. 44 (2020) 171–190. https://doi.org/10.1016/J.JMST.2020.01.022.

[179] Q. Li, X. Lin, Q. Luo, Y. Chen, J. Wang, B. Jiang, F. Pan, Kinetics of the hydrogen absorption and desorption processes of hydrogen storage alloys: A review, International Journal of Minerals, Metallurgy and Materials 2022 29:1 29 (2022) 32–48. https://doi.org/10.1007/S12613-021-2337-8.

[180] J.D. Robson, S.J. Haigh, B. Davis, D. Griffiths, Grain Boundary Segregation of Rare-Earth Elements in Magnesium Alloys, Metallurgical and Materials Transactions A 2015 47:1 47 (2015) 522–530. https://doi.org/10.1007/S11661-015-3199-3.

[181] D. Guan, W.M. Rainforth, J. Gao, J. Sharp, B. Wynne, L. Ma, Individual effect of recrystallisation nucleation sites on texture weakening in a magnesium alloy: Part 1- double twins, Acta Mater. 135 (2017) 14–24. https://doi.org/10.1016/J.ACTAMAT.2017.06.015.

[182] J.F. Nie, Y.M. Zhu, J.Z. Liu, X.Y. Fang, Periodic segregation of solute atoms in fully coherent twin boundaries, Science (1979). 340 (2013) 957–960. https://doi.org/10.1126/SCIENCE.1229369;JOURNAL:JOURNAL:SCIENCE;WGROUP:STRING:PUBLICATION.

[183] C.D. Barrett, A. Imandoust, A.L. Oppedal, K. Inal, M.A. Tschopp, H. El Kadiri, Effect of grain boundaries on texture formation during dynamic recrystallization of magnesium alloys, Acta Mater. 128 (2017) 270–283. https://doi.org/10.1016/J.ACTAMAT.2017.01.063.

[184] A. Ostapovets, P. Šedá, A. Jäger, P. Lejček, Characteristics of coincident site lattice grain boundaries developed during equal channel angular pressing of magnesium single crystals, Scr. Mater. 64 (2011) 470–473. https://doi.org/10.1016/J.SCRIPTAMAT.2010.11.011.

[185] B. Li, M. Liao, Q. Ma, Z. McClelland, Structure of grain boundaries with 30°[0 0 0 1] misorientation in dynamically recrystallized magnesium alloys, Comput. Mater. Sci. 101 (2015) 175–180. https://doi.org/10.1016/J.COMMATSCI.2015.01.034.

[186] M. Lentz, M. Risse, N. Schaefer, W. Reimers, I.J. Beyerlein, Strength and ductility with {10 11}-{1012} double twinning in a magnesium alloy, Nat. Commun. 7 (2016). https://doi.org/10.1038/ncomms11068.

[187] S. Mu, J.J. Jonas, G. Gottstein, Variant selection of primary, secondary and tertiary twins in a deformed Mg alloy, Acta Mater. 60 (2012) 2043–2053. https://doi.org/10.1016/J.ACTAMAT.2012.01.014.

[188] M.D. Nave, M.R. Barnett, Microstructures and textures of pure magnesium deformed in plane-strain compression, Scr. Mater. 51 (2004) 881–885. https://doi.org/10.1016/J.SCRIPTAMAT.2004.07.002.

[189] J.F. Nie, K.S. Shin, Z.R. Zeng, Microstructure, Deformation, and Property of Wrought Magnesium Alloys, Metall. Mater. Trans. A Phys. Metall. Mater. Sci. 51 (2020) 6045–6109. https://doi.org/10.1007/s11661-020-05974-z.

[190] Y. Yang, X. Xiong, J. Chen, X. Peng, D. Chen, F. Pan, Research advances in magnesium and magnesium alloys worldwide in 2020, Journal of Magnesium and Alloys 9 (2021) 705–747. https://doi.org/10.1016/j.jma.2021.04.001.

[191] J. Humphreys, G.S. Rohrer, A. Rollett, Recrystallization Textures, in: Recrystallization and Related Annealing Phenomena, Elsevier, 2017: pp. 431–468. https://doi.org/10.1016/b978-0-08-098235-9.00012-4.

[192] T. Nakata, S. Kamado, Towards tailoring basal texture of rolled Mg alloy sheet by recrystallization for high room-temperature formability: A review, Journal of Magnesium and Alloys 11 (2023) 3992–4010. https://doi.org/10.1016/j.jma.2023.08.006.

[193] A. Imandoust, C.D. Barrett, T. Al-Samman, K.A. Inal, H. El Kadiri, A review on the effect of rare-earth elements on texture evolution during processing of magnesium alloys, J. Mater. Sci. 52 (2017). https://doi.org/10.1007/s10853-016-0371-0.

[194] D. Guan, X. Liu, J. Gao, L. Ma, B.P. Wynne, W.M. Rainforth, Exploring the mechanism of “Rare Earth” texture evolution in a lean Mg–Zn–Ca alloy, Sci. Rep. 9 (2019). https://doi.org/10.1038/s41598-019-43415-z.

[195] N. Stanford, M.R. Barnett, The origin of “rare earth” texture development in extruded Mg-based alloys and its effect on tensile ductility, Materials Science and Engineering: A 496 (2008) 399–408. https://doi.org/10.1016/j.msea.2008.05.045.

[196] T. Mayama, M. Noda, R. Chiba, M. Kuroda, Crystal plasticity analysis of texture development in magnesium alloy during extrusion, in: Int. J. Plast., 2011: pp. 1916–1935. https://doi.org/10.1016/j.ijplas.2011.02.007.

[197] X. Huang, K. Suzuki, Y. Chino, Static recrystallization behavior of hot-rolled Mg-Zn-Ce magnesium alloy sheet, J. Alloys Compd. 724 (2017) 981–990. https://doi.org/10.1016/j.jallcom.2017.07.093.

[198] T. Al-Samman, X. Li, Sheet texture modification in magnesium-based alloys by selective rare earth alloying, Materials Science and Engineering: A 528 (2011) 3809–3822. https://doi.org/10.1016/j.msea.2011.01.080.

[199] J.D. Robson, S.J. Haigh, B. Davis, D. Griffiths, Grain Boundary Segregation of Rare-Earth Elements in Magnesium Alloys, Metall. Mater. Trans. A Phys. Metall. Mater. Sci. 47 (2016) 522–530. https://doi.org/10.1007/s11661-015-3199-3.

[200] J.D. Robson, Effect of rare-earth additions on the texture of wrought magnesium alloys: The role of grain boundary segregation, in: Metall. Mater. Trans. A Phys. Metall. Mater.

Sci., Springer Boston, 2014: pp. 3205–3212. https://doi.org/10.1007/s11661-013-1950-1.

[201] A. Issa, J.E. Saal, C. Wolverton, Formation of high-strength β ′ precipitates in Mg-RE alloys: The role of the Mg/β ″ interfacial instability, Acta Mater. 83 (2015) 75–83. https://doi.org/10.1016/j.actamat.2014.09.024.

[202] P. Minárik, J. Veselý, J. Čížek, M. Zemková, T. Vlasák, T. Krajňák, J. Kubásek, R. Král, D. Hofman, J. Stráská, Effect of secondary phase particles on thermal stability of ultra-fine grained Mg-4Y-3RE alloy prepared by equal channel angular pressing, Mater. Charact. 140 (2018) 207–216. https://doi.org/10.1016/j.matchar.2018.04.006.

[203] C. Antion, P. Donnadieu, F. Perrard, A. Deschamps, C. Tassin, A. Pisch, Hardening precipitation in a Mg-4Y-3RE alloy, Acta Mater. 51 (2003) 5335–5348. https://doi.org/10.1016/S1359-6454(03)00391-4.

[204] I. Basu, T. Al-Samman, Twin recrystallization mechanisms in magnesium-rare earth alloys, Acta Mater. 96 (2015) 111–132. https://doi.org/10.1016/j.actamat.2015.05.044.

[205] P. Hidalgo-Manrique, S.B. Yi, J. Bohlen, D. Letzig, M.T. Pérez-Prado, Effect of Nd additions on extrusion texture development and on slip activity in a Mg-Mn alloy, Metall. Mater. Trans. A Phys. Metall. Mater. Sci. 44 (2013) 4819–4829. https://doi.org/10.1007/s11661-013-1823-7.

[206] J.D. Robson, D.T. Henry, B. Davis, Particle effects on recrystallization in magnesium-manganese alloys: Particle-stimulated nucleation, Acta Mater. 57 (2009) 2739–2747. https://doi.org/10.1016/j.actamat.2009.02.032.

[207] J.J. Bhattacharyya, S.R. Agnew, G. Muralidharan, Texture enhancement during grain growth of magnesium alloy AZ31B, Acta Mater. 86 (2015) 80–94. https://doi.org/10.1016/j.actamat.2014.12.009.

[208] Q. Chen, R. Chen, J. Su, Q. He, B. Tan, C. Xu, X. Huang, Q. Dai, J. Lu, The mechanisms of grain growth of Mg alloys: A review, Journal of Magnesium and Alloys 10 (2022) 2384–2397. https://doi.org/10.1016/j.jma.2022.09.001.

[209] P. Peng, K. Zhang, J. She, A. Tang, J. Zhang, K. Song, Q. Yang, F. Pan, Role of second phases and grain boundaries on dynamic recrystallization behavior in ZK60 magnesium alloy, J. Alloys Compd. 861 (2021). https://doi.org/10.1016/j.jallcom.2020.157958.

[210] Z.R. Zeng, Y.M. Zhu, S.W. Xu, M.Z. Bian, C.H.J. Davies, N. Birbilis, J.F. Nie, Texture evolution during static recrystallization of cold-rolled magnesium alloys, Acta Mater. 105 (2016) 479–494. https://doi.org/10.1016/j.actamat.2015.12.045.

[211] F. Han, X. Luo, K. Marthinsen, G. Wu, Z. Hou, X. Huang, Effect of initial grain size on the recrystallization behavior and recrystallization texture of a Mg–3Gd alloy, J. Mater. Sci. Technol. 188 (2024) 169–182. https://doi.org/10.1016/j.jmst.2023.11.044.

[212] D. Guan, W.M. Rainforth, L. Ma, B. Wynne, J. Gao, Twin recrystallization mechanisms and exceptional contribution to texture evolution during annealing in a magnesium

alloy, Acta Mater. 126 (2017) 132–144. https://doi.org/10.1016/j.actamat.2016.12.058.

[213] D. Guan, W.M. Rainforth, J. Gao, J. Sharp, B. Wynne, L. Ma, Individual effect of recrystallisation nucleation sites on texture weakening in a magnesium alloy: Part 1- double twins, Acta Mater. 135 (2017) 14–24. https://doi.org/10.1016/j.actamat.2017.06.015.

[214] B.Q. Shi, Y.Z. Wang, X.L. Shang, L.Y. Zhao, C.Q. Li, D.C. Chen, B.H. Nie, R.S. Chen, W. Ke, Microstructure evolution of twinning-induced shear bands and correlation with 'RD-split' texture during hot rolling in a Mg-1.1Zn-0.76Y-0.56Zr alloy, Mater. Charact. 187 (2022). https://doi.org/10.1016/j.matchar.2022.111853.

[215] I. Basu, T. Al-Samman, G. Gottstein, Shear band-related recrystallization and grain growth in two rolled magnesium-rare earth alloys, Materials Science and Engineering: A 579 (2013) 50–56. https://doi.org/10.1016/j.msea.2013.04.076.

[216] D. Guan, W.M. Rainforth, J. Gao, L. Ma, B. Wynne, Individual effect of recrystallisation nucleation sites on texture weakening in a magnesium alloy: Part 2- shear bands, Acta Mater. 145 (2018) 399–412. https://doi.org/10.1016/j.actamat.2017.12.019.

[217] I. Basu, T. Al-Samman, Triggering rare earth texture modification in magnesium alloys by addition of zinc and zirconium, Acta Mater. 67 (2014) 116–133. https://doi.org/10.1016/j.actamat.2013.12.015.

[218] X. Zeng, P. Minárik, P. Dobroň, D. Letzig, K.U. Kainer, S. Yi, Role of deformation mechanisms and grain growth in microstructure evolution during recrystallization of Mg-Nd based alloys, Scr. Mater. 166 (2019) 53–57. https://doi.org/10.1016/j.scriptamat.2019.02.045.

[219] L.W.F. Mackenzie, M.O. Pekguleryuz, The recrystallization and texture of magnesium-zinc-cerium alloys, Scr. Mater. 59 (2008) 665–668. https://doi.org/10.1016/j.scriptamat.2008.05.021.

[220] M.R. Barnett, M.D. Nave, C.J. Bettles, Deformation microstructures and textures of some cold rolled Mg alloys, Materials Science and Engineering: A 386 (2004) 205–211. https://doi.org/10.1016/j.msea.2004.07.030.

[221] L. Li, B.C. Suh, J.S. Suh, C. Kim, Y. Go, Y.M. Kim, Static recrystallization behavior of the cold-rolled Mg-1Al-1Zn-0.1Ca-0.2Y magnesium alloy sheet, J. Alloys Compd. 938 (2023). https://doi.org/10.1016/j.jallcom.2022.168508.

[222] X. Zeng, H. Yi, Z. Zeng, L. Yuan, S. Yi, J. Gao, M. Rainforth, D. Guan, Track-Rex: A universal toolbox for tracking recrystallization nucleation and grain growth behaviors in polycrystalline materials, J. Mater. Sci. Technol. 197 (2024) 149–159. https://doi.org/10.1016/j.jmst.2024.02.013.

[223] A.S. Ebner, S. Jakob, H. Clemens, R. Pippan, V. Maier-Kiener, S. He, W. Ecker, D. Scheiber, V.I. Razumovskiy, Grain boundary segregation in Ni-base alloys: A combined atom probe tomography and first principles study, Acta Mater. 221 (2021). https://doi.org/10.1016/j.actamat.2021.117354.

[224] R. Mahjoub, M. Ferry, N. Stanford, Grain boundary kinetics in magnesium alloys from first principles, Comput. Mater. Sci. 210 (2022). https://doi.org/10.1016/j.commatsci.2021.111042.

[225] J. French, X.M. Bai, Molecular dynamics studies of grain boundary mobility and anisotropy in BCC γ-uranium, Journal of Nuclear Materials 565 (2022). https://doi.org/10.1016/j.jnucmat.2022.153744.

[226] J. Humphreys, G.S. Rohrer, A. Rollett, Grain Growth Following Recrystallization, in: Recrystallization and Related Annealing Phenomena, Elsevier, 2017: pp. 375–429. https://doi.org/10.1016/b978-0-08-098235-9.00011-2.

[227] Y. Li, A.J. Bushby, D.J. Dunstan, The Hall-Petch effect as a manifestation of the general size effect, Proceedings of the Royal Society A: Mathematical, Physical and Engineering Sciences 472 (2016). https://doi.org/10.1098/rspa.2015.0890.

[228] D. Li, G. Fan, X. Huang, D. Juul Jensen, K. Miao, C. Xu, L. Geng, Y. Zhang, T. Yu, Enhanced strength in pure Ti via design of alternating coarse- and fine-grain layers, Acta Mater. 206 (2021) 116627. https://doi.org/10.1016/J.ACTAMAT.2021.116627.

[229] Z. Zeng, J.F. Nie, S.W. Xu, C.H.J. Davies, N. Birbilis, Super-formable pure magnesium at room temperature, Nat. Commun. 8 (2017). https://doi.org/10.1038/s41467-017-01330-9.

[230] R. Zheng, M. Liu, Z. Zhang, K. Ameyama, C. Ma, Towards strength-ductility synergy through hierarchical microstructure design in an austenitic stainless steel, Scr. Mater. 169 (2019) 76–81. https://doi.org/10.1016/j.scriptamat.2019.05.017.

[231] M. Liu, W. Gong, R. Zheng, J. Li, Z. Zhang, S. Gao, C. Ma, N. Tsuji, Achieving excellent mechanical properties in type 316 stainless steel by tailoring grain size in homogeneously recovered or recrystallized nanostructures, Acta Mater. 226 (2022). https://doi.org/10.1016/j.actamat.2022.117629.

[232] Y. Zhang, Y. Li, Q. Huo, Exploring the dependence of creep behavior on the grain size of a peak-aged Mg-10.5Y alloy, J. Alloys Compd. 972 (2024) 172912. https://doi.org/10.1016/J.JALLCOM.2023.172912.

[233] R. Zheng, W. Gong, J. ping Du, S. Gao, M. Liu, G. Li, T. Kawasaki, S. Harjo, C. Ma, S. Ogata, N. Tsuji, Rediscovery of Hall-Petch strengthening in bulk ultrafine grained pure Mg at cryogenic temperature: A combined in-situ neutron diffraction and electron microscopy study, Acta Mater. 238 (2022) 118243. https://doi.org/10.1016/J.ACTAMAT.2022.118243.

[234] F. Najafkhani, S. Kheiri, B. Pourbahari, H. Mirzadeh, Recent advances in the kinetics of normal/abnormal grain growth: a review, Archives of Civil and Mechanical Engineering 21 (2021). https://doi.org/10.1007/s43452-021-00185-8.

[235] C.E. Krill Iii, E.A. Holm, J.M. Dake, R. Cohn, K. Holíková, F. Andorfer, Extreme Abnormal Grain Growth: Connecting Mechanisms to Microstructural Outcomes, 15 (2025) 19. https://doi.org/10.1146/annurev-matsci-080921.

[236] D. Guan, W.M. Rainforth, L. Ma, B. Wynne, J. Gao, Twin recrystallization mechanisms and exceptional contribution to texture evolution during annealing in a magnesium alloy, Acta Mater. 126 (2017) 132–144. https://doi.org/10.1016/J.ACTAMAT.2016.12.058.

[237] S. Takajo, C.C. Merriman, S.C. Vogel, D.P. Field, In-situ EBSD study on the cube texture evolution in 3 wt% Si steel complemented by ex-situ EBSD experiment — From nucleation to grain growth, Acta Mater. 166 (2019) 100–112. https://doi.org/10.1016/J.ACTAMAT.2018.11.054.

[238] C. Yildirim, N. Mavrikakis, P.K. Cook, R. Rodriguez-Lamas, M. Kutsal, H.F. Poulsen, C. Detlefs, 4D microstructural evolution in a heavily deformed ferritic alloy: A new perspective in recrystallisation studies, Scr. Mater. 214 (2022) 114689. https://doi.org/10.1016/J.SCRIPTAMAT.2022.114689.

[239] J. Sun, T. Yu, C. Xu, W. Ludwig, Y. Zhang, 3D characterization of partially recrystallized Al using high resolution diffraction contrast tomography, Scr. Mater. 157 (2018) 72–75. https://doi.org/10.1016/J.SCRIPTAMAT.2018.08.001.

[240] S. Schmidt, S.F. Nielsen, C. Gundlach, L. Margulies, X. Huang, D.J. Jensen, Watching the growth of bulk grains during recrystallization of deformed metals, Science (1979). 305 (2004) 229–232. https://doi.org/10.1126/SCIENCE.1098627;JOURNAL:JOURNAL:SCIENCE;WGROUP:STRING:PUBLICATION.

[241] P. Reischig, A. King, L. Nervo, N. Viganó, Y. Guilhem, W.J. Palenstijn, K.J. Batenburg, M. Preuss, W. Ludwig, Advances in X-ray diffraction contrast tomography: flexibility in the setup geometry and application to multiphase materials, Urn:Issn:0021-8898 46 (2013) 297–311. https://doi.org/10.1107/S0021889813002604.

[242] S.A. McDonald, P. Reischig, C. Holzner, E.M. Lauridsen, P.J. Withers, A.P. Merkle, M. Feser, Non-destructive mapping of grain orientations in 3D by laboratory X-ray microscopy, Sci. Rep. 5 (2015). https://doi.org/10.1038/srep14665.

[243] J. Sun, J.M. Dake, J. Oddershede, Grain structure evolution during heat treatment of a semisolid Al-Cu alloy studied with lab-based diffraction contrast tomography, Tomography of Materials and Structures 4 (2024) 100025. https://doi.org/10.1016/J.TMATER.2024.100025.

[244] Z. Xu, J. Sun, J.M. Dake, J. Oddershede, H. Kaur, S.K. Naghibzadeh, C.E. Krill, K. Dayal, G.S. Rohrer, Grain boundary properties and microstructure evolution in an Al-Cu alloy, Acta Mater. 292 (2025) 121041. https://doi.org/10.1016/J.ACTAMAT.2025.121041.

[245] N. Lu, J. Kang, N. Senabulya, R. Keinan, N. Gueninchault, A.J. Shahani, Dynamics of particle-assisted abnormal grain growth revealed through integrated three-dimensional microanalysis, Acta Mater. 195 (2020) 1–12. https://doi.org/10.1016/J.ACTAMAT.2020.04.049.

[246] J. Sun, A. Lyckegaard, Y.B. Zhang, S.A. Catherine, B.R. Patterson, F. Bachmann, N. Gueninchault, H. Bale, C. Holzner, E. Lauridsen, D. Juul Jensen, 4D Study of Grain Growth in Armco Iron Using Laboratory X-ray Diffraction Contrast Tomography, in: IOP

Conf. Ser. Mater. Sci. Eng., Institute of Physics Publishing, 2017. https://doi.org/10.1088/1757-899X/219/1/012039.

[247] J. Zhang, Y. Zhang, W. Ludwig, D. Rowenhorst, P.W. Voorhees, H.F. Poulsen, Three-dimensional grain growth in pure iron. Part I. statistics on the grain level, Acta Mater. 156 (2018) 76–85. https://doi.org/10.1016/J.ACTAMAT.2018.06.021.

[248] M.A. Groeber, M.A. Jackson, Groeber and Jackson Integrating Materials and Manufacturing Innovation, 2014. http://www.immijournal.com/content/3/1/5.

[249] A. Berger, M. Herwegh, J.O. Schwarz, B. Putlitz, Quantitative analysis of crystal/grain sizes and their distributions in 2D and 3D, J. Struct. Geol. 33 (2011) 1751–1763. https://doi.org/10.1016/J.JSG.2011.07.002.

[250] J. Zhang, S. Han, Y. Sun, X. Chen, P. Chen, Z. Li, G. Huang, F. Pan, Enhanced strength of WE43 magnesium-rare earth alloy via combining extrusion and aging, Materials Science and Engineering: A 880 (2023) 145329. https://doi.org/10.1016/J.MSEA.2023.145329.

[251] I. Basu, T. Al-Samman, G. Gottstein, Shear band-related recrystallization and grain growth in two rolled magnesium-rare earth alloys, Materials Science and Engineering: A 579 (2013) 50–56. https://doi.org/10.1016/J.MSEA.2013.04.076.

[252] Q. Chen, R. Chen, J. Su, Q. He, B. Tan, C. Xu, X. Huang, Q. Dai, J. Lu, The mechanisms of grain growth of Mg alloys: A review, Journal of Magnesium and Alloys 10 (2022) 2384–2397. https://doi.org/10.1016/j.jma.2022.09.001.

[253] R. Pei, S. Korte-Kerzel, T. Al-Samman, Normal and abnormal grain growth in magnesium: Experimental observations and simulations, J. Mater. Sci. Technol. 50 (2020) 257–270. https://doi.org/10.1016/J.JMST.2020.01.014.

[254] T. Breithaupt, L.N. Hansen, S. Toppaladoddi, R.F. Katz, The role of grain-environment heterogeneity in normal grain growth: A stochastic approach, Acta Mater. 209 (2021) 116699. https://doi.org/10.1016/J.ACTAMAT.2021.116699.

[255] E.F.F. Knipschildt-Okkels, Y.B. Zhang, X. Lei, T. Yu, W. Liu, S. Fæster, R.E. Sanders, D. Juul Jensen, Multimodal 3D quantification of particle stimulated nucleation in industrially manufactured aluminium AA5182 sheet, Acta Mater. 282 (2025) 120446. https://doi.org/10.1016/J.ACTAMAT.2024.120446.

[256] X. Zeng, H. Yi, Z. Zeng, L. Yuan, S. Yi, J. Gao, M. Rainforth, D. Guan, Track-Rex: A universal toolbox for tracking recrystallization nucleation and grain growth behaviors in polycrystalline materials, J. Mater. Sci. Technol. 197 (2024) 149–159. https://doi.org/10.1016/J.JMST.2024.02.013.

[257] D. Guan, J. Nutter, J. Sharp, J. Gao, W. Mark Rainforth, Direct observation of precipitation along twin boundaries and dissolution in a magnesium alloy annealing at high temperature, Scr. Mater. 138 (2017) 39–43. https://doi.org/10.1016/J.SCRIPTAMAT.2017.05.015.

[258] M.F. Ashby, R.M.A. Gentamore, The dragging of small oxide particles by migrating grain boundaries in copper, Acta Metallurgica 16 (1968) 1081–1092. https://doi.org/10.1016/0001-6160(68)90043-6.